A Second Generation URANS Approach for Application to Aerodynamic Design and Optimization in the Automotive Industry

by

Liangyu Xu

B.S., Shanghai Jiao Tong University (2011)
S.M., Shanghai Jiao Tong University (2014)

Submitted to the Department of Mechanical Engineering
in partial fulfillment of the requirements for the degree of

Doctor of Philosophy

at the

MASSACHUSETTS INSTITUTE OF TECHNOLOGY

February 2020

Signature redacted

Author .....
Department of Mechanical Engineering
January 14, 2020

Certified by ..... Signature redacted .....
Émilio Baglietto
Associate Professor of Nuclear Science and Engineering
Thesis Supervisor

Certified by ..... Signature redacted .....
Wim van Rees
Assistant Professor of Mechanical Engineering
Thesis Committee Chair

Accepted by ..... Signature redacted .....
Nicolas Hadjiconstantinou
Chairman, Department Committee on Graduate Theses

A Second Generation URANS Approach for Application to Aerodynamic Design and Optimization in the Automotive Industry

by

Liangyu Xu

Submitted to the Department of Mechanical Engineering
on January 14, 2020, in partial fulfillment of the
requirements for the degree of
Doctor of Philosophy

Abstract

In the U.S., transportation is responsible for approximately 70% of all petroleum consumption and is now the largest source of carbon emissions and air pollution. Aerodynamics is an important aspect for energy saving and emission reduction in the automotive industry. In the design stage, aerodynamic drag is minimized through optimization of the vehicle shape, and Computational Fluid Dynamics (CFD) has become an invaluable tool to support this process. In combination with advanced optimization methods, CFD promises to considerably reduce the carbon footprint of modern passenger and good transportation. However, its success is severely limited by the poor description of complex unsteady turbulence at a practicable computational cost. For the flow past a car, unsteady turbulent flow structures are generated in the separation off the windshield, the mirrors, the wheels, and in the wake of the car body. Capturing these turbulent structures is important for an accurate evaluation of the aerodynamic drag, especially for trains and freight trucks, where flow interaction between multiple bodies is involved and influences the overall drag. While high fidelity CFD techniques like Direct Numerical Simulation (DNS) and Large Eddy Simulation (LES) offer the ability to resolve the necessary turbulent structures and therefore predicting the drag with high accuracy, their computational costs are high that cannot allow efficient optimization. Reynolds Averaged Navier-Stokes (RANS) approach is most widely used for its computationally effectiveness and robustness, but current RANS models have turned out to have a poor description of complex unsteady turbulence. Hybrid models offer a potential balance between accuracy and computational cost. Despite increased accuracy, the present hybrid models suffer from lack of robustness, grid consistency, ease of use.

To address the issues of the existing hybrid models and to better address the industrial need for a robust, grid consistent, and widely applicable hybrid model, an interesting new approach has been proposed by Lenci [1] and Baglietto [2], which aims at increasing locally resolving the flow structures in the framework of second-

generation URANS approach (2G-URANS), and is named STRUCT. The idea has shown the potential to provide improved accuracy, robustness, and mesh consistency for wall-bounded flows. However, the specific formulation delivered requires an averaging approach that introduces some application challenges, in particular being very sensitive to inlet boundary conditions and leading to spurious hybrid activation in open boundary external flows.

This thesis assembles and demonstrates a new approach to support effective aerodynamic design and optimization through the delivery of an average-free STRUCT implementation applicable to all flow conditions. The new model introduces a source term in the ε equation of the standard k-ε model based on a time scale defined by the second invariant of the resolved velocity gradient tensor and therefore is named STRUCT-ε model. The new STRUCT-ε model is then validated on the fundamental cases and cases in the automotive industry, demonstrating improved accuracy in comparison with the most commonly used Realizable k-ε model (RKE), at a comparable computational cost and with low mesh sensitivity.

To further reduce the computational cost to support effective aerodynamic design, the extension of the STRUCT-ε model to fast running steady simulations is explored, and the results have shown improved performance with a better agreement with the reference data in comparison with the RKE model. On this basis, the STRUCT-ε model is applied to the optimization of a simplified tractor-trailer for demonstrating its value: at a computational cost amenable to industrial applications, it provides improved accuracy for the drag evaluation, and as a result, the optimal solution it generates through optimization is more accurate than the one obtained with the traditional RANS models.

Thesis Supervisor: Emilio Baglietto
Title: Associate Professor of Nuclear Science and Engineering

Acknowledgments

The past five years at MIT is a unique and memorable experience in my life. There are several people I would like to thank for helping me supporting me during my Ph.D. study and research.

First of all, I would like to express my sincere gratitude to my advisor, Professor Emilio Baglietto, for accepting me as one of your Ph.D. student, when I needed support as my former advisor left MIT. You are a knowledgeable and inspiring advisor during my research. Whenever I was stuck and skeptical about my approach, you could always give me some good suggestions to move forward, making my research in general smooth and on a good track. You are a good advisor to learn from, not only your expertise on CFD, but also your way of thinking about problems and your strong interpersonal skills. In addition, you were so supportive and considerate during the last year when I became pregnant and gave birth to my daughter and therefore was not very productive.

I am also greatly appreciative of Professor Stefano Brizzolara, my advisor at MIT in the first two years. You brought me in the field of CFD and nurtured my interest in this field. You gave me detailed guidance in my research and helped me solve practical problems.

Also, I would like to thank you, Professor Wim Van Rees, for being my committee chair and for your helpful suggestions in further analysis of the results to improve the completeness of the thesis. I also direct my thanks to Professor John Heywood, who provided valuable comments and helped me improve my thesis work.

Gratitude also goes to Professor Javier Garcia from UNIVERSIDAD POLITCNICA DE MADRID, for suggesting the simplified tractor-trailer test case for the optimization work. I would specially thank Peter Altmann from Siemens for the help with the geometry and mesh for the DrivAer model.

I would like to thank my MIT colleagues in the CFD research group: Jinyong Feng, Michael Acton, Giulia Agostinelli, Etienne Dermarly, Ravikishore Kommajosyula, Nazar Lubchenko, Benjamin Magolan, for offering me advice, inspiration,

and friendship. And I thank all my fantastic friends and schoolmates around MIT, who enriched my life immensely. Also, many thanks to my collaborators in the project of sodium cooled fast reactor key modeling and analysis for commercial deployment, Mark Anderson, James Alexander Schneider, Zeyun Wu, Cihang, Sarah Morgan, who helped me complete the project, providing me the financial support for my research.

Finally, I would like to thank my family for all your support during my Ph.D. life. Most of all, I give my special thanks to my husband, Xin Xu, who has always been there sharing my happiness, understanding and helping me relieve stress, and encouraging me when I feel frustrated. Thank you, my dear baby daughter, for being so lovely and your smile is the largest emotional support for me. Thank you, mom, for coming to the U.S. to help me take care of the baby girl so that Ive got more time to work on the thesis. Thank you, dad, for your continued support to guiding me through self-improvement.

Contents

List of Figures

List of Tables

Chapter 1

Introduction

1.1 Background: The role of aerodynamic optimization for energy saving and emission reduction

The global demand for energy is increasing rapidly due to population and economic growth. According to the U.S. Energy Information Administration [3], in 2018, 28% of all energy used in the United States is in the transportation sector. Of that used, approximately 92% is in the form of petroleum, 3.1% is natural gas, 5% is renewable, and less than 1% is electricity, unclear, or other fuels. Overall, transportation is responsible for approximately 70% of all U.S. petroleum consumption (Figure 1-1) and is now the largest source of carbon emissions and the main cause of air pollution in the US. Burning one gallon of gasoline creates about 20 pounds of CO2 - which means the average vehicle creates roughly 6 to 9 tons of CO2 each year. In the US, most states follow the emission regulations by the federal United States Environmental Protection Agency (EPA). Globally, the European Union has worked on plans to reduce vehicle emissions through setting up more stringent emissions standards. It proposes to reduce the 2021 limit for emissions from new cars and vans by 15% from 2025 and by 30% from 2030, which are the most challenging targets for reducing CO2 emissions in the world [19].

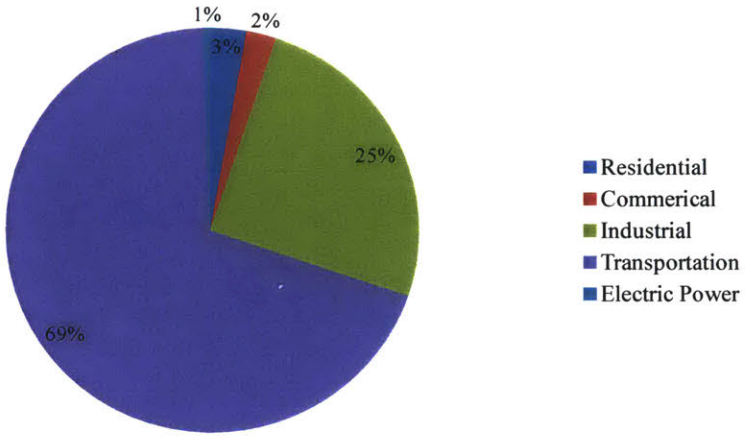

Figure 1-1: U.S. petroleum consumption by sector, 2018. Source: [3].

To save energy and reduce emissions, popular techniques include increasing engine fuel efficiency, improving the intake and exhaust systems, and introducing lightweight technologies. Hybrid or electric cars and new energy technology have gained wide applicability, and alternative fuel cars are also becoming more popular. Another effective way to reduce fuel consumption can be achieved by optimizing the car shapes and adopting new materials.

Aerodynamics plays a key role in energy saving and emission reduction in the automotive industry. It is concerned with the study of how air flows around a vehicle at speed, and the resultant forces and moments on the vehicle. The drag force, the force component anti-parallel to vehicle velocity, is the primary focus. This is because the aerodynamic drag increases quadratically with the speed of the vehicle; at freeway speeds, it is a larger contributor to the engine load than rolling resistance, drive-line friction, or accessory load. In the case of heavy-duty vehicles, for a typical modern Class 8 tractor-trailer, Figure 1-2 shows the estimated horsepower associated with aerodynamic drag in comparison to the power required to overcome rolling resistance and to supply needed auxiliary power, plotted as a function of speed. At 70 miles per hour, a common highway speed today, overcoming aerodynamic drag represents about 65% of the total energy expenditure for a typical heavy truck vehicle [20]. Stricter fuel economy and emissions regulations, consumer demand for better fuel economy,

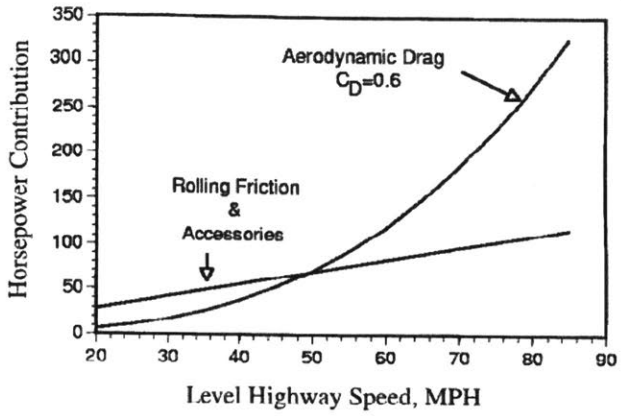

Figure 1-2: Horsepower required to overcome aerodynamic drag and rolling friction/accessories as a function of travel speed for a typical Class 8 tractor-trailer (from [4]).

and the advent of electric cars where driving range is at a premium due to limited battery capacity motivate manufacturers to decrease drag as much as possible.

Optimizing the vehicle shape is one of the most readily achievable solutions to decrease the aerodynamic drag and to reduce fuel consumption for vehicles. Through altering the vehicle shape, the flow structures responsible for generating aerodynamic drag can be altered or weakened, such as undesirable flow separation from the vehicle surface. For example, Song et al. (2012) [21] conducted shape optimization of a sedan by using an Artificial Neural Network (ANN). Six local parts from the end of the sedan namely, (i) hood (ii) windshield (iii) rear window (iv) side window (v) rear-end shrinkage and (vi) trunk lid was chosen as the design variables for modifying the sedan rear shape, and an ANN approximation model was established with 64 experimental points. The optimized rear shape resulted in 5.64% improvement in the aerodynamic performance in comparison with the baseline vehicle. Guo et al. (2018) [22] adopted an automatic process for optimization of the aerodynamic shape of a hatchback car. Eight design variables were selected and three phases of body optimization were conducted for the front, the rear, and the entirety of the vehicle, finally achieving a drag reduction of 10.34%. For heavy-duty vehicles, major influences on the drag include tractor design, trailer configuration, gap region between tractor and trailer, and appendages [23]. It is conceivable that present-day truck drag coefficients

might be reduced by as much as 50% [4]. This reduction in drag would represent approximately a 25% reduction in fuel use at highway speeds. An estimated total savings of $1.5 billion per year can be recognized in the United States alone for just a 6% reduction in fuel use [20].

1.2 Current use of CFD in the aerodynamic design and optimization of vehicles

In the aerodynamic design, wind tunnel testing is one of the most important tools to improve vehicle aerodynamics. In a wind tunnel, a full-scale or a reduced-scale model of the vehicle is fixed in place as a stream of air is blown towards it to simulate the airflow that the vehicle would encounter when driven on a real road. The amount of generated drag is then measured to estimate the drag coefficient and assess the overall aerodynamic performance of the vehicle. Wind tunnel testing can be used to observe the flow field around the vehicles and to acquire data on the aerodynamic forces, the variation of aerodynamic forces and moments with yaw, surface pressure distribution, the influence of different vehicle details, assessment of brake cooling flows, and more, to improve their designs. It is an accurate method for evaluating the vehicle aerodynamics, and can also be used to verify theoretical analyses and validate numerical simulation results. However, wind tunnel tests often require high costs in facilities and human resources, which are time-consuming and can considerably stretch the product design cycle. As wind tunnels that are large enough for full-scale vehicles are rare, tunnel tests are usually performed with scale-models. Besides, wind tunnel tests can not fully represent the complex flow conditions on a real road like wind gusts or atmospheric turbulence. Due to these differences, the direct application of drag changes measured on models in wind tunnels is not likely to agree with the actual on-road performance, which has been confirmed by the significant differences observed between the wind tunnel and on-road drag reductions [24, 25, 26]. Therefore, the industry is still forced to leverage road tests for a more accurate evaluation of

the vehicle drag for various loads and speed conditions, which provide valuable trend evaluations but are affected by considerable uncertainty [27, 28] .

With continuous advances in computational power and the development of turbulence theory, Computational Fluid Dynamics (CFD) has made great progress in both research and application. CFD is nowadays largely employed as an effective optimization tool in the automotive industry, especially for aerodynamic design driven by critical factors such as the reduction of drag force [29] . In CFD, high-performance computers are used to numerically solve the governing flow equations to study the airflow over a Computer Aided Design (CAD) representation of the vehicle. The strategy of CFD is to replace the continuous fluid domain with a discrete domain using a grid. In the continuous domain, each flow variable is defined at every grid cell. The boundary conditions are attributed to the corresponding cells and the governing partial differential equations are applied to each cell with consideration of the neighboring cells, which creates a system of algebraic equations. This system of equations is then solved with an iterative technique involving a very large number of repetitive calculations. The solutions represent the flow characteristics of every cell, from which the whole fluid behavior can be determined.

Compared to wind tunnel tests, CFD has the following advantages:

- The use of CFD simulations enables shorter design cycles. After the design of the vehicle body is completed in the computers, the existing body surface can be extracted for generating the surface mesh in a CFD software, from which the volume mesh and boundary conditions can be generated for numerical calculations. It is fast to use CFD simulations for recalculation and verification in the early stage design and adaptation of the vehicle body.

- CFD simulations can be integrated with the CAD/CAE/CAM system, making it possible to automate the design-evaluate-redesign cycle. With further integration of matured optimization algorithms, it is possible to realize the full potential of computer based design automation.

- CFD simulations do not abide by the constraints of the wind tunnels, for ex-

ample, the tunnel wall interference or the blocking effect of the test section. It is possible to eliminate these effects by defining a large computational domain. Also, it is easier to change the boundary conditions in the CFD simulations, enabling flow calculations under a larger variety of operating conditions. CFD simulations do not have the influence and limitations from inflow turbulence, Reynolds number, wind speed, wind direction, supporting structure interference, as in the wind tunnel tests. Besides, it is possible to study scenarios that are impossible for wind tunnel tests, such as the aerodynamic interaction between two vehicles driving in very close proximity.

- CFD simulations allow deeper insight into the flow behavior. Both the global and the detailed local flow patterns can be observed, enabling a better understanding of the flow process and mechanisms that cannot be obtained through wind tunnel tests.

Nevertheless, CFD also has limitations and shortcomings. First, the accuracy of the CFD solutions relies on reasonable physical assumptions and realizable mathematical models. The calculation error depends on many settings including the turbulence modeling, solution schemes, interpolation methods, etc. To obtain high-quality results, correct selection of all models and schemes is necessary and requires expert knowledge. Secondly, the generation of a proper computational mesh for discretizing the domain to a great extent depends on the skills and experience of the engineers. For example, to ensure simulation accuracy, many turbulence models with eddy-resolving capability, such as Large Eddy Simulation (LES) or Detached Eddy Simulation (DES), require the generation of a high-quality mesh, which conforms to both the geometrical constraints and the model restrictions. While creating such a high-quality mesh can be a difficult challenge, this requirement can be relaxed if the selected turbulence model does not have strong mesh sensitivity, and in this thesis, one of the key strengths of the new proposed model is low sensitivity to the mesh while maintaining the eddy-resolving capability.

1.3 Challenges in the aerodynamic evaluation of vehicles using CFD

Despite the widespread use of CFD as an optimization tool in the automotive industry, the quality and general reliability of the solution is still lacking. While academic demonstrations of the models applied on carefully constructed meshes have often shown excellent results, these have not been successfully translated to industrial applications. During the validation process, it is found that the predicted forces and flow fields can be inaccurate, and sometimes even contradicting the test results. These inaccuracies can be due to many factors, including simplifications in the model geometry, low quality of the computational meshes, sensitivity to uncertainties in the boundary conditions, etc. The most important factor is recognized as the shortfalls in the turbulence modeling, and additionally, these shortcomings often exacerbate the influence of computational meshes and boundary conditions.

Turbulence is a state of fluid motion that is characterized by apparently random and chaotic three-dimensional vorticity [30]. In contrast to a laminar flow, which can be described as a smooth and layered stream, a turbulent flow is always irregular in space and time, as shown in Figure 1-3(b). When turbulence is present, it usually dominates all other flow phenomena and results in increased energy dissipation, mixing, heat transfer, etc. The turbulent flow contains a continuous spectrum of eddies, from the largest ones that are comparable to the size of the object, to the smallest Kolmogorov dissipation scale can be as small as several mm [31]. Eddies overlap in space, with large ones carrying small ones. The kinetic energy enters turbulence at the largest scales, then is transferred to smaller and smaller scales through inertial effects, and finally the energy is dissipated into heat by viscous action at the smallest scale. This process is known as a turbulent energy cascade. Under the Kolmogorov local equilibrium hypothesis [32], as small-scale motions tend to have small time scales, one may assume that these motions are statistically independent of the relatively slow large scale turbulence and the mean flow, and the small scale eddies depend on the rate at which they receive energy from the larger scales and on the viscous dissipa-

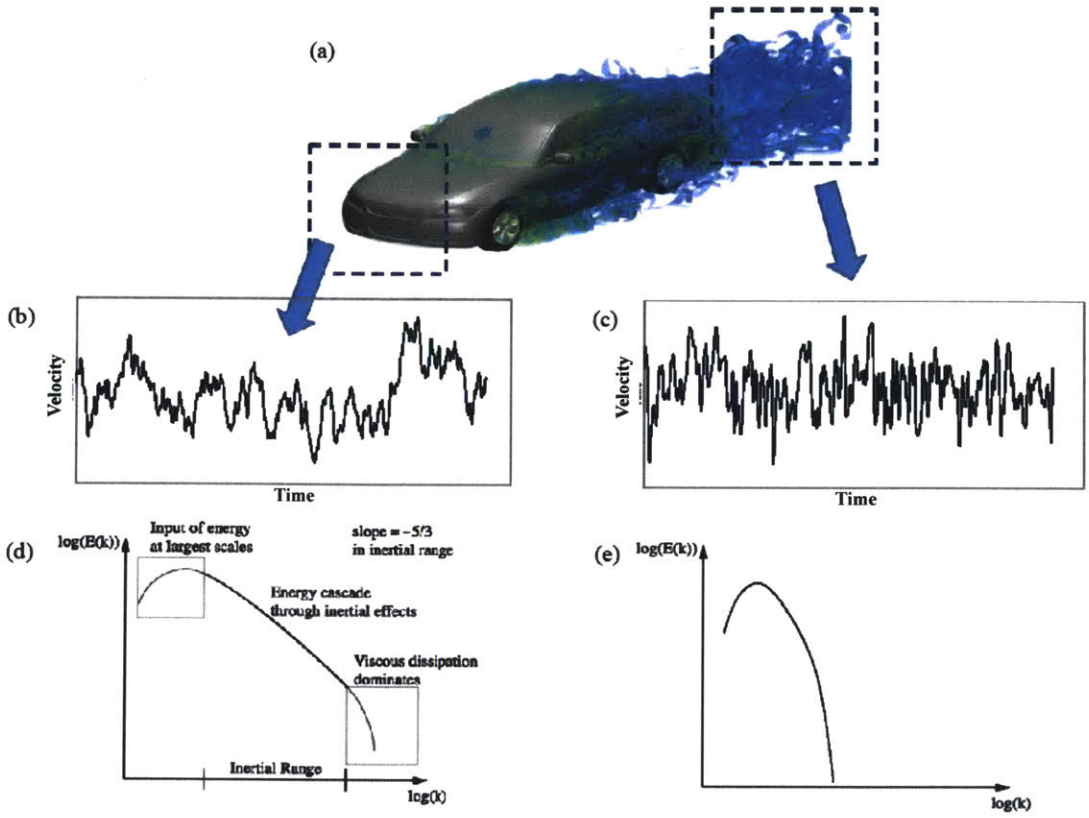

Figure 1-3: (a) unsteady flow structures around a car, (b) the velocity signal for the marked area in front of the car plotted in arbitrary units of time and velocity, (c) the velocity signals for the marked area in the car wake plotted in arbitrary units of time and velocity, (d) a qualitative depiction of the energy spectrum for the marked area in front of the car (from [5]), (e) a qualitative depiction of the energy spectrum for the marked area in the car wake.

tion. The rate of energy supply should be equal to the rate of dissipation because the net rate of change of small-scale energy is related to the time scale of the flow as a whole and is small compared to the rate at which energy is dissipated. Under this assumption, the energy spectrum is a power-law with an exponent very close to -5/3 in the inertia range of turbulent flows. The energy cascade can be presented as in Figure 1-3(d), where E(k) represents the energy at wavenumber k.

To support the design optimization of vehicles, we need efficient computational methods to model turbulence. Therefore the most popular approach in the industry is to use Reynolds-averaged Navier-Stokes (RANS) models to solve the mean flow based on the assumption of an equilibrium spectrum. The most commonly used RANS closures in the automotive industry include the Realizable k-ϵ model by Shih and coworkers [33] and the k-ω SST model by Menter [34, 35]. As the flow around a vehicle is by nature unsteady in the separation and wake regions, unsteady RANS (URANS) are also considered in practice aimed at capturing the unsteadiness through transient simulations, thus improving accuracy for the drag prediction. Besides, there has been a great deal of work to improve the traditional (U)RANS models with particular attention to external aerodynamic applications, such as the V2F k-ϵ model [36], the elliptic blending model [37], the Abe-Kondoh-Nagano model [38], etc.

However, the (U)RANS approach has demonstrated to be unable to deal with large separation, often providing even incorrect trends for the vehicle design with the prediction of large separation areas. This failure is expected as in the wake region, the concept of (U)RANS is not applicable. Large scale vortices are generated from the flow separation past the vehicle with scales close to the vehicle geometry; these vortices cannot decay to the dissipative scale sufficiently fast, therefore violating the equilibrium assumption. The corresponding energy spectrum is shown qualitatively in Figure 1-3(e), in which energy is all in the large scales being generated and the -5/3 exponent power-law is not observed. Due to the inadequacy of the (U)RANS concept for predicting separation, the large scale vortices should be resolved to improve prediction accuracy. It is obvious that this becomes a major challenge for heavy-duty vehicles, where the massive vortices off the cabin interact with the trailer,

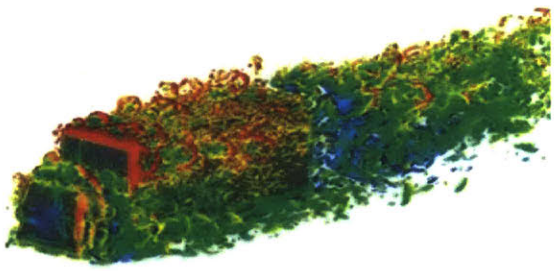

Figure 1-4: Instantaneous coherent structures around a truck obtained with an LES study (from [6]).

and the interaction and wakes have a dominant influence on the overall aerodynamic performance, as shown in Figure 1-4.

Turbulent resolving methods exist to accurately evaluate the drag on these vehicles. In particular Large Eddy Simulation (LES) methods have shown, when applied on well-constructed meshes, to be able to produce high-quality results [6, 16]. However, LES has two aspects that make it impractical for design and optimization. First, it requires high computational cost that limits the number of runs, making it unsuitable for optimization. Second, it has a high sensitivity to the mesh quality, boundary conditions, and geometrical details resolution. So the industry has looked at hybrid approaches to bridge the gap between URANS and LES and to provide increased flow resolution while limiting the computational cost amenable to effective design exploration. Popular hybrid models include Detached Eddy Simulation (DES) [39] and its variants [40, 41] and Scale Adaptive Simulation (SAS) [42]. Unfortunately, these methods have also shown weak general applicability and strong sensitivity to the mesh when under-resolved, therefore negating the advantage of the hybridization. These issues have been particularly noticeable in heavy vehicle applications, where the Lattice Boltzmann based approach (available solvers include Power-FLOW [43], XFlow [44], Palabos [45], etc.) has become popular since the high parallel performance of the method allows introducing a reasonable resolution of the wakes. This enables the industry to improve the trend predictions while abandoning the ability to predict the quantitative forces accurately due to the extremely poor resolution of the boundary layers [46].

Starting from the evidenced shortcomings of the existing turbulence approaches, we propose a list of features for a turbulence model that would ideally support aerodynamic optimization:

- It should be capable of resolving unsteady wakes contributing to more accurate drag evaluation at a low computational cost.
- The flow resolution should be controlled by the flow physics (characteristics of turbulent energy spectrum) and not by the mesh resolution so that users are not required to define a priori how much to resolve the flow.
- It should be able to yield accurate prediction of the drag coefficient within a 10% error on low-quality RANS type meshes.
- It should naturally recover the reference RANS solution in the absence of large wakes.
- It should demonstrate convergent predictions at increasing grid resolutions.
- The hybridization should be generally applicable in order to take advantage of future RANS closure advances.
- It should provide a physics-based approach that works not only for external aerodynamic applications but also for internal flow scenarios.

1.4 Proposal of the STRUCT approach and existing limitations

To address the shortcomings of existing hybrid models and the industrial need for a robust, grid consistent, and widely applicable hybrid model, Lenci [1] and Baglietto [2] proposed a new hybrid approach, STRUCT, which leverages the second invariant of the resolved velocity gradient tensor to identify the areas for hybridization. Unlike other hybrid models, the STRUCT approach combines the URANS features of robustness and grid consistency with the scale-resolving capability of LES. The improved performance of the STRUCT concept has been demonstrated through application to a variety of flow tests, including configurations that had not been addressed success-

fully by other hybrid models. A better agreement with the experimental data has been achieved in the mean velocity and turbulent stress profiles in comparison with URANS.

In the original STRUCT approach, the hybridization is implemented straightforwardly by reducing the overall eddy viscosity through a reduction parameter depending on the ratio of the resolved time scale and the modeled flow time scale. After testing on a controlled version of STRUCT to select case-dependent parameters a posterior, two fully self-adaptive formulations STRUCT-L and STRUCT-T have been proposed for the model completeness. However, both formulations suffer from a robustness problem: undesirable hybrid activation appears in open boundary external flow applications when improper inlet conditions are specified. This makes the model limited to a wall dominated flows and inapplicable to external aerodynamic applications.

1.5 Thesis objectives and contents

The objective of the thesis is to deliver an improved STRUCT model with robust applicability to external flow applications while keeping all the advantages of the original STRUCT approach including grid consistency, easy implementation, and the ability to obtain improved accuracy at a relatively low computational cost. The improved performance of the new STRUCT model will be demonstrated and validated against both fundamental benchmarks and relevant benchmarks in the automotive industry, to ensure its applicability and provide best practice guidelines to the industry. Finally, the model's ability to support design optimization for vehicles is to be demonstrated through testing on the optimization of a simplified tractor-trailer model and validation of the optimal solutions obtained. An additional objective of the thesis is to evaluate the applicability of the new STRUCT formulation to fast-running steady-state simulations (RANS) for design optimization.

This thesis is organized as follows: Chapter 2 introduces the idea and formulations of the original STRUCT approach by Lenci [1] and Baglietto [2]. Chapter 3

explains the problem of the original STRUCT approach and presents the proposal of an improved STRUCT model STRUCT- for robust application to external flow applications. Chapter 4 focuses on the validation of the new STRUCT- model through benchmarks on both fundamental cases and relevant cases in the automotive industry. Chapter 5 assesses the capability of extending the STRUCT- formulations to the steady simulations from a practical industrial need. Chapter 6 applies the STRUCT- model to the optimization of a simplified tractor-trailer model; the resulting optimal solutions are validated by LES. Chapter 7 summarizes the thesis findings and contributions.

Chapter 2

STRUCTure based turbulence resolution

This chapter introduces the fundamental ideas of turbulence modeling. RANS, LES, and hybrid methods are briefly reviewed to provide the reader with the basic concepts that allow introducing the concept of STRUCTure based turbulence resolution.

2.1 A primer on RANS, LES, and hybrid models

2.1.1 Governing equations and their statistical description

The instantaneous turbulent flow is governed by the conservation of mass, momentum, and energy. Assuming an incompressible and Newtonian fluid with constant density, the conservation equations can be written as:

(1) Continuity equation:

$$\frac{\partial u_i}{\partial x_i} = 0 \tag{2.1}$$

(2) Momentum equation:

$$\frac{\partial u_i}{\partial t} + \frac{\partial u_i u_j}{\partial x_j} = -\frac{1}{\rho}\frac{\partial p}{\partial x_i} + \frac{\partial}{\partial x_j}\left(\nu \frac{\partial u_i}{\partial x_j}\right) + g_i \tag{2.2}$$

(3) Energy equation:

$$\frac{\partial C_p T}{\partial t} + \frac{\partial C_p u_j T}{\partial x_j} = \frac{1}{\rho}\frac{\partial}{\partial x_j}\left(k\frac{\partial T}{\partial x_j}\right) + \varphi \tag{2.3}$$

The flow variables to be solved are the velocity component in the ith direction u_i , pressure p, and temperature T. Other variables include fluid density ρ , kinematic viscosity ν, gravity in ith direction g_i, pressure specific heat C_p , and thermal conductivity k. φ is the dissipation function representing the work done against the viscous forces and is given by:

$$\varphi = \nu\left(\frac{\partial u_i}{\partial x_j} + \frac{\partial u_j}{\partial x_i}\right)\frac{\partial u_i}{\partial x_j} \tag{2.4}$$

For incompressible flows when the viscosity is independent of the temperature the energy equation is decoupled from the Navier-Stokes equations (2.1)-(2.2) and is therefore neglected in the present work.

A generalized statistical description of the Navier-Stokes equations is first introduced, which is valid for many URANS and LES closures, and also the hybrid models. A linear and constant-preserving statistical operation [47] is applied to an instantaneous flow quantity marked with an overbar:

$$\phi = \bar{\phi} + \phi' \tag{2.5}$$

where the residual value is denoted by ϕ' . The overbar operation has different meanings in URANS and LES. In URANS, the overbar denotes an average defined as:

$$\bar{\phi}(x,t) = \frac{1}{T}\int_0^T \phi(x, t+\tau)\, d\tau \tag{2.6}$$

by assuming that the averaging time span T is greater than the turbulent time scale and is much lower than the period of slow variations in the flow field. In LES, the overbar denotes spatial filtering by convolution of the flow quantity with a kernel $G_\Delta(x)$ [48], representing a local average in a small region around the point of interest:

$$\bar{\phi}(x,t) = \int_{R^3} G_\Delta(x - x')\,\phi(x', t)\, d^3x' \tag{2.7}$$

Applying the overbar operation to equations (2.1) and (2.2) results in the following resolved equations:

$$\frac{\partial \bar{u}_i}{\partial x_i} = 0 \tag{2.8}$$

$$\frac{\partial \bar{u}_i}{\partial t} + \frac{\partial \bar{u}_i \bar{u}_j}{\partial x_j} = -\frac{1}{\rho}\frac{\partial \bar{p}}{\partial x_i} + \nu \frac{\partial^2 \bar{u}_i}{\partial x_j \partial x_j} - \frac{\partial \tau_{ij}}{\partial x_j} + g_i \tag{2.9}$$

where $\bar{u}_i$ and $\bar{p}$ denote the resolved velocity component and the resolved pressure, respectively. The residual stress τ_{ij} has the expression:

$$\tau_{ij} = \overline{u_i u_j} - \bar{u}_i \bar{u}_j \tag{2.10}$$

Its first term $\overline{u_i u_j}$ is a newly introduced unknown compared with the original Navier-Stokes equations, thus τ_{ij} should be modeled to close the equations. However, attempts to derive exact transport equations for τ_{ij} give rise to more higher-order unknowns [30], making the closure problem more complex. To solve the problem, some simplifying assumptions have to be made, and the most commonly used is the Boussinesq eddy-viscosity assumption [49]:

$$\tau_{ij} = -2\nu_t \bar{S}_{ij} + \frac{2}{3} k \delta_{ij} \tag{2.11}$$

where ν_t is the kinematic eddy viscosity; δ_{ij} is the Kronecker delta; the strain rate in the resolved velocity field $\bar{S}_{ij}$ and the residual turbulent kinetic energy k have the following expression:

$$\bar{S}_{ij} = \frac{1}{2}\left(\frac{\partial \bar{u}_i}{\partial x_j} + \frac{\partial \bar{u}_j}{\partial x_i}\right) \tag{2.12}$$

$$k \equiv \frac{1}{2}\tau_{kk} = \frac{1}{2}\overline{u'_k u'_k} \tag{2.13}$$

The Boussinesq assumption relates the residual stress to the resolved rate of strain by assuming that the turbulent transport is analogous to the viscous transport. It has been widely and successfully used in many industrial flows due to its simplicity and numerical stability, but limitations have been shown in predicting complex flows, such as swirling flows, transitional flows, stagnation, etc [50, 51]. This is because molecules

and turbulent eddies are fundamentally different, and the turbulent viscosity is in general not isotropic. The inadequacy of the isotropic-viscosity assumption can be addressed by introducing a nonlinear eddy viscosity formulation (NLEVM) and is discussed in later sections.

Applying the Boussinesq assumption to the resolved momentum equation (2.10) yields:

$$\frac{\partial \bar{u}_i}{\partial t} + \frac{\partial \bar{u}_i \bar{u}_j}{\partial x_j} = -\frac{1}{\rho}\frac{\partial \bar{p}_m}{\partial x_i} + (\nu + \nu_t)\frac{\partial^2 \bar{u}_i}{\partial x_j \partial x_j} + g_i \tag{2.14}$$

where the modified pressure $\bar{p}_m$ is defined as:

$$\bar{p}_m = \bar{p} + \frac{1}{3}\tau_{kk} \tag{2.15}$$

2.1.2 Reynolds-averaged Navier Stokes

As discussed in Section 2.1.1, in URANS, the overbar operation denotes an average defined in equation (2.6). In steady RANS, the averaging time span T goes to infinity for solving steady-state conditions. Let $\phi = \bar{\phi} + \phi'$, $\psi = \bar{\psi} + \psi'$, the following features of averaging hold:

$$\overline{\phi'} = 0 \tag{2.16}$$

$$\overline{\bar{\phi}} = 0, \overline{\bar{\phi}\phi'} = 0 \tag{2.17}$$

$$\overline{\phi\psi} = \overline{\left(\bar{\phi} + \phi'\right)\left(\bar{\psi} + \psi'\right)} = \bar{\phi}\bar{\psi} + \overline{\phi'\psi'} \tag{2.18}$$

Applying (2.18) to (2.10) generates the expression of the Reynolds stress tensor:

$$\tau_{ij} = \overline{u'_i u'_j} \tag{2.19}$$

Reynolds stress models (RSMs) [52] attempt to solve transport equations to compute the six independent Reynolds stress components. However, as described earlier, these models need to introduce many higher-order unknowns for closure, which greatly increases the complexity. In addition, the assumptions for the higher-order unknowns lack experimental and theoretical support, therefore the performance of

RSMs is usually not much superior to that of more simplified eddy-viscosity models (EVMs).

EVMs adopt the Boussinesq assumption, and model eddy viscosity using some additional differential transport equations. Depending on the number of additional transport equations to solve, EVMs can be classified into zero-equation models, one-equation models, two-equation models, etc. The most widely used EVMs are two-equation models to solve for both the velocity and time scales in turbulence. Some of the popular two-equation models in engineering applications are introduced in the following sections. Further, nonlinear eddy-viscosity models are also discussed to deal with the inadequacy of the linear EVMs.

Standard k-ε model

The k-ε model is one of the most widely used and validated turbulence models with accumulated industrial applications. The exact k-ε equations contain many unknown and unmeasurable terms. For a much more practical approach, the standard k-ε model is used to minimize these unknowns. It was first proposed by Jones and Launder (1972) [53], and then its coefficients were calibrated by Launder and Spalding (1974) [54]. The eddy viscosity is specified by two transport variables, the turbulent kinetic energy (TKE) k, and the turbulent dissipation rate (TDR) ε, determining the energy and the scale of the turbulence, respectively. The model formulations are:

$$\nu_t = C_\mu \frac{k^2}{\varepsilon} \tag{2.20}$$

$$\frac{\partial k}{\partial t} + \frac{\partial \bar{u}_j k}{\partial x_j} = \frac{\partial}{\partial x_j}\left[\left(\nu + \frac{\nu_t}{\sigma_k}\right)\frac{\partial k}{\partial x_j}\right] + P_k - \varepsilon \tag{2.21}$$

$$\frac{\partial \varepsilon}{\partial t} + \frac{\partial \bar{u}_j \varepsilon}{\partial x_j} = \frac{\partial}{\partial x_j}\left[\left(\nu + \frac{\nu_t}{\sigma_\varepsilon}\right)\frac{\partial \varepsilon}{\partial x_j}\right] + C_{\varepsilon 1}\frac{\varepsilon}{k}P_k - C_{\varepsilon 2}\frac{\varepsilon^2}{k} \tag{2.22}$$

where the TKE production term is:

$$P_k = -\tau_{ij}\frac{\partial \bar{u}_i}{\partial x_j} \tag{2.23}$$

The model coefficients are as follows:

$$C_\mu = 0.09, \sigma_k = 1.00, \sigma_\varepsilon = 1.30, C_{\varepsilon 1} = 1.44, C_{\varepsilon 2} = 1.92 \tag{2.24}$$

The k equation is derived from the exact equation by applying gradient-diffusion assumption (Daly and Harlow, 1970 [55]). The ε equation is created from an assumption of analogy with the k equation, as its exact equation is very difficult to model. Both the k and ε equations have terms representing the physical processes of convection by the mean flow, diffusion, production by the mean-flow gradients, and destruction. The standard k-ε model is not valid near the wall, therefore it is typically used in conjunction with wall functions to patch the core region of the flow to the wall [56].

The standard k-ε model has demonstrated high robustness through years of accumulated experience in industrial applications. But it has shown limitations with over-prediction of the eddy viscosity in complex strain conditions, including curvature, vortex flows, separation, stagnation, etc, due to the simplified linear eddy-viscosity assumption and insufficient physical description in the ε equation. A lot of k-ε model variants exist aimed at improving some specific aspects, of which the realizable k-ε (RKE) model is among the most popular ones.

Realizable k-ε model

The RKE model was proposed by Shih and coworkers [33]. A new form for the ε equation is derived from the exact dynamic equation for the resolved square vorticity fluctuation $\overline{\omega_i \omega_i}$ and by applying the relation $\varepsilon = \nu \overline{\omega_i \omega_i}$, which is valid at high Reynolds number [33]. Tis model overcomes the shortcoming of the standard k-ε model of being non-realizable. The term realizability in turbulence modeling denotes the model capability to ensure physical requirements. The usual realizablity constraints are that all normal stresses should be positive and the Cauchy-Schwarz

inequality should be satisfied for the shear stress:

$$\tau_{ij} \geq 0, i = j \tag{2.25}$$

$$\tau_{ij}^2 \leq \tau_{ii}\tau_{jj}, i \neq j \tag{2.26}$$

The standard k-ε model can violate these realizablity constraints in the case of large resolved strain rates. To ensure realizablity, the RKE model uses a nonconstant C_μ expression related to the resolved strain rate, while the eddy viscosity expression and the transport equation for k is the same as the standard k-ε model. The model formulations is given below:

$$\frac{\partial \varepsilon}{\partial t} + \frac{\partial \bar{u}_j \varepsilon}{\partial x_j} = \frac{\partial}{\partial x_j}\left[\left(\nu + \frac{\nu_t}{\sigma_\varepsilon}\right)\frac{\partial \varepsilon}{\partial x_j}\right] + C_1 S\varepsilon - C_2 \frac{\varepsilon^2}{k + \sqrt{\nu\varepsilon}} \tag{2.27}$$

$$\sigma_\varepsilon = 1.2, C_1 = \max\left(0.43, \frac{\eta}{\eta + 5}\right), \eta = S\frac{k}{\varepsilon}, S = \sqrt{2\bar{S}_{ij}\bar{S}i_j}, C_2 = 1.9 \tag{2.28}$$

$$C_\mu = \frac{1}{A_0 + A_s \frac{U^* k}{\varepsilon}} \tag{2.29}$$

$$U^* = \sqrt{\bar{S}_{ij}\bar{S}_{ij} + \bar{\Omega}_{ij}\bar{\Omega}_{ij}}, \bar{\Omega}_{ij} = \frac{1}{2}\left(\frac{\partial \bar{u}_i}{\partial x_j} - \frac{\partial \bar{u}_j}{\partial x_i}\right) \tag{2.30}$$

$$A_0 = 4.0, A_s = \sqrt{6}\cos\left(\frac{1}{3} arc\cos\left(\sqrt{6}\bar{S}_{ij}\bar{S}_{jk}\bar{S}_{ki}\left(\bar{S}_{ij}\bar{S}_{ij}\right)^{-\frac{3}{2}}\right)\right) \tag{2.31}$$

The RKE model overcomes some limitations of the standard k-ε model and provides more robust and improved predictions for complex flows involving strong streamline curvature, vortices, and rotation. Though it can hardly go beyond the limitations of a linear eddy viscosity model with insufficient accuracy across the board, the model has high robustness

Due to the improved performance and its robust behavior, it has become the default recommendation in many mainstream commercial software and is therefore chosen as the reference model to be compared in this research.

Standard k-ω model

Another popular family of two equation models is the k-ω model with the eddy viscosity specified by the transport variables of k and the specific dissipation rate defined as:

$$\omega = \frac{\varepsilon}{\beta^* k} \tag{2.32}$$

The first k-ω model can be dated back to Kolmogorov [57]. After that, several improved versions have been proposed, including the standard one proposed by Wilcox in 1988 [58] with formulations:

$$\nu_t = \frac{k}{\omega} \tag{2.33}$$

$$\frac{\partial k}{\partial t} + \frac{\partial \bar{u}_j k}{\partial x_j} = \frac{\partial}{\partial x_j}\left[\left(\nu + \frac{\nu_t}{\sigma_k}\right)\frac{\partial k}{\partial x_j}\right] + \tau_{ij}\frac{\partial u_i}{\partial x_j} - \beta^*\omega k \tag{2.34}$$

$$\frac{\partial \omega}{\partial t} + \frac{\partial \bar{u}_j \omega}{\partial x_j} = \frac{\partial}{\partial x_j}\left[\left(\nu + \frac{\nu_t}{\sigma_\omega}\right)\frac{\partial \omega}{\partial x_j}\right] + \frac{\gamma\omega}{k}\tau_{ij}\frac{\partial u_i}{\partial x_j} - \beta\omega^2 \tag{2.35}$$

$$\sigma_k = 2, \sigma_\omega = 2, \beta^* = 0.09, \beta = 3/40, \gamma = 5/9 \tag{2.36}$$

The main advantage of the k-ω model is that it can be applied throughout the boundary layer without the use of damping functions in the near-wall region as the k-ε model. The model is built to perform better in transitional flows and flows with adverse pressure gradients compared to the k-ε model, and therefore has gained popularity in the aerospace industry. But this leads to overestimated shear stress and underestimated turbulent kinetic energy in simple strain fields. The main disadvantage of the model is its sensitivity to the specified turbulence level at the free stream boundary, which is undesirable in engineering simulations.

k-ω SST model

The k-ω Shear Stress Transport (SST) model of Menter (1994) [35] is a blend of the k-ε model and the k-ω model. The Wilcox's k-ω model is implemented in the near wall region and the standard k-ε model in the free stream region, as the k-ω model has the advantage of having natural treatment in the boundary layers and the k-ε model has the advantage of being insensitive to the inlet conditions. The blend is

achieved by applying a blending function F_1. When the k-ε model is written in the k-ω form using variable substitution, an additional cross diffusion term appears in the transferred ω equation:

$$2\frac{\sigma_{\omega 2}}{\omega}\frac{\partial k}{\partial x_j}\frac{\partial \omega}{\partial x_j} \tag{2.37}$$

Therefore multiplying the term by (1-F_1) can realize control of the switch between the k-ω model and the k-ε model. When $F_1 = 1$, the resulting equations are the k-ω equations; when $F_1 = 0$, he resulting equations are the k-ε equations.

The formulations of the k-ω SST model are given by:

$$\nu_t = \frac{a_1 k}{\max(a_1\omega, \Omega F_2)} \tag{2.38}$$

$$\frac{\partial k}{\partial t} + \frac{\partial \bar{u}_j k}{\partial x_j} = \frac{\partial}{\partial x_j}\left[(\nu + \sigma_k \nu_t)\frac{\partial k}{\partial x_j}\right] + \tau_{ij}\frac{\partial u_i}{\partial x_j} - \beta^* \omega k \tag{2.39}$$

$$\frac{\partial \omega}{\partial t} + \frac{\partial \bar{u}_j \omega}{\partial x_j} = \frac{\partial}{\partial x_j}\left[(\nu + \sigma_\omega \nu_t)\frac{\partial \omega}{\partial x_j}\right] + \frac{\gamma}{\nu_t}\tau_{ij}\frac{\partial u_i}{\partial x_j} - \beta\omega^2 + 2(1 - F_1)\frac{\sigma_{\omega 2}}{\omega}\frac{\partial k}{\partial x_j}\frac{\partial \omega}{\partial x_j} \tag{2.40}$$

Each of the model constants , either σ_k, σ_ω, β, or γ, is represented by ϕ, which is a blend of an inner constant ϕ_1 and outer constant ϕ_2:

$$\phi = F_1\phi_1 + (1 - F_1)\phi_2 \tag{2.41}$$

Additional functions are given by:

$$F_1 = \tanh\left(\arg_1^4\right) \tag{2.42}$$

$$\arg_1 = \min\left[\max\left(\frac{\sqrt{k}}{\beta^*\omega y}, \frac{500\nu}{y^2\omega}\right), \frac{4\rho\sigma_{\omega 2}k}{CD_{k\omega}y^2}\right] \tag{2.43}$$

$$CD_{k\omega} = \max\left(2\rho\frac{\sigma_{\omega 2}}{\omega}\frac{\partial k}{\partial x_j}\frac{\partial \omega}{\partial x_j}, 10^{-20}\right) \tag{2.44}$$

$$F_2 = \tanh\left(\arg_2^2\right) \tag{2.45}$$

$$\arg_2 = max\left(\frac{2\sqrt{k}}{\beta^*\omega y}, \frac{500\nu}{y^2\omega}\right) \tag{2.46}$$

$$\Omega = \sqrt{2\bar{\Omega}_{ij}\bar{\Omega}_{ij}} \tag{2.47}$$

where y is the distance to the nearest wall. The model constants are:

$$a_1 = 0.31, \beta^* = 0.09 \tag{2.48}$$

$$\gamma_1 = \frac{\beta_1}{\beta^*} - \frac{\sigma_{\omega 1}\kappa^2}{\sqrt{\beta^*}}, \gamma_2 = \frac{\beta_2}{\beta^*} - \frac{\sigma_{\omega 2}\kappa^2}{\sqrt{\beta^*}}, \kappa = 0.41 \tag{2.49}$$

$$\sigma_{k1} = 0.85, \sigma_{k2} = 1.0, \sigma_{\omega 1} = 0.5, \sigma_{\omega 2} = 0.856, \beta_1 = 0.075, \beta_2 = 0.082 \tag{2.50}$$

The k-ω SST model overcomes the most serious drawback of the standard k-ω model when applied to practical flow simulations. With an ad-hoc limiter in the formulation of the eddy viscosity, the model improved the performance for predicting separation and reattachment and therefore has been widely used in the aerospace industry. On the other hand, the blending function behavior is arbitrary and could obscure some critical features of turbulence, leading to failures in some complex flow conditions. Also, the model maintains the inherent limitations as a linear eddy-viscosity model.

Nonlinear eddy-viscosity models

The linear eddy-viscosity models adopt the Boussinesq assumption and assume that the Reynolds stress τ_{ij} is linearly linked to the resolved strain rate $\bar{S}_{ij}$ by eddy viscosity ν_t. This assumption also implies isotropic turbulence, which is not valid for many flows. The simplified assumption causes inaccuracy in predicting complex flows involving features such as streamline curvature, rotation, swirl, stagnation, turbulence-induced secondary flow, etc. Nonlinear eddy-viscosity models (NLEVMs) go beyond the Boussinesq assumption by adding nonlinear terms to the Reynolds stress:

$$\tau_{ij} = -2\nu_t \bar{S}_{ij} + \frac{2}{3}k\delta_{ij} + f\left(\bar{S}_{ij}, \bar{\Omega}_{ij}\right) \tag{2.51}$$

where f is a nonlinear function dependent on the resolved strain and vorticity or other scalar turbulence variables. The idea of a non-linear stress-strain relation goes

back to the proposal of Pope in 1975 [59]. Such models have become fairly popular in recent years, having the potential of improving performance over linear EVMs with only a moderate increase in the computational cost.

One way of constructing a non-linear model is to initially include all tensor forms that satisfy symmetry and contraction properties:

$$\tau_{ij} = \tau_{ji} \tag{2.52}$$

$$k = \frac{1}{2}\tau_{ii} \tag{2.53}$$

A baseline form for a quadratic k-ε model is to include all possible terms that are quadratic in the resolved velocity gradients:

$$\begin{aligned}\tau_{ij} = {} & \tfrac{2}{3}k\delta_{ij} - 2\nu_t\bar{S}_{ij} + 4C_1\nu_t\tfrac{k}{\varepsilon}\left(\bar{S}_{ik}\bar{S}_{kj} - \tfrac{1}{3}\delta_{ij}\bar{S}_{kl}\bar{S}_{kl}\right) \\ & + 4C_2\nu_t\tfrac{k}{\varepsilon}\left(\bar{\Omega}_{ik}\bar{S}_{kj} + \bar{\Omega}_{jk}\bar{S}_{ki}\right) \\ & + 4C_3\tfrac{\nu_t}{\varepsilon}\left(\bar{\Omega}_{ik}\bar{\Omega}_{jk} - \tfrac{1}{3}\delta_{ij}\bar{\Omega}_{kl}\bar{\Omega}_{kl}\right)\end{aligned} \tag{2.54}$$

Then the model coefficients can be tuned to a range of flows. A number of quadratic models have been proposed with different coefficients given by Speziale (1987) [60], Nisizima and Yoshizawa (1987) [61], Rubinstein and Barton (1990) [62], and Myong (1990) [63]. There is little agreement between these models on the coefficient values, giving little confidence in their applicability over a wide range of flows. In addition, it is found that streamline curvature and swirl cannot be accounted for using a quadratic form. Higher order terms are therefore sought after. A cubic NLEVM has the baseline form:

$$\begin{aligned}\tau_{ij} = {} & \tfrac{2}{3}k\delta_{ij} - 2\nu_t\bar{S}_{ij} + 4C_1\nu_t\tfrac{k}{\varepsilon}\left(\bar{S}_{ik}\bar{S}_{kj} - \tfrac{1}{3}\delta_{ij}\bar{S}_{kl}\bar{S}_{kl}\right) + 4C_2\nu_t\tfrac{k}{\varepsilon}\left(\bar{\Omega}_{ik}\bar{S}_{kj} + \bar{\Omega}_{jk}\bar{S}_{ki}\right) \\ & + 4C_3\tfrac{\nu_t}{\varepsilon}\left(\bar{\Omega}_{ik}\bar{\Omega}_{jk} - \tfrac{1}{3}\delta_{ij}\bar{\Omega}_{kl}\bar{\Omega}_{kl}\right) + 8C_4\nu_t\tfrac{k^2}{\varepsilon^2}\left(\bar{S}_{ki}\bar{\Omega}_{lj} + \bar{S}_{kj}\bar{\Omega}_{li}\right)\bar{S}_{kl} \\ & + 8C_5\nu_t\tfrac{k^2}{\varepsilon^2}\left(\bar{\Omega}_{il}\bar{S}_{mj} + \bar{S}_{il}\bar{\Omega}_{mj} - \tfrac{2}{3}\delta_{ij}\bar{S}_{\ln}\bar{\Omega}_{mn}\right)\bar{\Omega}_{lm} \\ & + 8C_6\nu_t\tfrac{k^2}{\varepsilon^2}\bar{S}_{kl}\bar{S}_{kl}\bar{S}_{ij} + 8C_7\nu_t\tfrac{k^2}{\varepsilon^2}\bar{\Omega}_{kl}\bar{\Omega}_{kl}\bar{S}_{ij}\end{aligned} \tag{2.55}$$

Examples of cubic NLEVMs include the model by Suga (1995) [64], Lien et al.

(1996) [65], Baglietto and Ninokata (2006) [66]. It has been shown that $C_5 = 0$ and $C_6 = -C_7$, therefore only 5 coefficients need to be tuned to incorporate all necessary information.

Explicit Algebraic Reynolds Stress Models (EARSMs) are a class of NLEVMs derived from RSMs by a systematic approximation to the second moment closure. The idea of EARSM was first introduced by Pope in 1975 [59], in which a two-dimensional model is devised based on the RSM of Launder, Reece, and Rodi (1975) [67]. Later, Gatski and Speziale (1993) [68] extended the idea to a more general three-dimensional formulation derived from an RSM at the equilibrium limit. Another EARSM was proposed by Apsley and Leschziner (1998) [69] based on a truncated iterative solution of an algebraic Reynolds stress model. Abe, Jang, and Leschziner (2003) [70] proposed an EARSM formulation including additional tensorial terms in the stress-strain relation dependent on the wall distance, to improve the representation of stress anisotropy in wall-bounded flows.

2.1.3 Large-eddy simulation (LES)

As noted in Section 1.3, turbulent flows contain a wide range of eddy sizes. Large Eddy Simulation (LES) assumes that the larger and most energy-containing eddies are geometry-dependent and need to be resolved, while the smallest eddies, which contain a small amount of the turbulent energy, are universal and can be modeled. Therefore in LES, a velocity field containing only the large scale components is produced by spatial filtering given by equation (2.7), and the length scales smaller than the filter width (often the grid size) are averaged out. In the context of LES, the residual flow quantity ϕ' is nonzero and the residual stress tensor τ_{ij} is called the subgrid-scale (SGS) Reynolds stress that needs modeling. Often the SGS models are based on the eddy viscosity assumption, which supposes that the principal effects of SGS Reynold stress are increased transport and dissipation and the local effects associated with convection and diffusion can be neglected.

The earliest and most commonly used SGS model is the Smagorinsky model [71]. The form of the SGS eddy viscosity can be derived by the product of two dimensional

arguments, a length scale and a velocity scale, and has the expression:

$$\nu_t = C_S^2 \Delta^2 \sqrt{2\bar{S}_{ij}\bar{S}_{ij}} \tag{2.56}$$

where C_s is a model parameter to be determined, and Δ is the grid filter scale typically equal to the grid size. Methods applicable only to isotropic turbulence result in a C_s value of 0.2, but the value can be an order of magnitude smaller when applied to shear flows. In near-wall regions, the value is even smaller, and damping is necessary to reduce SGS eddy viscosity. While the introduction of the damping improves results, the damping value is ad-hoc and difficult to apply to complex geometries.

The dynamic Smagorinsky model [72] addresses the issue of the non-constant C_s. A test filter wider than Δ is applied to the resolved fields to obtain a large scale field. The difference between the two fields leads to an estimate of C_s, which can be updated at every grid point and every time step. The challenge is that the dynamic C_s is a rapidly varying function of spatial coordinates and time, so negative values of eddy viscosity can be generated and lead to numerical instability [8].

Among many LES closures proposed, the wall-adapting local eddy-viscosity (WALE) model by Nicoud and Ducros (1999) [73] has been the most successful in industrial applications. Unlike the Smagorinsky model which is based only on the resolved strain rate, the WALE model is based on true velocity gradients and hence can distinguish between strain and rotation rates. The WALE model formulations are:

$$\nu_t = C_w^2 \Delta^2 \frac{\left(S_{ij}^d S_{ij}^d\right)^{3/2}}{\left(\bar{S}_{ij}\bar{S}_{ij}\right)^{5/2} + \left(S_{ij}^d S_{ij}^d\right)^{5/4}} \tag{2.57}$$

$$S_{ij}^d = \frac{1}{2}\left(\bar{g}_{ij}^2 + \bar{g}_{ji}^2\right) - \frac{1}{3}\delta_{ij}\bar{g}_{kk}^2, \bar{g}_{ij} = \frac{\partial \bar{u}_i}{\partial x_j}, \bar{g}_{ij}^2 = \bar{g}_{ik}\bar{g}_{kj} \tag{2.58}$$

The WALE model has several advantages contributing to its popularity. The eddy viscosity naturally goes to zero at the wall without the need for damping or dynamic adjustment to compute wall bounded flows, therefore the model can be used for any grid and complex geometries. Also zero eddy viscosity is produced for pure shear

flow, making it amenable to reproducing the laminar to turbulent transition process. Also the model behavior is not very sensitive to the coefficient.

The computational cost for LES increases rapidly with the increase of the Reynolds number. In wall bounded flows, according to Chapman [74], the required number of grid points for LES to resolve the turbulent boundary layer is proportional to $Re^{1.8}$. For the Courant−Friedrichs−Lewy (CFL) condition [75], LES requires the courant number close to 1 for convergence and accuracy :

$$C = \Delta t \frac{\bar{u}_i}{\Delta x_i} \sim 1 \tag{2.59}$$

therefore the total cost is proportional to $Re^{2.4}$ considering the time advancement. In the case of isotropic turbulence, according to Pope [51], 80% of the energy is resolved with a filter size:

$$\Delta = \frac{1}{6} L_{11} \tag{2.60}$$

where L_{11} is the integral length scale of turbulence. To resolve the energy-containing eddies, LES requires a mesh with such a filter size, and in practice, the integral length scale is estimated from a precursor RANS as a guide for building up a proper LES mesh, and it has the following expression for a classical $k - \varepsilon$ model:

$$L_{11} \approx k^{1.5}/\varepsilon \tag{2.61}$$

2.1.4 Hybrid turbulence models

Although there is no universal definition of the hybrid turbulence models, they all combine the features of URANS and LES and are aimed at obtaining an improved accuracy compared with URANS by using fewer grid points than those needed for LES.

The combination of LES and URANS can be achieved in several ways, forming different categories ofhybrid models. According to Fröhlich and von Terzi (2008) [76], the hybrid models can be classified into:

- Blending turbulence models, in which the hybrid residual stress tensor is a weighted sum of the residual stress of URANS and LES:

$$\tau_{ij} = f^{\text{URANS}} \tau_{ij}^{\text{URANS}} + f^{\text{LES}} \tau_{ij}^{\text{LES}} \tag{2.62}$$

  where f^{URANS} and f^{LES} are local blending coefficients determined by the local value of a given criterion.

- Segregated models, in which URANS and LES are employed in different parts of the computational domain. At their interfaces, the resolved quantities are not continuous, and appropriate boundary conditions are needed for coupling. These models are also referred to as zonal models by Sagaut (2006) [77], while ambiguities are associated with the term *zonal* and *non-zonal* in different works of literature.

- Interfacing URANS and LES models, which are very similar to segregated models with URANS and LES being solved in different zones of the computational domain. The difference is that the transport equation for the velocity is the same in both zones, so the computed resolved velocity is continuous.

- Second-generation URANS models, which employ the same secondary transport equations everywhere and are characterized by containing an adjusting term sensing the amount of resolved fluctuations. These models are aimed at resolving a substantial part of the turbulent fluctuations without explicit dependency on the computational grid.

In the following sections, popular hybrid models falling in the different categories are introduced. Discussions are focused on their key aspects, strengths, and limitations.

Very Large Eddy Simulation (VLES)

Very large eddy simulation (VLES) proposed by Speziale [78, 79] is considered the first hybrid model proposed in the literature. The model aims at resolving appropriate

scales in the range between DNS and URANS by introducing resolution-dependent damping to a URANS model and falls into the blending model category. The damping function controls the ratio of the modeled to resolved energy and the residual stress has the following expression:

$$\tau_{ij} = \left(1 - \exp\left(-\frac{\beta\Delta}{\eta_k}\right)\right)^n \tau_{ij}^{\text{URANS}} \tag{2.63}$$

where β and n are empirical constants. η_k is the Kolmogorov length scale, the smallest scale in turbulence flow. In the limit when the grid size Δ is very small and comparable to η_k, all relevant scales are resolved and DNS is retrieved, whereas when Δ is very large, the model behaves as URANS. However, when the Reynolds number is very large implying a very small η_k, damping goes to zero and the model behaves like URANS independent of the grid size. Very fine mesh is needed to enable scale-resolving behavior. Nevertheless, as the first hybrid model, it opens the door to the development of many other hybrid models.

Embedded LES (ELES)

Embedded LES is a simple segregated or zonal model which solves for LES in a subdomain of interest inside the whole computational domain, where the remaining domain is solved using URANS. Typically URANS is applied at the inlet and outlet and LES is applied in a selected area of interest; their interfaces are defined before the simulation. A domain decomposition selected by Jørgensen and coworkers [7] for the flow around a floor-mounted cube is shown in Figure 2-1, where the LES region is selected near the cube and in the wake.

In ELES, the complex coupling is needed at the interfaces. At interfaces where the flow enters into the LES region, injection of synthetic fluctuations can be used to generate resolved turbulence and ensure a proper balance between URANS and LES turbulence across the interfaces. On returning to the RANS domain, a statistical averaging operation is needed to recover the mean flow data from the resolved turbulence produced from LES.

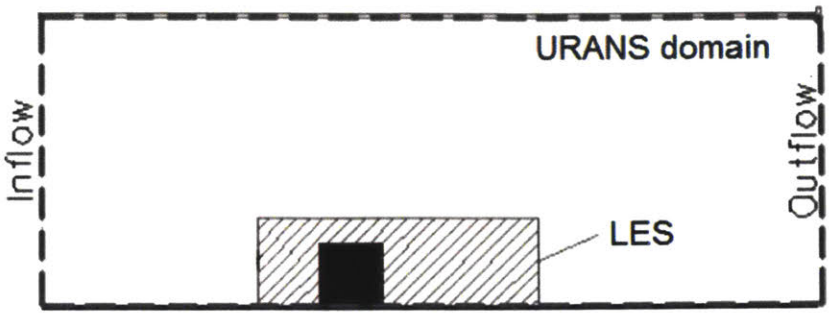

Figure 2-1: Domain decomposition in ELES for flow around a floor-mounted cube, recreated from Jørgensen et al. [7]

By introducing synthetic turbulence of sufficient quality, ELES can be applied to flows that other hybrid models like DES and SAS can hardly work on, for example mildly separated boundary layers [80]. In ELES, computational cost reduction can be reached by the possibility of sudden changes in the mesh size at the subdomain boundaries [81]. The main drawback of the model is the requirement of user-defined interfaces before the simulation. In case that the geometry or application is very complex, the good definition of explicit subdomains may be not possible.

Detached Eddy Simulation (DES) and its variants

Detached Eddy Simulation (DES) and its variants of Delayed Detached Eddy Simulation (DDES) and Improved Delayed Detached Eddy Simulation (IDDES) are among the most widely used hybrid models applied to industrial flows. They were empirically built to simulate high Reynolds number external flows with massive separation past obstacles.

The DES in its original version was developed by Spalart and co-workers in 1997 [39], which is referred to as DES97. In this approach, the model intends to switch from URANS mode in the boundary layer to LES mode in the core flow, depending on a criterion based on the grid resolution. DES97 is based on the Spalart-Allmaras (S-A) model [82], an one equation EVM, which is developed for applications of aerodynamic flows and has the formulations:

$$\nu_t = f_v \tilde{\nu} \tag{2.64}$$

$$\frac{\partial \tilde{\nu}}{\partial t} + \frac{\partial \bar{u}_j \tilde{\nu}}{\partial x_j} = C_{b1}\tilde{S}\tilde{\nu} + \frac{1}{\sigma_\nu}\left[\frac{\partial}{\partial x_j}\left((\nu + \tilde{\nu})\frac{\partial \tilde{\nu}}{\partial x_j}\right) + C_{b2}\frac{\partial \tilde{\nu}}{\partial x_j}\frac{\partial \tilde{\nu}}{\partial x_j}\right] - C_{w1}f_w\frac{\tilde{\nu}^2}{d_w^2} \quad (2.65)$$

where $\tilde{S}$ corresponds to the magnitude of the vorticity, d_w is the wall distance, f_ν is a function dependent on the the ratio $\chi = \tilde{\nu}/\nu$, the other parameters are defined in the original paper [82].

In DES, the wall distance d_w is replaced by $\tilde{d}$ involving the grid size Δ:

$$\tilde{d} = \min(d_w, C_{\text{DES}}\Delta) \quad (2.66)$$

where

$$\Delta = \max(\Delta_x, \Delta_y, \Delta_z) \quad (2.67)$$

The model coefficient C_{DES} value of 0.65 was obtained through calibration in the decaying homogeneous turbulence by Shur and coworks (1999) [83]. In the near wall region, $\tilde{d} = d_w$, the model operates as the S-A model, whereas far from the wall, the model acts as a subgrid scale model. The gray zone corresponds to the interface region where $d_w \approx C_{\text{DES}}\Delta$. The transition in the gray zone is made continuous, so the model falls into the category of the interfacing model.

The original DES has shown success for simulating several test cases, especially for cases involving massive separation. Limitations have also been pointed out that incorrect behavior occurs in thick boundary layers where the the grid size parallel to the wall is smaller than the boundary layer thickness. In this case, DES tends to switch to LES prematurely; the residual stresses decrease, while the resolved turbulence has not been developed. This issue is termed modeled-stress depletion (MSD), which may generate nonphysical adverse pressure gradients known as grid-induced separation (GIS) [84]. To overcome this issue, the DDES model was proposed by Spalart and coworkers (2006) [40] to keep DES in URANS mode even in thick boundary layers. The DES length scale is redefined as:

$$\tilde{d} = d_w - f_d \max(0, d_w - C_{\text{DES}}\Delta) \quad (2.68)$$

where f_d is a shielding function designed to be unity in the LES region, where the parameter $r_d \ll 1$, and zero elsewhere. It is formulated as:

$$f_d = 1 - \tanh\left((8r_d)^3\right) \tag{2.69}$$

$$r_d = \frac{\nu + \nu_t}{\sqrt{\frac{\partial \bar{u}_i}{\partial x_j}\frac{\partial \bar{u}_i}{\partial x_j}\kappa^2 d_w^2}} \tag{2.70}$$

where $\kappa = 0.41$ is the von Kármán constant.

A further improved model IDDES was proposed by Shur et al. [41] to combine DDES with wall modeled LES to avoid the mismatch between the inner modeled log layer and the outer resolved log layer. The length scale given by equation (2.68) is modified as follows:

$$\tilde{d} = \tilde{f}_d\left(1 + f_e\right) d_w + \left(1 - \tilde{f}_d\right) C_{\mathrm{DES}} \psi \tilde{\Delta} \tag{2.71}$$

where $\tilde{f}_d$, f_e and ψ are empirical functions. $\tilde{\Delta}$ is a modified grid size dependent on not only the grid size but also the wall distance, so that $\tilde{\Delta}$ has a more steep variation near the wall, generating instabilities in the resolved field.

While initially the DES approach was based on the S-A model, it was afterwards generalized to be applied on two-equation EVMs. Strelets [85] and Travin et al. [86] proposed a k-ω SST-DES model, while Menter et al. [87] presented a k-ω SST-DDES model. The basic idea is to modify the characteristic length scale:

$$L_{\mathrm{DES}} = \min\left(L_{\mathrm{URANS}}, C_{\mathrm{DES}}\Delta\right) \tag{2.72}$$

where L_{URANS} is the length scale computed by URANS.

DES and its variants have been successful in applications with massive separation. However, due to the grid dependency, they require carefully chosen grids to avoid inappropriate behavior. The user has to recognize a priori the separation regions and adopt LES-like local grid refinement, which may not be easy for complex systems. The DES approaches have main weaknesses in their responses to ambiguous grids, in

which the wall-parallel grid spacing is of the order of the boundary-layer thickness. In some situations, DES on a given grid is less accurate than URANS on the same grid or DES on a coarser grid [88].

Partially Averaged Navier Stokes (PANS)

The partially averaged Navier-Stokes (PANS) model was proposed by Girimaji et al [89, 90, 91]. Similarly to VLES, it follows the idea of introducing damping into the modeled terms of a URANS model to resolve part of the turbulence, but in an implicit way with no explicit dependency on the grid. A constant damping ratio is applied to each characteristic scale of a turbulence closure, which for the k-ε model has the following expression:

$$f_k = \frac{k_m}{k}, f_\varepsilon = \frac{\varepsilon_m}{\varepsilon} \tag{2.73}$$

where k_m and ε_m denote the modeled or unresolved kinetic energy and dissipation rate, and k and ε are the total kinetic energy and dissipation rate. The transport equations for k_m and ε_m can be derived from the k and ε equations:

$$\frac{\partial k_m}{\partial t} + \frac{\partial \bar{u}_j k_m}{\partial x_j} = \frac{\partial}{\partial x_j}\left[\left(\nu + \frac{\nu_{t,m}}{\sigma_{k,m}}\right)\frac{\partial k_m}{\partial x_j}\right] + P_{k,m} - \varepsilon_m \tag{2.74}$$

$$\frac{\partial \varepsilon_m}{\partial t} + \frac{\partial \bar{u}_j \varepsilon_m}{\partial x_j} = \frac{\partial}{\partial x_j}\left[\left(\nu + \frac{\nu_{t,m}}{\sigma_{\varepsilon,m}}\right)\frac{\partial \varepsilon}{\partial x_j}\right] + C_{\varepsilon 1}\frac{\varepsilon_m}{k_m}P_{k,m} - C^*_{\varepsilon 2}\frac{\varepsilon_m^2}{k_m} \tag{2.75}$$

The equations are very similar to the k and ε equations except for a different dissipation coefficient:

$$C^*_{\varepsilon 2} = C_{\varepsilon 1} + \frac{f_k}{f_\varepsilon}\left(C_{\varepsilon 2} - C_{\varepsilon 1}\right) \tag{2.76}$$

If assuming that the transport of k_m and ε_m is not driven by resolved fluctuations, the turbulence Prandtl numbers are:

$$\sigma_{k,m} = \sigma_k f_k^2, \sigma_{\varepsilon,m} = \sigma_\varepsilon f_\varepsilon^2 \tag{2.77}$$

The modeled eddy viscosity is:

$$\nu_t = C_\mu \frac{k_m^2}{\varepsilon_m} = C_\mu \frac{f_k^2}{f_\varepsilon} \frac{k^2}{\varepsilon} \tag{2.78}$$

The term f_k^2/f_ε represents the effective damping for URANS.

An important feature of PANS is that it contains no explicit dependency on the grid size, therefore it can be viewed as a second-generation URANS model. In the practice, the user needs to specify the constant damping ratios before the simulation. Therefore, how much of the kinetic energy and dissipation rate to be modeled has to be decided a priori with the construction of an ad-hoc computational mesh, making the model incomplete and hard to use. Besides, the ratios are constant in space; when a priori selection applies to specific flow regions, it may not be practical across the complete computational domain in large-scale industrial applications. Different levels of scale resolution and accuracy are produced at varying grids, resulting in a lack of monotonic convergence.

Scale Adaptive Simulation (SAS)

The scale-adaptive simulation (SAS) approach was developed by Menter and Egorov [42, 92] to simulate unsteady turbulent flows. It is derived from revising the *k-kl* model of Rotta [93] with removal of an assumption for isotropic turbulence, which results in the introduction of a new term dependent on the von Kármán length scale L_{vk}:

$$L_{vk} = \kappa \sqrt{\frac{2\bar{S}_{ij}\bar{S}_{ij}}{\frac{\partial^2 \bar{u}_i}{\partial x_k \partial x_k} \frac{\partial^2 \bar{u}_i}{\partial x_j \partial x_j}}} \tag{2.79}$$

where $\kappa = 0.41$ is the von Kármán constant.

By accounting the von Kármán length scale, the SAS model could dynamically adjust to the resolved structures for detecting unsteadiness, which results in a LES-like behavior in the unsteady regions of the flow and a URANS mode in stable flow regions. Then for simplification of the eddy viscosity expression, the variable $\phi = \sqrt{k}L$

is introduced, resulting in the proposed k-square-root k-l model:

$$\nu_t = C_\mu^{1/4}\phi \tag{2.80}$$

$$\frac{\partial k}{\partial t} + \frac{\partial \bar{u}_j k}{\partial x_j} = \frac{\partial}{\partial x_j}\left(\frac{\nu_t}{\sigma_k}\frac{\partial k}{\partial x_j}\right) - C_\mu^{3/4}\frac{k^2}{\phi} + P_k \tag{2.81}$$

$$\frac{\partial \phi}{\partial t} + \frac{\partial \bar{u}_j \phi}{\partial x_j} = \frac{\partial}{\partial x_j}\left(\frac{\nu_t}{\sigma_\phi}\frac{\partial \phi}{\partial x_j}\right) + \frac{\phi}{k}P_k\left(\zeta_1 - \zeta_2\left(\frac{L}{L_{vk}}\right)^2\right) - \zeta_3 k \tag{2.82}$$

$$P_k = -\tau_{ij}\frac{\partial \bar{u}_i}{\partial x_j} \tag{2.83}$$

$$C_\mu = 0.09, \sigma_k = \sigma_\phi = 2/3, \zeta_1 = 0.8, \zeta_2 = 1.47, \zeta_2 = 0.0288, C = 2, \kappa = 0.41 \tag{2.84}$$

Then the k-square-root k-l model is transformed to be based on the k-ω SST model using the relation:

$$\phi = C_\mu^{1/4}\frac{k}{\omega} \tag{2.85}$$

An additional source term appears in the ω equation involving the von Kármán length scale:

$$Q_{SAS} = \max\left[2\zeta_2\kappa\bar{S}_{ij}\bar{S}_{ij}\left(\frac{L}{L_{vk}}\right)^2 - C_{SAS}\frac{2k}{\sigma_\phi}\max\left(\frac{1}{\omega^2}\frac{\partial\omega}{\partial x_j}\frac{\partial\omega}{\partial x_j}, \frac{1}{k^2}\frac{\partial k}{\partial x_j}\frac{\partial k}{\partial x_j}\right), 0\right] \tag{2.86}$$

where $C_{SAS} = 2$ and the intergral length scale L is given by

$$L = \sqrt{k}/\left(C_\mu^{1/4}\omega\right) \tag{2.87}$$

In regions with strong unsteady flows, the source term C_{SAS} dominates the other terms in the ω equation, leading to an increase of ω and a decrease of the turbulent eddy viscosity, and hence an increase of the resolved turbulence; in stationary flows, the source term is null and the model behaves as the k-ω SST model.

The SAS method relies on local flow physics rather than the grid size for distinguishing areas of interest and making the transition from URANS to LES-like behavior and is a second-generation URANS model. It is also a complete model with automatic

triggering and control of the hybridization and does not require user-defined parameters or careful control of the computational mesh. Due to these advantages, SAS has successfully been used for industrial applications, especially for flows involving massive separation. Similar to DES, a downside of the model lies in that the transition between URANS and scale-resolving behavior does not necessarily produce the correct physics unless strong unsteadiness occurs. This issue causes its failure in predicting several flow scenarios, including mild separation in asymmetric diffuser [94], turbulent mixing in a T junction [95], flow over a three-dimensional axisymmetric hill [96].

2.2 The STRUCT approach

To overcome the shortcomings of current hybrid models, a novel second-generation URANS approach, STRUCT, was proposed by Lenci [1] and Baglietto [2], aimed at leveraging the robustness of URANS in suitable flow regions while introducing controlled eddy resolution in regions of poor URANS applicability. The idea originates from recognizing the URANS limitations. The inadequacy of the isotropic-viscosity hypothesis could be addressed by adopting an NLEVM as the baseline model. In particular, the NLEVM by Baglietto and Ninokata [97] is used. Another URANS limitation is the inapplicability of the scale-separation assumption in rapidly varying flows. As discussed in Section 2.1.1, URANS assumes that the averaging time span T is greater than the turbulent time scale and is much lower than the period of slow variations in the flow field, implying a scale separation between turbulence and slowly varying phenomena. However, the assumption of scale separation does not hold for rapidly varying flows, such as flows involving separation, vortices, curvature, intermittency, etc. The STRUCT approach addressed this issue by locally resolving a significant portion of the turbulent fluctuations in regions with rapidly varying flows. Identification of the regions and the resolution control are realized through a comparison of the resolved and the modeled time scale, in which the resolved scale is defined based on the second invariant of the resolved velocity gradient tensor. In

STRUCT, the local resolution is achieved without explicit dependency on the grid size, which fits the definition of second-generation URANS models. More detailed model concepts and formulations are provided in the following sections.

2.2.1 Basic STRUCT formulation

The core aspect of STRUCT is to identify the flow region's lack of scale separation and to increase the local resolution accordingly. Such regions are determined by comparing the resolved time scale and the modeled time scale.

The resolved time scale t_r is defined based on the second invariant of the resolved velocity gradient tensor $\overline{II}$, also referred to as Q-criterion for identification of coherent structures [98].

$$t_r = \left|\overline{II}\right|^{-1/2} \tag{2.88}$$

$$\overline{II} = -\frac{1}{2}\frac{\partial \bar{u}_i}{\partial x_j}\frac{\partial \bar{u}_j}{\partial x_i} = \frac{1}{2}\left(\bar{\Omega}_{ij}\bar{\Omega}_{ij} - \bar{S}_{ij}\bar{S}_{ij}\right) = Q \tag{2.89}$$

As an example, Figure 2-2 illustrates the iso-surfaces of $\overline{II}$ for the flow past a square cylinder. The approach based on the second invariant of the resolved velocity gradient tensor has several useful advantages for hybrid turbulence modeling [1]:

- $\overline{II}$ is one of the simplest nonzero invariants to describe flow deformation through velocity gradients. It is suitable for turbulence modeling as it has the following properties:
  - Galilean invariance
  - Frame-rotation invariance
  - Local description in time and space
- For simple shear flows, i.e. the flows in which the velocity vector, orthogonal to the wall, only varies in the wall-normal direction y:

$$\bar{\Omega}_{ij}\bar{\Omega}_{ij} = \bar{S}_{ij}\bar{S}_{ij} = \frac{1}{4}\left(\frac{\partial \bar{u}}{\partial y}\right)^2 \tag{2.90}$$

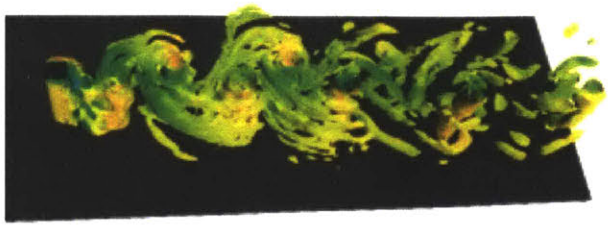

Figure 2-2: Iso-surfaces of $\overline{II}$ (or Q-criterion) for the flow past a square cylinder(from [1]).

As a result, $\overline{II}$ is null, ensuring the URANS behavior of STRUCT near the wall in simple shear layers.

- Regions with rapid distortion caused by either significant strain or large rotation would result in a high value of $\overline{II}$, and consequently a low resolved time scale.

The modeled time scale is defined as:

$$t_m = \langle t_{m,0} \rangle \tag{2.91}$$

where the chevron represents an average operation, applied to a parameter providing information on the modeled turbulent scales. In a k-ε model, as is leveraged by STRUCT, $t_{m,0}$ is defined as:

$$t_{m,0} = \frac{k}{\varepsilon} \tag{2.92}$$

The averaging operation in equation (2.91) serves the purpose of removing the smallest local variations of $t_{m,0}$ caused by resolved eddies, thus delivering a smooth t_m field around those eddies.

The increased flow resolution is achieved by reducing the eddy viscosity through a reduction parameter r:

$$\nu_t = C_\mu \frac{k^2}{\varepsilon} r \tag{2.93}$$

$$r = \begin{cases} 1, h \leq 1 \\ \phi, h > 1 \end{cases} \tag{2.94}$$

Two variables, varying in space and time, define the model: an activation parameter

h and a reduction coefficient ϕ. In STRUCT, h is defined as the ratio between the resolved time scale t_r and the modeled time scale t_m:

$$h = t_m/t_r \tag{2.95}$$

The basic STRUCT concept requires specification of two closure conditions: determination of the reduction coefficient and of the averaging operation in equation (2.91). Three closure options are proposed by Lenci [1]. Controlled STRUCT is a preliminary version for demonstrating general applicability of the STRUCT idea, in which the two closure conditions are obtained from a precursor RANS simulation. Then two complete models STRUCT-L and STRUCT-T are proposed.

2.2.2 Controlled STRUCT

The controlled STRUCT approach is a preliminary and incomplete version of the model that decides the model closure parameters, t_m and ϕ, from a precursor RANS simulation. In particular, the chevron operation in equation (2.91) is a geometric average of the RANS solutions in the domain of interest, yielding a constant value for t_m:

$$t_m = \exp\left(\frac{1}{V}\int_V \ln t_{m,0}\,(x)\,d^3x\right) \tag{2.96}$$

The value of the reduction parameter ϕ is optimized a posteriori to achieve the best accuracy. The controlled STRUCT demonstrates the general applicability and performance of the STRUCT approach. Simulation results obtained with the controlled approach have been helpful in the development of complete closures to identify bounding conditions for candidate scale-adaptive formulations.

2.2.3 Complete STRUCT-L closure

The STRUCT-L closure is the first complete closure proposed by Lenci [1] with a fully local formulation. The average operation in equation (2.91) is evaluated by a truncated Taylor series expansion of the geometric average performed in a sphere,

while the coefficient ϕ adopts a fixed value of 0.6. The truncated Taylor series expansion is used to approximate an explicit Gaussian test filter, similar to the work by Chester et al. (2001) [99]. The use of local operations is to avoid the significant computational burden that arises from an explicit non-local averaging when applied to unstructured girds in massively parallel computations.

Consider a generic function in time and space $f(x,t)$, its geometric average in a sphere with radius R centered around the location of interest is:

$$\langle f \rangle_R (x_0,t) = \exp\left(\frac{3}{4\pi R^3} \int_0^{2\pi} \int_0^{\pi} \int_0^{R} f_{x_0}(\rho,\alpha,\beta,t)\, \rho^2 \sin(\alpha)\, d\rho d\alpha d\beta \right) \tag{2.97}$$

where $f_{x_0}(\rho,\alpha,\beta,t)$ is the function in spherical coordinates centered at position x_0. Then it is approximated using a Taylor series expansion:

$$f_T(x_1,...,x_d) = \sum_{n_1=0}^{+\infty} \sum_{n_2=0}^{+\infty} \cdots \sum_{n_d=0}^{+\infty} \frac{(x_1-a_1)^{n_1} \cdots (x_d-a_d)^{n_d}}{n_1! \cdots n_d!} \left(\frac{\partial^{n_1+\cdots+n_d} f(a_1,\cdots,a_d)}{\partial x_1^{n_1} \cdots \partial x_d^{n_d}} \right) \tag{2.98}$$

Truncating to the second order results in the following expression:

$$\langle f \rangle_R (x,t) \approx \exp\left(\ln f(x,t) + \frac{R^2}{10} \nabla^2 (\ln f(x,t)) \right) \tag{2.99}$$

Substituting $t_{m,0}$ for f and t_m for f_R results in the STRUCT formulations. The radius R is selected as a multiple of the modeled turbulence length scale:

$$R = C_R \frac{k_m^{1.5}}{\varepsilon} \tag{2.100}$$

where $C_R = 2$ is obtained from posterior analysis of selected test cases. Finally, limiters are added to ensure stability and avoid local oscillations:

$$t_m \approx \exp\left(\ln t_{m,0} + \min\left(\max\left(\frac{R^2}{10} \nabla^2 (\ln t_{m,0}), -\ln 2 \right), \ln 2 \right) \right) \tag{2.101}$$

Despite being a complete model, the use of a fixed reduction parameter ϕ in STRUCT-

L evidences limitations. In cases where very large flow redistribution dominates over the convected turbulent components, smaller ϕ is needed to achieve higher levels of resolution.

2.2.4 Complete STRUCT-T closure

To address the limitation of using a fixed reduction parameter in STRUCT-L, another complete closure STRUCT-T is proposed by Lenci [17] that defines ϕ as a continuous variable. To increase the flow resolution at regions of strong overlap between resolved and modeled scales, the reduction parameter ϕ is determined as the inverse of the activation condition h:

$$\phi = \frac{1}{\alpha h} \tag{2.102}$$

where α is a calibration coefficient constant optimized to be 1.35.

In order to provide self-adapting resolution, the averaging operator in equation (2.91) should be able to generate a smooth field for t_m. In addition, the averaging operator should only involve local operations in time and space to reduce computational and memory burden for parallel computations. STRUCT-T uses a Lagrangian differential operator that extends the temporal Lagrangian filtering approach used by Meneveau et al. (1996) [100] through including the effect of spatial averaging. Considering a generic field $f(x,t)$, the differential Lagrangian averaging operator $\langle f \rangle_{T,L}$ is defined as follows, including a length scale L and a time scale, T:

$$f = T\frac{\partial \langle f \rangle_{T,L}}{\partial t} + T\frac{\partial \bar{u}_j \langle f \rangle_{T,L}}{\partial x_j} - L^2 \frac{\partial^2 \langle f \rangle_{T,L}}{\partial x_j \partial x_j} - \langle f \rangle_{T,L} \tag{2.103}$$

The operator can be expressed as the space and time integral of the function to be averaged, multiplied by an averaging kernel:

$$\langle f \rangle_{T,L} = \int_{-\infty} \int_{R^3} f(x',t') g_{T,L}(x-x', t-t')\, dx' dt' \tag{2.104}$$

In the simplified case of uniform and constant u, T, and L, the averaging kernel

corresponds to a Gaussian filter in space and a negative exponential in time :

$$g_{T,L}\left(x-x',t-t'\right)=\frac{1}{T}e^{-\frac{t-t'}{T}}\frac{1}{\left(4\pi\frac{L^2}{T}\left(t-t'\right)\right)^{3/2}}e^{-\frac{\left(x-x'-u\left(t-t'\right)\right)^2}{4\frac{L^2}{T}\left(t-t'\right)}} \tag{2.105}$$

While the formulation provides a balanced weight of space and time operations, for the application to turbulent flow, which is inherently variable in time, the averaging is biased towards the space component through using a damping factor β on the time scale.

$$\frac{\partial\langle f\rangle_{T,L}}{\partial t}+\frac{\partial\bar{u}_j\langle f\rangle_{T,L}}{\partial x_j}=\frac{1}{\beta}\left(\frac{L^2}{T}\frac{\partial^2\langle f\rangle_{T,L}}{\partial x_j\partial x_j}-\frac{1}{T}\left(f-\langle f\rangle_{T,L}\right)\right) \tag{2.106}$$

For the STRUCT-T model, substituting $t_{m,0}$ for f and t_m for $\langle f\rangle_{T,L}$ with added limiters results in:

$$\frac{\partial t_m}{\partial t}+\frac{\partial\bar{u}_j t_m}{\partial x_j}=\frac{1}{\beta}\left(\frac{L^2}{T}\frac{\partial^2 t_m}{\partial x_j\partial x_j}+s\right) \tag{2.107}$$

$$s=\min\left(\max\left(\frac{1}{T}\left(\frac{k_m}{\varepsilon}-t_m\right),-\frac{2t_m}{\Delta_t}\right),\frac{2t_m}{\Delta_t}\right) \tag{2.108}$$

where L and T are defined as the characteristic length and time scales:

$$L=\sqrt{C_\mu}\frac{k_m^{1.5}}{\varepsilon},T=\frac{k_m}{\varepsilon} \tag{2.109}$$

The model coefficients are:

$$C_\mu=0.09,\beta=0.01 \tag{2.110}$$

2.2.5 Model performance

In the work of Lenci [1], the three STRUCT closures have been tested on selected flow cases that are particularly relevant for the testing of hybrid models: flow past a square cylinder, turbulent mixing in a T-junction, and flow in an asymmetric diffuser. The mean velocity and turbulent stress profiles are compared with URANS and experimental results.

Through testing, the controlled STRUCT has confirmed that a consistent and

measurable increase in prediction accuracy can be obtained by introducing a local resolution of the turbulence. The two complete STRUCT models have shown to provide accurate results on RANS-type grids, with a better agreement with the experimental data in the mean velocity and turbulent stress profiles in comparison with URANS. Figure 2-3 shows the results for the case of flow in an asymmetric diffuser for example. The case description is given in Section 3.3.3.

The cost increase of STRUCT has been assessed to be in the range between 3% and 28%, in comparison with the baseline URANS implementation. This means that STRUCT simulations have a cost typically 50 times to several orders of magnitude lower than LES.

2.3 Summary

This chapter can be summarized as follows:

1) The basic concepts of URANS and LES are introduced under the same framework. URANS aims at resolving only the largest scales of flow at a low computational cost, but the simplified assumptions lead to inaccuracies in complex flow conditions, whereas LES has a high accuracy by resolving most of the turbulent fluctuations at a high computational cost. The hybrid models bridge URANS and LES, aiming at obtaining an improved accuracy compared with URANS at a computational cost much less than LES and amenable to industrial applications. Popular hybrid models in use are introduced, but they suffer from limitations, like strong grid sensitivity and inconsistent physical behavior, calling for a modern hybrid model.

2) To better address the industrial need for a robust and widely applicable hybrid model, Lenci [1] and Baglietto [2] proposed a new hybrid approach, STRUCT. The idea of the STRUCT approach is introduced together with the formulations. Through several tests, this approach has demonstrated consistently improved accuracy at a slightly higher computational cost compared with URANS.

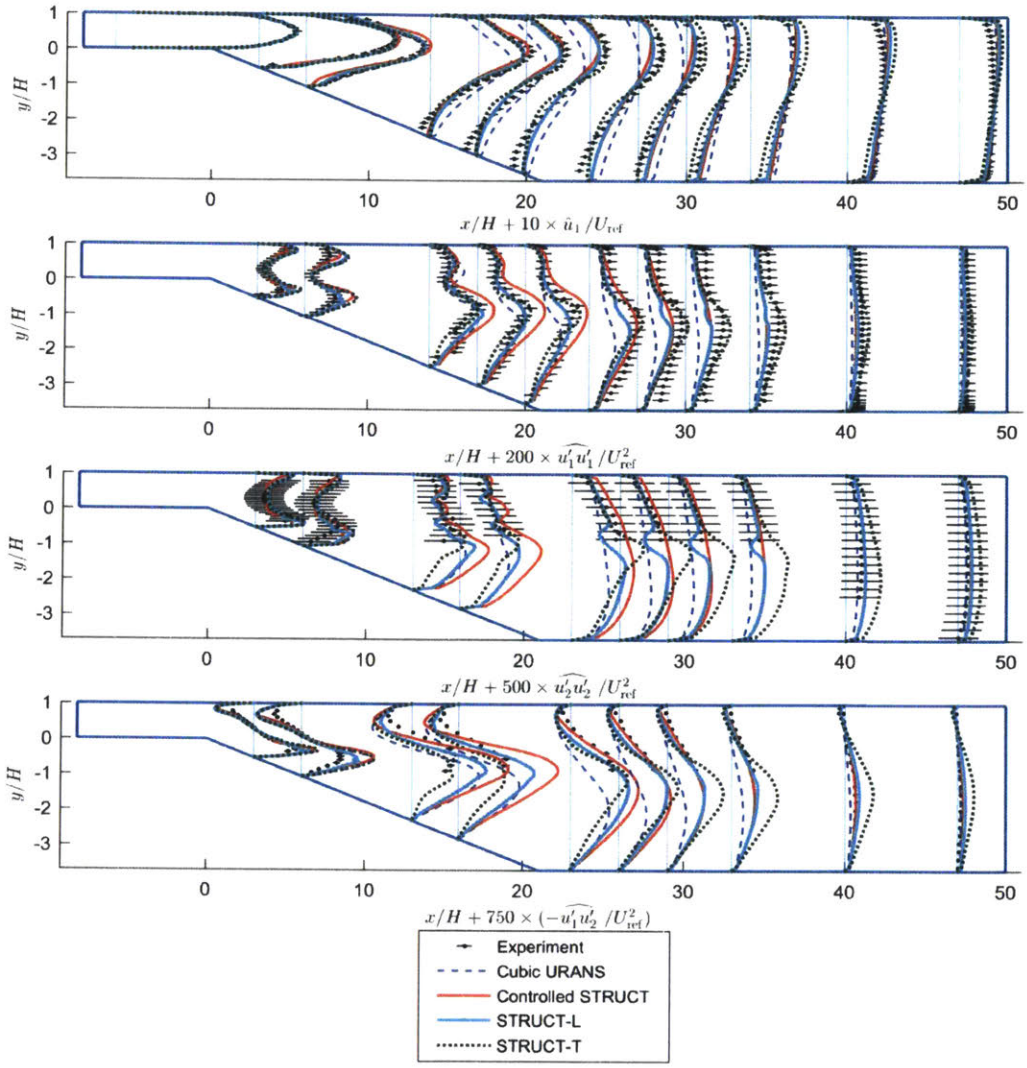

Figure 2-3: Model comparison for the asymmetric diffuser test case (from [1]).

Chapter 3

New proposed STRUCT-ε model

A key limitation is identified in the original STRUCT approach when extending its application to open boundary external flow cases. To deal with this problem, this chapter proposes a new improved STRUCT-ε model with robust applicability to external flow applications for simulating flow around vehicles. The new model introduces a source term in the ε equation of the standard k-ε model based on a resolved time scale defined by the second invariant of the resolved velocity gradient tensor; the baseline URANS model adopts a nonlinear eddy viscosity formulation. The numerical implementation of the new model is briefly discussed, and the model coefficient is selected through several test cases.

3.1 Numerical implementation

In this work, the new STRUCT-ε model is implemented and tested using the commercial finite-volume software STAR-CCM+ Version 13.02 for easy industrial application. Implementation of the STRUCT-ε model is based on the standard k- ε model already built into the software, with the addition of a source term in the turbulent dissipation rate provided by a user-defined field function. To include the nonlinear terms of the cubic NLEVM by Baglietto and Ninokata [66], the cubic constitutive relation needs to be activated and the model coefficients are modified according to Table 3.1.

In the finite volume approach, the computational domain is divided into a finite

number of control volumes (CVs); the differential governing equations are integrated over each CV and by applying the divergence theorem the following integral form is obtained:

$$\frac{d}{dt}\int_V \rho\phi dV + \int_S \rho\phi \mathbf{u}\cdot\mathbf{n}dS = \int_S \Gamma\nabla\phi\cdot\mathbf{n}dS + \int_V q_\phi dV \tag{3.1}$$

where ϕ represents a scalar quantity: $\phi = 1$ represents the mass conservation, and $\phi = u_i$ represents momentum conservation. The four terms included represent the transient term, convective flux, diffusive flux, and the source term. Collocated mesh arrangement is used in STAR-CCM+ with the computational node lying at the CV center. For a particular CV, to obtain an algebraic equation relating the variables at the CV center to the values at several neighbor CVs, several approximations need to be made, including the surface and volume integrals, and interpolation of ϕ and derivative of ϕ for the convective and diffusive terms, respectively.

In STAR-CCM+, the surface integral adopts the simplest second-order method – the midpoint rule, in which the integral is approximated as the product of the integrand at the cell face center and the cell face area, while the cell-face value needs approximation by interpolation.

$$F_e = \int_{S_e} f dS = \bar{f}_e S_e \approx f_e S_e \tag{3.2}$$

The volume integral uses the simplest second-order method by replacing the integral as the product of the mean value of the integrand and the CV volume, and the mean value is approximated by value at the cell center.

$$Q_P = \int_V q dV = \bar{q}\Delta V \approx q_P \Delta V \tag{3.3}$$

In this work, for the URANS and STRUCT-ε simulations, the interpolation of the convective terms uses the second-order upwind scheme, in which the value at the cell face center is determined by the cell center values in the upstream cells of the face. With the notation given in Figure 3-1, the expression is as follows:

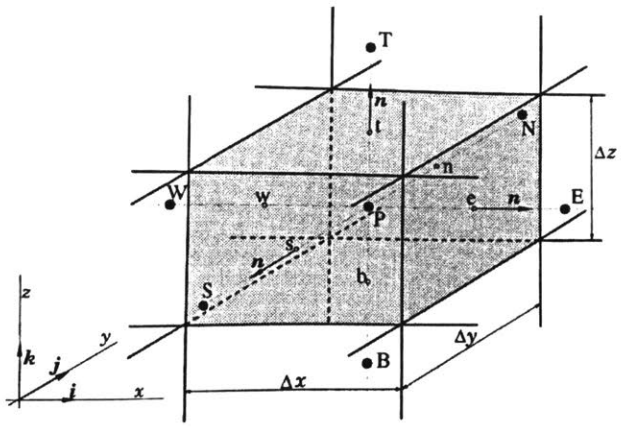

Figure 3-1: A typical CV and the notation used for a Cartesian 3D grid (from [8])

$$\phi_e = \begin{cases} \phi_P + (\mathbf{x}_e - \mathbf{x}_P) \cdot (\nabla\phi)_P & if \quad (\mathbf{u} \cdot \mathbf{n})_e > 0 \\ \phi_E + (\mathbf{x}_e - \mathbf{x}_E) \cdot (\nabla\phi)_E & if \quad (\mathbf{u} \cdot \mathbf{n})_e < 0 \end{cases} \tag{3.4}$$

The gradients included in (3.1) require reconstruction at the cell faces. In regions with strong gradients, the second-order upwind scheme can generate new local minima and maxima, causing stability issues and dispersive error. To overcome the problem, the Venkatakrishnan limiter [101] is combined with the second-order upwind scheme to achieve both accuracy and stability. For LES simulations, the interpolation of the convective terms uses a bounded central differencing scheme. For the IDDES simulations, a hybrid bounded central differencing scheme is used. Details can be found in the STAR-CCM+ User Guide [102].

For the gradient computation at cell centers and at cell-face centers, the hybrid Gauss least squares method is used, which blends two gradient computation methods: the least-square (LSQ) method and the Green-Gauss (GG) method. While the LSQ method is known to provide more accurate gradient construction in Cartesian grids, the GG method behaves better in thin and curved cells found in wall refinement regions [103]. A hybrid method takes advantage of the methods with a blending factor β depending on the geometrical properties of cells [102]. The unlimited (denoted by superscript u) reconstruction gradients in cell P are computed using the following

formula:

$$(\nabla\phi)_P^u = \sum\nolimits_f (\phi_n - \phi_P) w_f^P \tag{3.5}$$

$$w_f^P = \beta w_f^{lsq} + (1-\beta)\, w_f^G \tag{3.6}$$

$$w_f^{lsq} = \left[\sum\nolimits_f \frac{\mathbf{ds} \otimes \mathbf{ds}}{\mathbf{ds}^2}\right]^{-1} \frac{[\mathbf{ds}]}{\mathbf{ds}^2}, \mathbf{ds} = \mathbf{x}_n - \mathbf{x}_P \tag{3.7}$$

$$w_f^G = \frac{A_f}{V_P + V_n} \tag{3.8}$$

where ϕ_P and ϕ_n denote the quantity values in cell P and its neighboring cell n. $\mathbf{x}_P$ and $\mathbf{x}_n$ are the center coordinates at cell P and cell n, with interface f and face area vector A_f. V_P and V_n are the respective cell volumes, and β is the Gauss/LSQ gradient blending factor. When the gradient is used to determine face values, the Venkatakrishnan limiter is applied to the unlimited reconstruction gradient so that the reconstructed face value does not exceed the maximum and minimum of the neighboring cell values.

For transient simulations, the total time is divided into multiple time steps. The solution of the governing equations obtained at time level t requires the solutions at previous time levels. A second-order three-time-level implicit scheme is used for temporal discretization of the transient term:

$$\left(\frac{d\phi}{dt}\right)^{n+1} = \left(\frac{3}{2}\phi^{n+1} - 2\phi^n + \frac{1}{2}\phi^{n-1}\right)\frac{1}{\Delta t} \tag{3.9}$$

where ϕ^n is the quantity value at time level $n+1$ and Δt is the time step. For all the simulations in this work, the time step is chosen so that the maximum courant number is smaller than or close to 1.0.

When all the approximations are considered, the algebraic equation for each CV is produced. The system of equations for the whole computational domain is set up to be solved. However, solving for the flow field contains another difficulty. The momentum equation contains the gradient of the pressure, but there is no independent equation governing the pressure in the field. To deal with this complication, the semi-implicit method for pressure-linked equations (SIMPLE) algorithm [104] is used, in

which a pressure correction equation is derived to replace the continuity equation. The algorithm is iterative and its basic steps in the solution update are summarized as follows [102]:

1). Set the boundary condition for velocity and pressure.

2). Compute the gradients of the velocity and pressure.

3). Solve the discretized momentum equation to compute the intermediate velocity field $\mathbf{v}^*$.

4). Compute the uncorrected mass fluxes at faces $\dot{m}_f^*$.

5). Solve the pressure correction equation to produce cell values of the pressure correction p'.

6). Update the pressure field:

$$p^{k+1} = p^k + \omega p' \tag{3.10}$$

where ω is the under-relaxation factor for pressure.

7). Update the boundary pressure corrections p'_b.

8). Correct the face mass fluxes:

$$\dot{m}_f^{k+1} = \dot{m}_f^* + \dot{m}'_f \tag{3.11}$$

9). Correct the cell velocities:

$$\mathbf{v}_p^{k+1} = \mathbf{v}_p^* - \frac{V \nabla p'}{\mathbf{a}'^V_p} \tag{3.12}$$

where $\nabla p'$ is the gradient of the pressure corrections, $\mathbf{a}'^V_p$ is the vector of central coefficients for the discretized velocity equation, and V is the cell volume.

3.2 Problem of the original STRUCT approach

While the STRUCT approach is originally developed for application to wall-bounded flows, a key weakness has been identified when extending its application to open

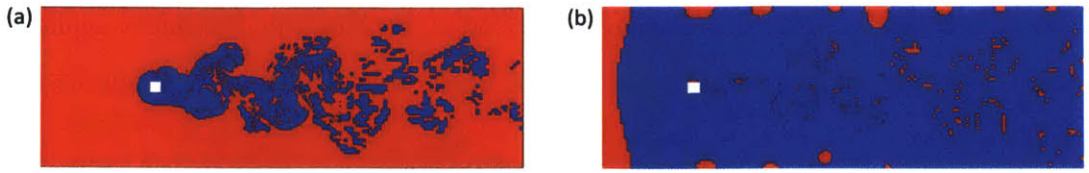

Figure 3-2: Comparison of the controlled STRUCT activation regions (shown in blue) for flow past a square cylinder with (a) non-slip wall boundaries and (b) slip wall boundaries on the top and bottom

boundary external flow cases: the hybridization regions depend on the user-defined inlet boundary conditions, therefore leading to spurious model activation when improper inlet conditions are specified. This problem exists for all the three STRUCT closures and is illustrated in Figure 3-2 by comparing the activation regions generated by controlled STRUCT for the flow past a square cylinder with different boundary conditions. In the figure, the left boundary is specified as velocity inlet with a uniform velocity, user-defined turbulent kinetic energy k, and user-defined turbulent dissipation rate ε. The right boundary is specified as a pressure outlet. For the top and bottom boundaries, when they are defined as non-slip walls, the resulting hybrid activation regions seem reasonable and lie in the areas with strong flow deformation independent of the specified inlet turbulence; when they are specified as slip walls corresponding to an open boundary scenario, however, undesirable hybridization regions are generated when the user-specified inlet k/ε value is too large.

The reason for the problem lies in the explicit dependence of the hybrid activation on the modeled time scale t_m. In the original STRUCT approach, hybridization is activated when $t_m > t_r$. In external flows, the user-defined inlet turbulence quantities k and ε transport to the whole flow domain, affecting t_m globally. Therefore, if the user defines k and ε corresponding to a very large t_m, the hybrid activation is almost everywhere, as the case in Figure 3-2(b). In wall-bounded flows, such a problem does not exist as the modeled time scale t_m is restricted by the geometry.

3.3 Proposal of the new STRUCT-ε model

To overcome the limitation of the original STRUCT approach, a new STRUCT-ε model is proposed. Instead of explicitly comparing the resolved and modeled time scales and introducing a reduction parameter on the eddy viscosity to enable hybridization in the original STRUCT approach, the new model reduces the eddy viscosity implicitly by adding a source term dependent on the second invariant of the resolved velocity gradient tensor $\overline{II}$ in the ε transport equation of the standard k-ε model. The idea is inspired from the work of Menter and Egorov [92]. The STRUCT-ε model formulation is as follows:

$$\nu_t = C_\mu \frac{k^2}{\varepsilon} \tag{3.13}$$

$$\frac{\partial k}{\partial t} + \frac{\partial \bar{u}_j k}{\partial x_j} = \frac{\partial}{\partial x_j}\left[\left(\nu + \frac{\nu_t}{\sigma_k}\right)\frac{\partial k}{\partial x_j}\right] + P_k - \varepsilon \tag{3.14}$$

$$\frac{\partial \varepsilon}{\partial t} + \frac{\partial \bar{u}_j \varepsilon}{\partial x_j} = \frac{\partial}{\partial x_j}\left[\left(\nu + \frac{\nu_t}{\sigma_\varepsilon}\right)\frac{\partial \varepsilon}{\partial x_j}\right] + C_{\varepsilon 1}\frac{\varepsilon}{k}P_k - C_{\varepsilon 2}\frac{\varepsilon^2}{k} + C_{\varepsilon 3} k \left|\overline{II}\right| \tag{3.15}$$

$$P_k = -\tau_{ij}\frac{\partial \bar{u}_i}{\partial x_j} \tag{3.16}$$

$$\sigma_k = 1.00, \sigma_\varepsilon = 1.30, C_{\varepsilon 1} = 1.44, C_{\varepsilon 2} = 1.92 \tag{3.17}$$

The expression of the additional source term $C_{\varepsilon 3} k \left|\overline{II}\right|$ comes from simple dimensional analysis. The value of the newly introduced model coefficient $C_{\varepsilon 3}$ is selected through sensitivity studies on several tests and is discussed in the next section. With this new STRUCT-ε model, the hybridization region no longer depends on the inlet turbulence. In addition, the new STRUCT-ε model concept is consistent with the original STRUCT idea implying the comparison of $|\overline{II}|^{1/2}$ and ε/k: the modification of the ε equation would only become noticeable when $|\overline{II}|^{1/2}$ is larger than ε/k.

The baseline URANS model plays an important part in the performance of the hybrid model. To overcome the inadequacy of the isotropic-viscosity hypothesis, the STRUCT-ε model adopts a cubic NLEVM formulation by Baglietto and Ninokata [66], which is the same as the original STRUCT approach. Other baseline URANS models could also be used, with the possibility of providing improved results, however,

Table 3.1: Cubic NLEVM coefficients

Coefficients	C_{a0}	C_{a1}	C_{a2}	C_{NL1}	C_{NL2}	C_{NL3}	C_{NL4}	C_{NL5}	C_{NL6}	C_{NL7}
Value	0.667	3.9	1.0	0.8	11.0	4.5	-5.0	-4.5	1000.0	1.0

this is not the focus of the current research and can be explored for a further work. In the cubic NLEVM formulation by Baglietto and Ninokata [66], the Reynolds stress tensor has the expression of equation (2.55) with the coefficients given below and in Table 3.1.

$$C_\mu = \frac{C_{a0}}{C_{a1} + C_{a2}\bar{S}^*}, \bar{S}^* = \frac{k}{\varepsilon}\sqrt{2\bar{S}_{ij}\bar{S}_{ij}} \tag{3.18}$$

$$C_1 = \frac{C_{NL1}}{\left(C_{NL6} + C_{NL7}\bar{S}^{*3}\right) C_\mu} \tag{3.19}$$

$$C_2 = \frac{C_{NL2}}{\left(C_{NL6} + C_{NL7}\bar{S}^{*3}\right) C_\mu} \tag{3.20}$$

$$C_3 = \frac{C_{NL3}}{\left(C_{NL6} + C_{NL7}\bar{S}^{*3}\right) C_\mu} \tag{3.21}$$

$$C_4 = C_{NL4}C_\mu^2, C_5 = 0, C_6 = -C_7 = C_{NL5}C_\mu^2 \tag{3.22}$$

For the case of flow past a square cylinder, the distribution of the additional source term $C_{\varepsilon 3}k\left|\overline{II}\right|$ is illustrated in Figure 3-3. The source term has a high value for the separation regions and the near wake past the square cylinder, while the term is almost negligible away from the square cylinder, returning to the mode of URANS. The hybridization is consistent with the STRUCT concept of increasing flow resolution in areas with strong deformation or rapidly varying flows.

Like the original STRUCT approach, the new STRUCT-ε model has no explicit dependency on the computational grid and therefore is consistent with the concept of a second-generation URANS model. The model formulation is very similar to its baseline model, therefore the computational cost is estimated to also be similar. Due to the similarity, the new model is also expected to have high efficiency and robustness, which has been proven for the standard k-ε model. Before applying the new model for aerodynamic applications, the model performance needs to be carefully studied

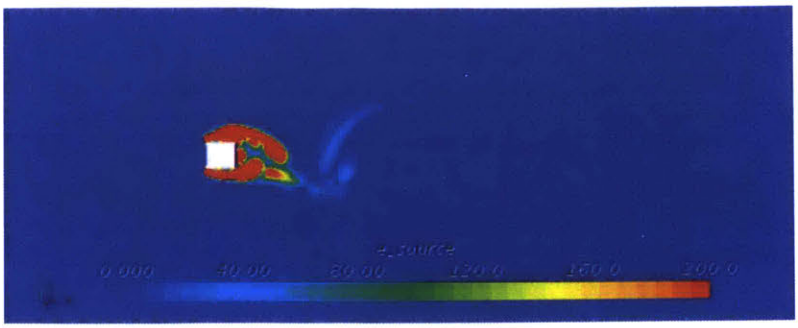

Figure 3-3: Distribution of the source term $C_{\varepsilon 3} k \left|\overline{II}\right|$ for flow past a square cylinder with $C_{\varepsilon 3} = 1.5$.

and validated against published results, which is the main content for Chapter 4.

3.4 Model coefficient selection

The model coefficient $C_{\varepsilon 3}$ introduced in the new STRUCT-ε model is selected through sensitivity analysis in the following test cases: natural transition on the back of a hydrofoil, decaying isotropic turbulence, and mild separation in an asymmetric diffuser. By introducing the source term, better agreement with the experiment is achieved compared with URANS, and variation of the model coefficient results in different levels of accuracy. The selected cases are the most sensitive to the variation of the coefficient, while several other cases do not show obvious sensitivity, including turbulent mixing in a T-junction and flow over periodic hills, therefore these cases are not provided in this work.

3.4.1 Natural transition on the back of a hydrofoil

Hydrofoils working in the low Reynolds number range can experience laminar to turbulent transition on the foil back. Depending on the foil shape, Reynolds number, and angle of attack (AOA), different transition modes may occur, and natural transition is one transition mode that is caused by inherent instabilities in the laminar boundary layer which becomes unstable beyond a critical Reynolds number while the freestream turbulence is very low ($< 1\%$). Predicting the natural transition is a great challenge

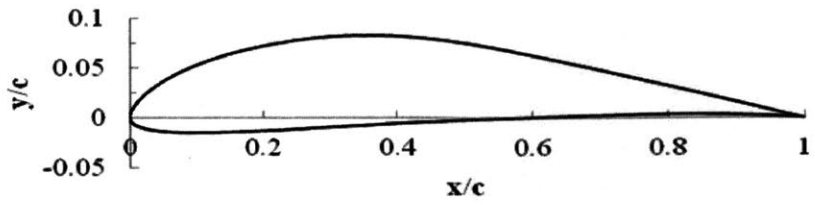

Figure 3-4: Eppler 387

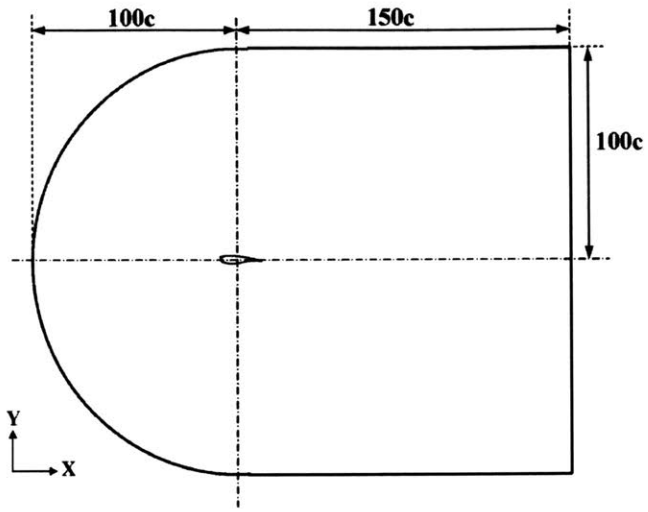

Figure 3-5: 2D section of the computational domain for natural transition on the back of a hydrofoil

for RANS/URANS simulations [105]. Our newly proposed STRUCT-ε model shows great improvement for simulating this challenging flow mechanism, while also showing sensitivity to the model coefficient, which is discussed and leveraged in this work.

The hydrofoil considered is Eppler 387 (Figure 3-4) at 7 degree AOA at Reynolds number of 30,000, corresponding to natural transition according to the wind tunnel experiments performed in NASA Langley Low-Turbulence Pressure Tunnel (LTPT) [106]. The $2D$ section of the computational domain is shown in Figure 3-5 with a C-type shape around the hydrofoil of unit chord length c, and the $3D$ domain is obtained through the extrusion of the $2D$ section in the z direction with an extrusion length of c. For eliminating far-field effects from the boundaries, this large domain has 100 chord length upstream the hydrofoil and towards the sides, and 150 chords downstream.

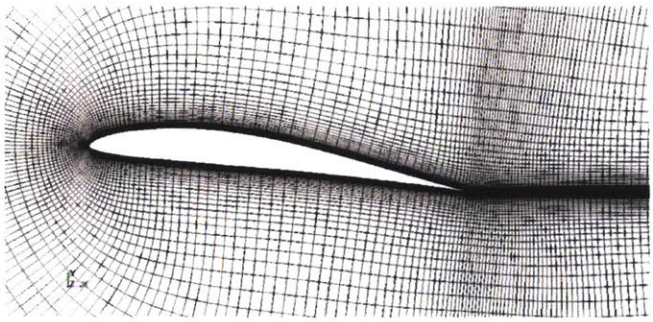

Figure 3-6: Computational mesh around Epper 387 at 7-deg AOA for the STRUCT-ε and the RKE models

Simulations have been performed using both the RKE model and the STRUCT-ε model with different coefficient values on the structured, C-topology computational mesh shown in Figure 3-6. The foil surface is discretized by 400 nodes on the $2D$ section, and 50 nodes in the z direction. The whole $3D$ computational domain contains 2,280,000 cells. The maximum $y+$ on the foil surface is 1.0 while the average value is 0.3. For validation of the results, a LES simulation has been performed using WALE subgrid model. The mesh for LES has similar topology with the mesh shown in Figure 3-6, and the total cell number is 18,336,000.

The front and sides of the domain are set as the constant velocity of 0.405 m/s corresponding to Reynolds number of 30,000 with seawater properties and unit chord length; pressure is extrapolated from inside the domain. The downstream boundary is set as a pressure outlet, with pressure specified and velocity extrapolated. A no-slip wall boundary is prescribed on the hydrofoil surface. For RKE and STRUCT-ε models, the inlet turbulence intensity is chosen as 0.001, corresponding to the average turbulence level in the series of LTPT experiments. For LES simulation, no synthetic turbulence is prescribed at the inlet, as in the experiment, the inlet turbulence intensity is very small 0.1%.

The drag coefficient is defined as:

$$C_d = \frac{F_d}{\frac{1}{2}\rho U^2 A} \tag{3.23}$$

where F_d is the drag force, the force component in the direction of the flow velocity,

Table 3.2: Comparison of the drag coefficient obtained by different turbulence models and the experiment; the last four columns represent the results of the STRUCT-ε model with different coefficient values

	Exp	LES	RKE	$C_{3\varepsilon} = 0.5$	$C_{3\varepsilon} = 1.0$	$C_{3\varepsilon} = 1.5$	$C_{3\varepsilon} = 2.0$
C_d	0.0129	0.0130	0.0206	0.0140	0.0140	0.0139	0.0149
C_d-error		1%	60%	9%	9%	8%	16%

ρ is the fluid density, U is the inlet velocity, and A is the reference area specified as the chord length c times the extrusion length in the simulations.

Table 3.2 compares the drag coefficient C_d obtained with the different turbulence models and the LTPT experiment. While the RKE model shows a 60% error for predicting the drag coefficient, the STRUCT-ε model provides considerably improved predictions with less than 10% error when the model coefficient $C_{\varepsilon 3}$ is less than or equal to 1.5. When the model coefficient is equal to 2.0, the drag error increases. From the drag prediction, it seems $C_{\varepsilon 3} = 1.5$ has the best performance and a value smaller than it can also be acceptable.

Figures 3-7 and 3-8 illustrate the comparison of the resolved turbulence structure and the modeled eddy viscosity; notice that the eddy viscosity for LES denotes the SGS eddy viscosity. As expected, the RKE model resolves almost no turbulence structures; the eddy viscosity is over-predicted at the leading edge of the hydrofoil, thus the predicted boundary layer is all turbulent without transition. LES gives the most accurate result with a detailed resolution of the turbulent eddies on the back and in the wake of the hydrofoil. The transition from laminar to turbulent flow can be observed in the resolved structures. The corresponding SGS eddy viscosity exhibits negligible value on the hydrofoil back, implying a well-resolved situation, and some value in the wake. In comparison with the RKE model, the STRUCT-ε model generates increased resolved turbulence structures, which is controlled by the model coefficient $C_{\varepsilon 3}$. As the coefficient value increases, the eddy viscosity decreases, and more turbulence structures are resolved. To predict transition, some level of turbulence resolution can be helpful as the transition is hardly generated only from

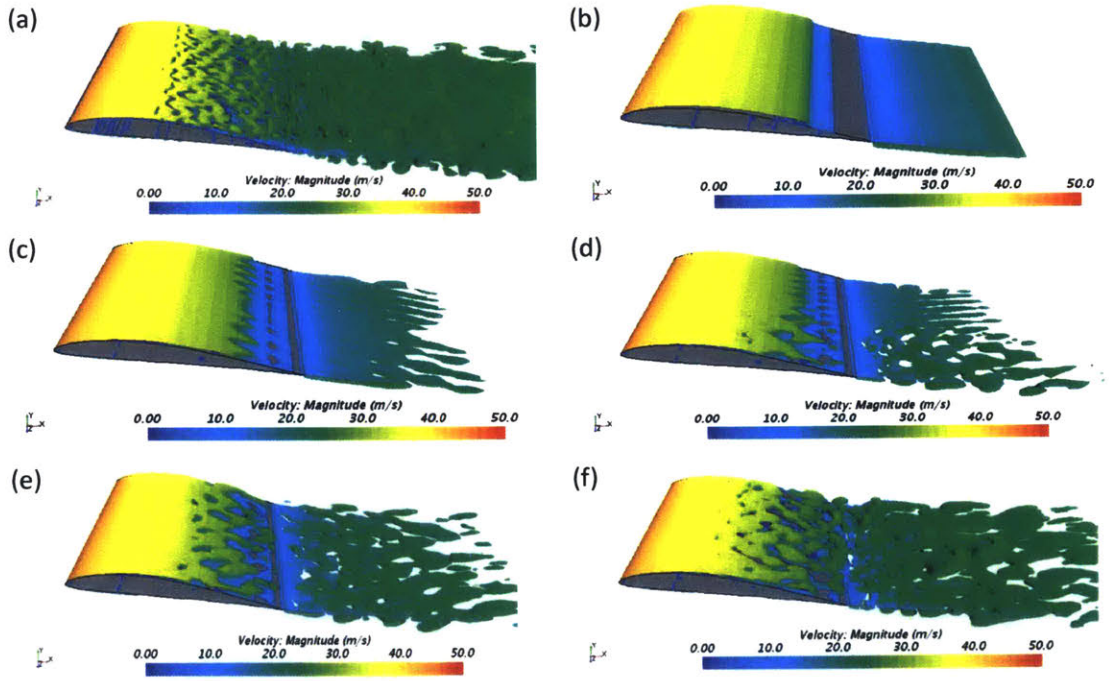

Figure 3-7: Isosurfaces of $Q = 200/s^2$ around Eppler 387 obtained with (a) LES, (b) the RKE model, (c) the STRUCT-ε model with $C_{3\varepsilon} = 0.5$, (d) the STRUCT-ε model with $C_{3\varepsilon} = 1.0$, (e) the STRUCT-ε model with $C_{3\varepsilon} = 1.5$, and (f) the STRUCT-ε model with $C_{3\varepsilon} = 2.0$.

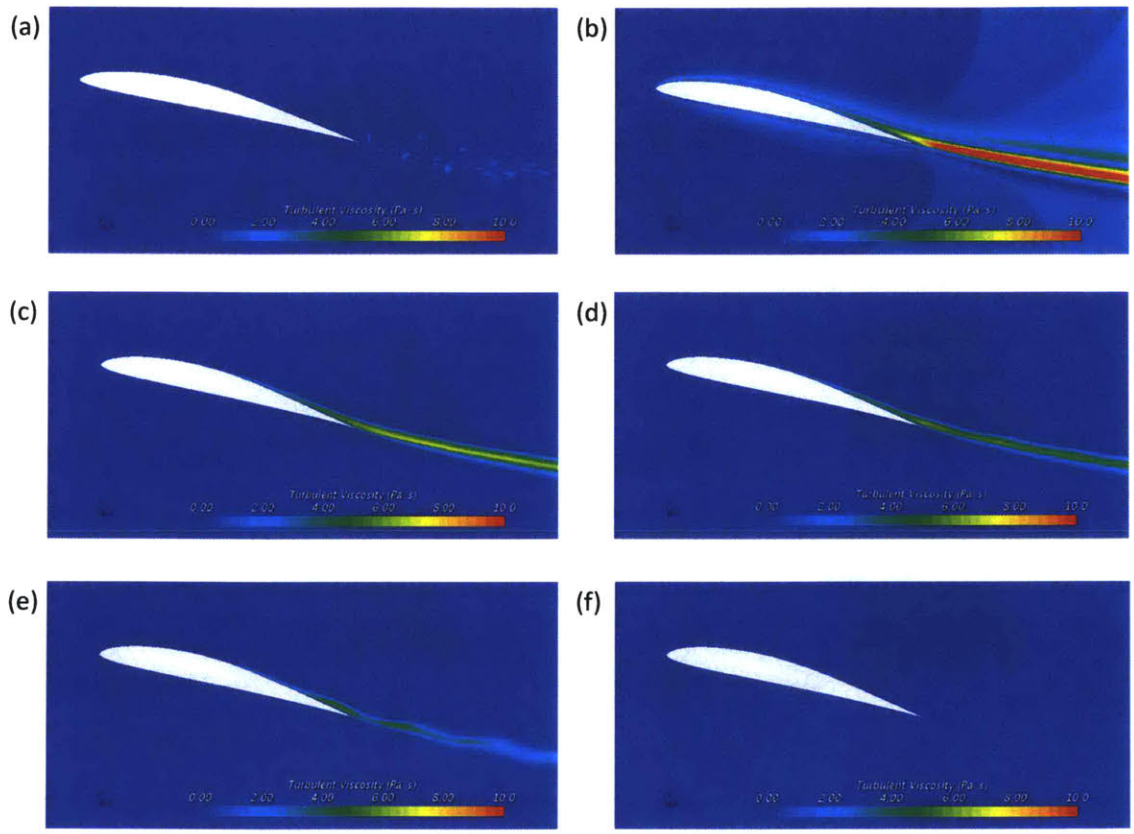

Figure 3-8: Eddy viscosity around Eppler 387 obtained with (a) LES, (b)the RKE model, (c) the STRUCT-ε model with $C_{3\varepsilon} = 0.5$, (d) the STRUCT-ε model with $C_{3\varepsilon} = 1.0$, (e) the STRUCT-ε model with $C_{3\varepsilon} = 1.5$, and (f) the STRUCT-ε model with $C_{3\varepsilon} = 2.0$.

the modeled part. However, the level of resolution should be consistent with the mesh density to avoid over-resolution. In this case, when the coefficient value is increased to 2.0, the eddy viscosity is decreased to zero, implying a DNS scenario, while the mesh is far from being a DNS mesh. Results with smaller coefficient values in the STRUCT-ε model are considered reasonable with transition observed in the resolved turbulence and the modeled eddy viscosity. A larger coefficient value of 1.5 is preferred to make the most of the existing mesh to resolve more structures.

3.4.2 Decaying homogeneous isotropic turbulence

Another case considered is decaying homogenous isotropic turbulence (DHIT). This case is typically used for calibrating model constants. The corresponding experiment was conducted by Comte-Bellot and Corrsin (1971) [107], in which the turbulence spectra were measured at three downstream locations corresponding to three different time T_0, T_1, and T_2. In the CFD simulation, the initial velocity field is generated through inverse Fourier transformation of the experimental spectrum at T_0, and then time advancement is run in the simulation till $T_2 - T_0$. The resulting spectrum is compared with the experimental spectrum at T_2.

The computational domain is a square box with periodic boundary conditions on opposite surfaces. A divergence-free initial velocity field based on the experimental spectrum at T_0 is generated using a code provided by Stanford University [108]. All simulations are computed on a LES-type 64^3 grid using a time step corresponding to the courant number of 0.5. Figure 3-9 shows the comparison of the resolved energy spectrum at T_2 obtained with the LES WALE model, the RKE model, the STRUCT-ε model with different coefficient values, and the experiment. The LES WALE model is in good agreement with the experimental spectrum on the large scales, while the difference in the small scales denotes the modeled energy due to the filtering in LES. As expected, the RKE model damps out the resolved turbulent energy very quickly. The STRUCT-ε model increases the resolved energy as the coefficient value increases. When $C_{\varepsilon 3}$ is larger than 1.0, the resulting energy spectrum is almost the same as the LES result, implying that the STRUCT-ε model has the potential of behaving like

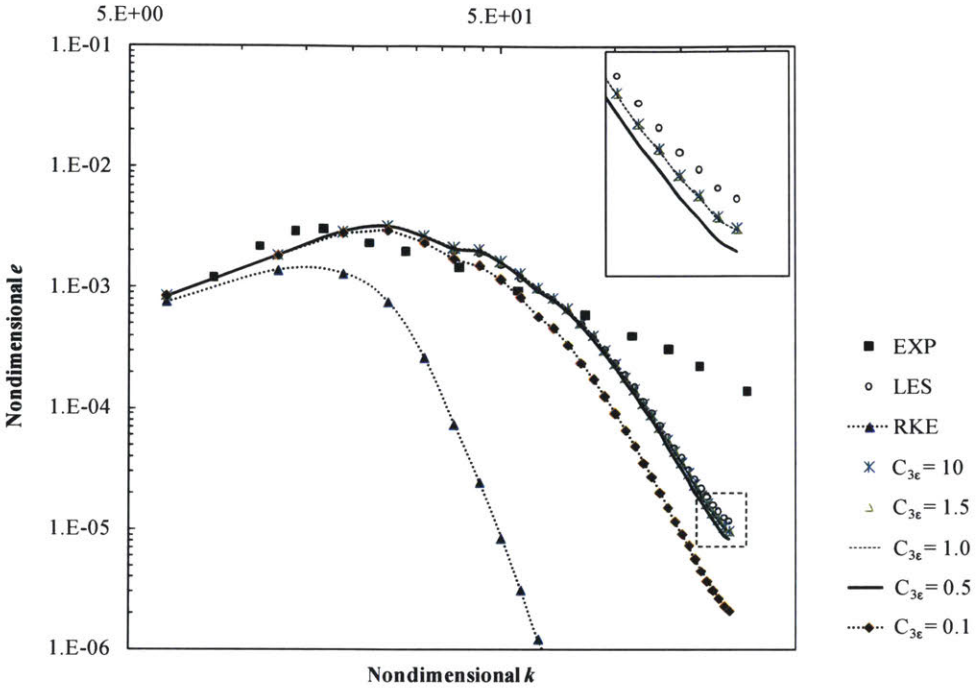

Figure 3-9: Comparison of the turbulent spectra for DHIT obtained with LES, the RKE model, the STRUCT-ε model with different coefficient values, and the experiment.

LES on a LES-type grid. In the corresponding analysis of the SAS model by Mentor and Egorov [92], increasing energy is produced at high wavenumbers exceeding the corresponding LES value, and additional damping is needed for remediation. While the STRUCT-ε model does not suffer from the issue, its performance is not very sensitive to its coefficient $C_{\varepsilon 3}$, especially when the value is larger than 1.0.

3.4.3 Mild separation in an asymmetric diffuser

The test case of flow in an asymmetric diffuser is widely used for evaluating the capability of turbulence models. This case involves mild separation caused by a slight adverse pressure gradient, which is a scenario particularly challenging for hybrid models. The poor performance of SAS has been demonstrated in the work by Davidson (2006) [94] with lower accuracy than the k-ω SST model when compared with the experiment. Due to the challenge, the case was considered in the validation

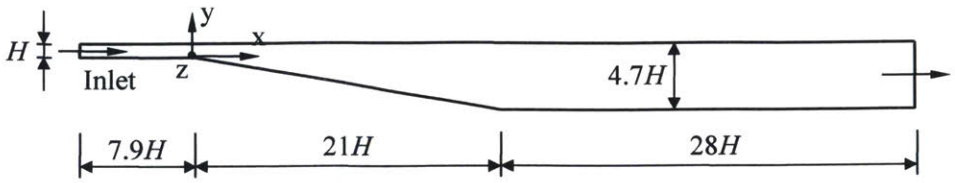

Figure 3-10: Geometry of the asymmetric diffuser

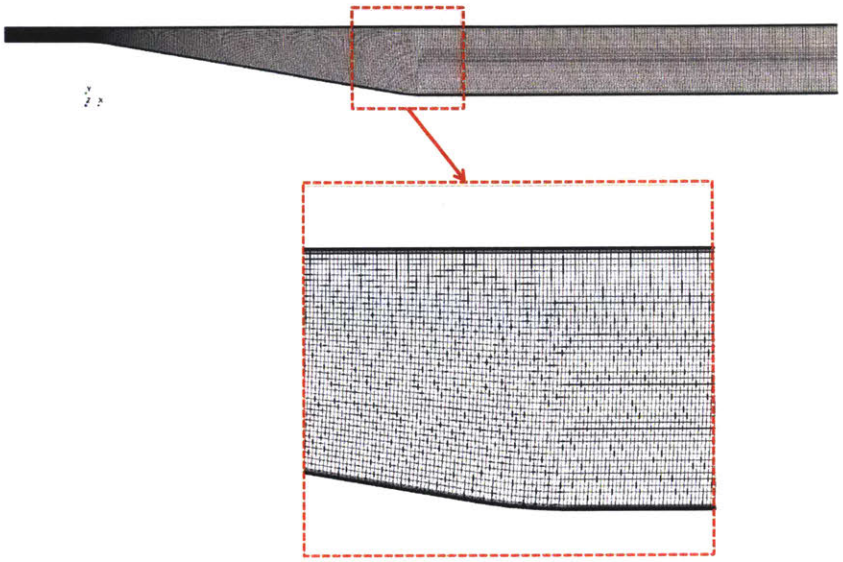

Figure 3-11: Computational mesh for the asymmetric diffuser

of the original STRUCT approach and improved accuracy has been obtained [1]. The present work follows that study, and simulations using the new STRUCT-ε model are performed.

The geometry of the asymmetric diffuser used is illustrated in Figure 3-10 with a 10-degree opening angle. The corresponding experiment was conducted by Buice (1997) [109]. A fully developed flow runs through a rectangular upstream channel with a height H of 1.5 cm. The Reynolds number considered is 20,000 based on the channel height and the bulk inlet velocity. The inlet conditions are taken from the experimental data. The downstream boundary is set as a pressure outlet. The top and bottom of the domain are specified as nonslip walls, while periodic boundary conditions are prescribed in the spanwise direction. The computational mesh is the same as used by Lenci [1] with 1,795,200 cells in total and shown in Figure 3-11. The

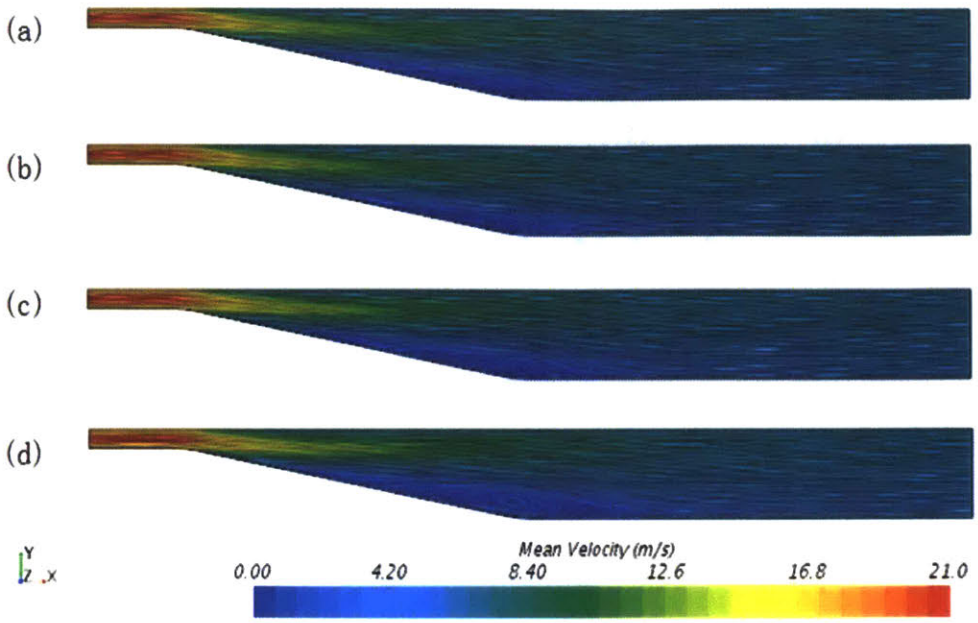

Figure 3-12: Time averaged streamlines for the asymmetric diffuser obtained with (a) the RKE model, (b) the STRUCT-ε model with $C_{3\varepsilon} = 0.5$, (c) the STRUCT-ε model with $C_{3\varepsilon} = 1.0$, (d) the STRUCT-ε model with $C_{3\varepsilon} = 1.5$.

mesh sensitivity study has been performed by Lenci; on the adopted mesh, URANS has achieved reasonable convergence. The $y+$ on the top and bottom walls is smaller than 1.0 for capturing the separation. In this study, simulations are performed using both the RKE model and the STRUCT-ε model with different coefficient values, and results are compared with the experiment by Buice [109].

Figure 3-12 shows the comparison of the mean streamlines predicted by different turbulence models. While the streamlines near the inlet and outlet are predicted very similarly, there is an obvious difference in the corner between the slope and the bottom wall. No recirculation is predicted by the RKE model, while all STRUCT-ε simulations generate a recirculation and the recirculation region increases as the coefficient value increases. The existence of a recirculation region is confirmed in the experiment by Buice [109], proving the improvement of the STRUCT-ε model. A comparison of the detailed velocity profiles is given in Figure 3-13, from which a closer agreement with the experiment is achieved for the STRUCT- ε model with coefficient

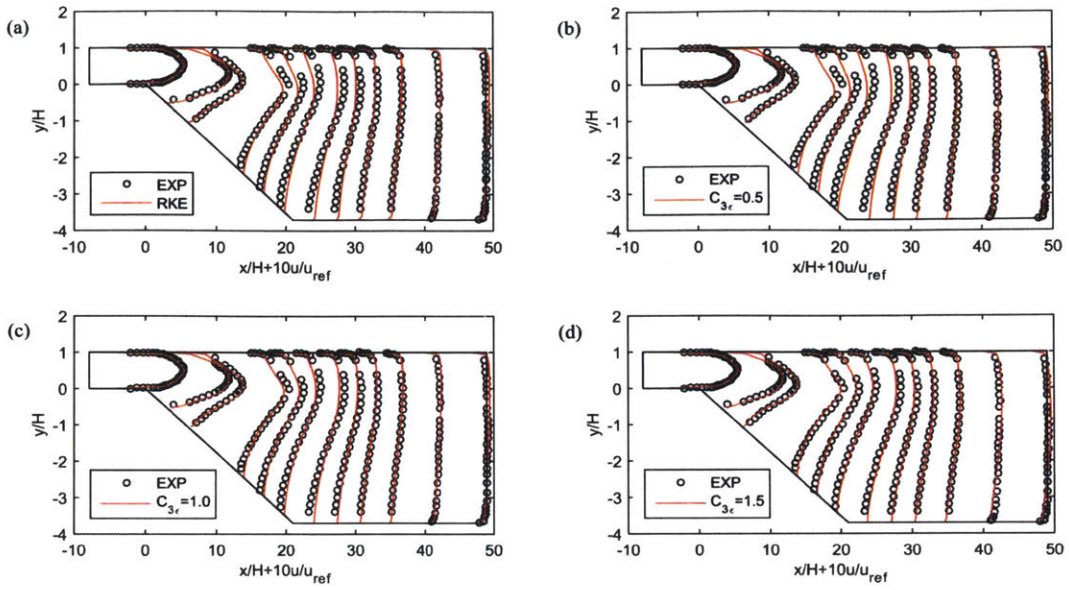

Figure 3-13: Time averaged velocity profiles in x direction for the asymmetric diffuser obtained with (a) RKE, (b) STRUCT-ε with $C_{3\varepsilon} = 0.5$, (c) STRUCT-ε with $C_{3\varepsilon} = 1.0$, (d) STRUCT-ε with $C_{3\varepsilon} = 1.5$, in comparison with the experiment.

Table 3.3: Comparison of the accuracy measure M_0 for the time averaged velocity profiles in the x direction between different turbulence models

RKE	$C_{3\varepsilon} = 0.5$	$C_{3\varepsilon} = 1.0$	$C_{3\varepsilon} = 1.5$
0.5310	0.5412	0.4487	0.4325

values of 1.0 and 1.5. When $C_{\varepsilon 3} = 0.5$, the velocity profiles are very similar to the ones generated by the RKE model. To quantify the accuracy of different models, a linear measure is introduced, which is defined as the average of the absolute deviation between the experimental data and the simulation data interpolated at the locations of the experimental data and has the expression:

$$M_0 = \frac{1}{N} \sum_i |S_i - E_i| \tag{3.24}$$

where E_i and S_i denotes the experiment data and the interpolated simulation data at location i, and N is the number of experimental data.

Table 3.3 compares the value for the mean velocity profiles shown in Figure 3-13 between different turbulence models; the improvement of the STRUCT-ε model with coefficient of 1.0 or 1.5 is obvious compared with the RKE model and the STRUCT-ε model with a coefficient value of 0.5. Considering also the results from the coefficient sensitivity study of natural transition on the back of a hydrofoil and decaying isotropic turbulence, the model coefficient is finally selected as a constant with value 1.5:

$$C_{\varepsilon 3} = 1.5 \tag{3.25}$$

3.5 Summary

In this chapter, first, a robustness problem of the original STRUCT approach for simulating open boundary flows is identified. To solve the problem, a new improved STRUCT-ε model is proposed. As the problem is found to be related to the explicit dependency of the hybrid activation on the modeled time scale, in the STRUCT-ε model, the eddy viscosity is reduced implicitly through introducing a source term in the ε equation depending on the second invariant of the resolved velocity gradient tensor. The introduced model coefficient is selected through sensitivity analyses on the cases of natural transition on the back of a hydrofoil, decaying homogeneous isotropic turbulence, and mild separation in an asymmetric diffuser. Finally, the numerical implementation is briefly discussed.

Chapter 4

Validation of the STRUCT-ε model

In this chapter, the newly proposed STRUCT-ε model is validated on both fundamental test cases and test cases in the automotive industry. Comparison has been performed with the RKE and the IDDES models, which are widely accepted as the best models in the automotive industry for URANS and hybrid models. The STRUCT-ε model demonstrates mesh consistency and improved accuracy across all reference validation data at a comparable computational cost with the RKE model.

The selection of the reference model is based on testing in our group as well as industrial finding at PACCAR (trucks) Daimler (Vehicles in general) and HAAS (F1). The testing has shown that the Realizable k-e model provides overall the most consistent results for a RANS/URANS model, while the DDES provides the best result for Hybrid type approaches.

Among 2nd generation URANS, the Menter SAS idea is the only one generally applicable, but the testing on the mild separation flow case and Ahmed flow cases in literature has shown that the model massively fails and cannot be used reliably.

The focus of the thesis was to compare to the best in class models

4.1 Mesh convergence analysis

Mesh convergence is fundamental to support error estimation due to spatial discretization and determining uncertainty. Existing hybrid models have demonstrated a lack

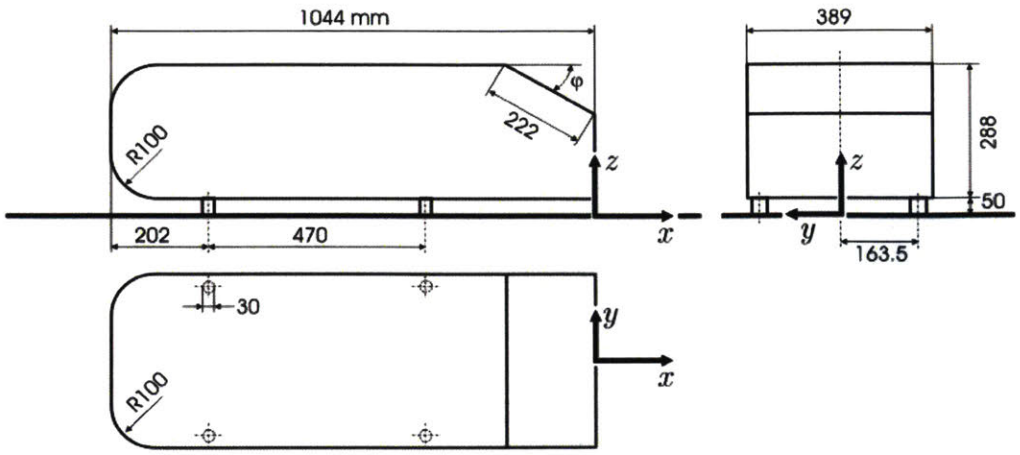

Figure 4-1: Side, rear, and top view of the Ahmed body with dimensions are in mm (from [9]). The slant angle $\phi = 25°$ in this study.

of mesh convergence, with a strong sensitivity to the mesh resolution [110, 88]. This weakness is typically not tolerated in industrial applications as it implies high risk, especially when the experimental data is not available. To explore the mesh convergence behavior of the new STRUCT-ϵ model, a detailed analysis is performed on the test case of the Ahmed body. The Ahmed body is a generic simplified vehicle model originally defined and experimentally studied by Ahmed et al. (1984) [111]. The body geometry is shown in Figure 4-1. It has length $L = 1044$ mm, width $W = 389$ mm, height $H = 288$ mm, and is 50 mm above the ground. The body is characterized by rounded corners on the windward face, a rectangle shape in the middle section, and a slant angle in the rear. In the experiment by Ahmed et al. [111], the body was connected to strain gauge balance, arranged below the ground plane, by four cylindrical stilts for force measurement, therefore the four cylindrical stilts are also included in the geometry. Abundant experimental and numerical studies have been performed on the Ahmed body, summarized in Section 4.4. In the numerical studies, prediction of the correct flow physics at Reynolds number 2,780,000 and slant angle 25° is especially challenging for different turbulence models and therefore is considered in this work.

The computational domain for the Ahmed body at 25° slant angle is shown in Figure 4-2. The domain extends 11 body lengths L, with $5L$ upstream and down-

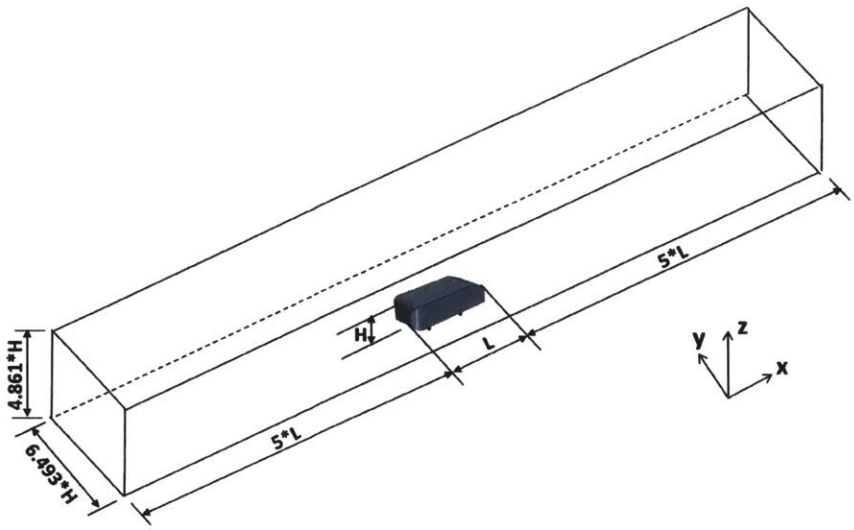

Figure 4-2: Computational domain for the Ahmed body at 25° slant angle.

stream respectively; the width and height of the domain in the y and z directions respectively are set as 6.493 and 4.861 times the body height H, as recommended for the ERCOFTAC Workshop on Refined Turbulence Modelling [112] and [113]. The origin of the coordinate system is located at the rear end of the Ahmed body as shown in Figure 4-1. Regarding boundary conditions, the left boundary is set as a constant velocity of 40 m/s corresponding to Reynolds number of 2,780,000 based on the body length L; the right boundary is set as pressure outlet. A no-slip wall boundary condition is prescribed on the body surface and the ground, while the top and sides of the domain are set as symmetry boundary conditions.

To study mesh dependency, a set of six meshes with a totally 0.3, 0.8, 1.7, 3.11, 8.49, and 25.6 million cells are used, denoted as Mesh_1 to Mesh_6. All mesh controlling parameters are refined consistently with a ratio of 1.5; the near-wall prism layer number and thickness are kept the same for the six meshes so that the wall $y+$ value is close to 1. Refinement boxes are defined around the model back and over the slant, and for Mesh_4 the corresponding cell sizes are 8.3 mm and 4.1mm. A view of Mesh_4 on the symmetry plane is given in Figure 4-3.

Simulations using the STRUCT-ε model are performed on the set of the six meshes. The simulations are stopped at 2 seconds of physical time when the mean

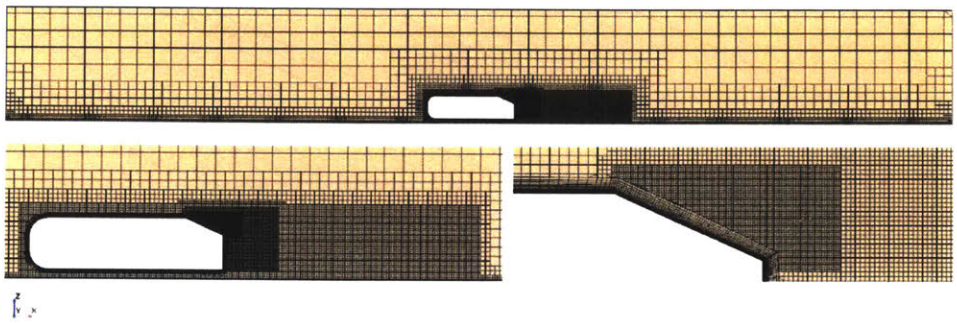

Figure 4-3: View of the Mesh_4 on the symmetry plane.

Table 4.1: Mesh convergence of Cd for the Ahmed body with 25° slant angle.

	Representative cell size [m]	Number of cells	C_d	Times taylor microscale	Times integral length scale
Mesh_1	0.100	0.3M	0.465	19.0	4.56
Mesh_2	0.072	0.8M	0.441	12.7	3.04
Mesh_3	0.026	1.7M	0.395	8.4	2.03
Mesh_4	0.021	3.1M	0.410	5.6	1.35
Mesh_5	0.015	8.5M	0.396	3.8	0.90
Mesh_6	0.010	25.6M	0.399	2.5	0.60

and RMS values of the flow velocity and the drag value are converged. Table 4.1 summarizes the resulting drag coefficient C_d with the definition:

$$C_d = \frac{F_d}{\frac{1}{2}\rho U^2 A} \tag{4.1}$$

where F_d is the drag force acting on the body, ρ is the air density, U is the inlet velocity, and A is the projected frontal area of the model. The representative cell size h is calculated as follows according to [114]:

$$h = \left[\frac{1}{N}\sum_{k=1}^{N}(\Delta V_k)\right]^{1/3} \tag{4.2}$$

where ΔV_k is the volume of the k-th cell, and N is the total number of cells used for the simulation. Estimation of the discretization error follows a least squares version of the Grid Convergence Index (GCI) method [114], in which the error estimation is obtained by Richardson extrapolation (RE) by assuming that the error has a power series representation in the grid spacing:

$$\delta_{RE} = \phi_i - \phi_0 = \alpha h_i^p \tag{4.3}$$

where ϕ_i is the numerical solution of a scalar quantity on a given mesh designated by the subscript i, ϕ_0 is the estimated exact solution, α is a constant, h_i is the representative grid cell size on a given mesh and p is the observed order of accuracy. ϕ_0 , α and p are obtained with a least squares root approach that minimizes the function:

$$S(\phi_0, \alpha, p) = \sqrt{\sum_{i=1}^{n_g}(\phi_i - \phi_0 - \alpha h_i^p)^2} \tag{4.4}$$

where n_g is the number of grids. The minimum of the function is found by setting the derivatives with respect to ϕ_0 , α and p equal to zero. The standard deviation of

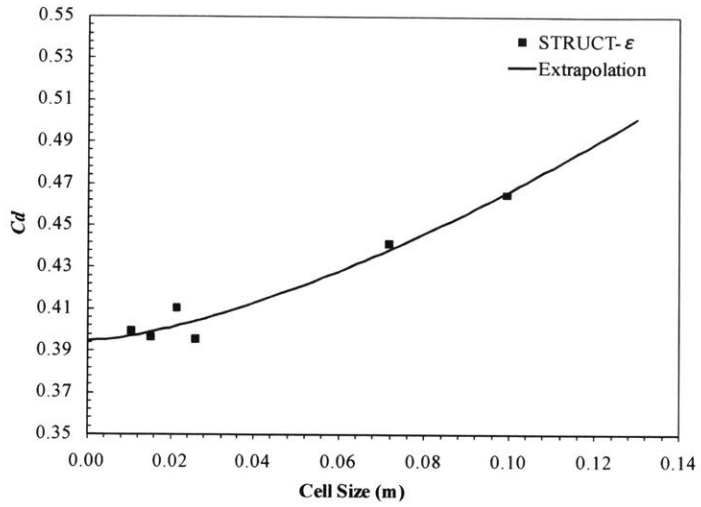

Figure 4-4: Discretization error estimation of C_d based on a least squares version of the GCI method.

the fit U_s is:

$$U_s = \sqrt{\frac{\sum_{i=1}^{n_g} (\phi_i - \phi_0 - \alpha h_i^p)^2}{n_g - 3}} \tag{4.5}$$

When the procedure is applied to the convergence of C_d for the Ahmed body with 25° slant angle, the following parameter values are obtained:

$$\phi_0 = 0.395, \alpha = 2.278, p = 1.5 \tag{4.6}$$

The extrapolation curve is given in Figure 4-4. The apparent order of convergence $p = 1.5$, and the estimated numerical uncertainty is calculated as:

$$U_\phi = 1.25\delta_{RE} + Us \tag{4.7}$$

which for the finest Mesh_6 has a value of 1.3%. For the estimated numerical uncertainty to be less than 5%, the coarsest mesh needed is Mesh_3, for which the mesh resolution corresponds to 8.4 times the Taylor length scale or 2.03 times the integral length scale in the regions of interest near the Ahmed body. As introduced in Section 2.1.3, the integral length scale L_{11} is a measure of scale in the energy-containing

range of turbulence, and LES requires a filter size smaller than $L_{11}/6$ to resolve the energy-containing eddies. The Taylor micro-scale λ does not have a clear physical interpretation, but its approximate position on turbulent energy spectra seems to indicate that it lies at the dissipation region end of the inertial subrange [115]. The Taylor micro-scale λ can be estimated from a classical $k-\varepsilon$ model and has the expression:

$$\lambda \approx \sqrt{10\nu k/\varepsilon} \tag{4.8}$$

where ν is the kinetic viscosity [116]. A LES based on the Taylor micro-scale would become over-resolved at higher Reynolds numbers; and a bound on the filter scale such as $\Delta = max(\lambda, L_{11}/10)$ could be recommended [115]. In this study, mesh resolution of about $2L_{11}$ is needed for the STRUCT-ε model to achieve less than 5% uncertainty. Assuming LES has a mesh size of $L_{11}/6$, the computational cost of the STRUCT-ε model is $1/12^4$ less than that of LES, considering the courant number equals 1.0 for both models.

Mesh convergence in the flow field can be observed in the streamlines near the wake of the Ahmed body as shown in Figure 4-5. For Mesh_1 and Mesh_2, the resulting flow field features a massive separation over the slant and the body back, while for finer meshes, separation becomes smaller with a recirculation bubble on the slant and two vortices right behind the body. It is also worth noting that the averaged velocity magnitude above the slant is different: Mesh_1 and Mesh_2 generate smaller values, Mesh_3 results in higher values, and the three finest meshes have the highest values and very similar distribution. The flow fields for Mesh_4 to Mesh_6 are generally consistent.

4.2 Fundamental cases

This section focuses on validating the STRUCT-ε model on the fundamental cases that are typically used for the validation of hybrid models. The behavior and activation of the STRUCT-ε model are carefully studied. The performance of the STRUCT-ε model is compared with other turbulence models to demonstrate its im-

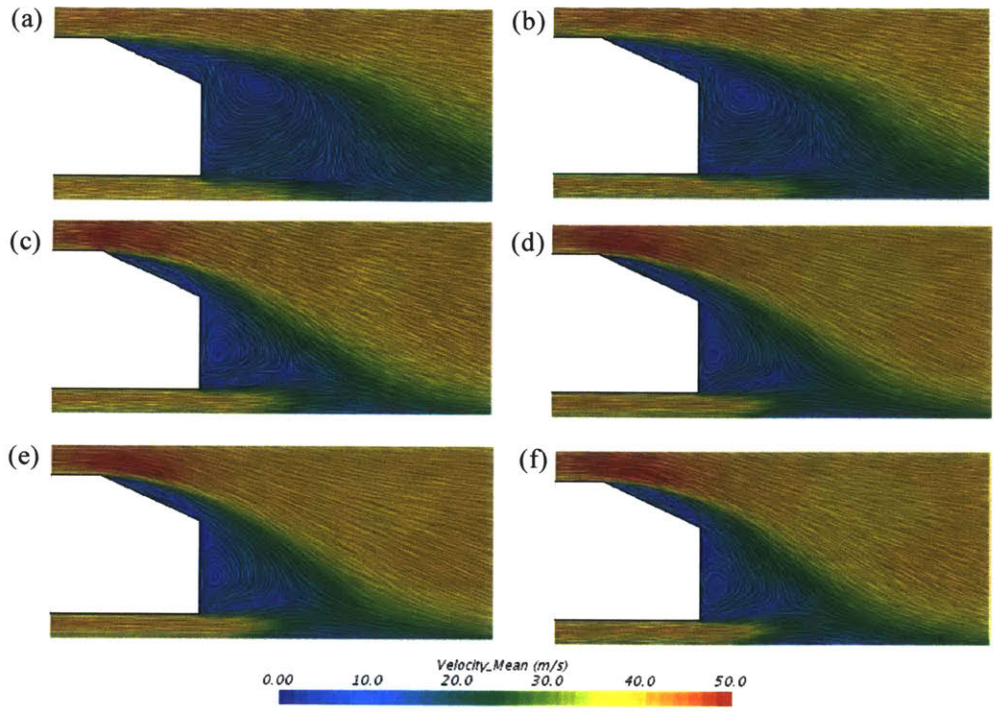

Figure 4-5: Streamlines near the wake of the Ahmed body on the symmetry plane $y = 0$ at different mesh resolutions obtained with the STRUCT-ε model: (a) Mesh_1, (b) Mesh_2, (c) Mesh_3, (d) Mesh_4, (e) Mesh_5, (f) Mesh_6.

proved behavior across different mesh resolutions. The cases considered are (1) flow over periodic hills and (2) flow in an asymmetric diffuser.

4.2.1 Flow over periodic hills

Flow over a series of periodic hills is a test case typically used for the validation of hybrid models. It consists in polynomial-shaped obstacles mounted on a flat plate (Fig. 4-6) and is characterized by turbulent flow separation, recirculation, reattachment, flow deceleration, and acceleration, streamline curvature, etc, inheriting all the features of a flow separating from a curved surface, with reattachment and recovery of the flow. The configuration was first introduced in the LES study by Mellen et al. (2000) [117], following which another LES study was conducted by Temmerman and Leschziner (2001) [10], both were analyzed in detail by Froehlich et al. (2005) [118]. The LES data by Temmerman and Leschziner is available in the ERCOFTAC database [119] and is used here for validation. The test case was presented at the 2002 and 2003 ERCOFTAC workshops [112] [113], where different RANS models were used, ranging from the Spalart-Allmaras one-equation model, standard linear and non-linear $k-\varepsilon$ and $k-\omega$ models, and Reynolds stress models. The RANS simulations involved were not able to capture all the important flow features, and displayed poor agreement with the LES data. In addition, some substantial differences were observed between different RANS models. The challenging character of this test case was also proven by the results obtained in the ATAAC (Advanced Turbulence simulation for Aerodynamic Application Challenges) project [120], in which ten groups contributed to the collaborative computation of the periodic hill. It has been known that flow separating from curved surfaces is very difficult to simulate accurately, as the separation and reattachment points oscillate in space and time, therefore it is not astonishing that RANS predictions tend to perform badly. The ATAAC project also involves several hybrid models including SAS, PANS, and DES and its variants; it showed that most of the hybrid models agree fairly well with the reference LES data.

The geometry has hill height $H = 28mm$, channel height $L_y = 3.035H$, and the

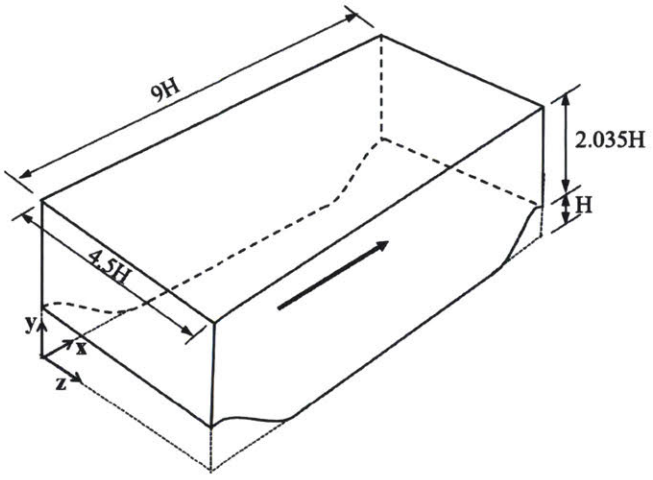

Figure 4-6: Computational domain for the periodic hill.

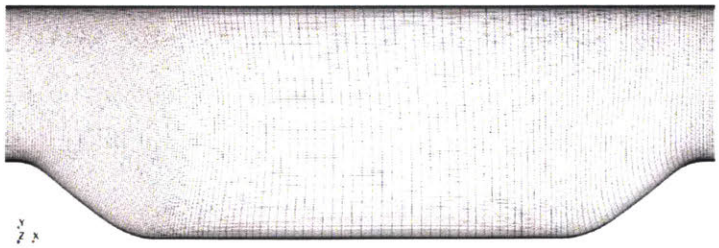

Figure 4-7: Computational mesh of the periodic hill on the x-y section of the geometry.

hill crests are separated by $L_x = 9H$, as shown in Figure 4-6. A spanwise width of $4.5H$ is used in the computational domain to be consistent with the LES study by Temmerman and Leschziner [10]. The domain consists of a single streamwise periodic segment and thus covers solely one complete hill; the domain starts and ends at the hill crest. Regarding the boundary conditions, the upstream and downstream boundaries are prescribed as fully developed periodic boundaries with a constant mass flow rate corresponding to a Reynolds number of 10595 based on the hill height H and bulk velocity at the hill crest U_b. The top and bottom are set as no-slip walls, while periodic boundary conditions are set for the sides in the spanwise direction. The computational mesh uses the mandatory mesh adopted in the ATAAC project, The mesh consists of $N_x \times N_y \times N_z$=$160 \times 160 \times 160$ cells and is available online [120].

In this work, unsteady simulations are performed using the RKE and STRUCT-ε models, and corresponding results are compared with the LES data obtained by Temmerman and Leschziner [10]. Figure 4-8 shows the hybrid activation regions of the STRUCT-ε model by illustrating the additional source term in the ε equation. The hybridization is mostly activated following the flow past the hill crest, where the separation starts and increased resolution is expected. The value of the added source is very low, but is enough to damp the turbulent viscosity significantly as shown in Figure 4-9. The turbulent viscosity generated by the STRUCT-ε model is several orders of magnitude lower than the turbulent viscosity of the RKE model, which mainly comes from a much lower residual turbulent kinetic energy k. The model behavior does change considerably when the source term is added: in this case, both k and ε decrease and a much lower k results in the reduced turbulent viscosity. While the predicted flow is almost steady using the RKE model, the flow is highly unsteady in the STRUCT-ε model. The decreased turbulent viscosity drives the increased resolution of flow unsteadiness. This can be visualized through the comparison of the resolved flow structures identified by the iso-surfaces of the Q criterion, as shown in Figure 4-10. While the RKE model does not resolve any coherent structure, the STRUCT-ε model resolves the large-scale eddies that originate from the shear layer and are convected downstream towards the windward slope of the subsequent hill,

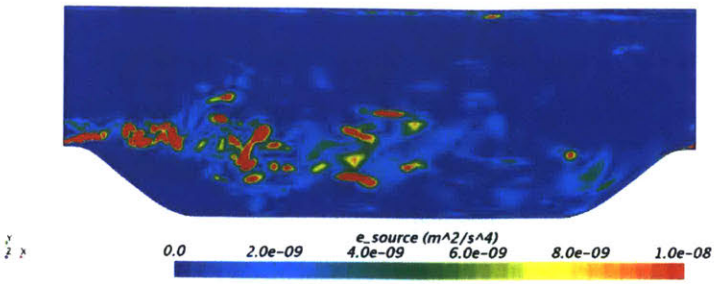

Figure 4-8: Instantaneous hybrid activation regions of the STRUCT-ε model represented by the distribution of the source term $C_{\varepsilon 3} k \left|\overline{II}\right|$ in the XY symmetry plane for the periodic hill.

which dominate the separation of the turbulent shear layer from the recirculation, allowing to capture the unsteady flow separation.

Figure 4-11 shows the time-averaged streamlines obtained using the RKE and the STRUCT-ε models, while the LES result is given in Figure 4-12. Although both models capture the flow topology with separation taken place from the front hill and reattachment observed at the bottom surface between the hills, the RKE model predicts a much longer recirculation zone with a later reattachment, while the streamlines generated by the STRUCT-ε model agrees well with LES. Figure 4-13 compares the time-averaged velocity profiles and the turbulent stress profiles obtained with the RKE, STRUCT-ε models and LES. The predicted turbulent stresses include both the modeled part and the resolved part from the variance of the resolved flow. For the RKE model, the stress value mostly comes from the modeled part as the RKE model does not resolve the flow turbulence; for the STRUCT-ε model, the resolved variance contributes mostly to the calculated turbulent stress. For all the velocity and stress profiles, the STRUCT-ε model shows an improvement over the RKE model with a better agreement with LES, especially for the streamline results and the shear stress, where the discrepancy between the results from the STRUCT-ε model and LES is very small. In the streamwise mean velocity profiles, at $4.0 < x/H < 7.0$, reverse flow is predicted near the bottom wall by the RKE model, while the flow has become attached for both the STRUCT-ε model and LES, which is consistent with the streamline observation. The RKE model predicts much lower turbulent

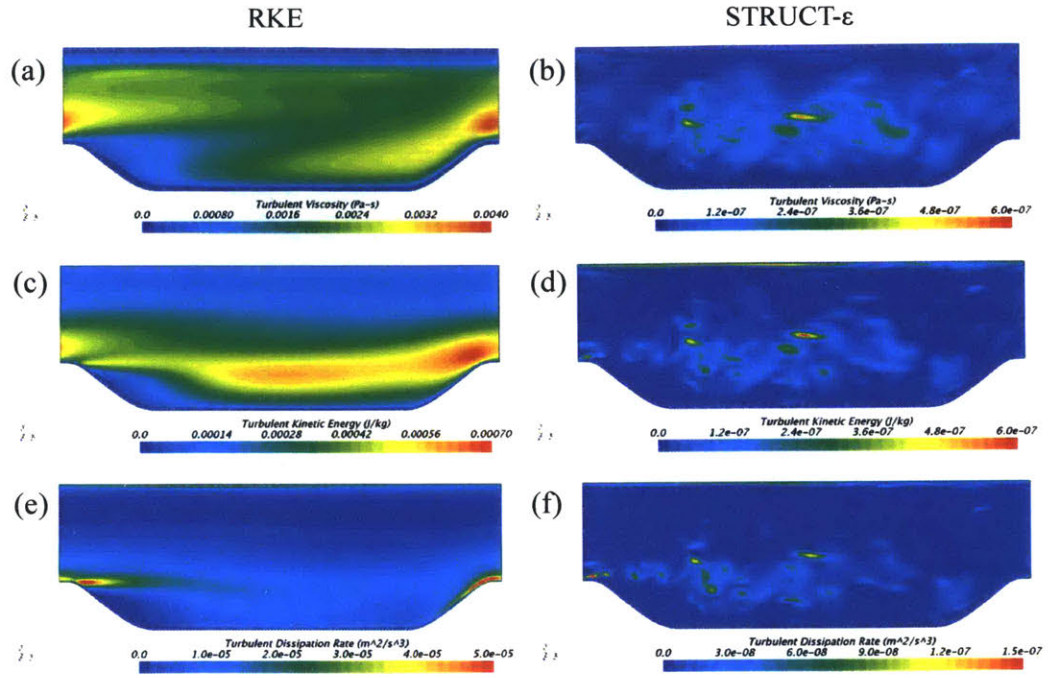

Figure 4-9: Comparison of the instantaneous turbulent viscosity, turbulent kinetic energy, and turbulent dissipation rate between the RKE (left) and STRUCT-ε (right) models in the XY symmetry plane of the periodic hill geometry.

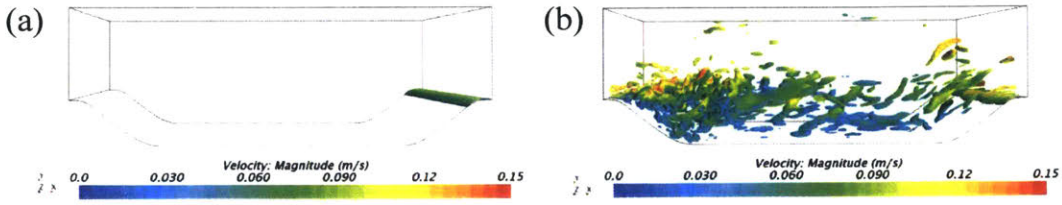

Figure 4-10: Instantaneous iso-surfaces of $Q = 0.05/s^2$ for the periodic hill obtained with (a) the RKE model, (b) the STRUCT-ε model.

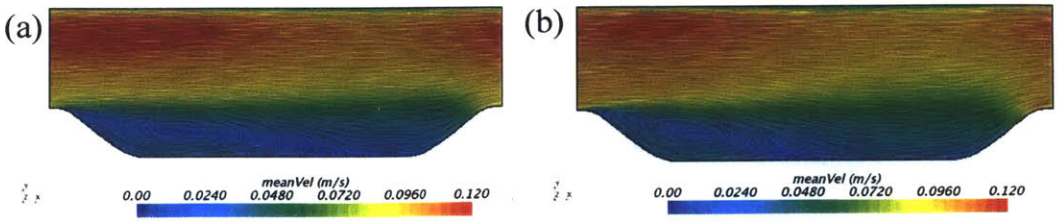

Figure 4-11: Time-averaged streamlines for the periodic hill obtained with (a) the RKE model, (b) the STRUCT-ε model.

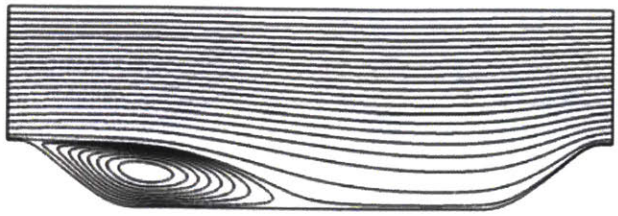

Figure 4-12: Time-averaged streamlines obtained from LES by Temmerman and Leschziner [10].

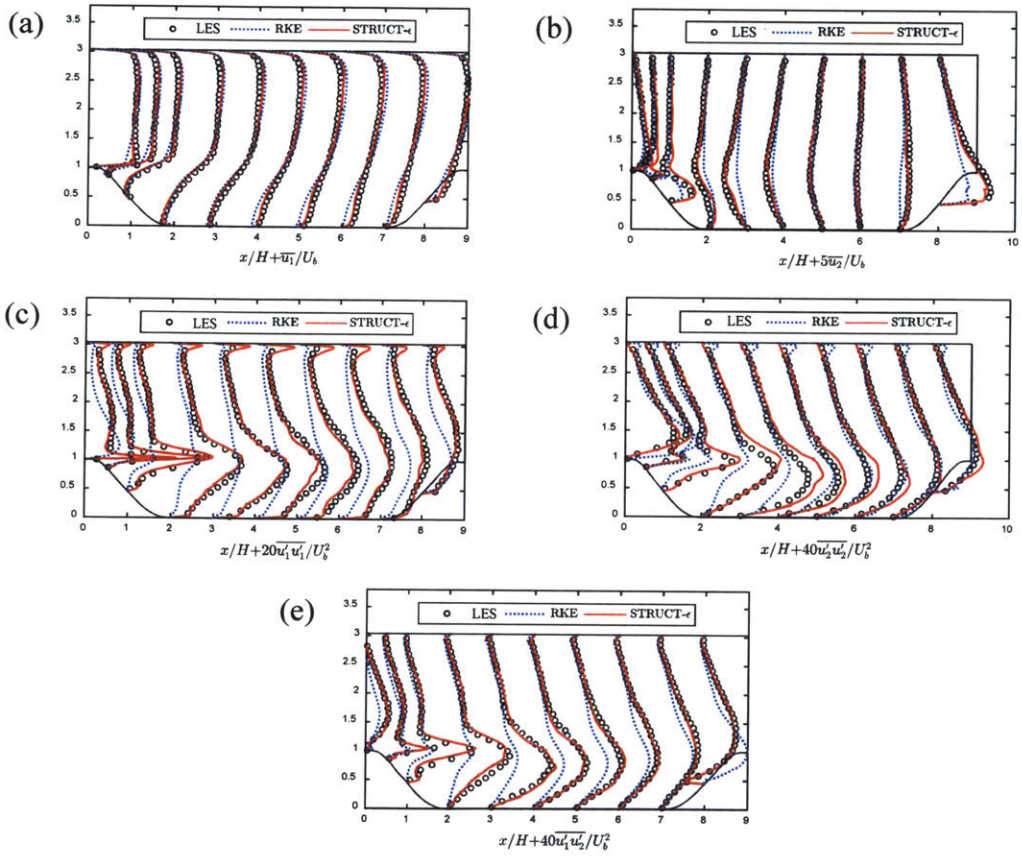

Figure 4-13: Comparison of (a) streamwise mean velocity profiles, (b) longitudinal mean velocity profiles, (c) turbulent streamwise stress profiles, (d) turbulent longitudinal stress profiles, (e) turbulence shear stress profiles, between the RKE, STRUCT-ε models and the LES in the XY symmetry plane of the periodic hill geometry.

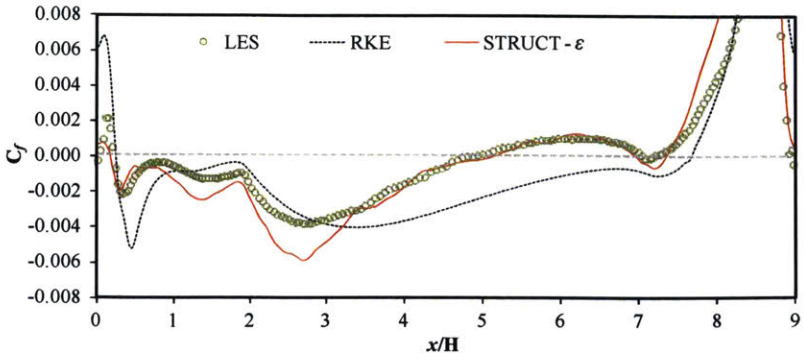

Figure 4-14: Comparison of friction coefficient along the bottom wall of the periodic hill between the RKE, STRUCT-ε models and the experimental data.

stress levels in the flow separation region; the lower shear stresses imply weaker fluid entrainment into the shear layer, explaining the predicted longer recirculation bubble. Contrary to this situation, the shear stresses are overestimated by the RKE model in the windward side of the hill, where the flow is accelerated.

Figure 4-14 compares the friction coefficient along the bottom wall between different turbulence models. The friction coefficient C_f is defined as:

$$C_f = \frac{\tau}{\frac{1}{2}\rho U_b^2} \tag{4.9}$$

where τ is the wall shear stress, ρ is the air density, and U_b is the bulk velocity taken at the hill crest. The positions of the separation and reattachment points can be identified at $C_f = 0$. The STRUCT-ε model predicts the separation and reattachment at $0.20H$ and $5.11H$, respectively, similar to the LES values of $0.22H$ and $4.72H$. The RKE model agrees well with the other models on the separation point at $0.26H$, however, the reattachment is predicted at a much farther position, at around the $7.7H$. Besides, the value and trend of C_f predicted by LES are better captured by the STRUCT-ε model in comparison with the RKE model. Right after the flow past the hill crest and before the separation, the friction coefficient is predicted much higher by the RKE model.

4.2.2 Flow in an asymmetric diffuser

The test case of the asymmetric diffuser was introduced in Section 3.3.3 for selecting the coefficient value for the STRUCT-ε model. The case is characterized by mild separation and reattachment, which is challenging for current hybrid models; extremely poor performance of the SAS model has for example been shown in the study by Davidson [94]. This section focuses on a detailed analysis of the STRUCT-ε model behavior in comparison with the RKE and IDDES models and the experimental data obtained by Buice and Eaton [11].

The geometry of the asymmetric diffuser, the mesh adopted, and the corresponding setting and boundary conditions have been discussed in Section 3.3.3, and comparisons of the streamlines and mean velocity profiles have been made between the RKE and STRUCT-ε models. Following the study, simulation is also performed using the $k-\omega$ SST-IDDES model for comparison. Figure 4-15 shows the mean streamlines obtained with different turbulence models while the experimental pattern is illustrated in Figure 4-16. Only the STRUCT-ε model predicts a large recirculation that resembles the one from the experiment. No recirculation is observed in the RKE result, and a large recirculation is predicted by IDDES in the mainstream. The different performance can be explained through a comparison of the resolved flow structures and the modeled turbulent viscosity shown in Figure 4-17 and Figure 4-18. In the IDDES simulation, the turbulent viscosity is suppressed excessively, becoming practically zero in the whole domain. As a consequence, excessive flow resolution is generated, and the model behaves like DNS but on an inappropriate mesh for DNS, explaining its complete failure to predict the flow topology. Compared to the RKE model, the STRUCT-ε model shows slightly decreased turbulent viscosity and increased flow resolution. It is relevant to note that the small change in turbulent viscosity makes a big difference in the predicted flow topology, implying that the STRUCT-ε model introduces a proper level of increased resolution. A comparison of the turbulent kinetic energy and turbulent dissipation rate generated by the RKE and STRUCT-ε models is provided in Figure 4-19 and Figure 4-20. The STRUCT-ε

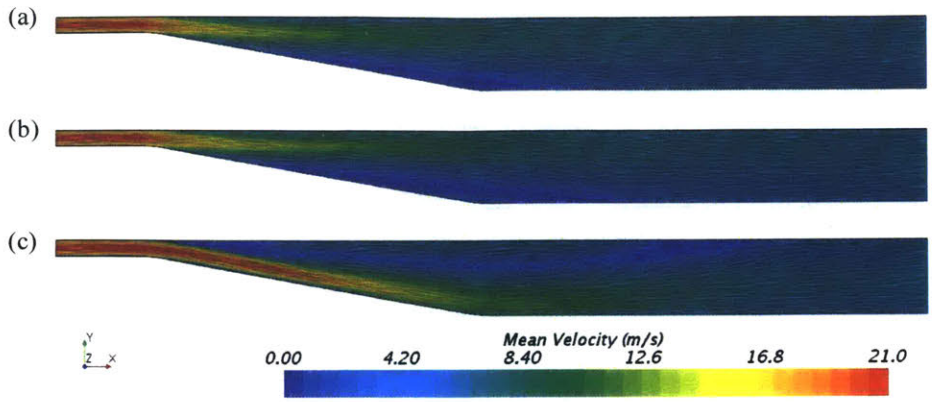

Figure 4-15: Time-averaged streamlines for the asymmetric diffuser obtained with (a) the RKE model, (b) the STRUCT-ε model, and (c) the IDDES model.

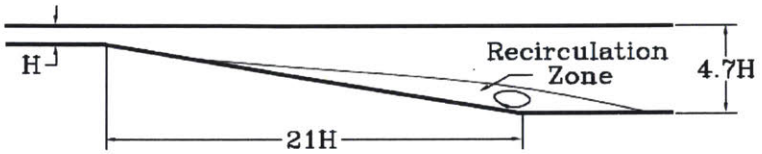

Figure 4-16: The recirculation zone for the asymmetric diffuser, from experiment by Buice and Eaton [11].

model shows increased value in both the turbulent kinetic energy and the turbulent dissipation rate; the combined effect results in the reduced turbulent viscosity. The trend is different from the case of the periodic hill, in which a much reduced turbulent viscosity is produced by the STRUCT-ε model resulting from both much decreased turbulent kinetic energy and turbulent dissipation rate. However, in both cases, the resulting flow topology agrees better with the experiment in comparison with the RKE model, demonstrating that the STRUCT-ε model can adjust the needed level of hybridization through the added source term. Figure 4-21 illustrates the hybrid activation regions of the STRUCT-ε model for the asymmetric diffuser. The strongest hybridization occurs near the sudden expansion of flow where significant deformation is expected, following which the activation also occurs in the mainstream where the turbulent structures are located.

Figure 4-22 compares the time-averaged velocity profiles and the turbulent stress profiles obtained with the RKE and the STRUCT-ε models and the experimental

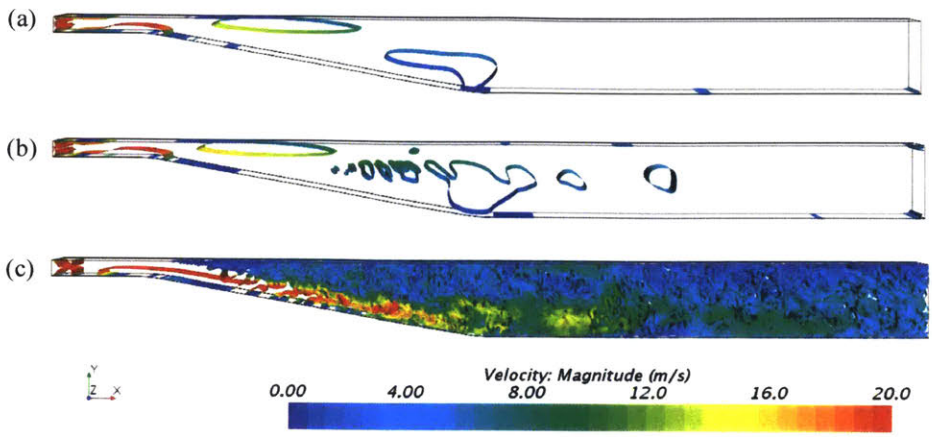

Figure 4-17: Instantaneous iso-surfaces of $Q = 100/s^2$ for the asymmetric diffuser obtained with (a) the RKE model, (b) the STRUCT-ε model, (c) the IDDES model.

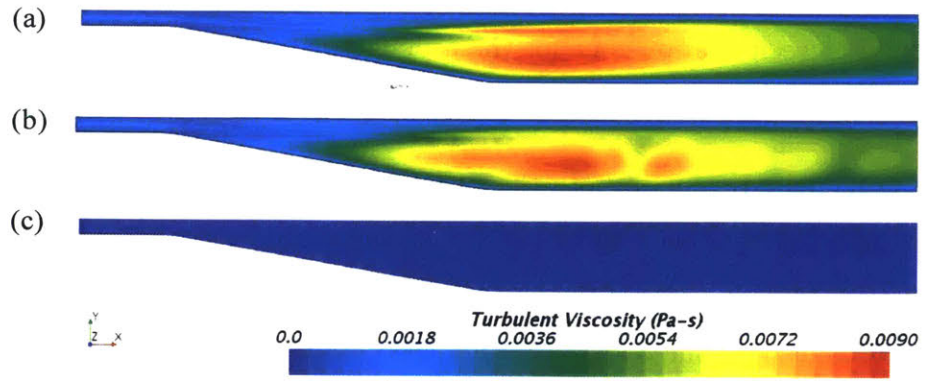

Figure 4-18: Instantaneous turbulent viscosity in the XY symmetry plane for the asymmetric diffuser obtained with (a) the RKE model (b) the STRUCT-ε model, (c) the IDDES model.

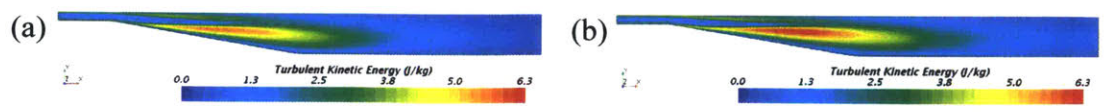

Figure 4-19: Instantaneous turbulent kinetic energy in the XY symmetry plane for the asymmetric diffuser obtained with (a) the RKE model (b) the STRUCT-ε model.

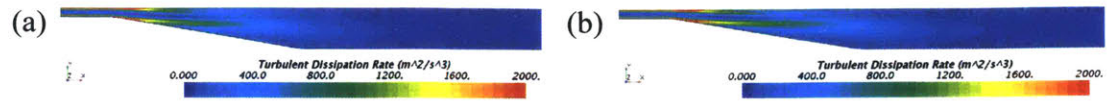

Figure 4-20: Instantaneous turbulent dissipation rate in the XY symmetry plane for the asymmetric diffuser obtained with (a) the RKE model (b) the STRUCT-ε model.

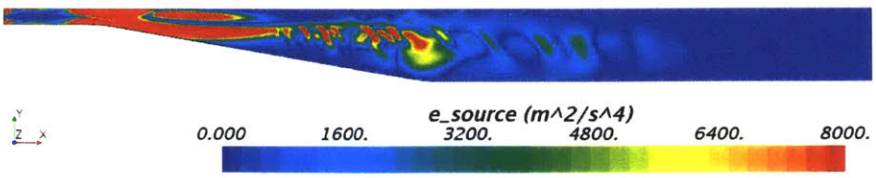

Figure 4-21: Instantaneous hybrid activation regions of the STRUCT-ε model represented by the distribution of the source term $C_{\varepsilon 3} k \left|\overline{II}\right|$ for the asymmetric diffuser.

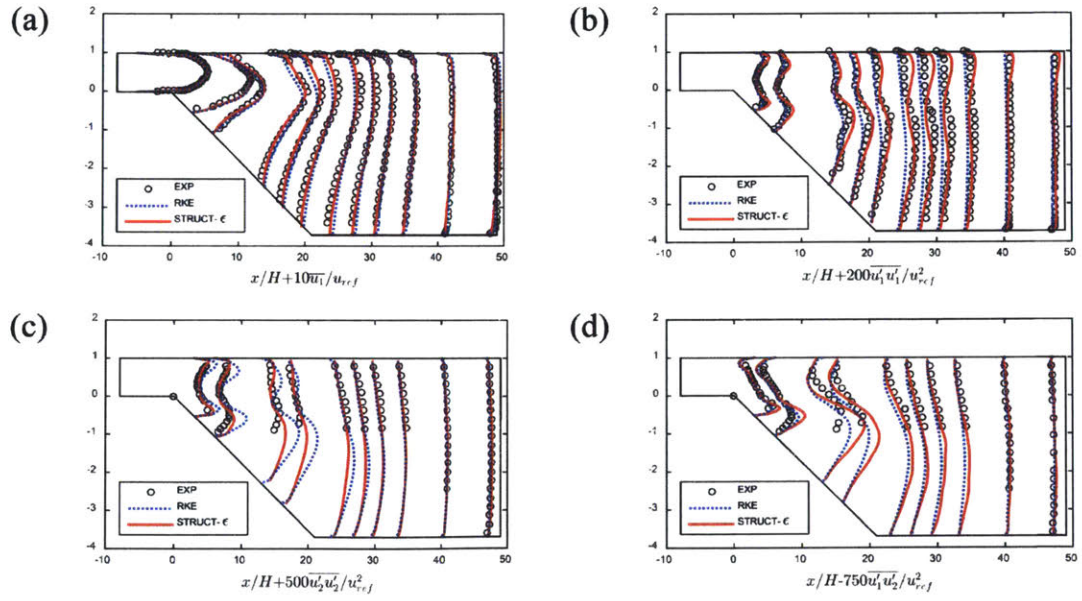

Figure 4-22: Comparison of (a) streamwise mean velocity profiles, (b) turbulent streamwise stress profiles, (c) turbulent longitudinal stress profiles, (d) turbulence shear stress profiles, between the RKE, STRUCT-ε models and the experimental data in the XY symmetry plane of the asymmetric diffuser.

Table 4.2: Accuracy measure M0 for different flow quantities predicted by the RKE and STRUCT-ε models in the asymmetric diffuser.

	$\bar{u}_1$	$\overline{u'_1u'_1}$	$\overline{u'_2u'_2}$	$\overline{u'_1u'_2}$
RKE	0.5310	0.8459	0.5688	0.5430
STRUCT-ε	0.4325	0.3950	0.2499	0.4985

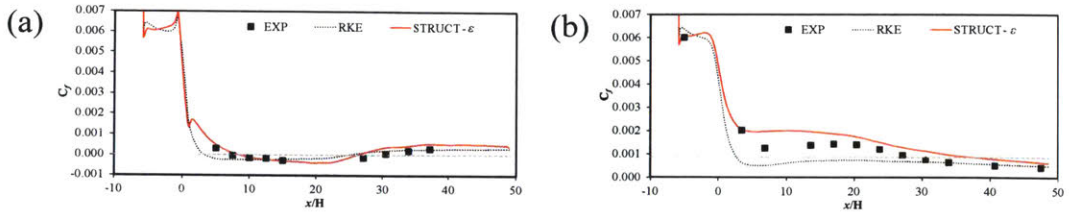

Figure 4-23: Comparison of friction coefficients along the a) bottom, b) top wall of the asymmetric diffuser between the RKE, STRUCT-ε models and the experimental data.

data. The stresses include both the modeled part and the resolved parts. For the RKE model, the stress value mostly comes from the modeled part, while for the STRUCT-ε model, both the modeled and resolved part make important contributions to the calculated stress value. Regarding the mean streamwise velocity profiles, in the regions near the inlet and outlet, both models agree fairly well with the experiment; in the central part, the RKE model exhibits lower velocity gradients with underestimated value in the upper part and overestimated value in the lower part of the domain while the STRUCT-ε model shows some improvement with a better agreement with the experiment. For the stress profiles, the STRUCT-ε model also shows a closer agreement with the experiment, especially in the expansion area. To better assess the model behavior, the linear measure is used for error quantification of the mean velocity and stress profiles with the expression in equation 3.24. The results are summarized in Table 4.2, and smaller errors are shown using the STRUCT-ε model than the RKE model for evaluating the different flow quantities.

Finally, the friction coefficients along the bottom and top wall of the asymmetric diffuser are compared between the models and the experiment given by Fig. 4-23. The friction coefficient follows the definition in equation (4.9), where the reference velocity

is the bulk velocity across the diffuser inlet. In the experiment, the separation occurs at $7.4H$ downstream the expansion start and reattachment takes place at $29.2H$, where H is the inlet height. The RKE predicts an early separation and reattachment at $3.3H$ and $24.5H$, respectively, while the STRUCT-ε model predicts separation and reattachment at $8.2H$ and $26.3H$, closer to the experimental values. In addition, the STRUCT-ε model better captures the experimental trend of C_f in Figure 4-23 (a). From the friction on the top wall, it can be seen that the RKE model predicts flow separation, which is not observed in the experiment. The STRUCT-ε model, on the other hand, does not show flow separation and a closer trend with the experiment is also achieved.

4.3 Cases in the automotive industry

In the fundamental cases, the STRUCT-ε model shows an improved agreement with experiment or LES, when compared to the RKE model, by introducing an increased resolution of turbulence structures. On this basis, the focus is moved to the validation of the STRUCT-ε model in the automotive industry in this section, where the accurate prediction of the flow separation and vortices is necessary and challenging for traditional (U)RANS methods.

4.3.1 Flow past the Ahmed body

The case of flow past the Ahmed body was introduced in Section 4.1 for the mesh convergence study of the STRUCT-ε model. In this section, the generic simplified vehicle model of the Ahmed body is used as the test case in the automotive industry for validation of the STRUCT-ε model in comparison with other relevant turbulence models. The proven pedigree of the experimental data, and most importantly the abundance of previous numerical studies are leveraged.

The Ahmed model was originally defined and experimentally studied by Ahmed et al. (1984) [111]. Further experimental campaigns have also been performed by Bayraktar et al. (2001) [121], who completed a test on an upscaled (4.7:1 ratio)

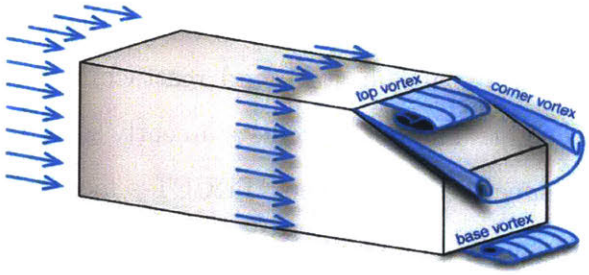

Figure 4-24: Flow topology around the Ahmed body at 25° slant angle (from [12]).

Ahmed body model at the NASA Langley Full-Scale Tunnel, representing a full-size vehicle. Lienhart et al. (2002, 2003) [122] and [123] provided detailed measurements of velocity profiles using the LDA technique in the LSTM wind tunnel; the experimental data are available in the ERCOFTAC database and are widely used for comparison with numerical simulations. Meile et al. (2011) [124] reported the change of the drag coefficient C_d with Reynolds number in an Ahmed body experiment carried out in the low-speed aerodynamic wind tunnel of the ISW at Graz University of Technology, for comparison with CFD results obtained using the Reynolds stress turbulence model. Conan et al. (2011) [125] investigated the drag of the Ahmed body with different slant angles in both an open and a closed test section of the VKI low-speed wind tunnel. Thacker et al. (2012) [126] evaluated the difference between two Ahmed body models respectively with the sharp and rounded edge at the connection between the roof and the rear slant, in the Lucien Malavard wind tunnel of the PRISME Laboratory, University of Orleans. Bello-Millán et al. (2016) [127] presented experiments conducted in the Vehicle Aero-Hydrodynamics Laboratory of Universidad de Málaga to investigate yaw angle effects on the drag force acting on the Ahmed body.

A large number of numerical studies have been conducted on the Ahmed body at 25° and 35° slant angles with different turbulence models including RANS, LES, DES and its variants. While the RANS and URANS approaches [128, 129, 130] have shown success in simulating the flow at 35° slant angle, which is characterized by complete separation over the rear surface of the body, they have all been challenged by the 25° slant angle case, where flow partially separates from the rear slant while

reattaching halfway down the slant back as a consequence of the complex interaction between 3D separation and the counter-rotating vortices coming off the rear window and side (Figure 4-24). All tested RANS and URANS simulations have failed to predict the correct flow topology, with either no separation on the slant or complete separation much like at 35° slant angle. The prediction of the correct flow physics at Reynolds number 2,780,000 and slant angle 25° remains challenging even for LES and DES. Hinterberger et al. (2004) [131] performed a LES study of the flow around the Ahmed body at 25° slant angle, obtaining improved agreement with the experiment in comparison to the RANS studies, but still showing incorrect separation in the lower part of the slant back. Krajnovi and Davidson (2005) [132] have been able to reproduce the correct flow physics and good agreement with the experimental measurements, using LES at 4 times lower Reynolds number to decrease the computational requirements, under the unconfirmed assumption that the position of the separation region is defined by the geometry rather than viscosity and the upstream conditions. Serre et al. (2013) [9] compared the performance of a near-wall modeled LES, a near-wall resolved LES, and a high order LES based on a spectral approximation stabilization technique in the framework of a French-German collaboration on LES of complex flows; only the high order LES approach obtained the correct flow topology, with partial detachment on the slant back. Aljure et al (2014) [133] assessed the performance of four LES models for simulating flow around the Ahmed body at 25° slant angle; the SIGMA, VMS, and WALE models outperformed the QR model for predicting correct flow topology on the slant. The DES studies of Menter and Kuntz ([134],[84]), Kapadia et al. [135], and Guilmineau et al. [136] demonstrated improvements in comparison to the RANS simulations, with good resolution of the vortex structures in the wake, but still did not recover the partial detachment on the slant. Ashton et al. (2015) [137] performed DDES simulations with conclusion that DDES offers an improvement compared to URANS models at sufficiently fine mesh resolution, but again not capturing partial detachment on the slant, while also producing worse results than URANS models at coarse mesh resolution; an embedded DES approach was also proposed by injecting synthetic turbulence at a preselected

interface upstream of the separation point, which resulted in excellent agreement with the experimental data. Recent work of Guilmineau et al. (2018) [138] has presented IDDES simulation of the Ahmed body at 25° slant angle and recovered partial detachment on the slant with good mean velocity agreement with experimental data, while some discrepancies still exist in the RMS values.

Given the challenge, it is valuable to assess the predictive capability of the proposed STRUCT-ε model on the Ahmed body with 25° slant angle and to compare the result to the present state-of-the-art IDDES solution and URANS models, in addition to the experimental data from Lienhart et al. [122] [123]

This section first compares the simulation results from the STRUCT-ε model to the $k-\omega$ SST-IDDES model on three consecutive mesh refinement levels, corresponding to Mesh_4 (coarse), Mesh_5 (medium), and Mesh_6 (fine) in Section 4.1, to assess the performance of the hybridization approach. Later, a comparison is made between the results of the STRUCT-ε and URANS models on the coarsest evaluated mesh (Mesh_4), to assess the improvement in the industrial applicability. The mean velocity and stresses are compared with experimental data by Lienhart et al.

Comparison of the STRUCT-ε and IDDES predictions

Figure 4-25 shows the mean flow streamlines in the symmetry plane $y = 0$ for the STRUCT-ε and IDDES models, together with the experimental streamlines recreated from the mean velocity data. While the IDDES model on the coarse mesh generates a massive separation over the slant and the body back, all other cases result in small separations with a recirculation bubble on the slant and two vortices right behind the body. However, the generated recirculation bubble extends over the whole slant, not recovering the partial detachment in the experiment. This phenomenon has been observed also in previous LES and DES studies. Note that the IDDES model here does not fully recover the correct flow topology as in Guilmineaus work [138]. This is perhaps related to mesh differences or code sensitivity.

Figure 4-26 presents the resolved vortex structures around the Ahmed body, represented by the iso-surfaces of the Q criterion. As the mesh is refined, better vortical

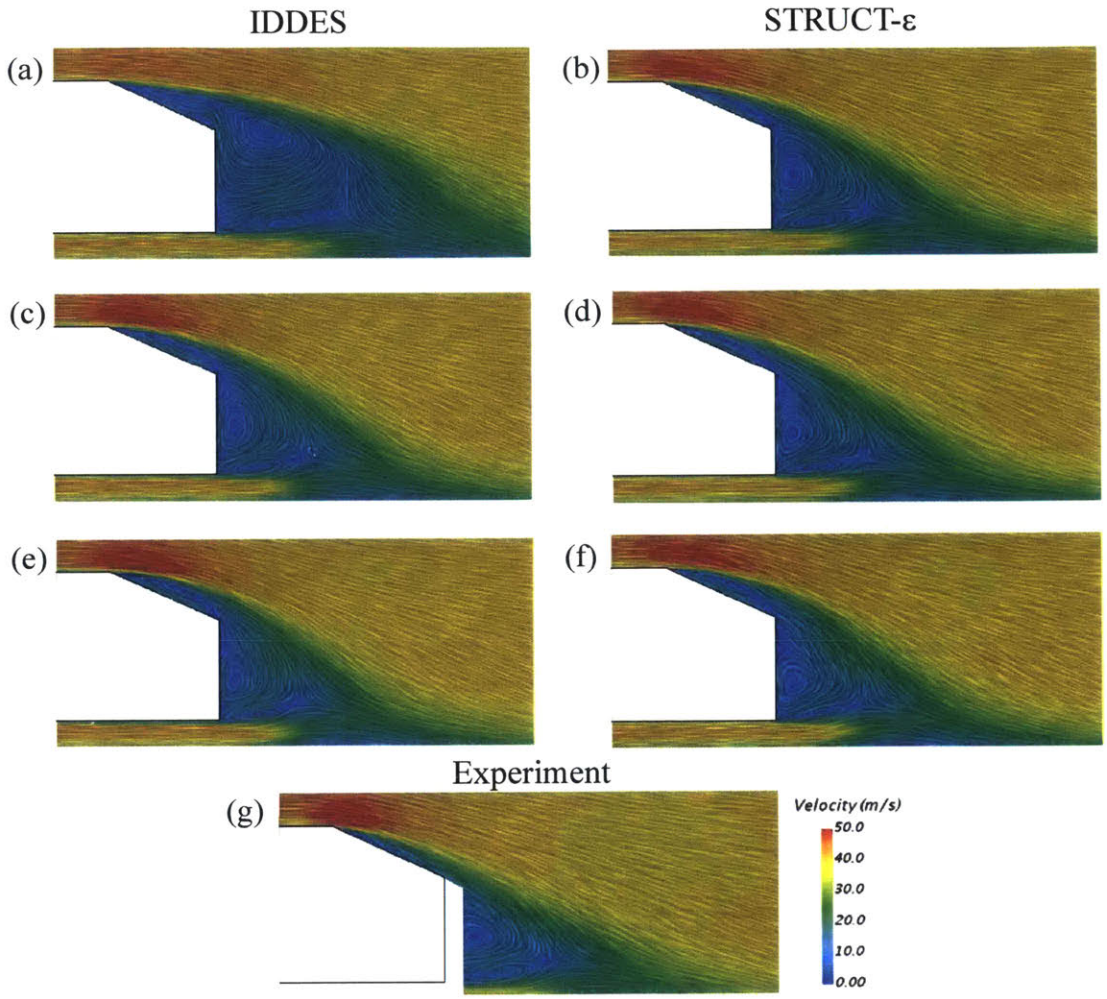

Figure 4-25: Time-averaged streamlines in the symmetry plane y = 0 obtained with (a) the IDDES model on the coarse mesh (b) the STRUCT-ε model on the coarse mesh (c) the IDDES model on the medium mesh (d) the STRUCT-ε model on the medium mesh, (e) the IDDES model on the fine mesh, (f) the STRUCT-ε model on the fine mesh, and (e) the experiment.

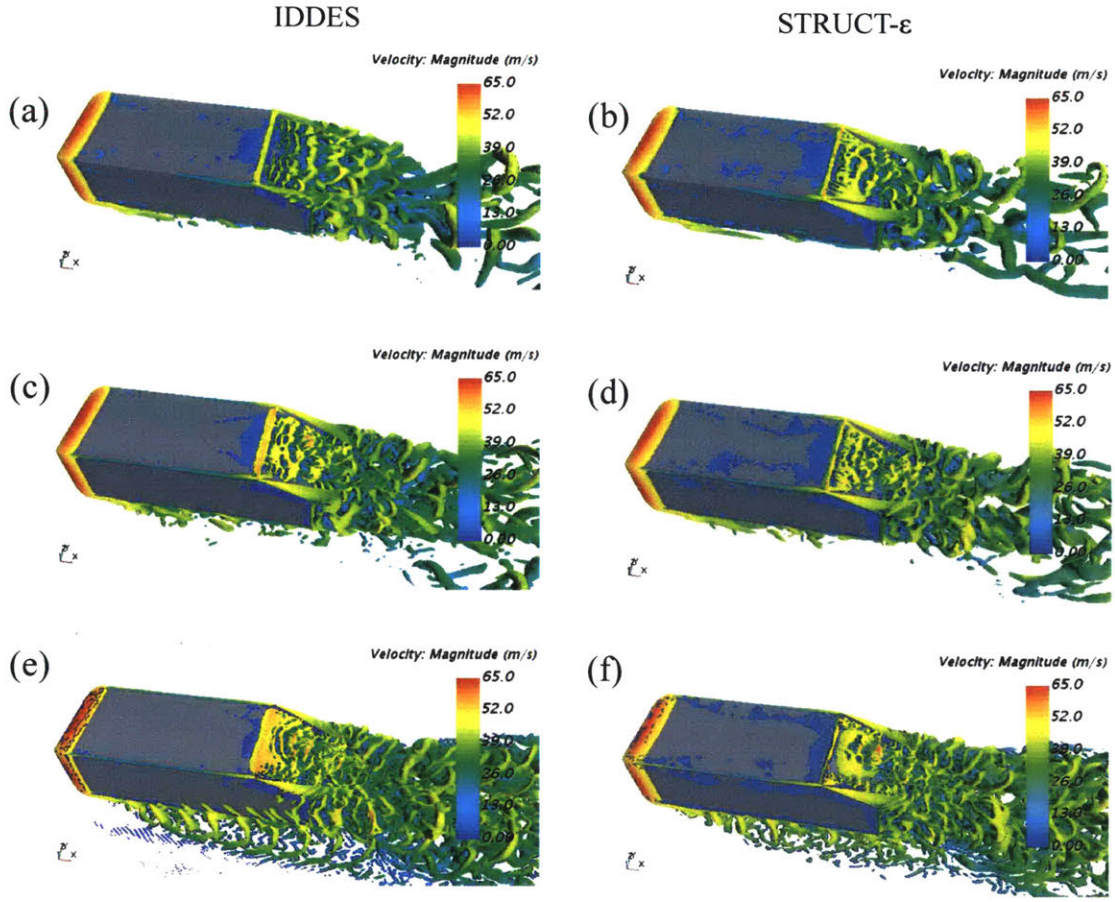

Figure 4-26: Instantaneous iso-surfaces of $Q = 50,000/s_2$ around the Ahmed body obtained with (a) the IDDES model on the coarse mesh (b) the STRUCT-ε model on the coarse mesh (c) the IDDES model on the medium mesh (d) the STRUCT-ε model on the medium mesh, (e) the IDDES model on the fine mesh, (f) the STRUCT-ε model on the fine mesh.

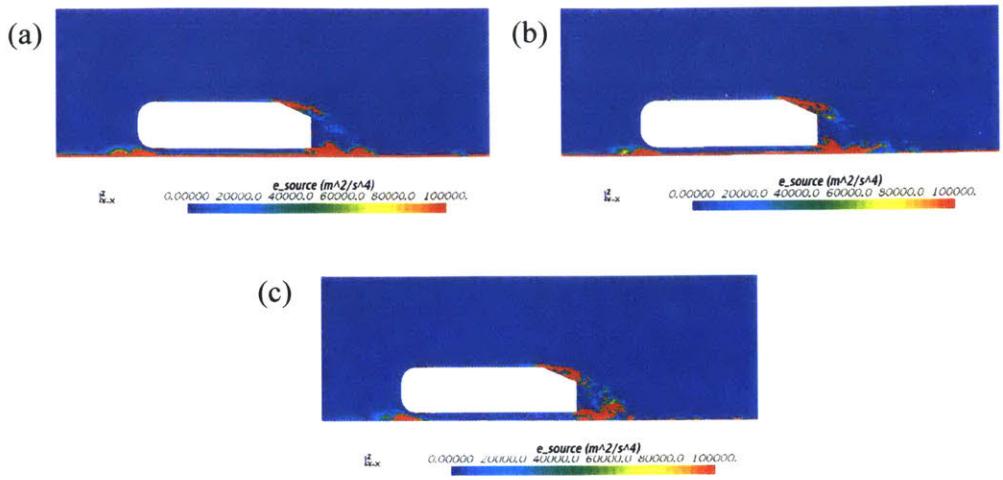

Figure 4-27: Instantaneous STRUCT-ε model activation regions identified by the $C_{\varepsilon 3} k \left|\overline{II}\right|$ source term on (a) the coarse mesh, (b) the medium mesh, (c) the fine mesh.

structures are captured. All combinations of mesh and model show two well-resolved counter-rotating, cone-shaped, vortices coming off the slant side, except for the IDDES model result on the coarse mesh. For the medium and fine meshes, the resolved vortex structures are similar between the IDDES model and the STRUCT-ε model.

The STRUCT-ε model activation is presented in Figure 4-27, and is identified by the additional $C_{\varepsilon 3} k \left|\overline{II}\right|$ source term in the ε equation. As the mesh is refined, the STRUCT-ε model demonstrates very consistent physics-based activation, with similar activation regions for all meshes, mostly on the slant and at the bottom back of the body, as well as some areas of the ground due to the structures developed from the stilts.

Figure 4-28 shows the mean streamwise velocity profiles over the slant of the Ahmed body in the symmetry plane, obtained with the IDDES and STRUCT-ε models for the three different meshes. Consistently with the observation in the streamline and vortex structure results, the mean velocity profiles obtained with the IDDES model on the coarse mesh deviate from the ones obtained with the medium and fine meshes, as the coarse mesh application produces a noticeable massive separation. The STRUCT-ε model reveals very consistent trends of the mean velocity profiles across different mesh refinements, while the finer meshes predict marginally larger separa-

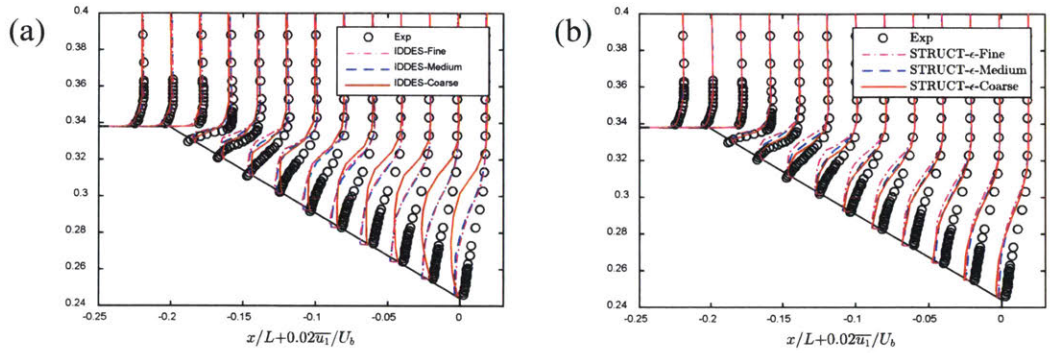

Figure 4-28: Mean streamwise velocity profiles over the slant in the symmetry plane obtained with (a) the IDDES model, b) the STRUCT-ε model.

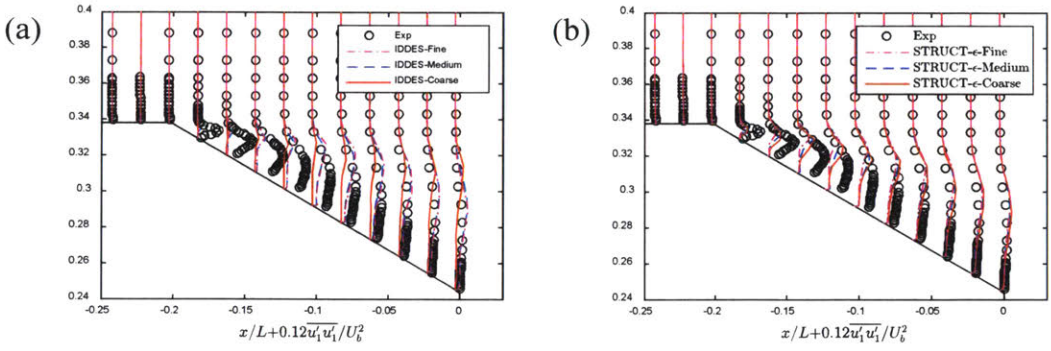

Figure 4-29: Turbulent streamwise stress profiles over the slant of the Ahmed body in the symmetry plane obtained with (a) the IDDES, b) the STRUCT-ε.

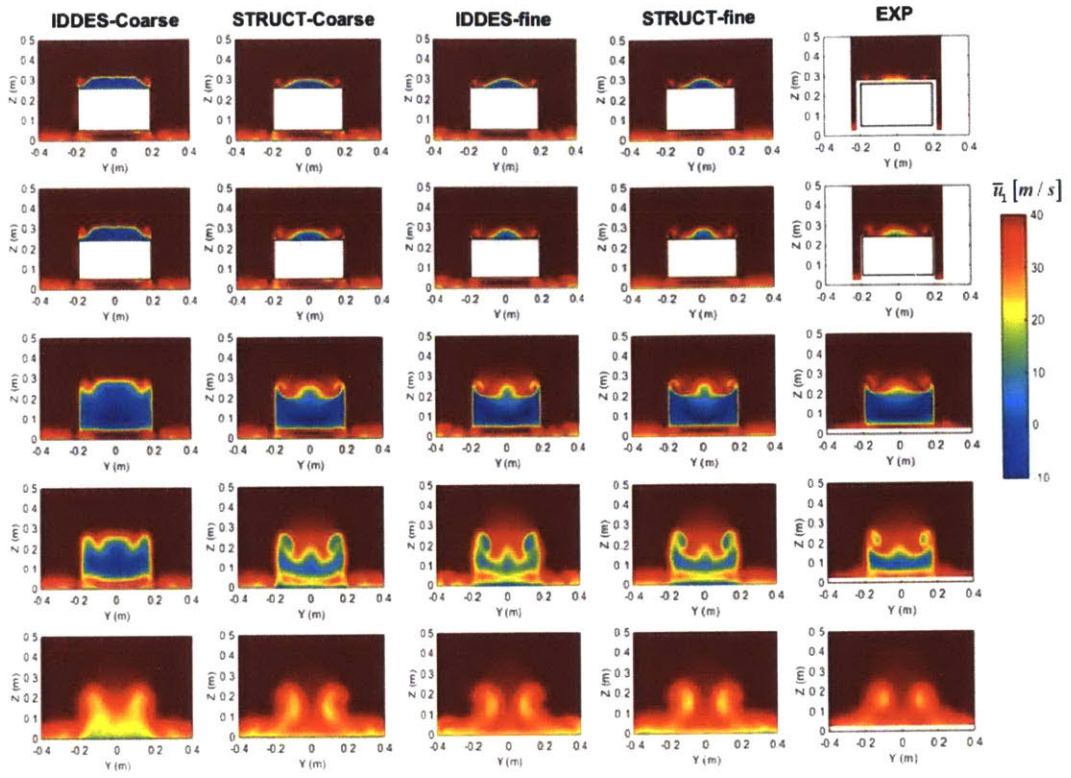

Figure 4-30: Mean streamwise velocity on successive YZ-planes. From top to bottom, the rows correspond to the location $X = -0.038$ m, 0 m, 0.08 m, 0.2 m, 0.5 m, respectively.

tion than the coarse mesh. Note that the IDDES and STRUCT-ε model results on the fine mesh are very similar. Turbulent streamwise stress profiles over the slant in the symmetry plane are presented in Figure 4-29. All cases exhibit similar results, in good agreement with the experimental data for the lower half of the slant, again except for the IDDES model on the coarse mesh. The STRUCT-ε model predicts larger stress on the upper half of the slant in comparison to the IDDES model and in closer agreement with the experimental data.

A comparison of the mean streamwise velocities on successive YZ-planes is presented in Figure 4-30 for the coarse and the fine meshes. The IDDES model on the coarse mesh again results in the worst agreement with the experiment, both over the slant and in the wake. Results for the other cases show close similarity, with some overprediction of the separation in the middle of the slant and good predictions of

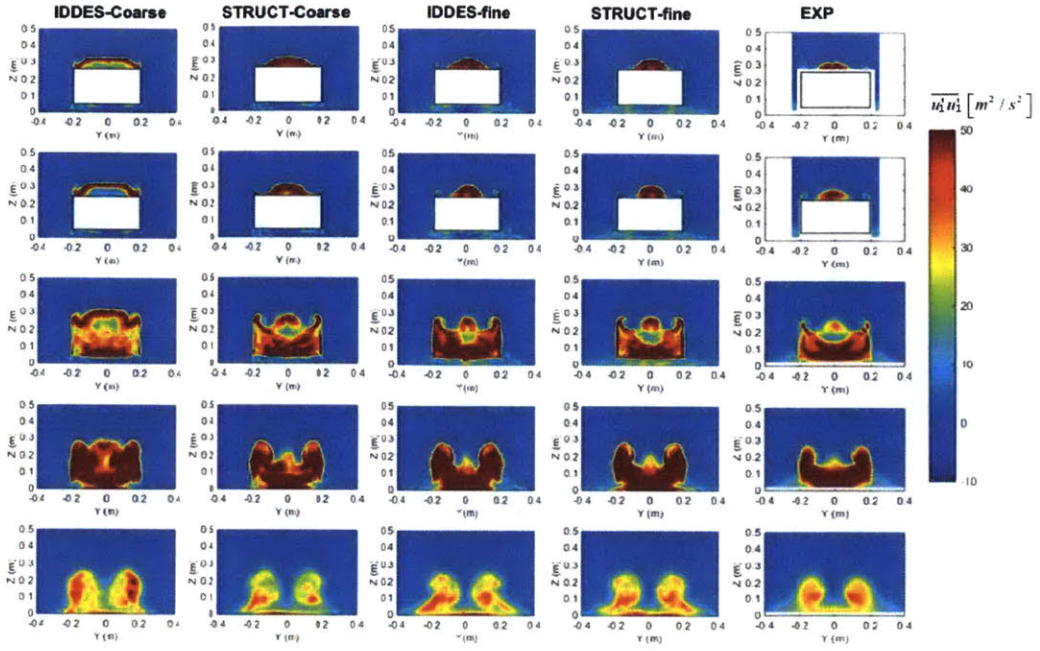

Figure 4-31: Turbulent streamwise stress on successive YZ-planes. From top to bottom, the rows correspond to the location $X = -0.038$ m, 0 m, 0.08 m, 0.2 m, 0.5 m, respectively.

the wake in comparison to the experiment. The separation region obtained from the coarse mesh is somewhat flatter than the one predicted by the fine mesh, explaining the trend seen in the mean streamwise velocity profiles over the slant on the symmetry plane. The comparison of the streamwise stress on successive YZ-planes is presented in Figure 4-31. The IDDES and the STRUCT-ε models with the fine mesh generate results in best agreement with the experiment, but with some overprediction of the turbulent streamwise stress. The STRUCT-ε model on the coarse mesh predicts similar results to the fine mesh case, with marginal differences in the separation region and wake, while the IDDES model with the coarse mesh generates generally inaccurate predictions.

A comparison of the drag coefficient C_d and lift coefficient C_l produced by the STRUCT-ε and IDDES models for different meshes is presented in Table 4.3. However, it is not possible to consistently assess the model performance from the prediction of the force coefficients, due to inconsistencies in the experimental data. Figure

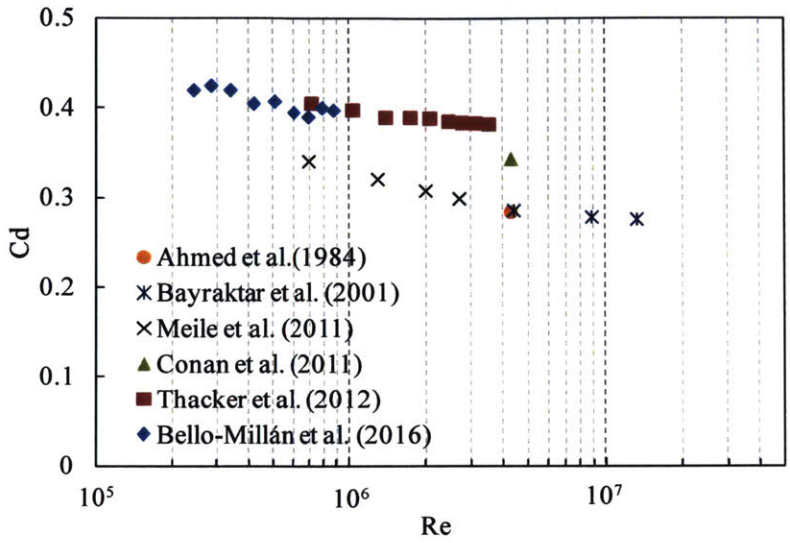

Figure 4-32: Comparison of C_d as a function of Reynolds number between various studies.

Table 4.3: Drag and lift coefficients obtained with the STRUCT-ε and IDDES models.

	C_d_IDDES	C_d_STRUCT-ε	C_l_IDDES	C_l_STRUCT-ε
Fine mesh	0.410	0.401	0.422	0.413
Medium mesh	0.394	0.396	0.409	0.408
Coarse mesh	0.372	0.413	0.199	0.431

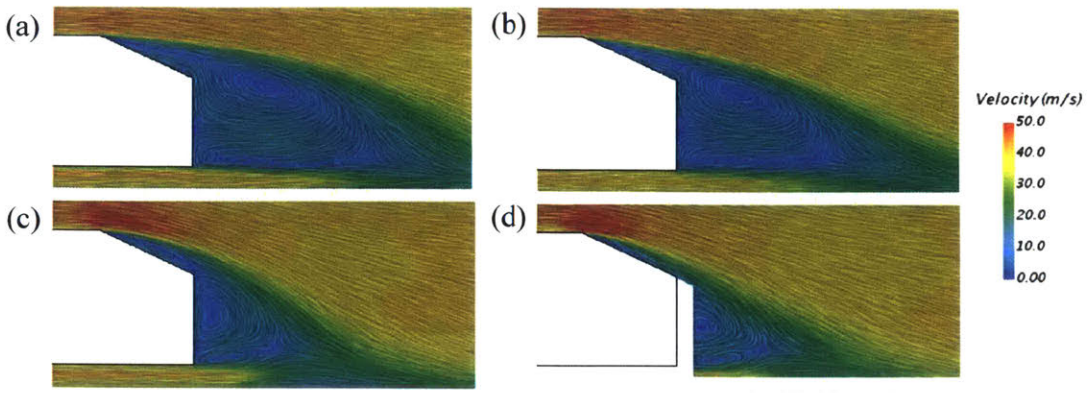

Figure 4-33: Comparison of streamlines in the symmetry plane y=0 obtained with (a) the $k-\omega$ SST model, (b) the RKE model , (c) the STRUCT-ε model, on the coarse resolution mesh, and (d) the experiment.

4-32 compares C_d as a function of Reynolds number between various experiments, and it shows clearly a large variation between different experiments, which is partly due to the high sensitivity of the separation produced by the sharpness of the roof/rear window edge connection, also noted by Thacker et al. [126]. It is encouraging that the predictions of force coefficients at Reynolds number 2,780,000 in this study are closest to the experiment values by Thacker et al. [126] with C_d of 0.384 and C_l of 0.422, as expected from the discussion in Bello-Milln et al. [127]. The discrepancy can be attributed to the small overprediction of separation over the slant, in addition to the experimental uncertainty.

Comparison of STRUCT-ε and URANS predictions

URANS simulations are performed using both the k-ω SST model and the RKE model. A comparison of the streamlines obtained with the URANS and STRUCT-ε models on the coarse mesh is presented in Figure 4-33. Both URANS models generate a very large separation over the slant and in the body wake, in comparison to the experiment. As already discussed, the STRUCT-ε model provides largely improved predictions of the separation region with a small separation bubble on the slant.

Figure 4-34 presents the vortex structures around the Ahmed body using iso-surfaces of the Q criterion. All models somewhat capture the two counter-rotating

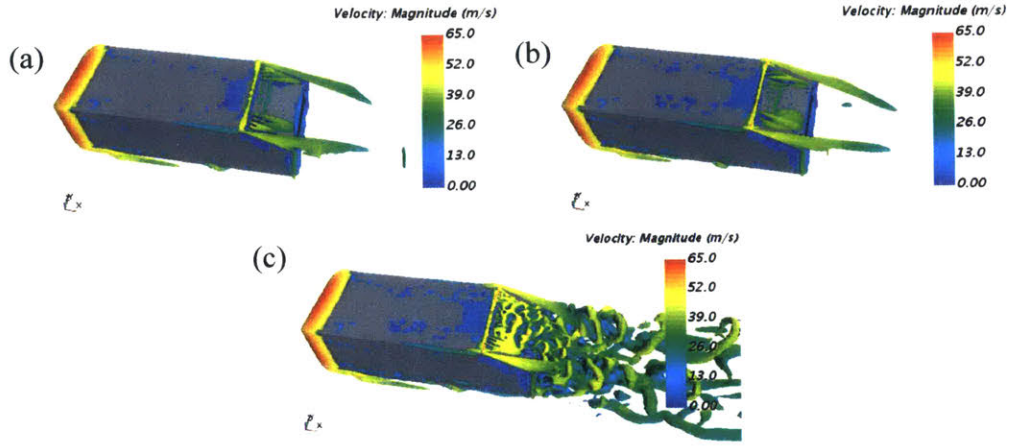

Figure 4-34: Iso-surfaces of $Q = 50,000/s_2$ around the Ahmed body obtained with (a) the k- ω SST model, (b) the RKE model , (c) the STRUCT-ε model, on the coarse resolution mesh.

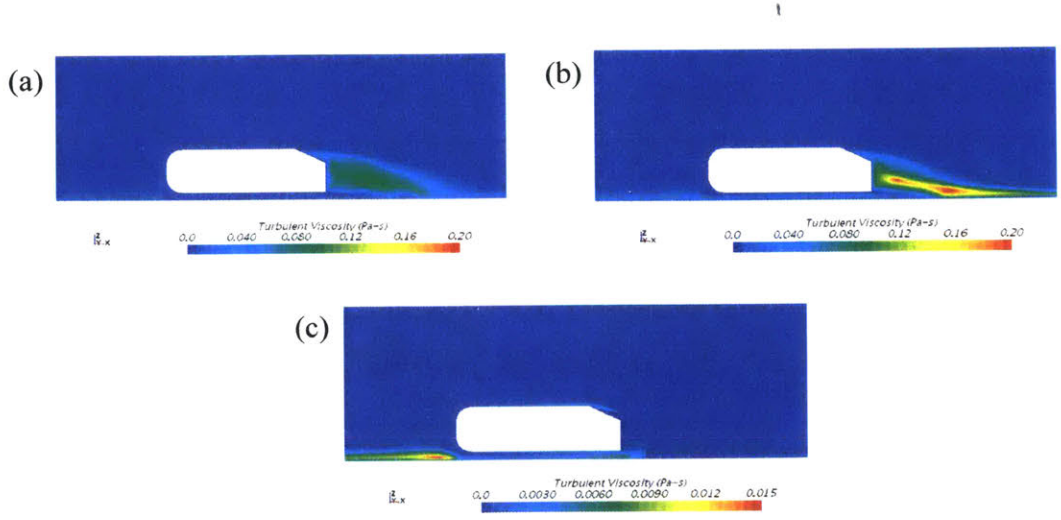

Figure 4-35: Turbulent viscosity around the Ahmed body generated by (a) the k-ω SST model, (b) the RKE model , (c) the STRUCT-ε model, on the coarse resolution mesh.

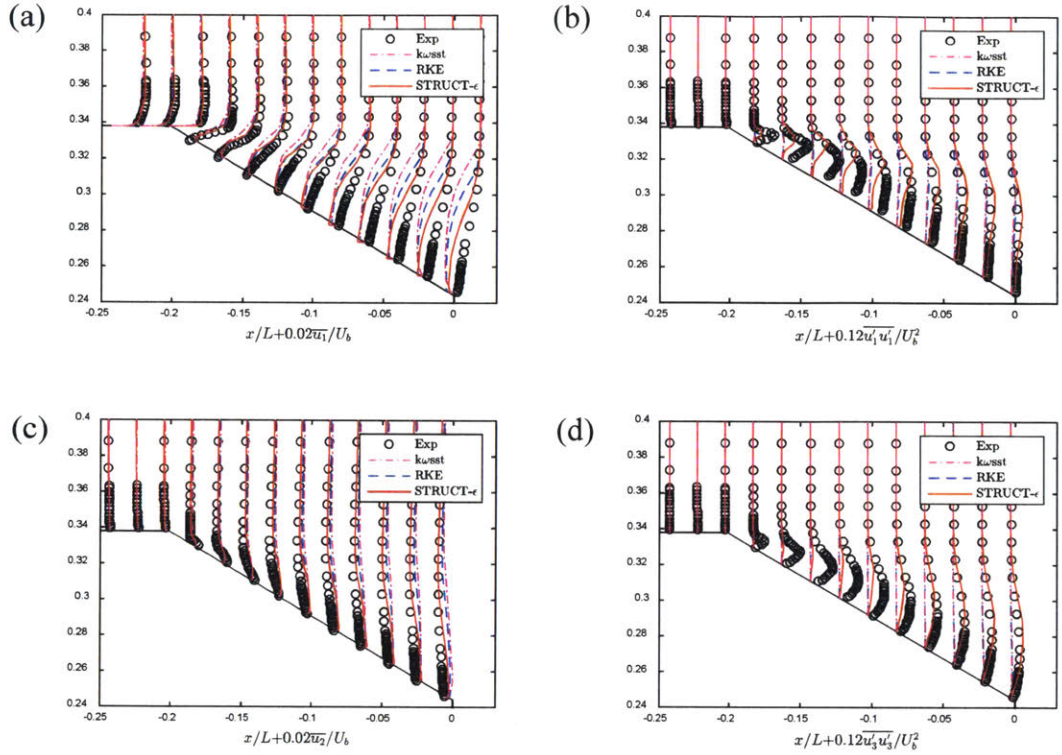

Figure 4-36: Mean velocity and turbulent stress profiles over the slant in the symmetry plane obtained on the coarse mesh: (a) streamwise velocity, (b) tubulent streamwise stress, (c) longitudinal velocity, (d) turbulent longitudinal stress.

cone-shaped vortices coming off the slant side. However, the two URANS models resolve practically no vortical structures in the body wake, while the STRUCT-ε model resolves much more vortex structures both on the slant and in the body wake. A comparison of the resulting turbulent viscosity is shown in Figure 4-35. While high value of the turbulent viscosity is generated on the slant and in the wake of the Ahmed body by the k-ω SST and the RKE models, the STRUCT-ε model shows much lower value in these regions, and as a consequence, introducing the increased flow resolution and better agreement with the experiment in the flow fields.

Figure 4-36 (a) and (b) present the mean streamwise velocity and turbulent streamwise stress profiles over the slant, obtained with the URANS and STRUCT-ε models on the coarse mesh resolution. The improvement from the STRUCT-ε model is obvious: the mean streamwise velocity is closer to the experimental value with a smaller separation on the slant when compared to the URANS results; further, the

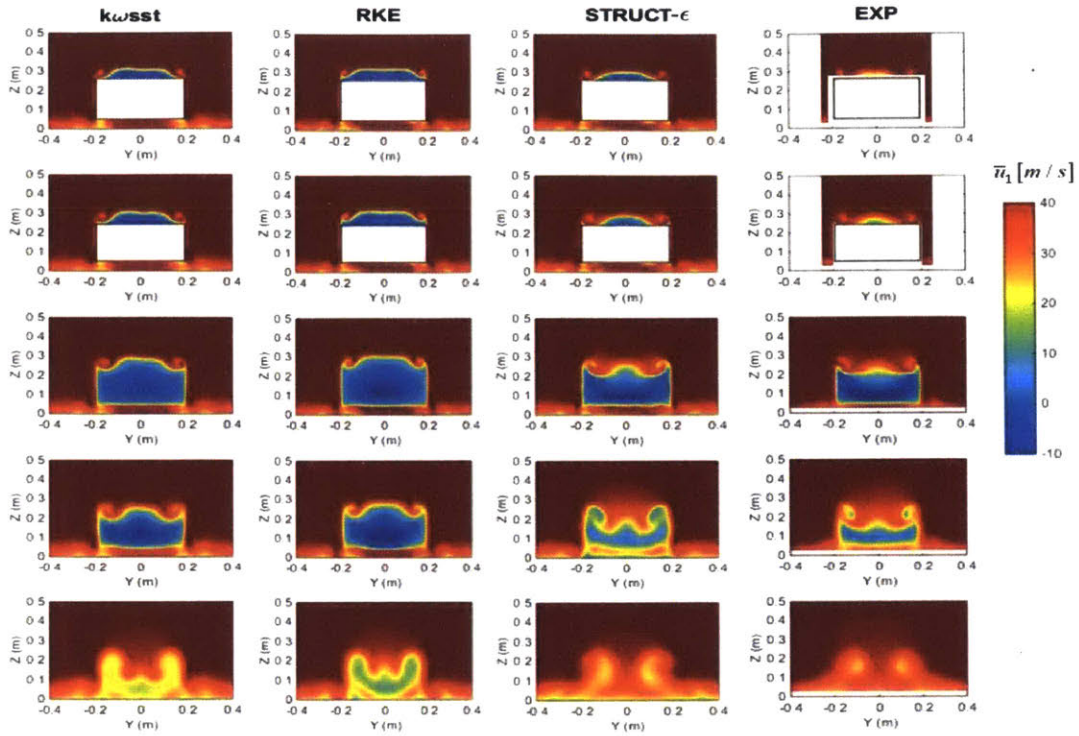

Figure 4-37: Mean streamwise velocities in successive YZ-planes obtained on the coarse mesh resolution. From top to bottom, the rows correspond to the location $X = -0.038$ m, 0 m, 0.08 m, 0.2 m, 0.5 m, respectively.

velocity stress also shows better agreement with the experiment, where the stress values are heavily underpredicted by the URANS models. Figure 4-36 (c) and (d) present the results of the mean longitudinal velocity and turbulent longitudinal stress profiles. Again, the STRUCT-ε model provides the best agreement with the experiment, though there still exists some discrepancies in the stress values on the upper half of the slant.

The comparison of the mean streamwise velocity and turbulent streamwise stress on successive YZ-planes, obtained for different turbulence models in comparison with the experiment, are shown in Figure 4-37 and 4-38. Results of the k-ω SST and the RKE models are very similar, with comparable shapes of the separation regions in the successive planes. The STRUCT-ε model shows the best agreement with the experiment, generally capturing the shapes of the mean velocity and stress. The predicted separation region is smaller, with higher stress than the URANS results

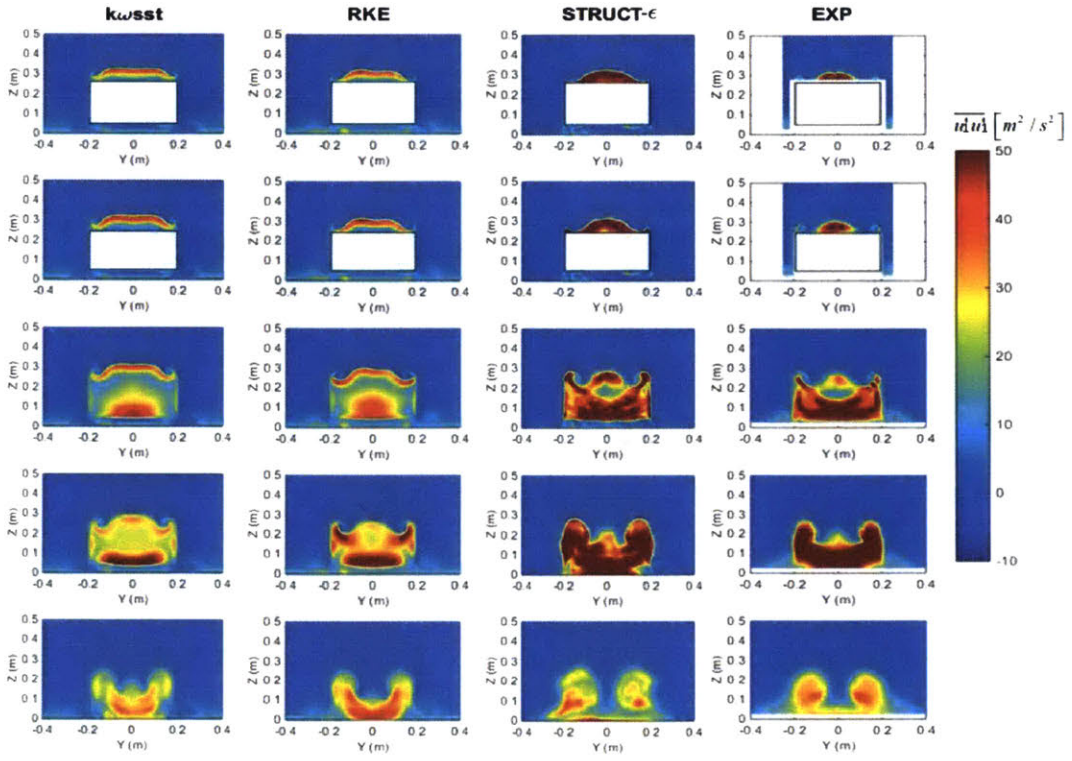

Figure 4-38: Streamwise velocity stress in successive YZ-planes obtained with the coarse mesh resolution. From top to bottom, the rows correspond to the location $X = -0.038$ m, 0 m, 0.08 m, 0.2 m, 0.5 m, respectively.

Table 4.4: Drag and lift coefficients obtained with different turbulence models on the coarse mesh for the Ahmed body.

	EXP (Thacker)	k-ω SST	RKE	STRUCT-ε
C_d	0.384	0.324	0.342	0.413
C_l	0.422	0.173	0.276	0.431

Table 4.5: Comparison of the total computational time for the Ahmed body.

	k-ω SST_ Coarse	RKE_ Coarse	STRUCT-ε_Coarse	IDDES_ Medium
Total computational time (hr)	39	42	41	122

both on the slant and in the body wake.

Table 4.4 summarizes the force coefficients obtained for the URANS and STRUCT-ε models. The improved accuracy of the STRUCT-ε model is further confirmed by the largely different predictions of the lift coefficient. Table 4.5 compares the total computational time cost on the three unsteady simulations with the coarse mesh and the IDDES simulation with the medium mesh, on five 12-core workstations. The runtime for the STRUCT-ε model is on the same level as the URANS models with less than 3% difference, while the runtime for the IDDES model with the medium mesh is nearly three times higher, which confirms the computational efficiency of the STRUCT-ε model.

and much less than the IDDES model with the medium mesh, confirming its computational efficiency.

4.3.2 Flow past the DrivAer model

After validation of the STRUCT-ε model on the simplified vehicle model of the Ahmed body, the generic DrivAer car model is considered for further validation purposes. The DrivAer model was introduced by Heft et al. (2012) [14] to overcome the absence of realistic generic car models open to the public. The geometry of the DrivAer model is based on the geometries of the Audi A4 and the BMW 3 series and has three

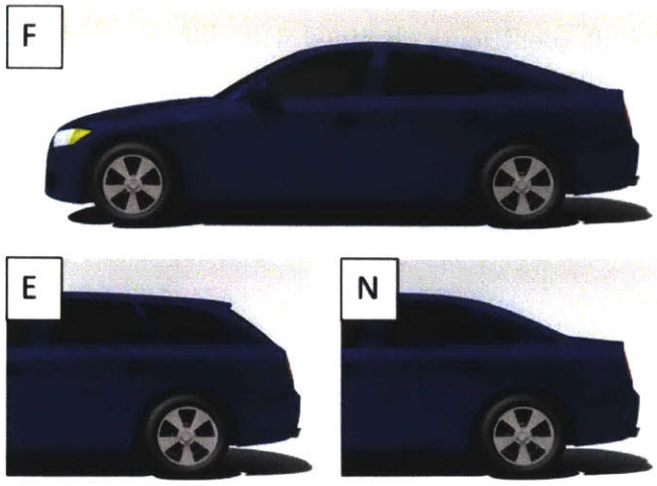

Figure 4-39: Different configurations of the DrivAer model: F-Fastback, E-Estate back, N- Notchback (From [13])

alternative rear end configurations: fastback, notchback, and estate back (Figure 4-39). In the experiment by Heft et al. [14], for each rear end configuration, several variants were investigated: smooth and detailed underbody, with and without mirrors, with and without wheels, and with and without moving ground. This study focuses on the fastback and estate back geometries with the detailed underbody, mirrors, rotating wheels, and moving ground, aiming at incorporating the full complexity of the model.

The introduction of the DrivAer model has given rise to several studies both experimentally and numerically. Strangfeld et al. (2013) [139] performed an experimental study at the wind tunnel of TU-Berlin on the DrivAer fastback configuration with smooth underbody, mirrors, wheels, and without moving ground, with focus on detailed analysis of the unsteady flow phenomena in the models near wake. The experiment showed that the drag coefficient becomes independent of the Reynolds number for $Re > 2.25 \times 10^6$, much less than the value of 4.87×10^6 reported by Heft et al. [14]. Wieser et al. (2014) [140] conducted experiments also at the wind tunnel of TU-Berlin using the same fastback configuration as Strangfeld et al. [139]; the notchback configuration was also considered for comparison under different crosswind conditions. Some deviation from the experiment by Heft et al. [14] in the drag was

observed and may be explained by the difference in their test facilities. Avadiar et al. (2018) [141] performed an experiment on the full-scale DrivAer estate model with smooth underbody, mirrors, wheels, and fixed ground in the Monash Large Wind Tunnel and the measured drag coefficient showed good agreement with the experiment by Heft et al [14] at a larger Reynolds number of 8×10^6. Numerically, Heft et al. (2012) [15] conducted steady RANS simulations of the DrivAer fastback model using the k-ω SST model. Good agreement with the experiment was obtained for the drag, but discrepancies were observed in the pressure distribution. Guilmineau (2014) [13] simulated the DrivAer fastback model with the fixed ground and non-rotating wheels using Explicit Algebraic Reynolds Stress Model (EARSM) and DES. It turned out that the drag coefficient is well predicted by both EARSM and DES, while DES has outperformed EARSM in predicting the lift coefficient. Peters et al. (2015) [142] simulated the DrivAer fastback model using a structured finite difference code with overset mesh and has proven it as an alternative to finite volume codes for automotive CFD. Yazdani (2015) [143] compared the three rear end configurations of the DrivAer model with both detailed and smooth underbody and without ground simulation using the RKE model and the DDES model. The results showed that the DDES model has a better capability of predicting drag force trends. Ashton et al. (2016) [144] compared a variety of RANS models and DES for simulating fastback and estate configurations of DrivAer with smooth underbody and without ground simulation. The results showed the advantage of DES over all RANS models in predicting force coefficients and the general flow field, but DES still exhibited inaccuracies even at the finest mesh level. Jakirlic et al. (2016) [145] investigated the effects of the underbody geometry and wheel rotation on the aerodynamic performance of DrivAer notchback model using Very Large Eddy Simulation (VLES), and a good agreement with the experiment by Heft et al. [14] was obtained. Aljure et al. (2018) [146] compared LES and wall modeled LES (WMLES) on simulating the DrivAer fastback model with the smooth underbody, mirrors, simplified wheels, and moving ground consideration; WMLES was shown to predict high-quality unsteady flow features at a lower computational cost than LES. Ruttgers et al. (2019) [147] performed LES on

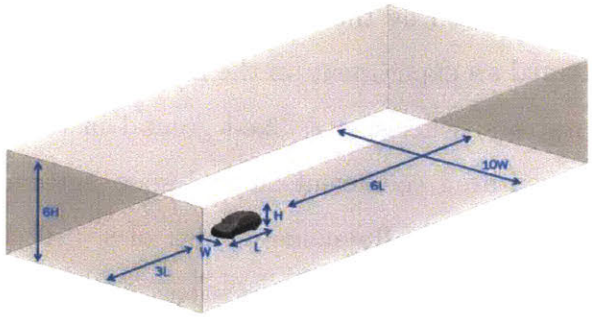

Figure 4-40: Computational domain for the DrivAer case

the DrivAer fastback model with the smooth underbody, mirrors, wheels, and moving ground. A detailed analysis of the flow field was performed with an emphasis on flow separation and vortical structures.

As most of the research was performed on the fastback configuration of the DrivAer model, the estate configuration has not been widely studied. The research of Yazdani [143] and Ashton et al. [144] involved simulation of the estate configuration and showed that it is more challenging to simulate than the fastback configuration. Both the predicted drag coefficient and the flow field differ a lot when using different turbulence models, while for the fastback configuration it is easy to reach a reasonable accuracy on the drag prediction using even the simplest RANS model. Therefore, both the fastback and estate configurations are considered in the present study for validating the new STRUCT-ε model on the realistic automotive DrivAer model, in terms of accuracy and computational cost. Results of the RKE model are also presented for comparison purposes.

The fastback and estate configurations of the DrivAer model are studied with the detailed underbody, mirrors, wheels, and moving ground consideration. The computational domain is shown in Figure 4-40 with dimensions $10L \times 10W \times 6H$, where $L = 4.6126$ m, $W = 1.7529$ m, and $H = 1.4182$ m represent the full-scale length, width, and height of the DrivAer model. The blockage ratio is 1.2%, whereas it is 8% in the experiment by Heft et al. [14]. The imposed inlet boundary condition is a uniform velocity of 40 m/s, corresponding to the driving speed of around 140 km/h. The Reynolds number is therefore 1.22×10^7 with respect to the vehicle length. The

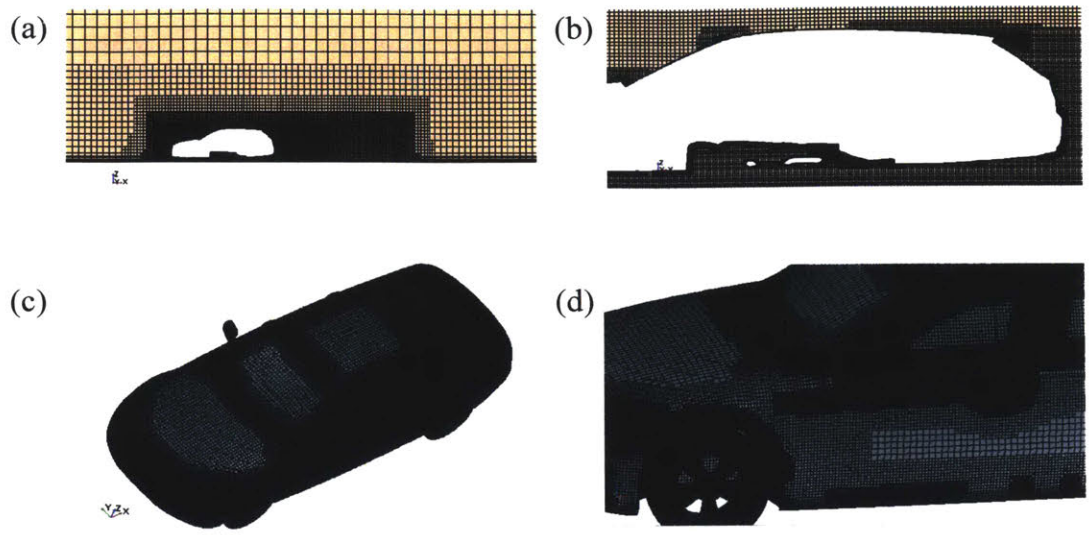

Figure 4-41: Views of the coarse mesh with the estate DrivAer model: (a) mesh in the $x - z$ middle plane, (b) mesh refinement around the vehicle in the $x - z$ middle plane, (c) estate DrivAer surface mesh. (d) zoomed in surface mesh.

simulation focuses on the real-life conditions, while the experiment was performed on a 1:2.5 model at a reduced Reynolds number of 4.87×10^6 with verification that the drag coefficient reached a constant level when $Re > 4.87 \times 10^6$. A pressure condition is imposed at the outlet. A no-slip wall boundary condition is prescribed on the DrivAer vehicle surface, as well as the top and sides of the domain. The moving ground is considered with a no-slip moving wall condition with a uniform velocity of 40 m/s. The rotating wheels are considered by setting rotational reference frames at wheel coordinate systems.

A set of three meshes for each DrivAer configuration is adopted to study mesh dependency. For mesh refinement, all controlling parameters are decreased consistently with a ratio of 1.5; the near-wall prism layer number and thickness are kept the same for the set of meshes so that the average value of wall $y+$ is kept smaller than 1. Views of the coarse mesh with the estate DrivAer model are shown in Figure 4-41. Different levels of refinement blocks are defined around the vehicle, and further refinements are added to capture the geometry details. For the estate configuration, the meshes contain 79.1, 38.6, and 19.1 million cells; for the fastback configuration, the meshes contain 80.4, 39.0, and 19.1 million cells.

Table 4.6: Comparison of the mean drag coefficient for the fastback DrivAer configuration obtained using the STRUCT-ϵ model and the RKE model with different mesh solutions.

	Fastback	Percentage Difference	Cell Number
Exp.	0.275		
STRUCT-ϵ_fine	0.276	0.4%	80.4 M
STRUCT-ϵ_medium	0.279	1.5%	39.0 M
STRUCT-ϵ_coarse	0.283	2.9%	19.1 M
RKE_fine	0.273	0.7%	80.4 M
RKE_medium	0.275	0.0%	39.0 M
RKE_coarse	0.278	1.1%	19.1 M

Table 4.7: Comparison of the mean drag coefficient for the estate DrivAer configuration obtained using the STRUCT-ϵ mesh and the RKE model with different mesh resolutions.

	Estate	Percentage Difference	Cell Number
Exp.	0.319		
STRUCT-ϵ_fine	0.320	0.3%	79.1 M
STRUCT-ϵ_medium	0.322	0.9%	38.6 M
STRUCT-ϵ_coarse	0.324	1.6%	19.1 M
RKE_fine	0.289	9.4%	79.1 M
RKE_medium	0.294	7.8%	38.6 M
RKE_coarse	0.295	7.5%	19.1 M

For post-processing, the drag coefficient C_d is investigated and defined as:

$$C_d = \frac{F_d}{\frac{1}{2}\rho U^2 A_{ref}} \tag{4.10}$$

where F_d is the total drag force, ρ the air density, U the inlet velocity, and A_{ref} stands for the largest cross-sectional area of the vehicle. The lift coefficient is not discussed as no data was provided in the experiments for the cases involved.

Table 4.6 shows the comparison of the mean drag coefficient for the fastback configuration obtained with the new STRUCT-ε model and the RKE model on the fine, medium, and coarse mesh resolutions. Both models exhibit good mesh consistency and the drag values agree well with the experiment. Previous numerical studies have

Table 4.8: Difference in the drag coefficient moving from the fastback to the estate configuration for different turbulence models and different mesh resolutions.

	Difference in C_d from Fastback to Estate	Percentage Difference
Exp.	0.044	
STRUCT-ϵ_fine	0.044	0%
STRUCT-ϵ_medium	0.043	2%
STRUCT-ϵ_coarse	0.041	7%
RKE_fine	0.016	64%
RKE_medium	0.019	57%
RKE_coarse	0.017	61%

also shown a good agreement with the experiment for the fastback configuration though most of them only consider smooth underbody and without ground simulation. Heft et al. [15] simulated the same case using the k-ω SST model and obtained a drag coefficient of 0.278, also close to the experiment value of 0.275. Table 4.7 shows the drag coefficient comparison on the more challenging estate configuration. The RKE model underpredicts the drag by 7-10% for the three meshes, while the STRUCT-ε model exhibits not able improvement with less than 2% difference with the experiment even for the coarse mesh. The magnitude and direction of the trend are typically more important than the absolute drag value for industrial automotive flows, therefore the differences in the drag coefficient between the fastback and estate configurations are compared in Table 4.8. While both the STRUCT-ε and the RKE models capture the trend of an increase in the drag moving from the fastback to the estate configuration, only the STRUCT-ε model behaves well on capturing the magnitude, with less than 10% error for all meshes, as well as an error decreasing trend as the mesh resolution increases; around 60% error is shown for the RKE model.

Pressure drag is the dominant component of the total drag for both configurations of the DrivAer model. In all the simulations, the skin friction drag composes less than 10% of the total drag and has less variation between the STRUCT-ε model and the RKE model than the pressure drag. Therefore, a detailed pressure drag distribution analysis is conducted for model comparison.

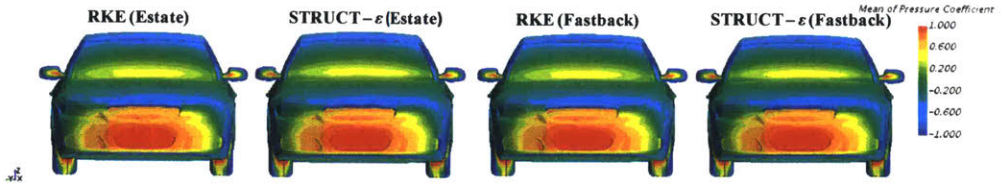

Figure 4-42: Front view of the mean pressure coefficient distribution over the vehicle surface on the medium mesh.

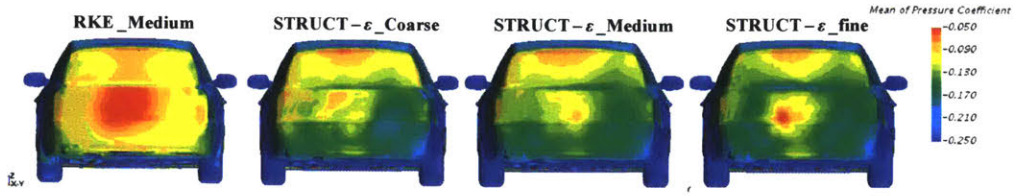

Figure 4-43: Rear view of the mean pressure coefficient distribution over the vehicle surface for the estate configuration.

The pressure coefficient (C_p) is computed as follows:

$$C_p = \frac{p - p_{ref}}{\frac{1}{2}\rho U^2} \tag{4.11}$$

where p_{ref} is the freestream pressure, ρ the air density, and U the inlet velocity,

Figure 4-42 compares the front view of the mean pressure coefficient distribution over the vehicle surface for both the estate and fastback configurations and the two turbulence models on the medium mesh resolution. No obvious difference can be observed between the solutions: in all the cases, very high pressure is found at the stagnation region in the very front of the vehicle with gradual reduction moving towards the back of the vehicle. The main difference in the pressure coefficient predictions

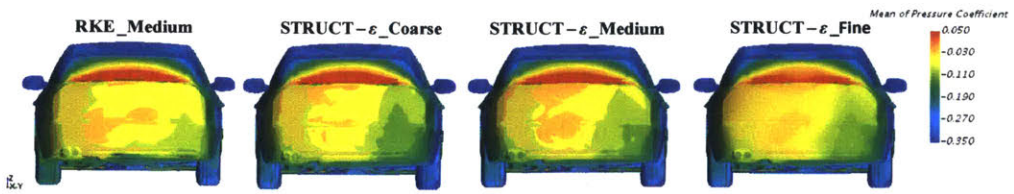

Figure 4-44: Rear view of the mean pressure coefficient distribution over the vehicle surface for the fastback configuration.

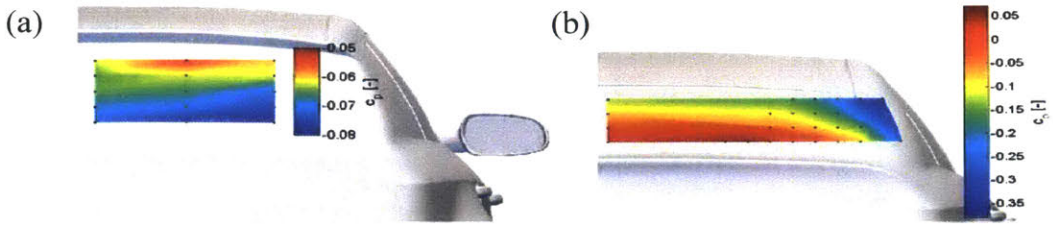

Figure 4-45: Distribution of the pressure coefficient at the rear window: (a) estate (b) fastback (from experiment [14])

can be observed in the rear view as shown in Figures 4-43 and 4-44 for the estate and fastback configurations, respectively. For the estate configuration, the RKE model generates overall higher C_p on the rear vehicle surface than the STRUCT-ε model, resulting in the lower drag predicted. Solutions of the STRUCT-ε model on the three different mesh resolutions exhibit a similar pattern in the pressure distribution with only small differences. The trend of the pressure coefficient distribution is similar to the experimental values given in Figure 4-45, but the values are inconsistent, indicating the possible existence of some error cancellation in the drag prediction for the STRUCT-ε model. It is also interesting to note that the results are very similar with the study of Ashton et al. (2016) [144]: the pressure distribution on the rear window obtained by our STRUCT-ε model agrees well with the IDDES result by Ashton et al. For the fastback configuration, the pressure distribution over the rear vehicle surface predicted using different turbulence models on the three mesh resolutions is in general consistent, contributing to similar drag prediction. Comparison with the experiment (Figure 4-45(b)) also shows good agreement. The discrepancy shown for the estate configuration and the consistency shown for the fastback configuration proves the challenge for a turbulence model to capture different flow phenomena. The STRUCT-ε model shows improved adaption to different flows with better predictive capability for separation and vortices.

Figure 4-46 shows the comparison of the mean pressure coefficient on the x-z symmetry plane at the top of the car surface for the estate and fastback configurations. The pressure distribution is in general similar for all the simulation cases except slight differences at the cowl top and the edge of the rear window for both the estate and

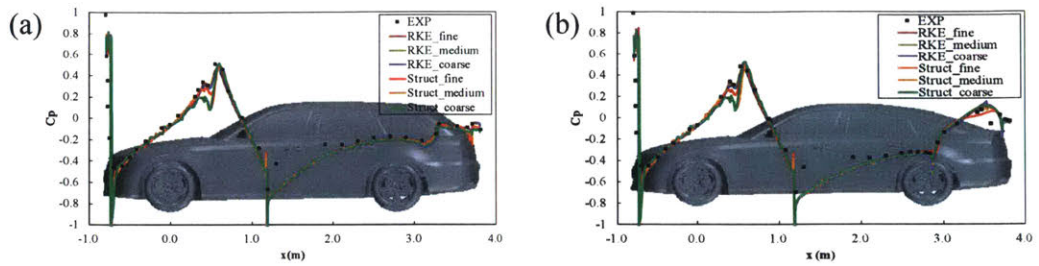

Figure 4-46: Mean pressure coefficient over the top of the estate and fastback configuration on the x-z symmetry plane for different and turbulence models and mesh resolutions: (a) estate configuration, (b) fastback configuration.

Figure 4-47: Experimental setup in the wind tunnel (from [15])

fastback configurations. At the cowl top, the RKE model shows more consistent pressure distribution, while the STRUCT-ε model solution converges to the experimental value as the mesh resolution increases. A similar trend was also found in the study of Ashton et al. [144]: the IDDES model showed pressure convergence with mesh refinement at the cowl top. All the simulations underpredict the pressure coefficient over the roof of the vehicle, which is likely caused by the lack of a strut used for holding the DrivAer model in the wind tunnel experiment (Figure 4-47). It is noted however that this discrepancy does not contribute to the drag as the roof surface is parallel to the inlet flow.

Figure 4-48 compares the mean velocity streamlines on the x-z symmetry plane for the fastback and estate configurations obtained by the RKE model and the STRUCT-ε model on the medium mesh resolution. For the fastback configuration, the RKE model and the STRUCT-ε model generate a similar pattern in the wake with two

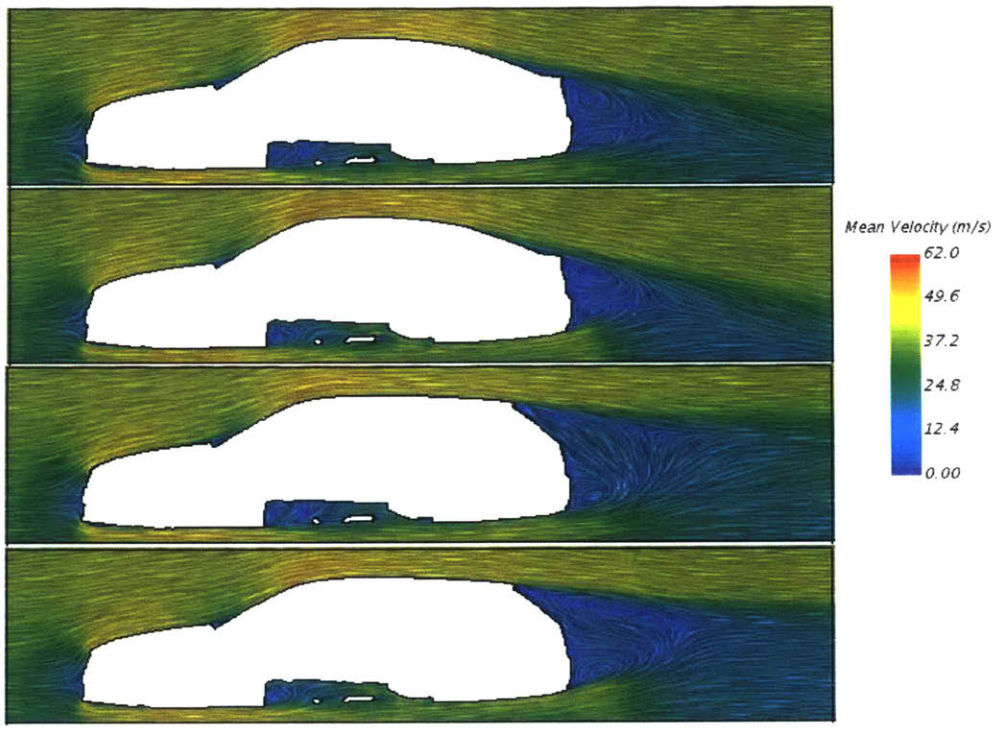

Figure 4-48: Mean velocity streamlines on the x-z symmetry plane for (a) the fastback configuration obtained using the STRUCT-ε model on the medium mesh, (b) the fastback configuration obtained using the RKE model on the medium mesh, (c) the estate configuration obtained using the STRUCT-ε model on the medium mesh, (d) the estate configuration obtained using the RKE model on the medium mesh.

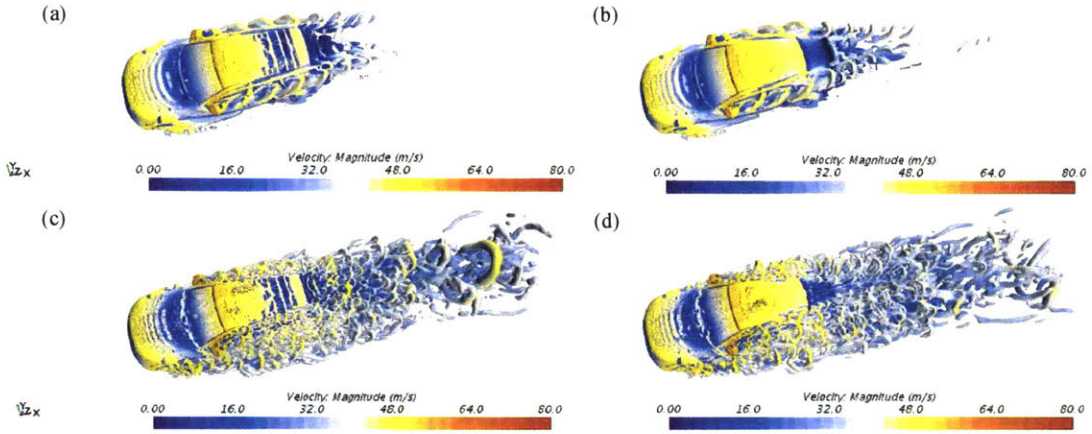

Figure 4-49: Top view of the iso-surfaces of the instantaneous Q criterion ($Q = 1000/s^2$) for (a) the estate configuration obtained using the RKE model on the medium mesh, (b) the fastback configuration obtained using the RKE model on the medium mesh, (c) the estate configuration obtained using the STRUCT-ε model on the medium mesh, (d) the fastback configuration obtained using the STRUCT-ε model on the medium mesh.

counter-rotating vortices, which is consistent with the same level of pressure obtained in the rear. For the estate configuration, there exists an obvious difference in the wake pattern for the two turbulence models especially in the top part of the wake, explaining the large discrepancy found in the drag and pressure predictions. Besides the difference in the wake pattern, flow differences around the vehicle underbody are also observed between the RKE model and the STRUCT-ε model.

Figures 4-49 and 4-50 illustrate the top and bottom view of instantaneous vortex structures around the vehicle with the iso-surfaces of the Q criterion for the estate and fastback configurations on the medium mesh resolution. The STRUCT-ε model shows a strongly increased flow resolution in comparison to the RKE model. Additional vortex structures can be seen at the cowl top, the upper edge of the rear window, the side mirrors, the wheels, the rear end, and in the regions of A-, B-, and C-pillars. These are the regions where large flow separation occurs, and where the STRUCT-ε model has an advantage over the RANS models. Figure 4-51 shows the activation regions of the STRUCT-ε model for the estate and fastback configurations on different mesh resolutions. It can be seen that the STRUCT-ε model activates only in a small

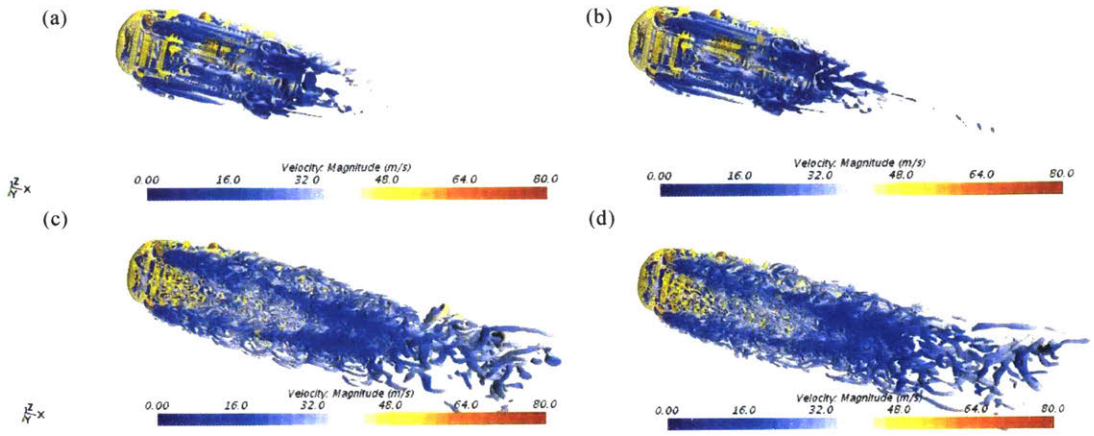

Figure 4-50: Bottom view of the iso-surfaces of the instantaneous Q criterion ($Q = 1000/s^2$) for (a) the estate configuration obtained using the RKE model on the medium mesh, (b) the fastback configuration obtained using the RKE model on the medium mesh, (c) the estate configuration obtained using the STRUCT-ε model on the medium mesh, (d) the fastback configuration obtained using the STRUCT-ε model on the medium mesh.

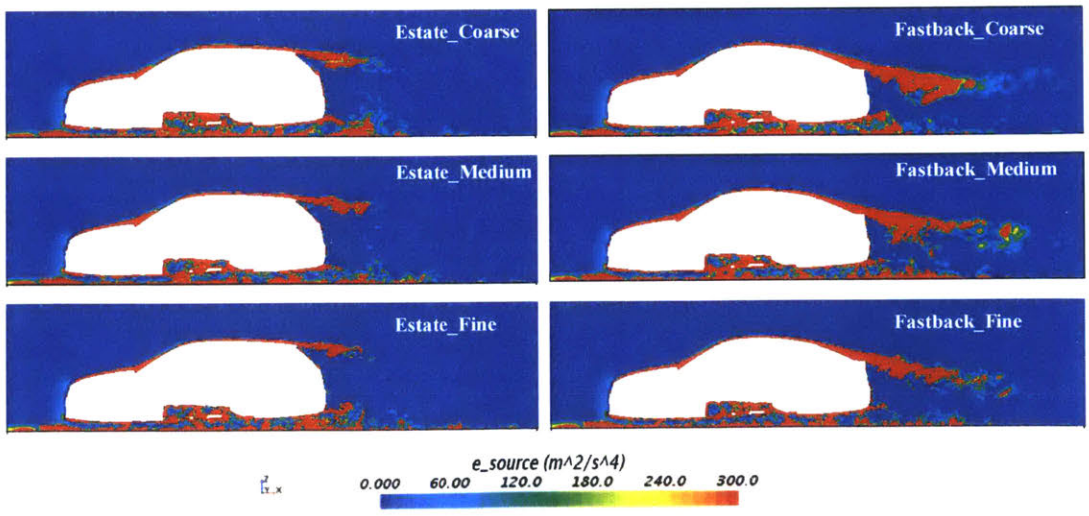

Figure 4-51: Instantaneous STRUCT-ε model activation for the estate and fastback configurations on different mesh resolutions (distribution of the source term $C_{\varepsilon 3} k \left|\overline{II}\right|$ on the x-z symmetry plane)

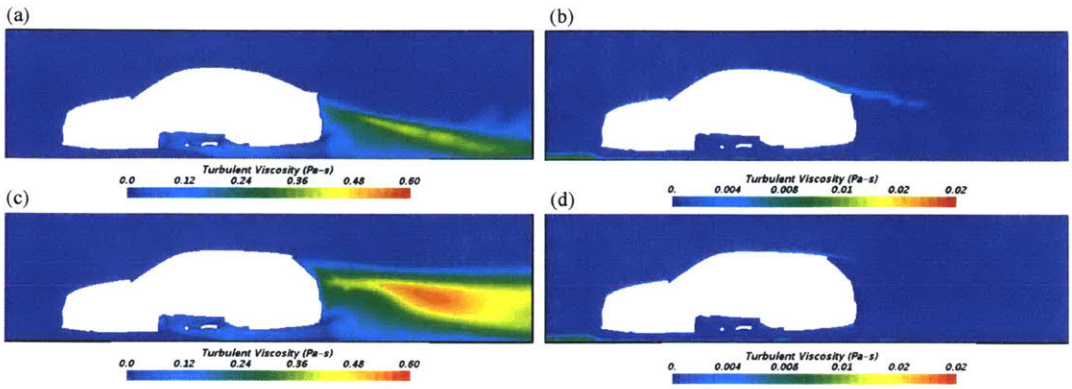

Figure 4-52: Turbulent viscosity for (a) the fastback configuration obtained with the RKE model on the coarse mesh, (b) the fastback configuration obtained with the STRUCT-ε model on the coarse mesh, (c) the estate configuration obtained with the RKE model on the coarse mesh, (d) the estate configuration obtained with the STRUCT-ε model on the coarse mesh.

Table 4.9: Computational expense of the unsteady simulations.

Case	Cell Number	Cores	Compute time
Fastback_RKE_Coarse	19.1 M	60	45 h
Fastback_RKE_Medium	39.0 M	60	135 h
Fastback_RKE_Fine	80.4 M	60	720 h
Fastback_STRUCT-ε_Coarse	19.1 M	60	54 h
Fastback_STRUCT-ε_Medium	39.0 M	60	148 h
Fastback_STRUCT-ε_Fine	80.4 M	60	824 h
Estate_RKE_Coarse	19.1 M	60	56 h
Estate_RKE_Medium	38.6 M	60	162 h
Estate_RKE_Fine	79.1 M	60	956 h
Estate_STRUCT-ε_Coarse	19.1 M	60	66 h
Estate_STRUCT-ε_Medium	38.6 M	60	168 h
Estate_STRUCT-ε_Fine	79.1 M	60	1220 h

part of the flow region which covers the start of large separations. In most of the flow region, the added source term in the ε equation is negligible. Despite the small coverage in the flow region, the STRUCT-ε model activation is strong enough to significantly suppress the tubulent viscosity as shown in Figure 4-52, which results in the increased flow resolution over a much larger flow region. With different mesh resolutions, the activation region generated is in general consistent.

It is important to consider the computational cost of the simulations from the industrial application point of view, and Table 4.9 shows the comparison for all the unsteady simulations. Each simulation was conducted on five 12-core workstations in parallel. It shows that the computational expense of the STRUCT-ε model is on the same level as the RKE model with an average of 13% increase (maximum of 22%) from the addition of the source term.

4.4 Conclusions

This chapter focused on validation of the newly proposed STRUCT-ε model both on fundamental cases and specific cases in the automotive industry. First, a mesh convergence study was performed on the Ahmed body and consistent behavior is observed as the mesh becomes sufficiently fine. The mesh consistency is extremely valued for hybrid models, as for many existing hybrid models, inconsistent hybridization often occurs and the solutions are overly sensitive to the mesh quality. This is one of the most important features of the STRUCT-ε model

Following the mesh convergence study, the STRUCT-ε model is tested on the fundamental flow cases including flow over periodic hills and flow in an asymmetric diffuser. While the former one is characterized by flow separation and reattachment and is often used as a test case for validation of hybrid models, the latter case involves mild separation, which is challenging to correctly simulate for hybrid models. The model behavior is analyzed in detail and the results are compared with other turbulence models and the experiment or LES results. In both cases, decreased turbulent viscosity leads are generated by the STRUCT-ε model when compared with

the RKE model, which results in the increased resolution of the flow structures and the improved prediction of the flow topology. In the case of the flow over periodic hills, the RKE model predicts a longer recirculation zone with a latter reattachment, while the STRUCT-ε model exhibits better agreement with LES. In the case of the asymmetric diffuser flow, the recirculation region predicted by the STRUCT-ε model is close to the experiment, while no recirculation is observed in the RKE results. A comparison of the mean velocity and turbulent stress profiles also shows the improvement of the STRUCT-ε model with a better agreement with the reference result. In the challenging case of the flow in an asymmetric diffuser, the IDDES simulation is performed for comparison, and the recirculation region predicted is different from the experiment and is non-phased; the IDDES model excessively suppresses the turbulent viscosity, resulting in highly inaccurate predictions.

Based on the success of the STRUCT-ε model in producing improved results for fundamental cases, the focus was moved to the automotive industry, where the accurate prediction of the flow separation and vortices is necessary and challenging for traditional (U)RANS methods. First, the STRUCT-ε model was validated on the generic simplified vehicle model of the Ahmed body, and then the generic DrivAer car model was considered.

Accurate prediction of the flow past the Ahmed body with 25° slant angle is challenging as the flow partially separates from the rear slant while reattaching halfway down the slant back as a consequence of the complex interaction between 3D separation and the counter-rotating vortices coming off the rear window and side. The STRUCT-ε model is validated on the case, and the results are compared against the IDDES solution as well as solutions from two URANS models, namely the k-ω SST model and the RKE model. The STRUCT-ε and the IDDES models provide practically equivalent predictions of the flow topology and similar values for the mean velocity and turbulent stress. As the mesh becomes coarser however the IDDES approach fails, driving the formation of an incorrect large separation, both over the slant and in the body wake, and with very small counter-rotating vortices (even smaller than URANS results on the same computational mesh). The STRUCT-ε model in-

stead consistently demonstrated improved solution also for the coarse mesh results. Comparison between the STRUCT-ε and the URANS models has been further presented to elucidate the industrial applicability advantage of the proposed approach. Simulations have been conducted only on the coarse mesh intended for industrial applications. While the two URANS models incorrectly generate large separation regions over the slant and in the body wake, the STRUCT-ε model consistently predicts a small separation with a separation bubble over the slant. The STRUCT-ε model can resolve vortical turbulent structures on the slant and in the body wake, in contrast to the URANS solutions, and further results in a much closer agreement with the experimental data on the mean velocity and turbulent stress.

The STRUCT-ε is then applied to the fastback and estate configurations of the DrivAer model. The full complexity of the DrivAer model is considered by incorporating the detailed underbody, mirrors, rotating wheels, and moving ground. Simulation results are compared with the RKE model and the wind tunnel experiment. While both the STRUCT-ε and the RKE models agree well with the experiment on the fastback configuration, the STRUCT-ε model shows an advantage on the more challenging estate configuration with improved accuracy in the drag prediction. For the estate configuration, the RKE model overpredicts the pressure in the vehicle wake, therefore underestimating the drag coefficient. Improvement is obtained by using the STRUCT-ε model, but still there exist some discrepancies with the experiment on the pressure distribution at the rear window. The STRUCT-ε model also shows an advantage over the RKE model for predicting the flow separation and vortices by generating increased flow resolution around the vehicle.

In addition to the improved accuracy, the STRUCT-ε model also provides low computational cost. As shown in the cases of flow past the Ahmed body and the DrivAer model, the computational cost of the STRUCT-ε model is at the same level as the tested URANS approaches with a maximum difference of 22% in the test cases. The addition of a source term does not change the computational cost. In summary, the newly proposed STRUCT-ε model has shown the potential to provide improved accuracy and mesh-consistent solutions, as a key to industrial simulations.

Chapter 5

Extension of the STRUCT-ε model to steady simulations

Driven by the industrial need for accelerating CFD simulations in the optimization of vehicles, this chapter explores the possibility of extending the STRUCT-ε applicability to fast-running steady simulations. Several test cases are used for assessing their accuracy and limitations.

5.1 Introduction

In the design of vehicles, a large number of simulations are needed for optimizing the design of components such as mirrors, spoilers, intake and exhaust systems, etc, and the run time for the unsteady calculations is often too high. Therefore the number of runs and alternative designs is limited for effective optimization. In some other cases, restrictions exist for limiting the CPU use. For example, while CFD is used by the Formula One racing teams to optimize vehicle aerodynamics, the computing power used is restricted by the Federation Internationale de l'Automobile (FIA). Currently, each Formula One team is only allowed to use 25 teraflops (trillions of floating-point operations per second) of double-precision computing power for the aerodynamic simulations. This regulation is in place to prevent a large investments in enormous computational clusters, also suggesting that the restrictions might increase

the use of more efficient CFD tools that automate most of the modeling process. 25 teraflops is not a lot of processing power in the scheme of supercomputers. For all the simulations of the thesis, Intel Xeon E5-2620 cores are used. When using AVX2 and FMA3 instructions, each core provides about 250 gigaflops; the restriction of 25 teraflops corresponds to about 100 cores if the same core type is used. As the car model is complicated with details like the spoiler, suspension, mirrors, wheels, engine cover, etc, the computational mesh often consists of large number of cells on the order of tens to hundreds of millions. Therefore one unsteady simulation can take up to about one month, failing to meet the requirement of a large number of simulations in industrial design and optimization.

Due to the high computational cost needed for the unsteady simulations of vehicles and the restrictions on the computing power, in practice, faster running steady simulations are mostly used for the optimization of the vehicle components in the design, even though the flow past vehicles is inherently unsteady, and therefore the accuracy is considerably limited. In this scenario, usually, the mean value is obtained through average over the iterations. Accurate prediction of the vehicle drag using steady simulations is a great challenge as the traditional RANS models cannot capture the separation and vortices, which contribute strongly to the total drag, correctly. The automotive industry is seeking methods to improve accuracy within the computational restriction.

Given the practical industrial need to improve accuracy at a much reduced computational cost, it is meaningful to evaluate the applicability of the newly proposed STRUCT-ε model to steady-state simulations for design optimization, while certainly pushing the boundaries of the model concept. Conceptually, the direct extension from 2G-URANS to RANS is challenging to rigorously defend, as the concept of resolved and modeled turbulence at the base of the hybridization is not applicable to a steady-state simulation. However, this unique approach can be seen as controlling the overproduction of turbulence viscosity in areas of time scale overlap. In this sense, the concept applies also to RANS, where the areas of STRUCT activation are areas of lack of applicability of RANS and the amount of scale overlap provides a scale of the

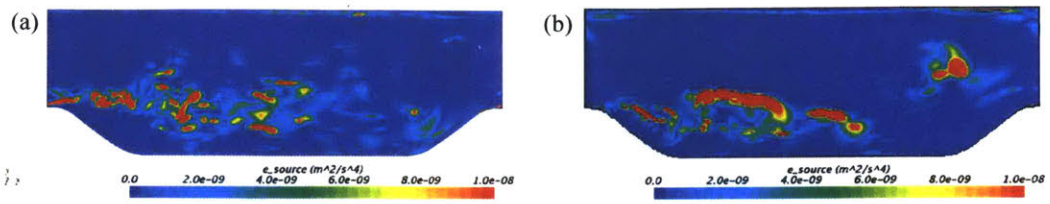

Figure 5-1: Instantaneous hybrid activation regions of the STRUCT-ε model represented by the distribution of the source term $C_{\varepsilon 3} k \left|\overline{II}\right|$ in the XY symmetry plane for the periodic hill, (a) unsteady simulation, (b) steady simulation.

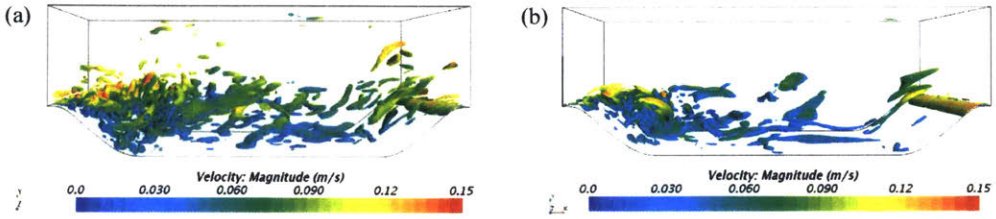

Figure 5-2: Instantaneous iso-surfaces of $Q = 0.05/s^2$ for the periodic hill obtained with the STRUCT-ε model using (a) unsteady simulation, (b) steady simulation.

inadequacy of RANS. For this evaluation, the test cases discussed in previous chapters are run again using the STRUCT-ε model with the steady-state solver. In the steady-state solver, the transient terms in the governing equations are not included, and the mean solution is directly solved through iterations.

5.1.1 Test cases results

In this section, the four test cases discussed in detail in previous chapters are simulated using the STRUCT-ε model with the steady-state solver on the same mesh resolutions. The results are compared with the ones obtained with steady simulations using the RKE model, the unsteady simulation results, and the reference data.

5.1.2 Flow over periodic hills

Figures 5-1 and 5-2 compare the instantaneous activation region and the iso-surfaces of the Q-criterion for the unsteady and steady simulations using the STRUCT-ε model. Here "instantaneous" in the steady simulation denotes the solution in one iter-

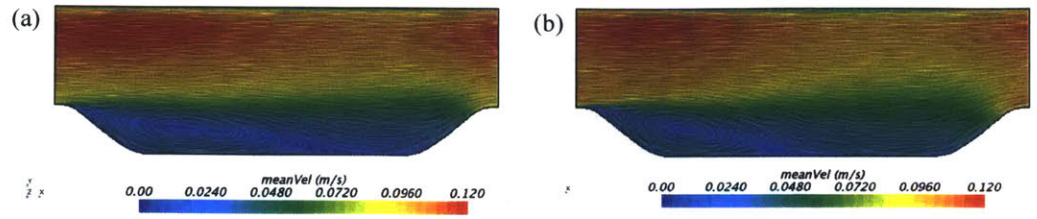

Figure 5-3: Mean streamlines for the periodic hill obtained with steady simulations using (a) the RKE model, (b) the STRUCT-ε model.

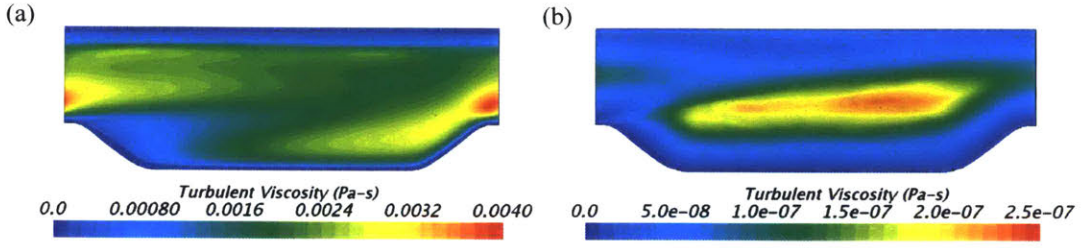

Figure 5-4: Mean turbulent viscosity for the periodic hill obtained with steady simulations using (a) the RKE model, (b) the STRUCT-ε model.

ation. It is important to point out that for the steady simulation using the STRUCT-ε model, the solution does not fully converge to a steady value, instead, it oscillates between iterations. This phenomenon is often observed when the flow is inherently unsteady, and theoretically, an unsteady solver is appropriate. Due to the limitations in industrial applications, steady simulation and average over iterations are used to obtain an approximate mean solution. The hybrid activation regions generated with the steady solver are in general similar to the ones generated with the unsteady simulation. The hybridization is mostly activated following the flow past the hill crest, where the separation starts. Fewer flow structures are obtained with the steady solver than the unsteady case, but the location of the structures is in general similar.

Figure 5-3 shows the mean streamlines obtained with steady simulations using the RKE and the STRUCT-ε models. The streamlines are almost identical to the corresponding unsteady results. While the RKE model predicts an elongated recirculation zone, the streamlines predicted by the STRUCT-ε model agree well the LES by Temmerman and Leschziner [10]. Figure 5-4 compares the mean turbulent viscos-

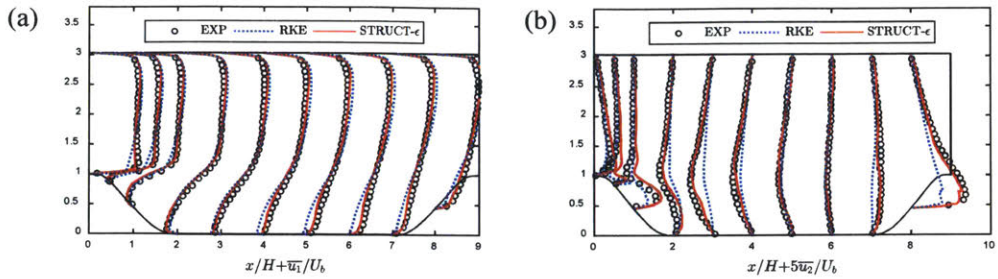

Figure 5-5: Comparison of (a) streamwise mean velocity profiles, (b) longitudinal mean velocity profiles between the RKE, STRUCT-ε models with steady simulations and the experimental data in the XY symmetry plane of the periodic hill geometry

Table 5.1: Comparison of the total computational time for the periodic hill case.

	Computational time	Cores
RKE_Steady	1.3h	60
STRUCT-ε_Steady	1.5 h	60
RKE_Unsteady	26h	60
STRUCT-ε_Unsteady	30h	60

ity generated by the steady simulations using the RKE and the STRUCT-ε models. Similar to the unsteady scenario, the turbulent viscosity is much reduced when using the STRUCT-ε model in comparison with the RKE model. A comparison of the mean velocity profiles obtained with the steady simulations is given in Figure 5-5; the results are almost the same as the unsteady ones.

Table 5.1 compares the total computational time spent on the steady and unsteady simulations using different turbulence models on the same computational mesh. The simulations are stopped when the mean solutions converge. The run time for the steady calculations is much reduced compared with the unsteady calculations, and in this case, the difference is about 20 times when the same computing power is applied. The difference between the computational time using the RKE model and the STRUCT-ε models is not very obvious, and using the STRUCT-ε model slightly increases the computational time spent by 13%.

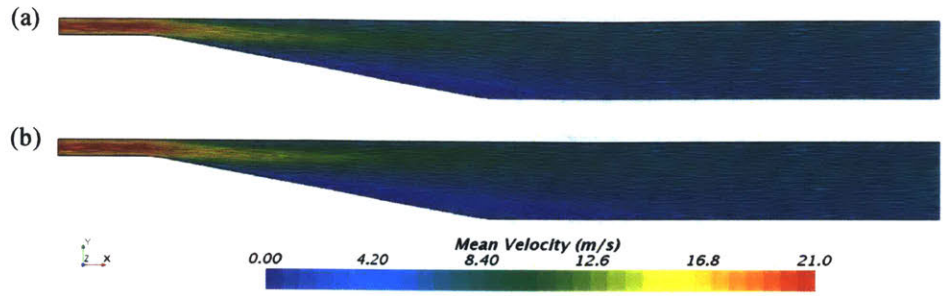

Figure 5-6: Mean streamlines for the asymmetric diffuser obtained with steady simulations using (a) the RKE model, (b) the STRUCT-ε model.

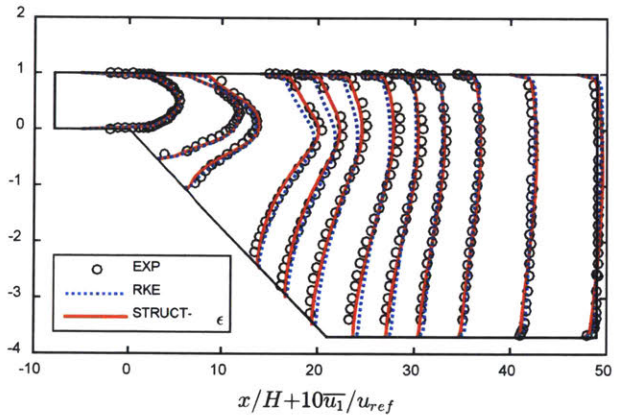

Figure 5-7: Comparison of streamwise mean velocity profiles between the RKE, STRUCT-ε models with steady simulations and the experimental data in the XY symmetry plane of the asymmetric diffuser.

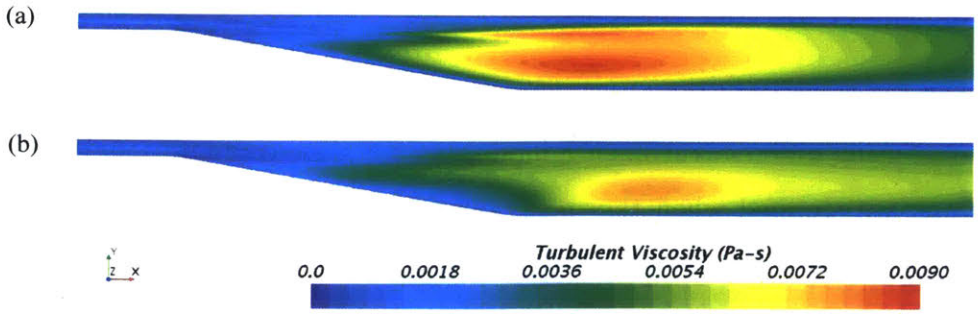

Figure 5-8: Mean turbulent viscosity in the XY symmetry plane for the asymmetric diffuser obtained with steady simulations using (a) the RKE model, (b) the STRUCT-ε model.

Table 5.2: Comparison of the total computational time for the asymmetric diffuser.

	Computational time	Cores
RKE_Steady	1.2h	60
STRUCT-ε_Steady	1.3h	60
RKE_Unsteady	16h	60
STRUCT-ε_Unsteady	18h	60

5.1.3 Flow in an asymmetric diffuser

For the flow in an asymmetric diffuser, the steady simulations results are shown in Figures 5-6, 5-7, and 5-8, for the comparison of the mean streamlines, the mean streamwise velocity profiles, and the mean turbulent viscosity distribution between the RKE and the STRUCT-ε model. The results are very similar to the corresponding unsteady results. The STRUCT-ε model predicts a large recirculation that resembles the one from the experiment by Buice and Eaton [109], while no recirculation is observed in the streamlines predicted by the RKE model. In addition, the mean velocity profiles predicted by the STRUCT-ε model agree better with the experiment. Compared with the traditional RANS model RKE, the improvement of the STRUCT-ε model comes from a reduced turbulent viscosity in areas where the RANS averaging is inadequate. Table 5.2 compares the computational time spent on the steady and unsteady simulations using the RKE and the STRUCT-ε models. Similar to what has been shown in the case of flow over periodic hills, over ten times reduction of the computational time is achieved by using the steady simulations compared with unsteady simulations, and the time spent using the STRUCT-ε model is slightly higher than the time spent using the RKE model with about 10% difference.

Flow past the Ahmed body

Steady simulations are performed using both the RKE and the STRUCT-ε models on the coarse resolution mesh as described in Section 4.3.1 or Mesh_4 in Section 4.1. Figure 5-9 shows the comparison of the mean streamlines obtained with the two models and the experiment. While the streamlines generated by the RKE model

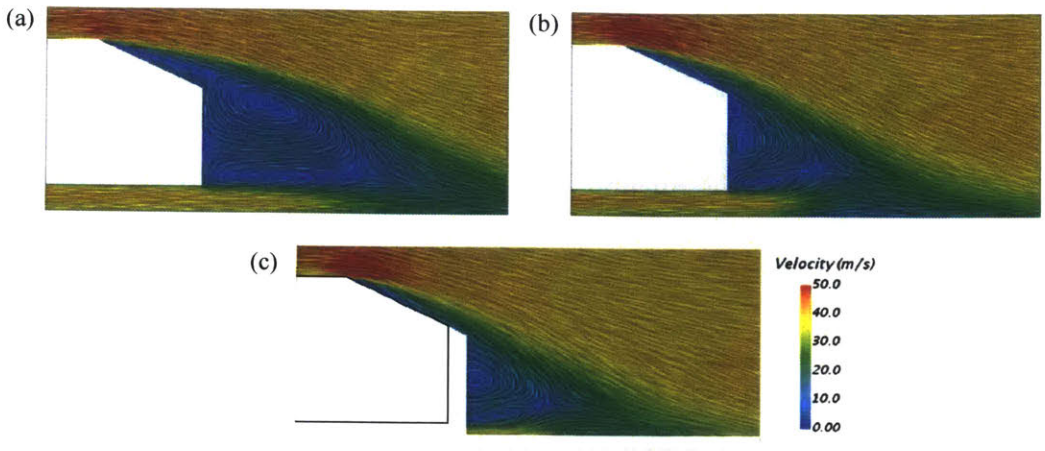

Figure 5-9: Comparison of the mean streamlines near the Ahmed body wake in the symmetry plane $y = 0$ obtained with steady simulations using (b) the RKE model , (b) the STRUCT-ε model, on the coarse resolution mesh, and (c) the experiment.

are almost identical to its unsteady results as shown in Figure 4-33 with a massive separation over the slant and the body back, the STRUCT-ε model unexpectedly shows an improvement by using the steady simulation in comparison to the unsteady simulation. The mean streamlines obtained with the unsteady simulation using the STRUCT-ε model show a recirculation bubble over the whole slant and two vortices right behind the Ahmed body; in the steady scenario, the recirculation bubble predicted is smaller and shorter, recovering the experimental data with partial separation over the slant, although the reattachment position still does not agree with the experiment. This improvement with the steady simulation is not necessarily expected since the STRUCT-ε model is proposed based on the unsteady concepts, but it is appreciated for industrial applications to achieve higher accuracy with a reduced computational cost. The improvement may be deriving from the steady approach remaining more stable, in the boundary layer region, where the unsteady STRUCT-ε might at times try to resolve near-wall structures with insufficient mesh resolution. If the improvement for predicting partial separation using the steady simulation with the STRUCT-ε model can be proven to be consistent, it could be of great value. A better agreement with the experimental data can also be observed in the mean velocity profiles using the steady simulation with the STRUCT-ε model as shown

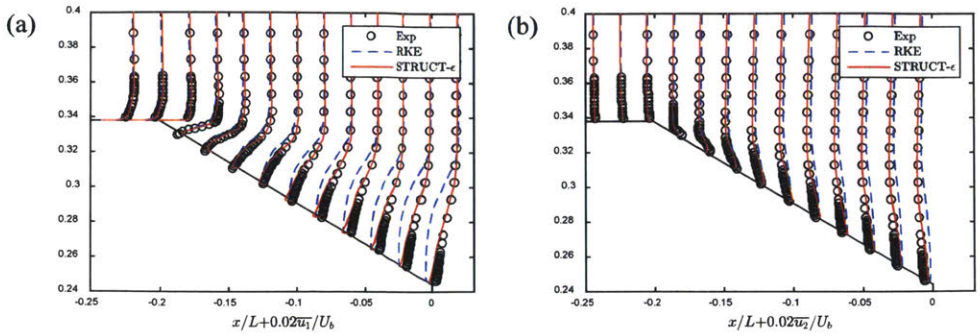

Figure 5-10: Mean velocity profiles a) in the streamwise direction, b) in the longitudinal direction, over the slant in the symmetry plane obtained on the coarse mesh.

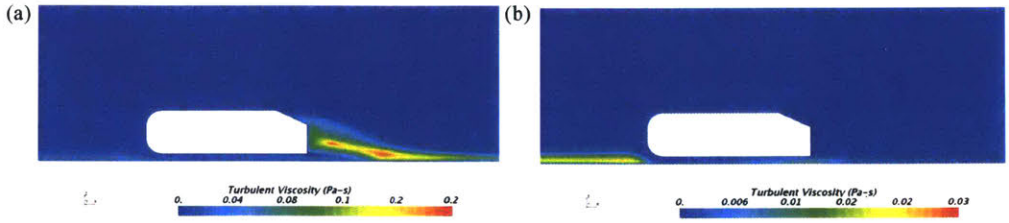

Figure 5-11: Turbulent viscosity around the Ahmed body generated by steady simulations using (a) the RKE model , (b) the STRUCT-ε model, on the coarse resolution mesh.

in Figure 5-10, even when compared with the unsteady results given in Figure 4-36. The comparison of the turbulent viscosity using the RKE and the STRUCT-ε models with steady simulations is illustrated in Figure 5-11. Compared to the RKE model, the STRUCT-ε model shows a much lower value on the slant and in the wake of the Ahmed body, consistent with the unsteady results discussed in Section 4.3.1.

Table 5.3 compares the drag and lift coefficients obtained with the RKE and the STRUCT-ε models with both steady and unsteady simulations. For the RKE model, the predicted force coefficients are very close between the steady and unsteady simulations, but both values deviate from the experimental data by Thacker et al. [126]. There are some differences in the drag and lift coefficients between the steady and unsteady simulations using the STRUCT-ε model, and the drag coefficient obtained with the steady simulation agrees better with the experiment, which can be attributed to the improved predicted flow topology with partial detachment over the slant.

Table 5.4 compares the total computational time spent on the steady and unsteady

Table 5.3: Drag and lift coefficients obtained with different models on the coarse mesh for the Ahmed body.

	C_d	C_l
EXP (Thacker)	0.384	0.422
RKE_Steady	0.340	0.277
STRUCT-ε_Steady	0.391	0.444
RKE_Unsteady	0.342	0.276
STRUCT-ε_Unsteady	0.410	0.431

Table 5.4: Comparison of the total computational time on the coarse mesh for the Ahmed body.

	Computational time	Cores
RKE_Steady	1.7h	60
STRUCT-ε_Steady	1.9h	60
RKE_Unsteady	42h	60
STRUCT-ε_Unsteady	43h	60

simulations using the RKE and the STRUCT-ε models on the coarse resolution mesh for the Ahmed body. All the simulations are performed in parallel on five 12-core workstations. The runtime for the STRUCT-ε model is on the same level as the RKE model with no more than 10% difference, while the steady simulations require 25 times less computational time than the unsteady simulations.

5.1.4 Flow past the DrivAer model

Both the RKE and the STRUCT-ε models are used for steady simulations of the flow past the DrivAer model on the set of three meshes for each configuration described in Section 4.3.2. Table 5.5 summarizes the drag coefficients for both the fastback and estate configurations obtained with steady and unsteady simulations using the RKE and the STRUCT-ε models. For the fastback configuration, the drag coefficients obtained with the steady simulations are very close to the ones obtained with the unsteady simulations on the same computational mesh for both the RKE and the STRUCT-ε models; also the predicted drag coefficients agree well with the experi-

Table 5.5: Comparison of the mean drag coefficient for the DrivAer model.

	Fastback_ Unsteady	Fastback_ Steady	Estate_ Unsteady	Estate_ Steady
Exp.	0.275		0.319	
STRUCT-ε_fine	0.276	0.276	0.320	0.318
STRUCT-ε_medium	0.279	0.279	0.322	0.316
STRUCT-ε_coarse	0.283	0.282	0.324	0.316
RKE_fine	0.273	0.273	0.289	0.288
RKE_medium	0.275	0.276	0.294	0.292
RKE_coarse	0.278	0.279	0.295	0.293

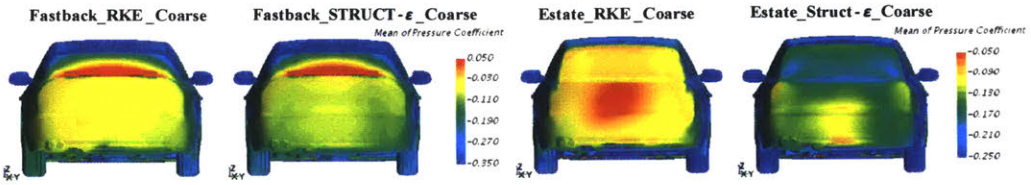

Figure 5-12: Rear view of the mean pressure coefficient distribution over the vehicle surface obtained with steady simulations.

ment. For the more challenging estate configuration, when using the RKE model, the steady and unsteady simulation results are similar, while the differences are larger when using the STRUCT-ε model. But both of the drag coefficients obtained with steady and unsteady simulations using the STRUCT-ε model agree well with the experiment, while the drag coefficient is largely underpredicted by the RKE model.

Figure 5-12 compares the rear view of the mean pressure coefficient distribution over the vehicle surface for both the fastback and estate configurations obtained with steady simulations using the RKE and the STRUCT-ε models on the coarse resolution meshes. For the fastback configuration, the results obtained using the two turbulence models are in general similar and consistent with the unsteady results shown in Figure 4-48; for the estate configuration, the RKE model generates overall higher C_p on the rear vehicle surface than the STRUCT-ε model, resulting in the lower drag predicted. Note that the C_p distribution generated by the STRUCT-ε model is different from the unsteady simulation results shown in Figure 4-46. The pressure on the rear

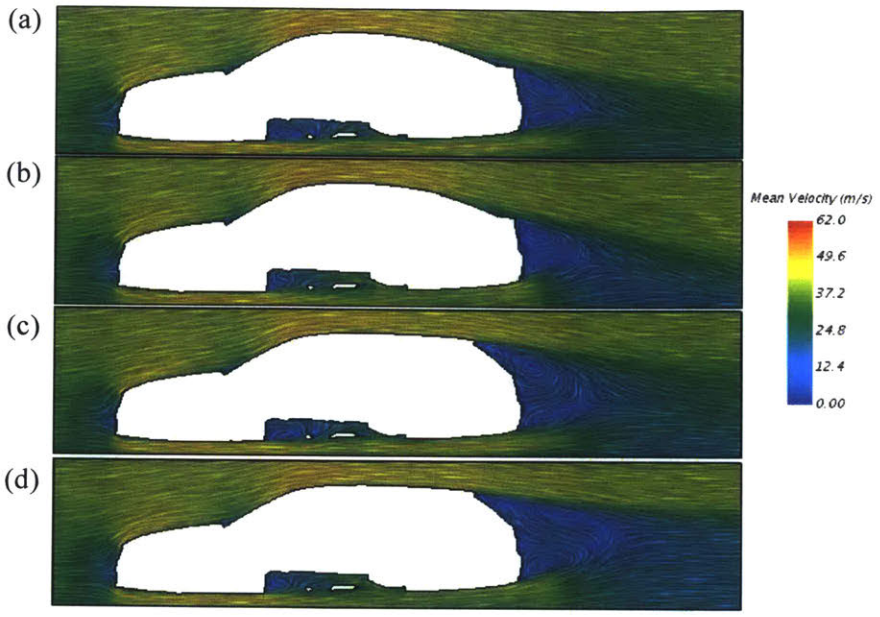

Figure 5-13: Mean streamlines on the x-z symmetry plane for (a) the fastback configuration obtained using the STRUCT-ε model, (b) the fastback configuration obtained using the RKE model, (c) the estate configuration obtained using the STRUCT-ε model, (d) the estate configuration obtained using the RKE model; all results are obtained on the coarse mesh using steady simulations.

window predicted by the steady simulation is lower than the unsteady simulation result, but neither of the distributions is fully consistent with the experimental value provided in Figure 4-49. The discrepancy in the pressure distribution explains the difference in the predicted drag coefficients and is also illustrated when comparing the mean streamlines obtained using the steady simulations shown in Figure 5-13 and the ones obtained using the unsteady simulations shown in Figure 4-52. For the fastback configuration, the streamlines generated with either steady or unsteady simulation using either the RKE or the STRUCT-ε model are all very similar. For the estate configuration, the streamlines from steady and unsteady simulations using the RKE model are consistent and different from the streamlines predicted by the STRUCT-ε model in the vehicle wake. On the other hand, the streamlines obtained with the steady and unsteady simulations using the STRUCT-ε model for the estate configuration are not consistent: two counter-rotating vortices are predicted in the streamlines obtained with the steady simulation while a different pattern is predicted

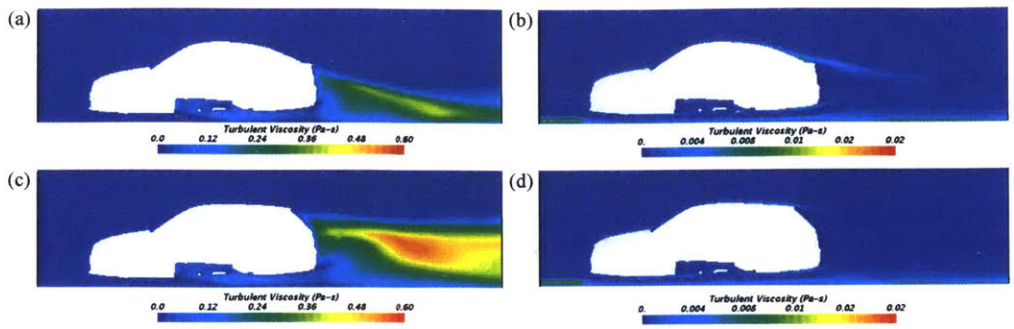

Figure 5-14: Mean turbulent viscosity for (a) the fastback configuration obtained with the RKE model, (b) the fastback configuration obtained with the STRUCT-ε model, (c) the estate configuration obtained with the RKE model, (d) the estate configuration obtained with the STRUCT-ε model; all results are obtained on the coarse mesh using steady simulations.

Table 5.6: Comparison of the total computational time for the DrivAer model on the coarse mesh resolution.

	Computational time	Cores
Fastback_RKE_Steady	5.1h	60
Fastback_STRUCT-ε_Steady	5.8h	60
Fastback_RKE_Unsteady	45h	60
Fastback_STRUCT-ε_Unsteady	52h	60
Estate_RKE_Steady	4.9h	60
Estate_STRUCT-ε_Steady	5.4h	60
Estate_RKE_Unsteady	56h	60
Estate_STRUCT-ε_Unsteady	66h	60

with the unsteady simulation. It is hard to judge which streamline pattern is closer to reality as no experimental data is available. But the improvement in comparison with the RKE model can be proven as the predicted drag coefficients agree much better with the experiment.

Figure 5-14 compares the mean turbulent viscosity generated with the RKE and the STRUCT-ε models for the fastback and estate configurations using the steady simulations. The turbulent viscosity is remarkably suppressed when using the STRUCT-ε model and the distribution of the turbulent viscosity is very similar to the unsteady simulation results.

Finally, Table 5.6 compares the total computational time spent on both the steady

and unsteady simulations using the RKE and the STRUCT-ε model on the coarse resolution meshes for the fastback and estate configurations. The conclusion is similar to the previous test cases: the run time for the STRUCT-ε model is less than 15% higher than the RKE model, and the run time for steady simulations is about 10 times less than the unsteady simulations.

5.2 Conclusions

This chapter discussed the extension of the newly proposed STRUCT-ε model to steady-state simulations driven by the practical industrial need for further reduction of the computational cost. All test cases discussed in Chapter 4 are simulated with the steady-state solver using the STRUCT-ε model and the RKE model for comparison, and the results are also compared with unsteady simulation results and the reference data. In all the test cases discussed, the STRUCT-ε model showed significant improvement with an improved agreement with the reference data in comparison with the RKE model. For the cases of flow over periodic hills and flow in an asymmetric diffuser, the results obtained with the steady simulations are almost identical to those of the unsteady simulations, while for the flow past the Ahmed body and the DrivAer model, the results from steady and unsteady simulations using the STRUCT-ε model are in general consistent but some discrepancies exist. Despite the discrepancies, the improved accuracy by using the STRUCT-ε model has been demonstrated for both the steady and unsteady simulations at comparable computational costs to the simulations using the RKE model. Therefore, the industrial need for achieving reasonable solutions using the fast-running steady simulations can be achieved with the STRUCT-ε model, especially for complex flows including separation and vortices where the traditional RANS models like RKE fail to capture the correct flow physics. On the other hand, as the STRUCT-ε model is proposed for unsteady simulations and the direct extension to steady simulations lacks strong theoretical support, it is suggested that careful validation be performed before applying the STRUCT-ε model for extensive simulation calculations.

Chapter 6

Application of the STRUCT-ε model to the optimization of a simplified tractor-trailer model

In this chapter, the STRUCT-ε model is applied to the optimization of a simplified tractor-tractor model in order to demonstrate the value of the improved physical representation and accuracy. First, the STRUCT-ε model is validated through comparison with an experiment and a published LES study, then optimization of the gap and the height difference between the tractor and trailer is performed using both the STRUCT-ε model and the RKE model to minimize the drag. Finally, the optimized solutions are validated using LES.

6.1 Introduction

Over the past few years, there has been a growing interest in the automotive industry to reduce the aerodynamic drag of commercial heavy vehicles, and particular attention has been directed to the combination of a truck and a semi-trailer, a tractor-trailer. One characteristic of this vehicle type is the interaction between the tractor and trailer: flow separation occurs behind the tractor and interacts with the trailer, and the complicated gap flow influences the pressure distribution both on the rear surface

Table 6.1: Properties of the wind tunnel experiment by Allan (1981) [18]

Property	Value
Wind tunnel	2.1m × 1.7 m
Inlet Velocity U	24.4 m/s
Trailer width b	0.305 m
Reynolds number	5.1×10^7
Ground Velocity	24.4 m/s

of the tractor and on the front surface of the trailer, impacting the overall drag. Accurate prediction of the drag is challenging as the interaction is hard to capture using existing RANS models and high computational cost is involved when using unsteady eddy-resolving models such as LES and DES. The STRUCT-ε model is expected to have an advantage over traditional methods, especially when associated with steady simulations. As shown in Chapter 5, the STRUCT-ε model has the potential of providing improved accuracy at a comparable computational cost as the existing RANS models.

To demonstrate the value of the STRUCT-ε model in the design, in this study it is applied to the optimization of a simplified tractor-trailer model in comparison with the commonly used RKE model using steady RANS. The adoption of a simplified model is to reduce the number of computational cells. The simplified tractor-trailer model is selected as the one defined in the wind tunnel experiments by Allan [18] and adopted in the LES study by Östh and Krajnović [16], as shown in Figure 6-1. The model consists of two boxes in tandem, with the front one representing the cab and the rear one representing the load. The reference length is the rear-box width $b = 0.305m$ (1.0 ft). The heights of the boxes above the ground are typical of those used in practice. In the wind tunnel experiments, the tractor was supported from the trailer by two metal tubes with outside diameter 0.09 b, and different gap widths were considered for studying the gap effects on the drag. The properties of the wind tunnel experiment by Allan [18] are summarized in Table 6.1. Corresponding LES studies were conducted by Östh and Krajnović [16], considering two gap widths of 0.17 b and 0.67 b. The computational domain is illustrated in Figure 6-2 with 8.0

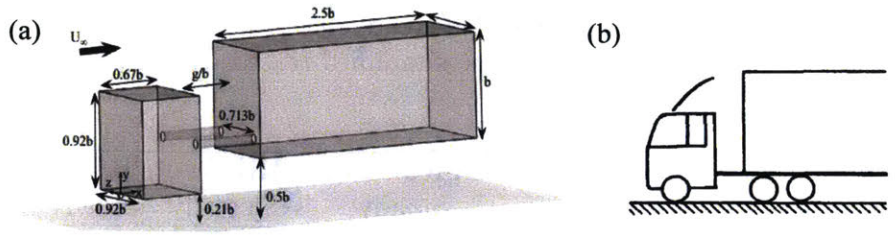

Figure 6-1: (a) Dimensions of the simplified tractor-trailer model (from [16]), and (b) its geometric relevance (from [17]).

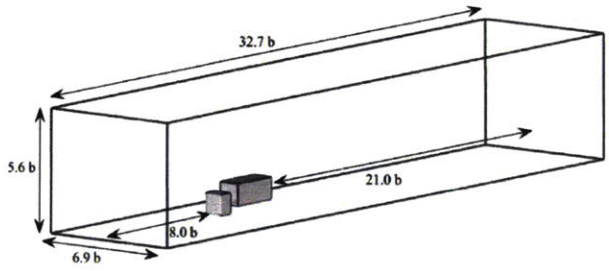

Figure 6-2: The computational domain used in the LES study by Östh and Krajnović (from [16]).

b upstream the tractor-trailer model and 21.0 b downstream. Two computational meshes are adopted for the LES simulations. Regarding the boundary conditions, no turbulence intensity was specified at the velocity inlet on the front surface of the domain; pressure outlet was specified in the downstream surface; the moving ground was considered with a no-slip boundary condition and prescribed streamwise velocity; no-slip boundary condition was specified on the sides and the roof.

6.2 Validation of the STRUCT-ε model for simulating the simplified tractor-trailer model

Before applying the STRUCT-ε model for optimization of the simplified tractor-trailer model, it is first validated against the wind tunnel experiment [18] and the LES study [16]. Two gap sizes (0.17 b and 0.67 b) are considered, to be consistent with the LES study. The same computational domain and the boundary conditions as the LES study by Östh and Krajnović [16] are also adopted. Steady and unsteady simulations

Table 6.2: Drag coefficients obtained with steady and unsteady simulations using the RKE and the STRUCT-ε models for the simplified tractor-trailer model with gap of 0.17 b.

	STRUCT-ε_ Unsteady	STRUCT-ε_ Steady	RKE_ Unsteady	RKE_ Steady	Cell Number
$g/b = 0.17$_Fine	1.05	1.03	0.88	0.88	2.3 M
$g/b = 0.17$_Medium	1.07	1.02	0.90	0.90	1.3 M
$g/b = 0.17$_Coarse	1.07	1.02	0.93	0.93	0.74 M

Table 6.3: Drag coefficients obtained with experiment by Allan [18] and LES by Östh and Krajnović [16] for the simplified tractor-trailer model with gap of 0.17 b.

	EXP	LES_fine	LES_coarse
$g/b = 0.17$	1.02	1.023	1.022

are performed using the STRUCT-ε model and the RKE model for comparison.

6.2.1 $g/b = 0.17$

In the case with a gap size 0.17 b, a set of three meshes is considered with the controlling parameters decreased consistently with a ratio of 1.25. Near-wall prism layers are only applied to the walls of the tandem boxes, as there is no need to resolve the lateral walls and the walls on the roof and ground. The number and thickness of prism layers are kept the same for the set of meshes so that the wall $y+$ is always smaller than 1.0. Refined meshes are defined near the simplified tractor-trailer model as shown in Figure 6-3 for the fine resolution mesh.

The drag coefficient follows the definition in equation (4.10) with the reference area of b^2. Table 6.2 compares the drag coefficients obtained with the steady and unsteady simulations using the RKE and the STRUCT-ε models. The RKE model generates identical drag coefficients for the steady and unsteady simulations with good convergence, however, the drag coefficients predicted are much lower than the experiment and LES results given in Table 6.3. The drag coefficients predicted by the STRUCT-ε model are much closer to the reference data with some differences

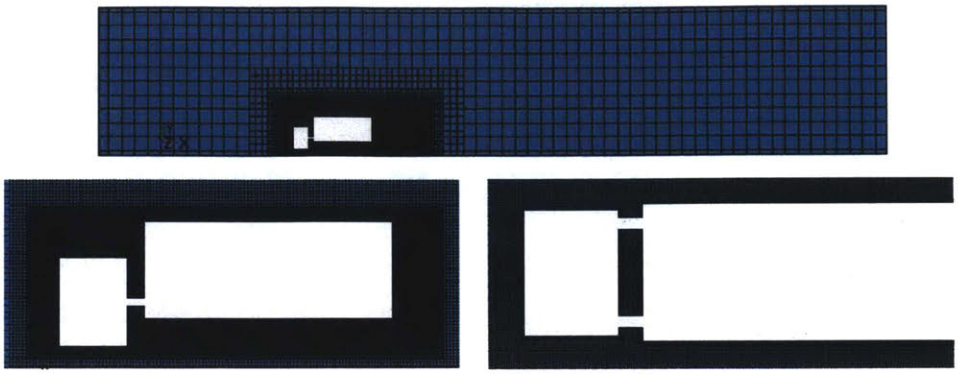

Figure 6-3: View of the fine mesh for the tractor-trailer model with gap of 0.17 b.

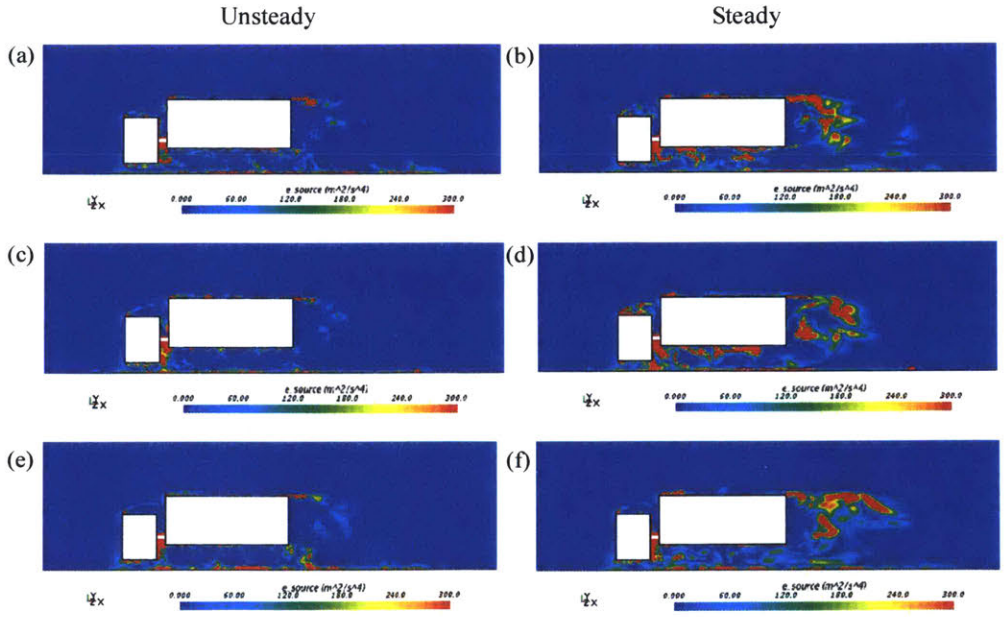

Figure 6-4: Instantaneous STRUCT-ε model activation regions identified by the distribution of the source term in the $z = 0$ plane around the simplified tractor-trailer model with gap of 0.17 b obtained with (a) unsteady simulation on the fine mesh, (b) steady simulation on the fine mesh, (c) unsteady simulation on the medium mesh, (d) steady simulation on the medium mesh, (e) unsteady simulation on the coarse mesh, (d) steady simulation on the coarse mesh.

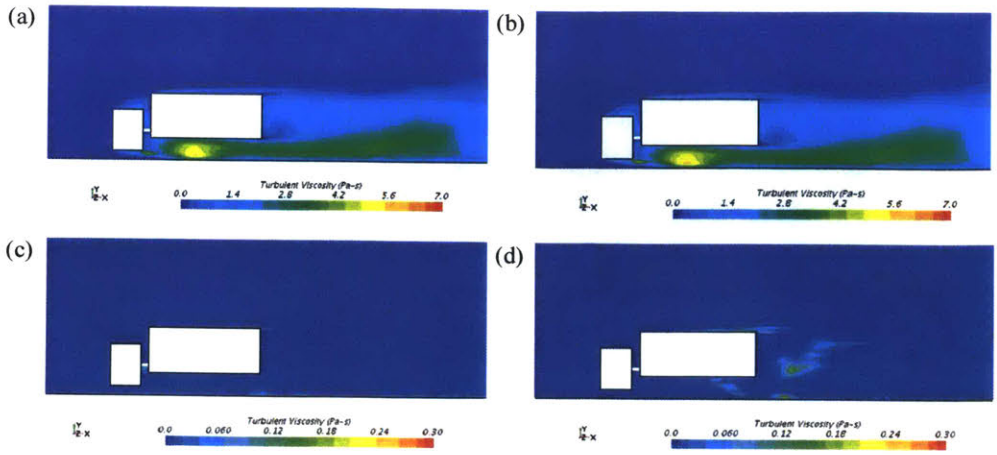

Figure 6-5: Instantaneous turbulent viscosity around the tractor-trailer model with gap of 0.17 b generated by (a) unsteady simulation using the RKE model, (b) steady simulation using the RKE model, (c) unsteady simulation using the STRUCT-ε model, (d) steady simulation using the STRUCT-ε model, on the medium resolution mesh.

between the steady and unsteady simulations. The results are in general consistent for different mesh resolutions.

Figure 6-4 shows the STRUCT-ε model activation for different simulations. For both steady and unsteady simulations, activation is consistent between different mesh resolutions and mostly appears near the start of the separation past the front surfaces of both boxes, in the gap, and in the wake of the trailer. The activation regions generated by the steady simulations are larger than the ones generated by the unsteady simulations, especially in the wake of the trailer. Due to the model activation, the turbulent viscosity is much lower when compared to the RKE model, shown in Figure 6-5 for the medium mesh resolution. As a result, the STRUCT-ε model provides a considerably increased resolution of the turbulent structures. As shown in Figure 6-6, the RKE model predicts almost no turbulence structures, while vortices shedding off the front surfaces of both boxes and in the model wake can be clearly observed in the results of the STRUCT-ε model. The increased resolution of unsteady flow structures is extremely helpful for capturing the flow interaction between the tractor and trailer and the flow separation in the model wake, providing improved accuracy in the drag prediction.

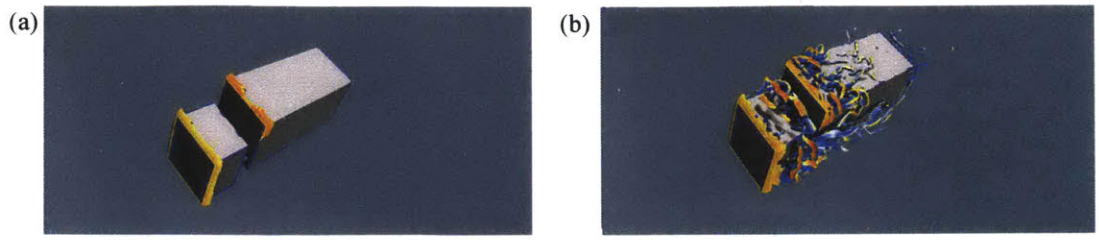

Figure 6-6: Iso-surfaces of $Q = 1000/s^2$ for flow past the simplified tractor-trailer model with gap of 0.17 b obtained with unsteady simulations using (a) the RKE model, (b) the STRUCT-ε model, on the medium resolution mesh.

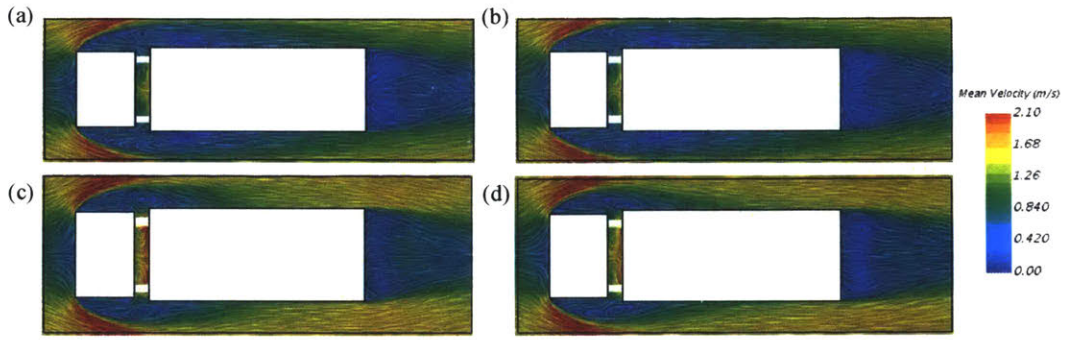

Figure 6-7: Mean streamlines around the tractor-trailer model with gap of 0.17 b on the plane $y = 0.46\ b$ obtained with (a) unsteady simulation using the RKE model, (b) steady simulation using the RKE model, (c) unsteady simulation using the STRUCT-ε model, (d) steady simulation using the STRUCT-ε model, on the medium resolution mesh.

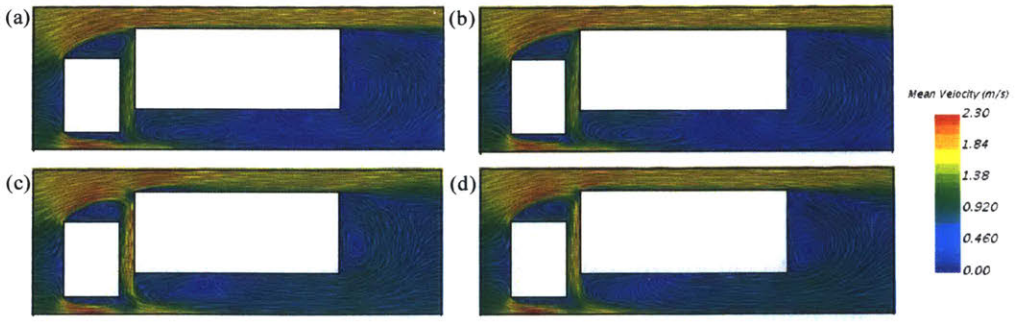

Figure 6-8: Streamlines around the tractor-trailer model with gap of 0.67 b on the plane $z = 0$ obtained with (a) unsteady simulation using the RKE model, (b) steady simulation using the RKE model, (c) unsteady simulation using the STRUCT-ε model, (d) steady simulation using the STRUCT-ε model, on the medium resolution mesh.

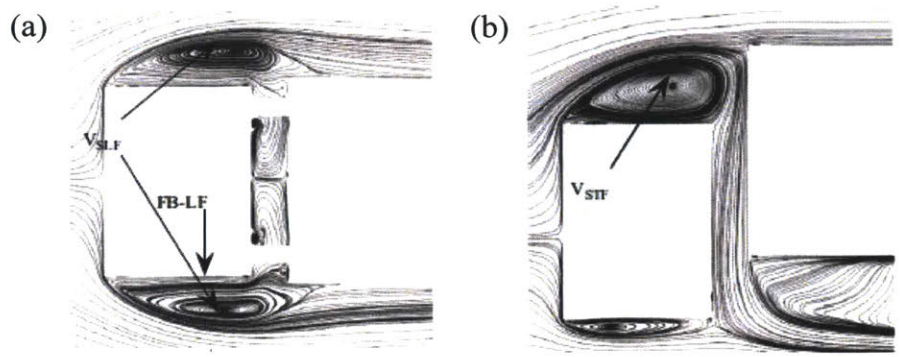

Figure 6-9: Streamlines around the tractor-trailer model with gap of 0.17 b on the planes (a) $y = 0.46\ b$, (b) $z = 0$, obtained with the LES study (From [16]).

Figures 6-7 and 6-8 compare the mean streamlines predicted by the different simulations on the medium resolution mesh on the planes $y = 0.46\ b$ and $z = 0$. Streamlines generated by the LES study on the corresponding planes are provided in Figure 6-9. On the plane $y = 0.46\ b$, the RKE model predicts a much longer separation region after the front surface of the tractor, extending to the middle of the trailer. The STRUCT-ε model, on the other hand, predicts a smaller separation region with earlier attachment, closer to the LES result. On the $z = 0$ plane, the RKE model again overpredicts the separation region. On the tractor top, the separation extends to the front surface of the trailer and enters the gap, causing lower velocity in the gap and lower pressure on the front face of the trailer, leading to low drag predicted. Also, the gap flow influences the flow pattern below the trailer generating a large recirculation, which does not exist in the results of the LES study and the STRUCT-ε simulations.

The different flow patterns predicted by the RKE and the STRUCT-ε models lead to the discrepancies in the prediction of the pressure distribution. As most of the drag on bluff bodies comes from the pressure drag, the difference in the pressure distribution directly relates to the difference in the overall drag predicted. Figure 6-10 compares the distribution of the pressure coefficient C_p (defined in equation (4.11)) on the front and rear surfaces of the tractor and trailer predicted by the steady and unsteady simulations using the RKE and the STRUCT-ε models on the medium

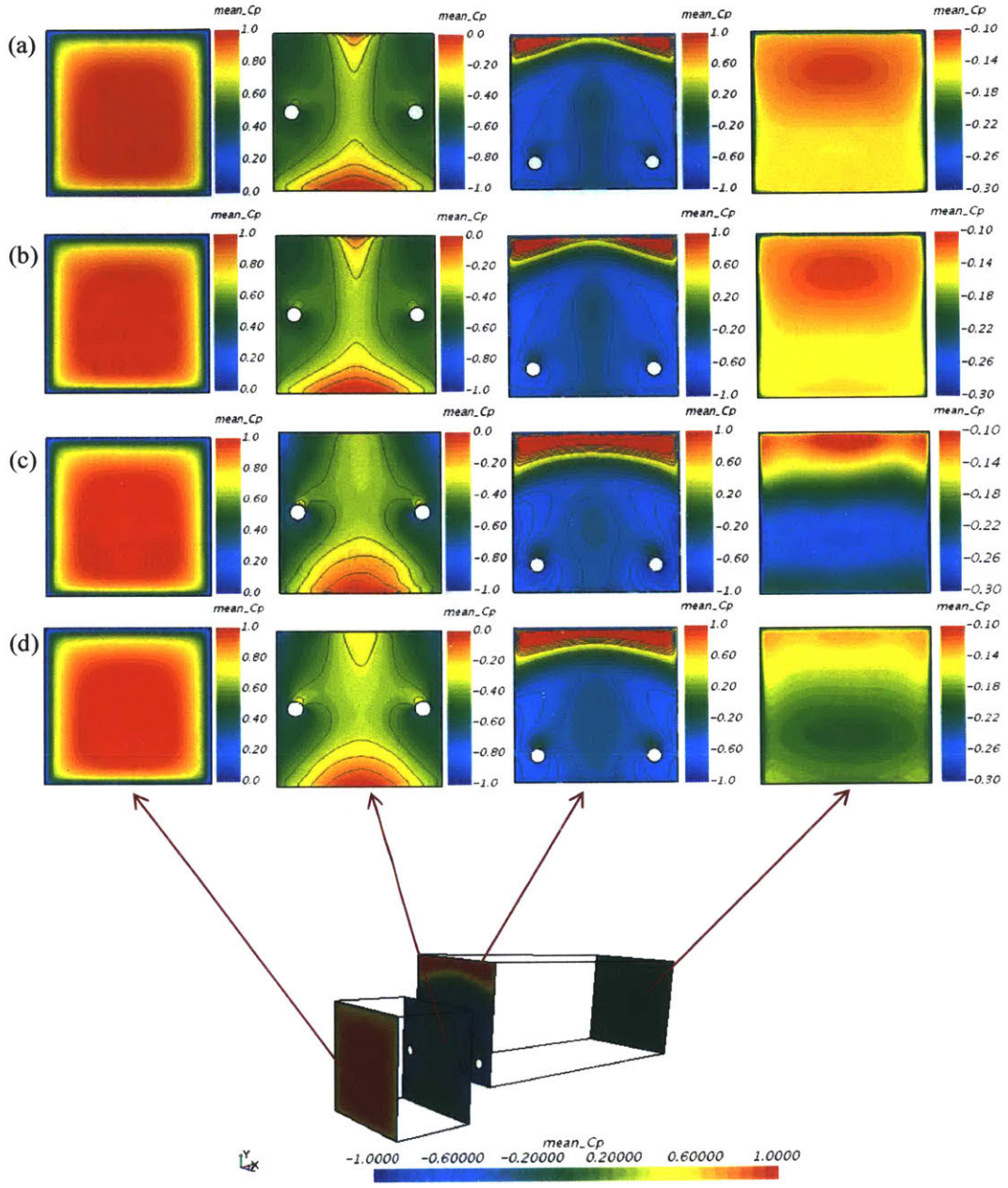

Figure 6-10: Distribution of the mean pressure coefficient on the front and back surfaces of the tractor and trailer with gap of 0.17 b obtained with (a) unsteady simulation using the RKE model, (b) steady simulation using the RKE model, (c) unsteady simulation using the STRUCT-ε model, (d) steady simulation using the STRUCT-ε model, on the medium resolution mesh. From left to right, the columns correspond to the front surface of the tractor, the back surface of the tractor, the front surface of the trailer, and back surface of the trailer, respectively.

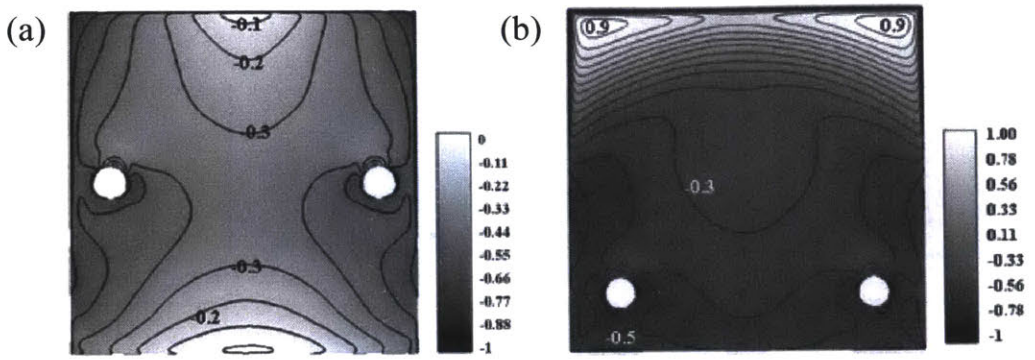

Figure 6-11: Distribution of the mean pressure coefficient (a) on the back surface of the tractor, (b) on the front surface of the trailer, when the gap size is 0.17 b.

Table 6.4: Drag coefficient contribution C_d_p from the pressure on the front and back surfaces of the tractor and trailer with gap size of 0.17 b.

	Tractor_Front surface	Tractor_Back surface	Trailer_ Front surface	Trailer_Back surface
EXP		0.34	-0.17	
RKE_Unsteady	0.70	0.33	-0.28	0.14
RKE_Steady	0.69	0.32	-0.26	0.14
STRUCT-ε_Unsteady	0.70	0.34	-0.20	0.21
STRUCT-ε_Steady	0.69	0.33	-0.18	0.17

resolution mesh. Corresponding LES results on the rear surface of the tractor and the front surface of the trailer are available and provided in Figure 6-11. The surface integral of the pressure distribution results in the pressure drag contribution from the surface, and the contributing drag coefficient can be calculated as:

$$C_d\_p = \frac{n_x \int_A C_p dA}{A_{ref}} \tag{6.1}$$

where A_{ref} is the reference area b^2 being consistent with the definition for the drag coefficient, and n_x is the x component of the unit normal vector of the plane pointing inside of the body. The drag coefficient contributions from the pressure on the front and back surfaces of the tractor and trailer are given in Table 6.4. On the front surface of the tractor, the pressure distribution is predicted similarly by all the simulations, with higher pressure in the middle of the surface and gradually decreasing

Table 6.5: Total computational time for simulations of the simplified tractor-trailer model with gap of 0.67 b on the medium mesh resolution using 60 cores.

	STRUCT-ε_ Unsteady	STRUCT-ε_ Steady	RKE_ Unsteady	RKE_ Steady
Computational time (hr)	5.31	0.36	4.42	0.31

pressure towards the edges. As a result, the C_d_p value is almost the same for all the simulations. On the rear surface of the tractor, the pressure distribution is predicted quite differently by the RKE model and the STRUCT-ε model, especially over the top half; the pressure distribution predicted by the STRUCT-ε model is very close to that of the LES study. Despite the difference in the pressure distribution, the average pressure level is similar, resulting in a similar C_d_p values varying between 0.32 to 0.34, close to the experimental value of 0.34. On the front surface of the trailer, the RKE model predicts a lower pressure level with lower drag coefficient contribution for both the steady and unsteady simulations, while the STRUCT-ε model predicts a pressure level closer to the experiment as identified by the better agreement on the C_d_p value. On the rear surface of the trailer, the pressure predicted by the RKE model is much higher than the pressure predicted by the STRUCT-ε model, resulting in the lower drag contribution, and the underpredicted overall drag. There is also an observable difference in the pressure distribution between the steady and unsteady simulations using the STRUCT-ε model: the unsteady simulation generates higher pressure in the top part of the plane and lower pressure in the bottom part, while the steady simulation generates a more even pressure distribution. Due to the difference, the C_d_p value is slightly higher in the unsteady simulation than the steady simulation, leading to the difference in the overall drag. It is hard to judge whether the steady or the unsteady simulation agrees better with the experiment or LES due to a lack of detailed data. However, the results confirm a clear improvement when compared the RKE to STRUCT-ε solution.

Table 6.5 compares the total computational time spent on the steady and unsteady simulations using the RKE and the STRUCT-ε model computed in parallel

Table 6.6: Total computational time for simulations of the simplified tractor-trailer model with gap of 0.67 b on the medium mesh resolution using 60 cores.

	STRUCT-ε_ Unsteady	STRUCT-ε_ Steady	RKE_ Unsteady	RKE_ Steady	Cell Number
$g/b = 0.67$_Fine	1.17	1.18	0.85	0.85	2.6M
$g/b = 0.67$_Medium	1.17	1.16	0.87	0.86	1.4 M
$g/b = 0.67$_Coarse	1.12	1.13	0.90	0.89	0.81M

Table 6.7: Drag coefficients obtained with experiment by Allan [18] and LES by Östh and Krajnović [16] for the simplified tractor-trailer model with gap of 0.67 b.

	EXP	LES_fine	LES_coarse
$g/b = 0.67$	1.09	1.16	1.157

on 60 cores. Steady simulations are much more computationally effective than the unsteady simulations with 15 times smaller runtime, and the computational time for the STRUCT-ε simulations is 20% higher than the time used for the RKE simulations.

6.2.2 $g/b = 0.67$

Similar to the case with a gap size of 0.17 b, in the case with gap size 0.67 b, a set of three meshes are also used with the controlling parameters decreased consistently with a ratio of 1.25. The near-wall prism layer and the refinement settings are the same as the case with a gap size of 0.17 b. Table 6.6 compares the drag coefficients obtained with the steady and unsteady simulations using the RKE and the STRUCT-ε models. The RKE model generates similar drag coefficients for the steady and unsteady simulations with good convergence, but the drag coefficients predicted are much lower than the experiment and LES results given in Table 6.7. The drag coefficients predicted by the STRUCT-ε model show good convergence with different mesh resolutions and the values agree well with the LES study and higher than the experimental value. Note that there is some difference in the drag coefficients given by the experiment and the LES simulation.

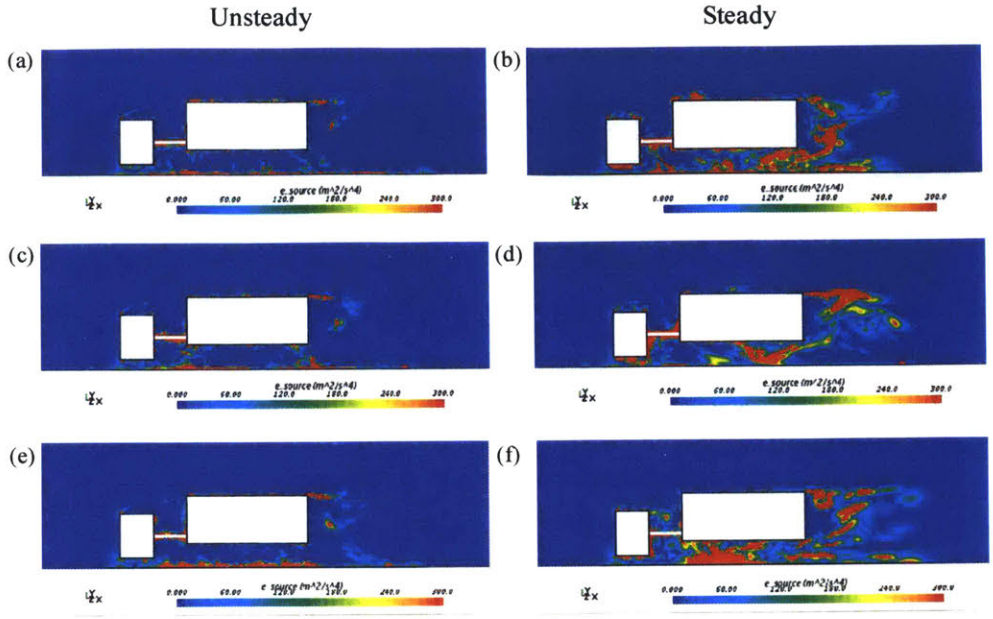

Figure 6-12: Instantaneous STRUCT-ε model activation regions identified by the distribution of the source term in the XY symmetry plane around the simplified tractor-trailer model with gap of 0.67 b obtained with (a) unsteady simulation on the fine mesh, (b) steady simulation on the fine mesh, (c) unsteady simulation on the medium mesh, (d) steady simulation on the medium mesh, (e) unsteady simulation on the coarse mesh, (d) steady simulation on the coarse mesh.

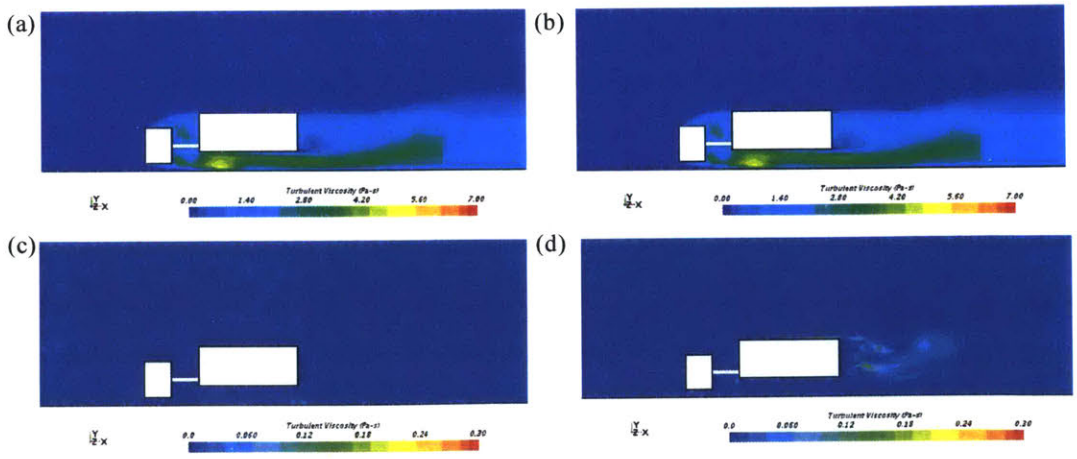

Figure 6-13: Instantaneous turbulent viscosity around the tractor-trailer model with gap of 0.67 b generated by (a) unsteady simulation using the RKE model, (b) steady simulation using the RKE model, (c) unsteady simulation using the STRUCT-ε model, (d) steady simulation using the STRUCT-ε model, on the medium resolution mesh.

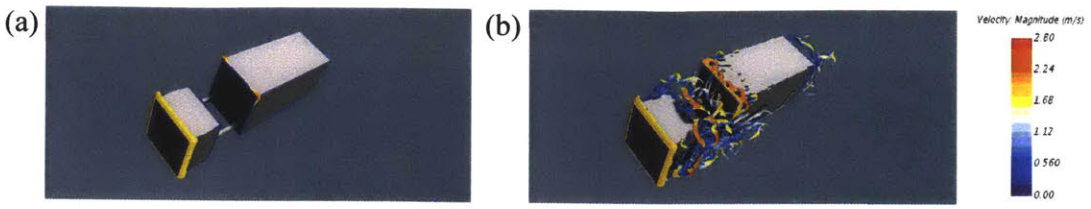

Figure 6-14: Iso-surfaces of $Q = 1000/s^2$ for flow past the simplified tractor-trailer model with gap of 0.67 b obtained with unsteady simulations using (a) the RKE model, (b) the STRUCT-ε model, on the medium resolution mesh.

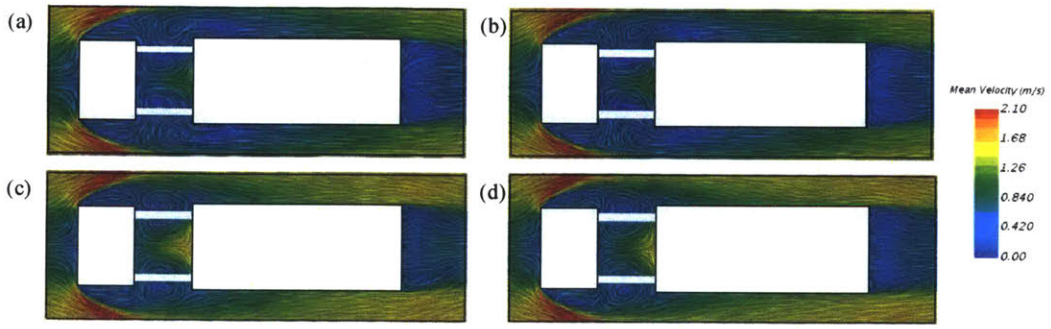

Figure 6-15: Streamlines around the tractor-trailer model with gap of 0.67 b on the plane $y = 0.46\ b$ obtained with (a) unsteady simulation using the RKE model, (b) steady simulation using the RKE model, (c) unsteady simulation using the STRUCT-ε model, (d) steady simulation using the STRUCT-ε model, on the medium resolution mesh.

Figure 6-12 shows the STRUCT-ε model activation identified by the distribution of the source term for different simulations. For both steady and unsteady simulations, activation is consistent between different mesh resolutions and mostly appears near the start of the separation past the front surfaces of both boxes, in the gap, and in the wake of the trailer. The activation regions generated by the steady simulations are larger than the ones generated by the unsteady simulations. Figure 6-13 shows the much decreased turbulent viscosity generated by the STRUCT-ε model in comparison to the RKE model, and Figure 6-14 shows the increase of the resolved turbulence structures with vortices off the front surfaces of both boxes and in the model wake. These results are very similar to the case with a gap of 0.17 b.

Figures 6-15 and 6-16 compare the mean streamlines predicted by the different simulations on the medium resolution mesh on the planes $y = 0.46\ b$ and $z = 0$. Streamlines generated by the LES study on the corresponding planes are provided in

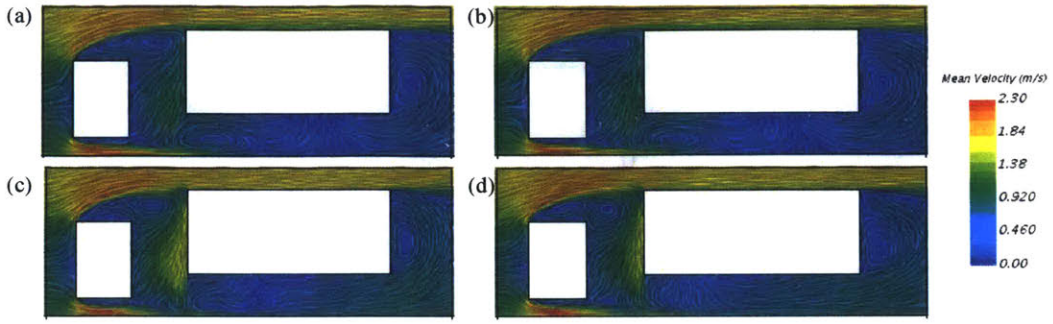

Figure 6-16: Streamlines around the tractor-trailer model with gap of 0.67 b on the plane $z = 0$ obtained with (a) unsteady simulation using the RKE model, (b) steady simulation using the RKE model, (c) unsteady simulation using the STRUCT-ε model, (d) steady simulation using the STRUCT-ε model, on the medium resolution mesh.

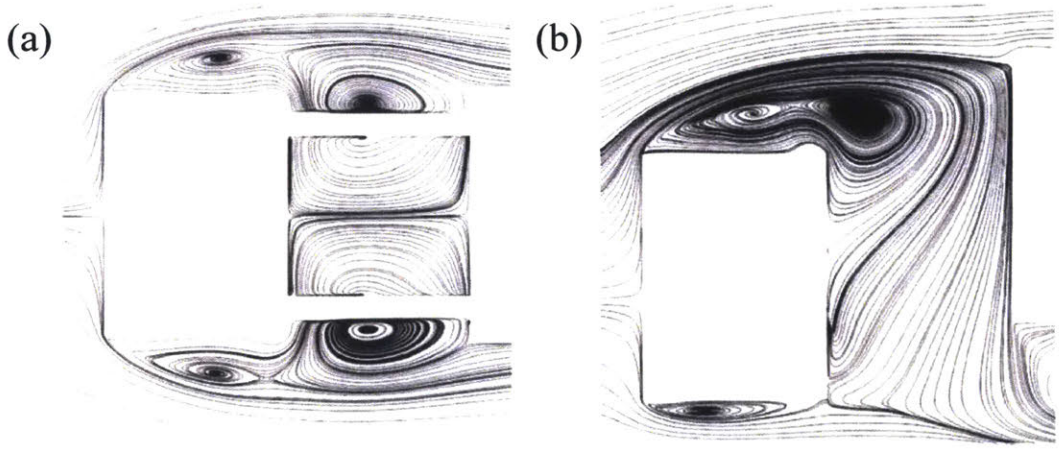

Figure 6-17: Streamlines around the tractor-trailer model with gap of 0.67 b on the planes (a) $y = 0.46\ b$, (b) $z = 0$, obtained with the LES study (From [16]).

Table 6.8: Drag coefficient contribution from the pressure on the front and back surfaces of the tractor and trailer with gap size of 0.67 b on the medium mesh resolution.

	Tractor_Front surface	Tractor_Back surface	Trailer_ Front surface	Trailer_Back surface
EXP		0.36	-0.18	
RKE_Unsteady	0.70	0.36	-0.34	0.13
RKE_Steady	0.70	0.36	-0.34	0.13
STRUCT-ε_Unsteady	0.70	0.36	-0.13	0.21
STRUCT-ε_Steady	0.69	0.35	-0.07	0.17

Table 6.9: Total computational time for simulations of the simplified tractor-trailer model with gap of 0.67 b on the medium mesh resolution.

	STRUCT-ε_ Unsteady	STRUCT-ε_ Steady	RKE_ Unsteady	RKE_ Steady
Computational time (hr)	5.8	0.38	4.7	0.33

Figure 6-17. On the plane $y = 0.46\ b$, again the RKE model predicts a much longer separation region after the front surface of the tractor, and the STRUCT-ε model predicts a smaller separation region with earlier attachment. The streamline pattern in the gap is better predicted by the STRUCT-ε model with good agreement with the LES study. On the $z = 0$ plane, the RKE model overpredicts the separation region. On the tractor top, the separation extends to the front surface of the trailer and enters the gap, causing lower velocity in the gap and lower pressure on the front face of a trailer, leading to low drag predicted. Also, the gap flow influences the flow pattern below the trailer generating a large recirculation, which does not exist in the results of the LES study and the STRUCT-ε simulations.

Figure 6-18 compares the distribution of the pressure coefficient C_p on the front and rear surfaces of the tractor and trailer predicted by the steady and unsteady simulations using the RKE and the STRUCT-ε models on the medium resolution mesh. Corresponding LES results on the front surface of the trailer are given by Figure 6-19. The drag coefficient contribution from the pressure on the front and back surfaces of the tractor and trailer is given in Table 6.8. Again, the results are

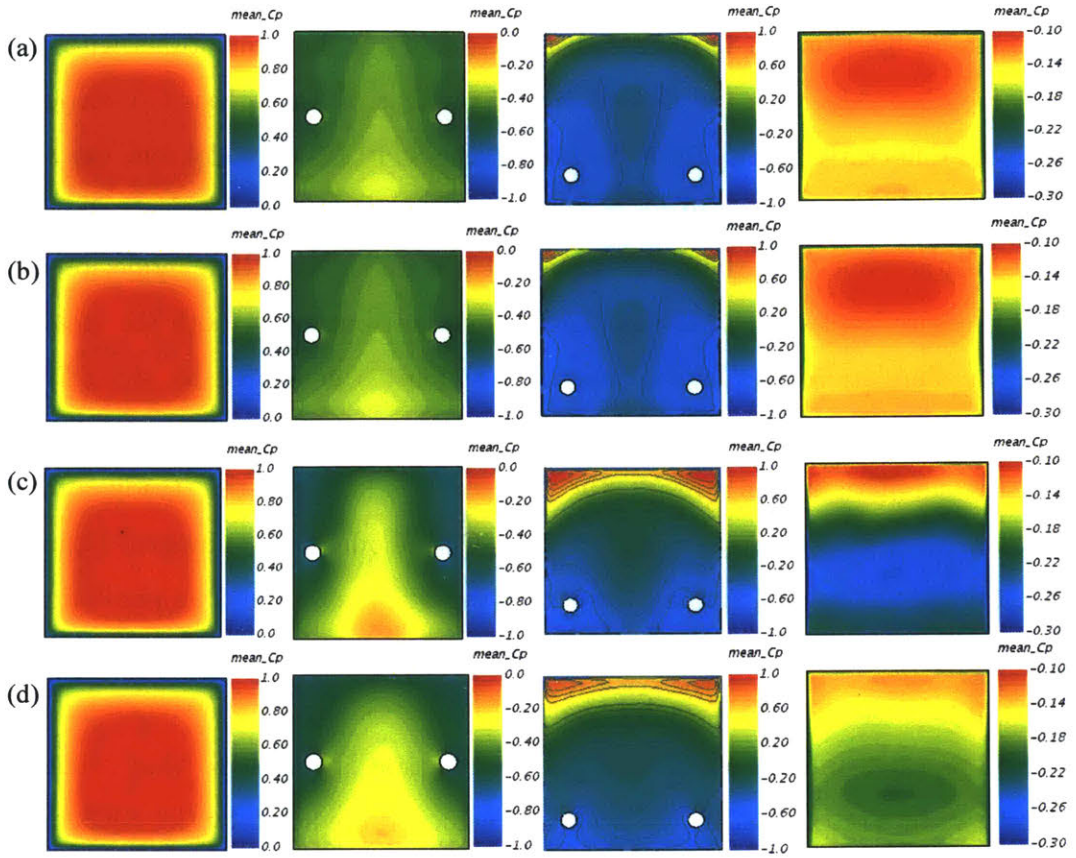

Figure 6-18: Distribution of the mean pressure coefficient on the front and back surfaces of the tractor and trailer with gap of 0.67 b obtained with (a) unsteady simulation using the RKE model, (b) steady simulation using the RKE model, (c) unsteady simulation using the STRUCT-ε model, (d) steady simulation using the STRUCT-ε model, on the medium resolution mesh. From left to right, the columns correspond to the front surface of the tractor, the back surface of the tractor, the front surface of the trailer, and the back surface of the trailer, respectively.

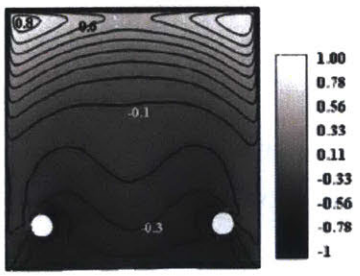

Figure 6-19: Distribution of the mean pressure coefficient on the front surface of the trailer when the gap size is 0.67 b.

very similar to the case with a gap of 0.17 b. On the front surface of the tractor, the pressure distribution is predicted the same by all the simulations with almost the same C_{d_p} value. On the rear surface of the tractor, the pressure distribution is predicted differently by the RKE model and the STRUCT-ε model, but the average pressure level is similar, resulting in a similar C_{d_p} values, which agree well with the experimental value. On the front surface of the trailer, the RKE model predicts a lower pressure level with lower drag coefficient contribution for both the steady and unsteady simulations, while the pressure distribution generated by the STRUCT-ε model is closer to the LES result with some differences between the steady and unsteady simulations. As a result, the C_{d_p} value is higher in the steady simulation than the unsteady simulation using the STRUCT-ε model; both values are higher than the experimental one, explaining the higher value in the overall drag prediction than the experiment. However, since the pressure distribution is close to the LES result, the C_{d_p} value is likely to resemble that of LES, especially for the steady simulation with STRUCT-ε model, whose pressure distribution is closest to that of LES. On the rear surface of the trailer, the pressure coefficient predicted by the RKE model is much higher than that predicted by the STRUCT-ε model, resulting in the lower drag contribution, and the underpredicted overall drag. There is also an obvious difference in the pressure distribution between the steady and unsteady simulations using the STRUCT-ε model: the unsteady simulation generates higher pressure in the top part of the plane and lower pressure in the bottom part, while the steady simulation generates a more even pressure distribution. Due to the difference, a slightly higher C_{d_p} value is predicted in the unsteady simulation when compared to the steady simulation, however, due to the error cancellation on the front surface of the trailer, the overall drag coefficients predicted using steady and unsteady simulations with the STRUCT-ε model are very similar. Despite this error cancellation, the improved accuracy is obvious in comparison with the RKE model.

Table 6.9 compares the total computational time spent on the steady and unsteady simulations using the RKE and the STRUCT-ε model computed in parallel on 60 cores. The same conclusions are obtained for the case with the smaller gap size:

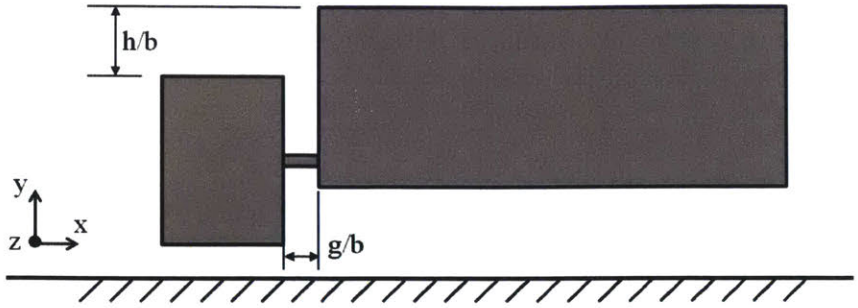

Figure 6-20: Design variables used for the optimization of the simplified tractor-trailer model.

Table 6.10: Drag coefficients obtained with the steady simulations using the STRUCT-ε model for different values of the design variables.

h/b \ g/b	0.2	0.25	0.3	0.35	0.4
0.1	0.988	0.972	0.977	0.984	1.001
0.2	1.007	0.988	0.992	1.016	1.061
0.3	1.032	0.998	1.018	1.042	1.091
0.4	1.048	1.040	1.033	1.058	1.106
0.5	1.096	1.079	1.073	1.087	1.117

the runtime for steady simulations are 15 times less than that for the unsteady simulations, and the computational time for the STRUCT-ε simulations is 18% higher than that for the RKE simulations.

6.2.3 Optimization of the simplified tractor-trailer model

Through validation of the STRUCT-ε model for the drag prediction of the simplified tractor-trailer model, the improvement has been proven with the better agreement with the reference data in comparison with the commonly used RKE model for both steady and unsteady simulations in the automotive industry. Optimization of the simplified tractor-trailer model is then explored in this section based on the drag coefficients obtained the RKE and the STRUCT-ε simulations, to demonstrate the influence of the modeling approach on the optimal solutions obtained. To be consistent with the industrial applications, only steady simulations are performed.

Table 6.11: Drag coefficients obtained with the steady simulations using the RKE model for different values of the design variables.

h/b \ g/b	0.2	0.25	0.3	0.35	0.4
0.1	0.919	0.871	0.853	0.888	0.911
0.2	0.925	0.878	0.857	0.872	0.950
0.3	0.926	0.879	0.853	0.854	0.910
0.4	0.928	0.885	0.856	0.849	0.879
0.5	0.932	0.891	0.863	0.852	0.871

For simplification of the optimization, only two design variables are considered: the width of the gap g/b between the trailer and tractor, and the height difference h/b between the top surface of the tractor and trailer through varying the height of the tractor, as shown in Figure 6-20. The ranges for the design variables are chosen to be [0.1, 0.5] for g/b and [0.2, 0.4] for h/b. Steady simulations are performed using the STRUCT-ε model and the RKE model for 25 combinations of the design variables; the meshes are generated in a similar way as the validation study at the medium resolution; the resulting drag coefficients are summarized in Tables 6.10 and 6.11. It can be seen that the drag coefficients predicted by the two turbulence models have significant differences and that the values obtained using the STRUCT-ε model are much larger than the ones predicted by the RKE model, consistently with results shown in the previous validation study. Surrogate surfaces (Figure 6-21) are built from the drag values obtained in the 25 simulations using the Kriging approximation model [148] for the STRUCT-ε model and the RKE model, respectively.

Optimization is performed on the surrogate surfaces using a Genetic Algorithm (GA), one of the most popular stochastic optimization algorithms based on the evolutionary ideas of natural selection and genetics. The GA adopted in this study can be summarized by the following steps:

1) An initial population of $N_p = 50$ individuals is randomly generated. Each individual is represented by a chromosome which represents the design variables as binary strings.

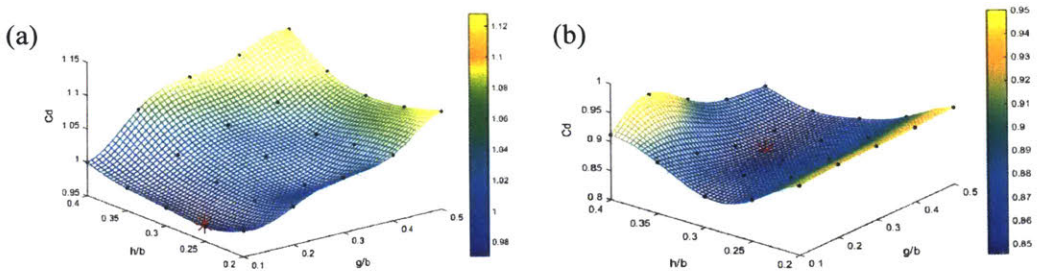

Figure 6-21: Surrogate surfaces built from the drag coefficients obtained with (a) the STRUCT-ε model, (b) the RKE model; the corresponding optimal solutions are marked with red stars.

2) Individuals are evaluated by their fitness values. The fitness function, defined by the objective function, should be positive and reaches a maximum when the objective function is minimized. Notice that any minimization problem can be turned into an equivalent maximization problem. In this study, the fitness function is defined as the sequence number after all the N_p drag coefficient values are sorted in descending order.

3) Offspring are produced through three genetic operators: selection, crossover, and mutation. Pairs of individuals to produce offspring are selected from the existing population (parent population) through roulette wheel sampling [149], in which the selection probability of one individual is proportional to its fitness value. With probability $P_c = 0.7$, the crossover is applied to a pair of selected individuals by choosing a random point on a chromosome and swapping the gene beyond the point, resulting in two offspring. With probability $P_m = 0.05$, mutation alters random bits on each offsprings chromosome from 1 to 0 or vice versa.

4) After generating the offspring, $\mu+\lambda$ selection scheme is used for forming the new generation. The best individuals are chosen out of parents and λ offspring like the parent population for the next generation. $\mu=\lambda=N_p$ is used in this study.

5) Check whether convergence is achieved. If so, return the best individual and the minimum value of the objective function found up to now; otherwise, go to

Table 6.12: The optimal solutions obtained with different models.

	g/b	h/b	C_d
STRUCT-ε	0.11	0.26	0.97
RKE	0.33	0.33	0.85

step 2) and start the next iteration (generation). Convergence is defined by a level of similarity between the individuals.

Through successive iterations, the initial population of individuals is evolved towards better ones with higher fitness values. Correspondingly, the drag coefficient value is decreased and optimization is realized.

The optimal solutions obtained for the STRUCT-ε model and the RKE model are given in Table 6.12 and illustrated in Figure 6-21. As the surrogate surfaces for the two turbulence models are significantly different, their optimal solutions also deviate greatly from each other. For the STRUCT-ε model, the smallest drag coefficient of 0.97 occurs when the gap is 0.11 b and the height difference is 0.26 b ; for the RKE model, the minimal drag coefficient of 0.85 is achieved when the gap and the height difference are all 0.33 b.

6.3 Validation of the optimal solutions

The optimal solutions obtained based on the steady simulations using the STRUCT-ε model and the RKE model are validated through LES simulations. A much finer mesh is adopted for the LES simulations with over 12 million cells; the refinement method is similar to the meshes used in the STRUCT-ε model validation study. In addition, steady simulations using the STRUCT-ε and RKE models have also performed at the optimal solutions on the medium resolution meshes.

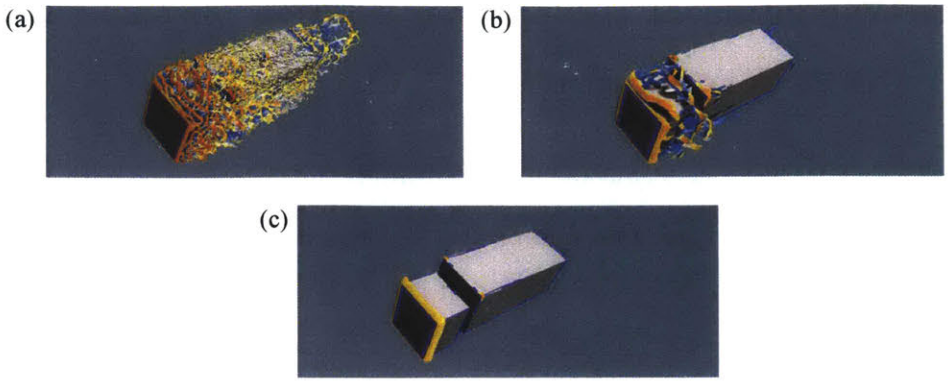

Figure 6-22: Instantaneous iso-surfaces of $Q = 1000/s^2$ for flow past the simplified tractor-trailer model with $g/b = 0.11$ and $h/b = 0.26$ obtained with (a) LES, (b) steady simulation using the STRUCT-ε model, (c) steady simulation using the RKE model.

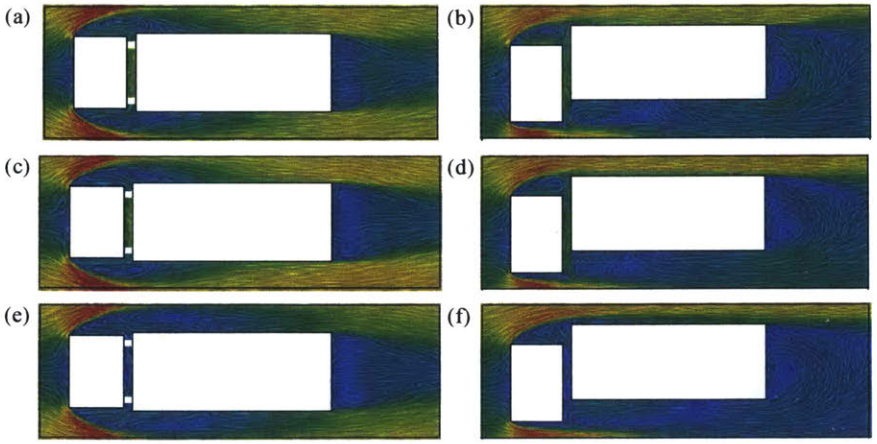

Figure 6-23: Mean streamlines around the tractor-trailer model with $g/b = 0.11$ and $h/b = 0.26$ (a) on the plane $y = 0.46\ b$ obtained with LES, (b) on the plane $z = 0$ obtained with LES, (c) on the plane $y = 0.46\ b$ obtained with steady simulation using the STRUCT-ε model, (d) on the plane $z = 0$ obtained with steady simulation using the STRUCT-ε model, (e) on the plane $y = 0.46\ b$ obtained with steady simulation using the RKE model, (f) on the plane $z = 0$ obtained with steady simulation using the RKE model.

Table 6.13: Drag coefficients predicted by different simulations at the optimal solution obtained with the STRUCT-ε model.

	C_d	Cell number
LES	0.98	12.1 M
STRUCT-ε_Steady	0.98	1.3 M
RKE_Steady	0.87	1.3 M

6.3.1 Validation of the optimal solution obtained with the STRUCT-ε model

First, the simulations are performed at the optimal solution obtained with the STRUCT-ε model, and Table 6.13 gives the comparison of the drag coefficients predicted by LES and steady simulations using the RKE and the STRUCT-ε models. While the drag coefficients obtained by LES and the STRUCT-ε model are the same, the coefficient value obtained by the RKE model is 11% smaller. The STRUCT-ε model provides increased accuracy for the drag prediction in comparison with the RKE model. The instantaneous iso-surfaces are illustrated in Figure 6-22, and clearly the STRUCT-ε model captures some of the turbulent flow structures, enabling better prediction of the flow separation and interaction between the tractor and trailer, therefore resulting in an improved agreement with LES.

The streamline pattern also shows that STRUCT-ε model agrees better with LES, see Figure 6-23. On the plane $y = 0.46\ b$, the RKE model predicts a longer separation region with later reattachment while LES and the STRUCT-ε model generate a smaller region with earlier reattachment, as shown before in the validation of the STRUCT-ε model. On the plane $z = 0$, the streamline patterns generated by the STRUCT-ε model and LES, in general, agree very well. On the other hand, the RKE model overpredicts the separation region on the tractor top, and the separation flow impinges on the front surface of the trailer and enters the gap, causing lower velocity in the gap, and lower pressure on the front surface of the trailer, leading to the lower drag predicted. The gap flow also influences the flow pattern below the trailer with a large circulation, which does not appear in the streamlines generated by LES and the STRUCT-ε model.

Figure 6-24 shows the comparison of the distribution of the pressure coefficient C_p on the front and rear surfaces of the tractor and trailer predicted by LES and steady simulations using the RKE and the STRUCT-ε models on the medium resolution mesh. The drag coefficient contribution from the pressure on the front and back surfaces of the tractor and trailer is given in Table 6.14. On the front surface of

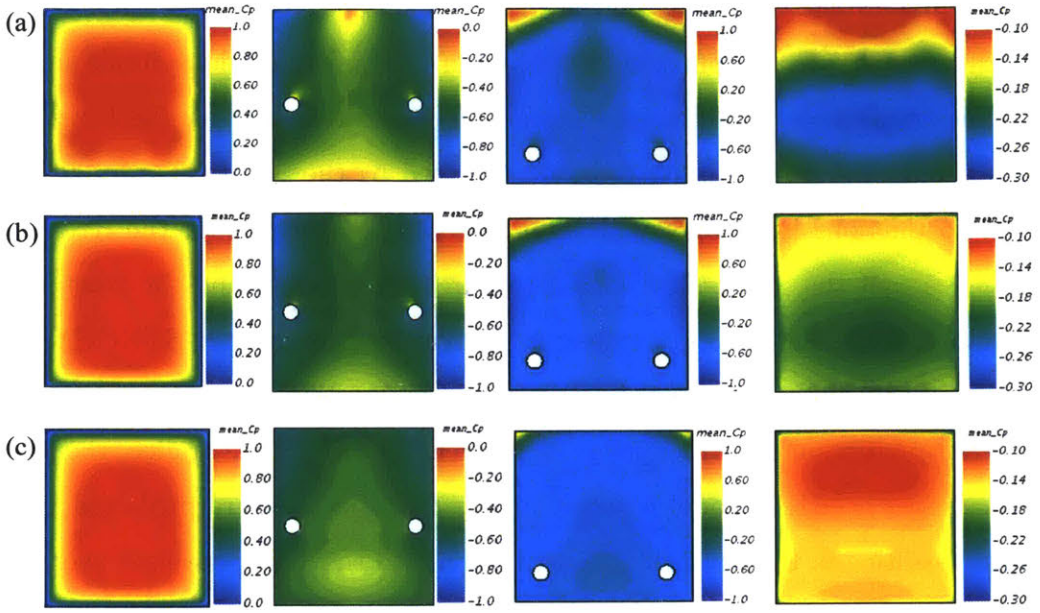

Figure 6-24: Distribution of the mean pressure coefficient on the front and back surfaces of the tractor and trailer with $g/b = 0.11$ and $h/b = 0.26$ obtained with (a) LES, (b) steady simulation using the STRUCT-εmodel, (c) steady simulation using the RKE model. From left to right, the columns correspond to the front surface of the tractor, back surface of the tractor, front surface of the trailer, and back surface of the trailer, respectively.

Table 6.14: Drag coefficient contribution from the pressure on the front and back surfaces of the tractor and trailer with $g/b = 0.11$ and $h/b = 0.26$.

	Tractor_Front surface	Tractor_Back surface	Trailer_Front surface	Trailer_Back surface
LES	0.76	0.45	-0.44	0.21
STRUCT-ε_Steady	0.77	0.47	-0.45	0.17
RKE_Steady	0.77	0.46	-0.51	0.13

the tractor, the pressure distribution predicted by the RKE and the STRUCT-ε model is the same and differs slightly with the distribution generated by LES; this is likely due to the difference in the mesh resolution. The slight difference does not influence the drag coefficient contribution and all simulations result in almost the same C_d_p value. On the rear surface of the tractor and on the front surface of the trailer, the pressure distribution generated by the STRUCT-ε model is very similar to that of LES, while some difference can be observed for the RKE model; this proves that the STRUCT-ε model captures the gap flow and the tractor-trailer interaction. The resulting C_d_p values are similar for LES and the STRUCT-ε result while significant difference exists for the C_d_p value on the front surface of the trailer. The wake prediction is challenging; on the rear surface of the trailer, the pressure predicted by the RKE model is much higher than the pressure predicted by other models, resulting in the lower drag contribution, and the underpredicted overall drag. The difference also exists in the distribution generated by LES and the STRUCT-ε model: LES generates higher pressure in the top part of the plane and lower pressure in the bottom part, while the STRUCT-ε model generates a more even pressure distribution. Due to the difference, the C_d_p value is slightly higher predicted in LES than the STRUCT-ε model. As the overall drag is predicted the same for LES and the STRUCT-ε model, there exists some error cancellation in the drag contribution from different surfaces. However, the improvement of using the STRUCT-ε model is significant when compared with the RKE model whose results significantly deviate from LES.

6.3.2 Validation of the optimal solution obtained with the RKE model

Simulations are then performed at the optimal solution obtained with the RKE model, and Table 6.15 gives the comparison of the drag coefficients predicted by different simulations. While the drag coefficients obtained by LES and the STRUCT-ε model are very similar, the coefficient value obtained by the RKE model is much smaller.

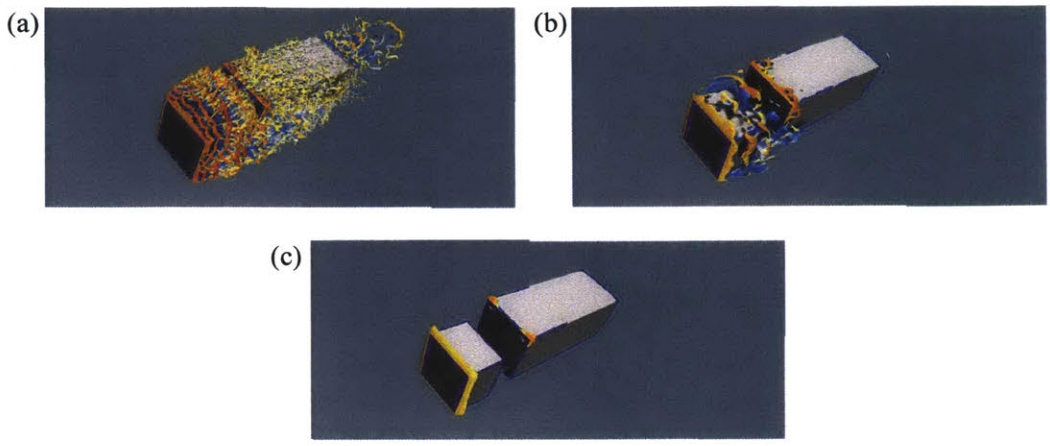

Figure 6-25: Instantaneous isosurfaces of $Q = 1000/s^2$ for flow past the simplified tractor-trailer model with $g/b = 0.11$ and $h/b = 0.26$ obtained with (a) LES, (b) steady simulation using the STRUCT-ε model, (c) steady simulation using the RKE model.

Table 6.15: Drag coefficients predicted by different simulations at the optimal solution obtained with the RKE model.

	C_d	Cell number
LES	1.02	12.2 M
STRUCT-ε_Steady	1.01	1.4 M
RKE_Steady	0.85	1.4 M

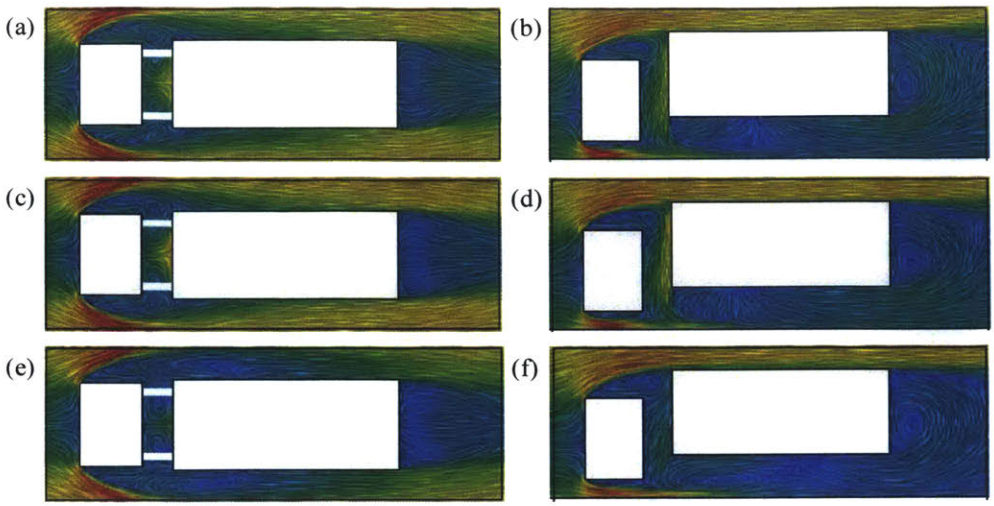

Figure 6-26: Mean streamlines around the tractor-trailer model with $g/b = 0.33$ and $h/b = 0.33$ (a) on the plane $y = 0.46\ b$ obtained with LES, (b) on the plane $z = 0$ obtained with LES, (c) on the plane $y = 0.46\ b$ obtained with steady simulation using the STRUCT-ε model, (d) on the plane $z = 0$ obtained with steady simulation using the STRUCT-ε model, (e) on the plane $y = 0.46\ b$ obtained with steady simulation using the RKE model, (f) on the plane $z = 0$ obtained with steady simulation using the RKE model.

The instantaneous iso-surfaces are illustrated in Figure 6-25. The STRUCT-ε model captures increased turbulent flow structures in comparison with the RKE model, therefore it is able to capture the flow separation and interaction between the tractor and trailer, leading to improved accuracy.

Figure 6-26 shows the comparison of the mean streamlines obtained with different simulations, and the conclusions are very similar to the case of the optimal solution for the STRUCT-ε model. The RKE model tends to overpredict the separation off the tractor, and the inaccurate gap flow predicted leads to the underprediction of the drag and deviation from LES.

Figure 6-27 shows the comparison of the distribution of the pressure coefficient C_p on the front and rear surfaces of the tractor and trailer, and Table 6.16 gives the corresponding drag coefficient contribution. On the front surface of the tractor, the pressure distribution predicted by the RKE and the STRUCT-ε model is the same and differs slightly with the distribution generated by LES, but the drag coefficient contribution is consistent for all simulations. On the rear surface of the tractor and on

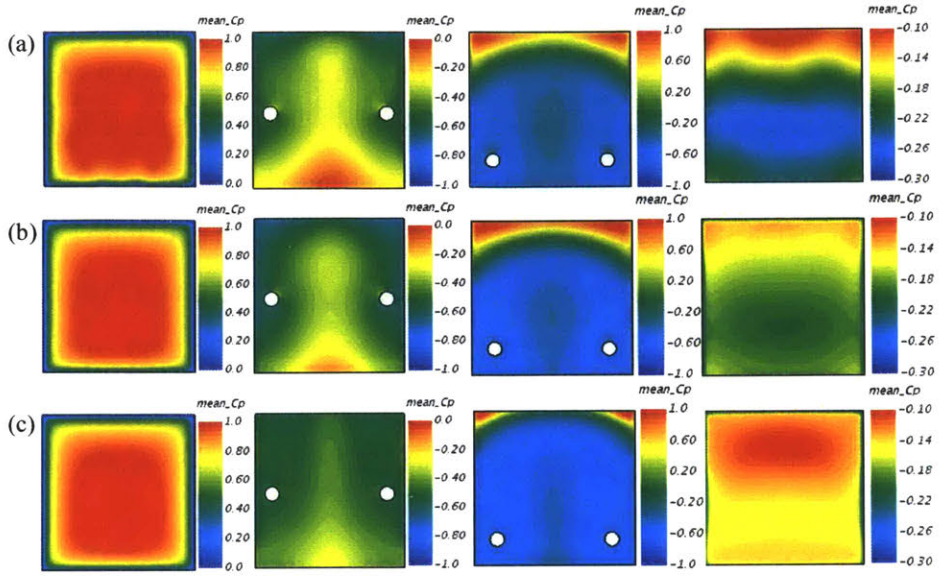

Figure 6-27: Distribution of the mean pressure coefficient on the front and back surfaces of the tractor and trailer with $g/b = 0.33$ and $h/b = 0.33$ obtained with (a) LES, (b) steady simulation using the STRUCT-ε model, (c) steady simulation using the RKE model. From left to right, the columns correspond to the front surface of the tractor, back surface of the tractor, front surface of the trailer, and back surface of the trailer, respectively.

Table 6.16: Drag coefficient contribution from the pressure on the front and back surfaces of trailer and trailer with $g/b = 0.33$ and $h/b = 0.33$.

	Tractor_Front surface	Tractor_Back surface	Trailer_Front surface	Trailer_Back surface
LES	0.72	0.34	-0.27	0.21
STRUCT-ε_Steady	0.71	0.38	-0.28	0.18
RKE_Steady	0.72	0.40	-0.43	0.14

the front surface of the trailer, the pressure distribution generated by the STRUCT-ε model is closer to that of LES compared with the RKE result. The resulting C_{d_p} values are in general consistent between LES and the STRUCT-ε model, while significant difference exists for the RKE model on the front surface of the trailer. On the rear surface of the trailer, the pressure predicted by the RKE model is much higher than that predicted by other models, resulting in the lower C_{d_p} value. The STRUCT-ε model generates a more even pressure distribution than LES, and the resultant C_{d_p} value predicted in LES is slightly higher than the STRUCT-ε model. Some error cancellation exists in the drag contribution from different surfaces, leading to the agreement in the overall drag coefficient between LES and the STRUCT-ε model. Despite the error cancellation, the STRUCT-ε model has again shown much-improved accuracy compared with the RKE model.

6.4 Conclusions

This chapter applied the newly proposed STRUCT-ε model to the optimization of a simplified tractor-trailer to demonstrate the fundamental role of accurate flow resolution to support design optimization. The work was performed in three steps:

1) First, validation of the STRUCT-ε model is performed through comparison with published experiments and LES studies. Simulations using the RKE model are also conducted for comparison purposes. The results show that the STRUCT-ε model outperforms the RKE model for predicting the flow phenomenon and the drag coefficient with a better agreement with the reference data. With the STRUCT-ε model, increased turbulent flow resolution is obtained through the reduction of the turbulent viscosity, which is beneficial for capturing the flow interaction between the tractor and trailer and the flow separation in the wake, leading to the improved accuracy in the drag prediction. The improvement is valid for both steady and unsteady simulations.

2) Optimization of the simplified tractor-trailer model is performed using both the

STRUCT-ε model and the RKE model for comparison. To reduce the computational cost, steady simulations are performed and only two design variables are considered: the gap size and the height difference between the tractor and trailer. Corresponding surrogate models are constructed based on the drag coefficients obtained with 25 steady simulations for different design variables using the STRUCT-ε model and the RKE model, respectively. The shapes of the surrogate surfaces are significantly different, giving rise to the difference of the optimal solutions obtained by minimizing the drag coefficient on the surrogate surfaces using the Genetic Algorithm.

3) Finally, the optimal solutions are validated by LES. Comparison of the results of the steady simulations using the STRUCT-ε model and the RKE model with LES shows that the drag coefficient is underpredicted by the RKE model and the resultant optimal solution is incorrect, while the drag coefficient predicted by the STRUCT-ε model is consistent with the LES result. It demonstrates the value of using the STRUCT-ε model: at a computational cost amenable to industrial applications, it provides improved accuracy for the drag evaluation, and as a result, the optimal solution it generates through optimization is more accurate than the one obtained with the RANS models typically in use.

Chapter 7

Conclusions and futher work

7.1 Summary

The global demand for energy is increasing rapidly due to the population and economic growth. Transportation of passengers and valuable goods share a common energy-intensive trait, due to the high value of the time component of their performance, justifying the higher costs related to the use of more energy. In the U.S., approximately 70% of all petroleum consumption is attributed to transportation, which has become the largest source of carbon emissions and air pollution. In the automotive industry, aerodynamics is a driving factor for energy saving and emission reduction, and optimization of the vehicle shape to minimize the aerodynamic drag has become one of the most significant objectives in the design.

Computational Fluid Dynamics (CFD) is nowadays largely employed as an effective optimization tool in the automotive industry, where high-performance computers are used to numerically solve the flow past the vehicle to estimate the drag. CFD has the potential to provide a high accuracy optimization method, however, its success is severely limited by the poor description of complex unsteady turbulence at a practical computational cost. For the flow past a car, unsteady turbulent flow structures are generated in the separation off the windshield, the mirrors, the wheels, and in the wake of the car body. Capturing these turbulent structures is important for an accurate evaluation of the aerodynamic drag, especially for trains and freight trucks,

where flow interaction between multiple bodies is involved and influences the overall drag. While high fidelity CFD techniques like Direct Numerical Simulation (DNS) and Large Eddy Simulation (LES) are able to capture very well the turbulent structures and to predict the drag with high accuracy, their computational costs are very high for flows at a large Reynolds number, making them infeasible for routine use in the design. The Reynolds Averaged Navier-Stokes (RANS) approach is most widely used for its computationally effectiveness and robustness, but current RANS models have a poor description of complex unsteady turbulence. The need for accurate, computationally effective methods has drawn particular attention to hybrid LES/RANS models, which are aimed at providing increased flow resolution at an achievable computational cost. However, existing hybrid formulations suffer from weaknesses such as strong sensitivity to the grid quality or generation of significant error for complex flows.

To deal with the issues of the existing hybrid models and to better address the industrial need for a robust, grid consistent, and widely applicable hybrid model, Lenci [1] and Baglietto [2] proposed a new hybrid approach, STRUCT, belonging to the category of second-generation URANS models, as introduced by Fröhlich and von Terzi (2008) [76]. The model originates from the recognition of the URANS limitations and the improved performance of the concept has been demonstrated through application to a variety of flow tests, including configurations that had not been addressed successfully by other hybrid models. The STRUCT approach was initially developed aimed at internal flows. When its application is extended to open boundary flows, a robustness issue is identified: undesirable hybrid activations appear when improper inlet conditions are specified.

This thesis addresses the robustness issue of the original STRUCT approach by proposing an improved STRUCT-ε model. The new model replaces the need for Lagrangian average of the original approach with a source term in the ε equation of the standard $k-\varepsilon$ model based on a resolved time scale, as defined by the second invariant of the resolved velocity gradient tensor; the baseline URANS model adopts the nonlinear eddy viscosity formulation of Baglietto and Ninokata [66]. The model

coefficient introduced is selected through sensitivity studies on several test cases including natural transition on the back of a hydrofoil, decaying homogeneous isotropic turbulence, and mild separation in an asymmetric diffuser.

The newly proposed STRUCT-ε model is validated on fundamental flow cases including the flow over periodic hills and the flow in an asymmetric diffuser. While the former one is characterized by flow separation and reattachment and is often used as a test case for hybrid models, the latter case involves mild separation, which has proven to be challenging for current hybrid models. In both cases, reduced turbulent viscosity is generated by the STRUCT-ε model, resulting in the increased resolution of the turbulent structures and improved accuracy in predicting the flow topology in comparison with the commonly used RKE model.

On the basis of the success of the STRUCT-ε model in providing improved accuracy for the fundamental cases, the focus is moved to the automotive industry, and validation studies are performed for the generic simplified vehicle model of the Ahmed body and the generic DrivAer car model. The Ahmed body is characterized by a slant angle in the rear part; at 25° slant angle, the flow partially separates from the rear slant with reattachment half way down the slant back due to the complex interaction between the separation and the counter-rotating vortices coming off the rear window and sides. The STRUCT-ε and the IDDES models provide practically equivalent predictions of the flow topology and similar values for the mean velocity and turbulent stress on the medium and fine resolution meshes. As the mesh becomes coarser however the IDDES approach fails, driving the formation of an incorrect large separation, while the STRUCT-ε model instead consistently demonstrated improved solution also for the coarse mesh results. Comparison between the STRUCT-ε model and the URANS models have elucidated the industrial applicability advantage of the proposed approach: better agreement with the experimental data on the mean velocity and turbulent stress has been achieved through resolving vortical turbulent structures on the slant and in the body wake. For the DrivAer model, two alternative rear configurations (fastback and estate) are validated. While both the STRUCT-ε and the RKE models agree well with the experiment on the fastback configuration,

the STRUCT-ε model shows an advantage on the more challenging estate configuration with improved accuracy for the drag prediction through capturing the flow separation and vortices by generating increased flow resolution.

In addition to the improved accuracy, the STRUCT-ε model also demonstrates mesh consistency and relatively low computational cost. The mesh consistency is much valued for hybrid models, as for many existing hybrid models, inconsistent hybridization often occurs and the solutions are extremely sensitive to the mesh resolution. The computational cost of the STRUCT-ε model is at the same level as the tested URANS approaches, and can be several orders of magnitude lower than LES.

Driven by a practical industry need to further reduce the computational cost in the design optimization, an additional objective of the thesis has been to evaluate the applicability of the STRUCT-ε model to fast running steady-state simulations. The test cases used in the validation studies are simulated with the steady state solver using the STRUCT-ε model and the RKE model for comparison. In all the test cases discussed, the STRUCT-ε model has shown significant improvement with a better agreement with the reference data in comparison with the RKE model. Therefore, the industrial need of achieving reasonable solutions using the fast-running steady simulations can be achieved with the STRUCT-ε model, especially for complex flows including separation and vortices where the traditional RANS models like RKE often fail to capture the correct flow physics.

Finally, the STRUCT-ε model is applied to the optimization of a simplified tractor-trailer to demonstrate its industrial value to support design optimization. First, the STRUCT-ε model is validated through comparison with the published experiment and LES on the tractor-trailer case and compared with the RKE model. Results show that the STRUCT-ε model outperforms the RKE model for predicting the flow phenomenon and the drag coefficient with a better agreement with the reference data. Then optimization of the simplified tractor-trailer model is performed to minimize the drag coefficient using both the STRUCT-ε model and the RKE model for comparison. Corresponding surrogate models are constructed, and optimization is performed on the surrogate surfaces. Different optimal solutions are obtained for the STRUCT-ε

model and the RKE model. Validation by LES shows that the drag coefficient is underpredicted by the RKE model and the resultant optimal solution is incorrect, while the drag coefficient predicted by the STRUCT-ε model is consistent with the LES result. It demonstrates the value of using the STRUCT-ε model: at a computational cost amenable to industrial applications, it provides improved accuracy for the drag evaluation, and as a result, the optimal solution it generates through optimization is more accurate than the one obtained with the RANS models typically in use.

7.2 Futher work

1) The hybridization approach proposed is very general, and the baseline URANS model adopted in this thesis could be modified or replaced for further improvement of the model generality. There are several models that have the potential of addressing the URANS limitation of the inadequacy of the isotropic-viscosity hypothesis. Optimization of the baseline model selection could be conducted based on the industrial applications presented.

2) The near-wall asymptotic behavior of the STRUCT-ε model needs further analysis. In the thesis, near-wall flows are resolved with $y+$ values smaller than 1.0. In typical applications with the classical URANS models, the near-wall flows are modeled with damping functions to achieve consistent behavior integrated to the wall. The same consistent behavior between the core and the near-wall flow of the STRUCT-ε model needs further verification. Additional insights on this aspect have been discussed by Ka-Yau (2019) [150].

3) Currently, the steady-state adoption of the STRUCT-ε model is proposed from an application point of view. Further work should attempt to derive theoretical adjustment to the model formulation. Attempts have been made towards this purpose but were not successful. More work may be needed for a clear mathematical deduction of the proposed steady model if at all possible.

Bibliography

[1] Giancarlo Lenci. *A methodology based on local resolution of turbulent structures for effective modeling of unsteady flows.* PhD thesis, Massachusetts Institute of Technology, 2016.

[2] Emilio Baglietto, Giancarlo Lenci, and Davide Concu. Struct: A second-generation urans approach for effective design of advanced systems. In *ASME 2017 Fluids Engineering Division Summer Meeting.* American Society of Mechanical Engineers Digital Collection, 2017.

[3] Energy information administration, annual energy review, 2009. https://www.eia.gov/totalenergy/data/monthly/index.php.

[4] Rose McCallen, Richard Couch, Juliana Hsu, Fred Browand, Mustapha Hammache, Anthony Leonard, Mark Brady, Kambiz Salari, Walter Rutledge, James Ross, et al. Progress in reducing aerodynamic drag for higher efficiency of heavy duty trucks (class 7-8). Technical report, SAE Technical Paper, 1999.

[5] Nikolaus Adams. Mathematics of large eddy simulation of turbulent flows. by lc berselli, t. iliescu & wj layton. springer, 2006. 348 pp. isbn 987 3 540 26316 6. 74.85. *Journal of Fluid Mechanics*, 582:473–475, 2007.

[6] Nainesh Patel, Mingzhe He, Hassan Hemida, and Andrew Quinn. Large-eddy simulation of the airflow around a truck. https://www.birmingham.ac.uk/research/railway/research/aerodynamics/cfd/nainesh-patel-large-eddy-simulations.aspx.

[7] Nina Gall Jørgensen, Holger Koss, and J Bennetsen. Embedded-les and experiment of turbulent boundary layer flow around a floor-mounted cube. In *The Seventh International Colloquium on Bluff Body Aerodynamics and Applications*, 2012.

[8] Joel H Ferziger and Milovan Perić. *Computational methods for fluid dynamics*, volume 3. Springer, 2002.

[9] Eric Serre, Matthieu Minguez, Richard Pasquetti, Emmanuel Guilmineau, Gan Bo Deng, Michael Kornhaas, Michael Schäfer, Jochen Fröhlich, Christof Hinterberger, and Wolfgang Rodi. On simulating the turbulent flow around the ahmed body: A french–german collaborative evaluation of les and des. *Computers & Fluids*, 78:10–23, 2013.

[10] Lionel Temmerman and Michael A Leschziner. Large eddy simulation of separated flow in a streamwise periodic channel constriction. In *TSFP Digital Library Online*. Begel House Inc., 2001.

[11] Carl U. Buice and John K. Eaton. Experimental Investigation of Flow Through an Asymmetric Plane Diffuser: (Data Bank Contribution)1. *Journal of Fluids Engineering*, 122(2):433–435, 01 2000.

[12] Neil Ashton and Alistair Revell. Comparison of rans and des methods for the drivaer automotive body. Technical report, SAE Technical Paper, 2015.

[13] Emmanuel Guilmineau. Numerical simulations of flow around a realistic generic car model. *SAE International Journal of Passenger Cars-Mechanical Systems*, 7(2014-01-0607):646–653, 2014.

[14] Angelina I Heft, Thomas Indinger, and Nikolaus A Adams. Introduction of a new realistic generic car model for aerodynamic investigations. Technical report, SAE Technical Paper, 2012.

[15] Angelina I Heft, Thomas Indinger, and Nikolaus A Adams. Experimental and numerical investigation of the drivaer model. In *ASME 2012 Fluids Engineering Division Summer Meeting collocated with the ASME 2012 Heat Transfer Summer Conference and the ASME 2012 10th International Conference on Nanochannels, Microchannels, and Minichannels*, pages 41–51. American Society of Mechanical Engineers Digital Collection, 2012.

[16] Jan Östh and Siniša Krajnović. The flow around a simplified tractor-trailer model studied by large eddy simulation. *Journal of Wind Engineering and Industrial Aerodynamics*, 102:36–47, 2012.

[17] Wolf Hucho and Gino Sovran. Aerodynamics of road vehicles. *Annual review of fluid mechanics*, 25(1):485–537, 1993.

[18] JW Allan. Aerodynamic drag and pressure measurements on a simplified tractor-trailer model. *Journal of Wind Engineering and Industrial Aerodynamics*, 9(1-2):125–136, 1981.

[19] Regulation (eu) 2019/631 of the european parliament and of the council of 17 april 2019 setting co2 emission performance standards for new passenger cars and for new light commercial vehicles, and repealing regulations (ec) no 443/2009 and (eu) no 510/2011 (text with eea relevance.). https://eur-lex.europa.eu/eli/reg/2019/631/oj.

[20] Rose McCallen, Kambiz Salari, Jason Ortega, Paul Castellucci, Fred Browand, Mustapha Hammache, Tsun-Ya Hsu, James Ross, Dale Satran, JT Heineck, et al. Doe's effort to reduce truck aerodynamic drag-joint experiments and computations lead to smart design. In *34th AIAA Fluid Dynamics Conference and Exhibit*, page 2249, 2004.

[21] Ki-Sun Song, Seung-On Kang, Sang-Ook Jun, Hoon-Il Park, Jung-Do Kee, Kyu-Hong Kim, and Dong-Ho Lee. Aerodynamic design optimization of rear body shapes of a sedan for drag reduction. *International Journal of Automotive Technology*, 13(6):905–914, 2012.

[22] Ziyu Guo, Yingchao Zhang, and Wei Ding. Optimization of the aerodynamic drag reduction of a passenger hatchback car. *Proceedings of the Institution of Mechanical Engineers, Part G: Journal of Aerospace Engineering*, 233(8):2819–2836, 2019.

[23] Jeff Patten, Brian McAuliffe, William Mayda, and Bernard Tanguay. Review of aerodynamic drag reduction devices for heavy trucks and buses. *National Research Council Canada NRC Technical Report CSTT-HVC-TR*, 205:3, 2012.

[24] Jeffrey W Saunders, Simon Watkins, Peter H Hoffmann, and Frank T Buckley. Comparison of on-road and wind-tunnel tests for tractor-trailer aerodynamic devices, and fuel savings predictions. Technical report, SAE Technical Paper, 1985.

[25] S Watkins, PH Hoffmann, and JW Saunders. Comparison of on-road and wind-tunnel tests for rigid truck aerodynamic devices. In *9th Australasian Fluid Mechanics Conference*, 1988.

[26] S Watkins, JW Saunders, and PH Hoffmann. Comparison of road and wind-tunnel drag reductions for commercial vehicles. *Journal of Wind Engineering and Industrial Aerodynamics*, 49(1-3):411–420, 1993.

[27] WR Davis, ND Eryou, and JC Patry. Operational road tests of truck aerodynamic drag reduction devices. Technical report, SAE Technical Paper, 1977.

[28] Frank T Buckley Jr. Aspects of over-the-road testing of truck aerodynamic drag reducing devices. *SAE Transactions*, pages 4131–4152, 1982.

[29] VK Krastev and G Bella. On the steady and unsteady turbulence modeling in ground vehicle aerodynamic design and optimization. Technical report, SAE Technical Paper, 2011.

[30] William K George. Lectures in turbulence for the 21st century. *Chalmers University of Technology*, 2013.

[31] Hans van Haren. Philosophy and application of high-resolution temperature sensors for stratified waters. *Sensors*, 18(10):3184, 2018.

[32] Hendrik Tennekes, John Leask Lumley, JL Lumley, et al. *A first course in turbulence*. MIT press, 1972.

[33] Tsan-Hsing Shih, William W Liou, Aamir Shabbir, Zhigang Yang, and Jiang Zhu. A new k-ε eddy viscosity model for high reynolds number turbulent flows. *Computers & Fluids*, 24(3):227–238, 1995.

[34] Florian Menter. Zonal two equation kw turbulence models for aerodynamic flows. In *23rd fluid dynamics, plasmadynamics, and lasers conference*, page 2906, 1993.

[35] Florian R Menter. Two-equation eddy-viscosity turbulence models for engineering applications. *AIAA journal*, 32(8):1598–1605, 1994.

[36] PA Durbin. Pa, 1995,separated flow computations with the ke-v2 model,. *AIAA Journal*, 33(4):659–664.

[37] F Billard and D Laurence. A robust k- ε- v2/k elliptic blending turbulence model applied to near-wall, separated and buoyant flows. *International Journal of Heat and Fluid Flow*, 33(1):45–58, 2012.

[38] K Abe, T Kondoh, and Y Nagano. A new turbulence model for predicting fluid flow and heat transfer in separating and reattaching flowsi. flow field calculations. *International journal of heat and mass transfer*, 37(1):139–151, 1994.

[39] Philippe R Spalart. Comments on the feasibility of les for wings, and on a hybrid rans/les approach. In *Proceedings of first AFOSR international conference on DNS/LES*. Greyden Press, 1997.

[40] Philippe R Spalart, Shur Deck, Michael L Shur, Kyle D Squires, M Kh Strelets, and Andrei Travin. A new version of detached-eddy simulation, resistant to ambiguous grid densities. *Theoretical and computational fluid dynamics*, 20(3):181, 2006.

[41] Mikhail L Shur, Philippe R Spalart, Mikhail Kh Strelets, and Andrey K Travin. A hybrid rans-les approach with delayed-des and wall-modelled les capabilities. *International Journal of Heat and Fluid Flow*, 29(6):1638–1649, 2008.

[42] Florian Menter, Martin Kuntz, and Roland Bender. A scale-adaptive simulation model for turbulent flow predictions. In *41st aerospace sciences meeting and exhibit*, page 767, 2003.

[43] https://www.3ds.com/products-services/simulia/products/powerflow/.

[44] https://www.3ds.com/products-services/simulia/products/xflow/.

[45] J Latt et al. Palabos, parallel lattice boltzmann solver. *FlowKit, Lausanne, Switzerland*, 2009.

[46] David P Lockard, Li-Shi Luo, Bart A Singer, and Dennis M Bushnell. Evaluation of the lattice-boltzmann equation solver powerflow for aerodynamic applications. 2000.

[47] Massimo Germano. On the hybrid rans-les of compressible flows. In *Progress in Hybrid RANS-LES Modelling*, pages 253–263. Springer, 2015.

[48] A Leonard. Energy cascade in large-eddy simulations of turbulent fluid flows. In *Advances in geophysics*, volume 18, pages 237–248. Elsevier, 1975.

[49] Joseph Boussinesq. *Essai sur la théorie des eaux courantes.* Impr. nationale, 1877.

[50] David C Wilcox et al. *Turbulence modeling for CFD*, volume 2. DCW industries La Canada, CA, 1998.

[51] Stephen B. Pope. *Turbulent Flows.* Cambridge University Press, 2000.

[52] K Hanjalić and BE Launder. A reynolds stress model of turbulence and its application to thin shear flows. *Journal of fluid Mechanics*, 52(4):609–638, 1972.

[53] WP Jones and Brian Edward Launder. The prediction of laminarization with a two-equation model of turbulence. *International journal of heat and mass transfer*, 15(2):301–314, 1972.

[54] Brian Edward Launder and Dudley Brian Spalding. The numerical computation of turbulent flows. In *Numerical prediction of flow, heat transfer, turbulence and combustion*, pages 96–116. Elsevier, 1983.

[55] Ludwig Prandtl and Karl Wieghardt. *Über ein neues Formelsystem für die ausgebildete Turbulenz.* Vandenhoeck & Ruprecht, 1947.

[56] Wolfgang Rodi. *Turbulence models and their application in hydraulics.* Routledge, 2017.

[57] Andrej Nikolaevich Kolmogorov. Equations of turbulent motion in an incompressible fluid. In *Dokl. Akad. Nauk SSSR*, volume 30, pages 299–303, 1941.

[58] David C Wilcox. Reassessment of the scale-determining equation for advanced turbulence models. *AIAA journal*, 26(11):1299–1310, 1988.

[59] SB Pope. A more general effective-viscosity hypothesis. *Journal of Fluid Mechanics*, 72(2):331–340, 1975.

[60] Charles G Speziale. On nonlinear kl and k-ε models of turbulence. *Journal of Fluid Mechanics*, 178:459–475, 1987.

[61] Shoiti Nisizima and Akira Yoshizawa. Turbulent channel and couette flows using an anisotropic k-epsilon model. *AIAA journal*, 25(3):414–420, 1987.

[62] Robert Rubinstein and J Michael Barton. Nonlinear reynolds stress models and the renormalization group. *Physics of Fluids A: Fluid Dynamics*, 2(8):1472–1476, 1990.

[63] HK Mayong and N Kasagi. prediction of anisotropy of the near-wall turbulence with an anisotropic low-reynolds-number k-ε turbulence model. *ASME J. Fluids Eng*, 112:521–524, 1990.

[64] Kazuhiko Suga. Development and application of a non-linear eddy viscosity model sensitized to stress and strain invariants. *Ph. D. thesis, U. Manchester*, 1995.

[65] FS Lien. Low-reynolds-number eddy-viscosity modelling based on non-linear stress-strain/vorticity relations. In *Proceedings of 3ˆ¡ rd¿ Symposium on Engineering Turbulence Modelling and Measurement, 1996*, 1996.

[66] Emilio Baglietto and Hisashi Ninokata. Anisotropic eddy viscosity modeling for application to industrial engineering internal flows. *International Journal of Transport Phenomena*, 8(2):109, 2006.

[67] Brian Edward Launder, G Jr Reece, and W Rodi. Progress in the development of a reynolds-stress turbulence closure. *Journal of fluid mechanics*, 68(3):537–566, 1975.

[68] Thomas B Gatski and Charles G Speziale. On explicit algebraic stress models for complex turbulent flows. *Journal of fluid Mechanics*, 254:59–78, 1993.

[69] David D Apsley and Michael A Leschziner. A new low-reynolds-number nonlinear two-equation turbulence model for complex flows. *International Journal of Heat and Fluid Flow*, 19(3):209–222, 1998.

[70] K Abe, Y-J Jang, and Michael A Leschziner. An investigation of wall-anisotropy expressions and length-scale equations for non-linear eddy-viscosity models. *International Journal of Heat and Fluid Flow*, 24(2):181–198, 2003.

[71] Joseph Smagorinsky. General circulation experiments with the primitive equations: I. the basic experiment. *Monthly weather review*, 91(3):99–164, 1963.

[72] Massimo Germano, Ugo Piomelli, Parviz Moin, and William H Cabot. A dynamic subgrid-scale eddy viscosity model. *Physics of Fluids A: Fluid Dynamics*, 3(7):1760–1765, 1991.

[73] Franck Nicoud and Frédéric Ducros. Subgrid-scale stress modelling based on the square of the velocity gradient tensor. *Flow, turbulence and Combustion*, 62(3):183–200, 1999.

[74] Dean R Chapman. Computational aerodynamics development and outlook. *AIAA journal*, 17(12):1293–1313, 1979.

[75] Richard Courant, Kurt Friedrichs, and Hans Lewy. Über die partiellen differenzengleichungen der mathematischen physik. *Mathematische annalen*, 100(1):32–74, 1928.

[76] Jochen Fröhlich and Dominic Von Terzi. Hybrid les/rans methods for the simulation of turbulent flows. *Progress in Aerospace Sciences*, 44(5):349–377, 2008.

[77] Pierre Sagaut. *Large eddy simulation for incompressible flows: an introduction.* Springer Science & Business Media, 2006.

[78] Charles G Speziale. Computing non-equilibrium turbulent flows with time-dependent rans and vles. In *Fifteenth International Conference on Numerical Methods in Fluid Dynamics*, pages 123–129. Springer, 1997.

[79] C Speziale. Turbulence modeling for time-dependent rans and vles: a review. *AIAA journal*, 36(2):173–184, 1998.

[80] Florian R Menter, Jochen Schütze, and Mikhail Gritskevich. Global vs. zonal approaches in hybrid rans-les turbulence modelling. In *Progress in Hybrid RANS-LES modelling*, pages 15–28. Springer, 2012.

[81] Dominic A Terzi, Jochen Fröhlich, and Wolfgang Rodi. Hybrid techniques for large–eddy simulations of complex turbulent flows. In *High Performance Computing in Science and Engineering'08*, pages 317–332. Springer, 2009.

[82] Philippe Spalart and Steven Allmaras. A one-equation turbulence model for aerodynamic flows. In *30th aerospace sciences meeting and exhibit*, page 439, 1992.

[83] M Shur, PR Spalart, M Strelets, and A Travin. Detached-eddy simulation of an airfoil at high angle of attack. In *Engineering turbulence modelling and experiments 4*, pages 669–678. Elsevier, 1999.

[84] FR Menter and M Kuntz. Adaptation of eddy-viscosity turbulence models to unsteady separated flow behind vehicles. In *The aerodynamics of heavy vehicles: trucks, buses, and trains*, pages 339–352. Springer, 2004.

[85] M Strelets. Detached eddy simulation of massively separated flows. In *39th Aerospace sciences meeting and exhibit*, page 879, 2001.

[86] A Travin, M Shur, MM Strelets, and PR Spalart. Physical and numerical upgrades in the detached-eddy simulation of complex turbulent flows. In *Advances in LES of complex flows*, pages 239–254. Springer, 2002.

[87] Florian R Menter, Martin Kuntz, and Robin Langtry. Ten years of industrial experience with the sst turbulence model. *Turbulence, heat and mass transfer*, 4(1):625–632, 2003.

[88] Philippe R Spalart. Detached-eddy simulation. *Annual review of fluid mechanics*, 41:181–202, 2009.

[89] Sharath S Girimaji, Ravi Srinivasan, and Euhwan Jeong. Pans turbulence model for seamless transition between rans and les: fixed-point analysis and preliminary results. In *ASME/JSME 2003 4th Joint Fluids Summer Engineering Conference*, pages 1901–1909. American Society of Mechanical Engineers Digital Collection, 2009.

[90] Sharath S Girimaji. Partially-averaged navier-stokes model for turbulence: A reynolds-averaged navier-stokes to direct numerical simulation bridging method. *Journal of Applied Mechanics*, 73(3):413–421, 2006.

[91] Sharath S Girimaji, Eunhwan Jeong, and Ravi Srinivasan. Partially averaged navier-stokes method for turbulence: Fixed point analysis and comparison with unsteady partially averaged navier-stokes. *Journal of Applied Mechanics*, 73(3):422–429, 2006.

[92] FR Menter and Y Egorov. The scale-adaptive simulation method for unsteady turbulent flow predictions. part 1: theory and model description. *Flow, Turbulence and Combustion*, 85(1):113–138, 2010.

[93] Julius C Rotta. Turbulente scherströmungen. In *Turbulente Strömungen*, pages 127–186. Springer, 1972.

[94] Lars Davidson. Evaluation of the sst-sas model: channel flow, asymmetric diffuser and axi-symmetric hill. In *European Conference on Computational Dynamics, ECCOMAS CFD*. Citeseer, 2006.

[95] BL Smith, JH Mahaffy, and K Angele. A cfd benchmarking exercise based on flow mixing in a t-junction. *Nuclear Engineering and Design*, 264:80–88, 2013.

[96] Piotr Zacharzewski, Kathy Simmons, Richard Jefferson-Loveday, and Luigi Capone. Evaluation of the sst-sas model for prediction of separated flow inside turbine internal cooling passages. In *ASME Turbo Expo 2016: Turbomachinery Technical Conference and Exposition*. American Society of Mechanical Engineers Digital Collection, 2016.

[97] Emilio Baglietto and Hisashi Ninokata. Improved turbulence modeling for performance evaluation of novel fuel designs. *Nuclear technology*, 158(2):237–248, 2007.

[98] Julian CR Hunt, Alan A Wray, and Parviz Moin. Eddies, streams, and convergence zones in turbulent flows. 1988.

[99] Stuart Chester, Fabrice Charlette, and Charles Meneveau. Dynamic model for les without test filtering: quantifying the accuracy of taylor series approximations. *Theoretical and computational fluid dynamics*, 15(3):165–181, 2001.

[100] Charles Meneveau, Thomas S Lund, and William H Cabot. A lagrangian dynamic subgrid-scale model of turbulence. *Journal of fluid mechanics*, 319:353–385, 1996.

[101] Venkat Venkatakrishnan. On the accuracy of limiters and convergence to steady state solutions. In *31st Aerospace Sciences Meeting*, page 880, 1993.

[102] CD-adapco. Star-ccm+ documentation version 13.02, 2018.

[103] Eiji Shima, Keiichi Kitamura, and Takanori Haga. Green–gauss/weighted-least-squares hybrid gradient reconstruction for arbitrary polyhedra unstructured grids. *AIAA journal*, 51(11):2740–2747, 2013.

[104] Suhas V Patankar and D Brian Spalding. A calculation procedure for heat, mass and momentum transfer in three-dimensional parabolic flows. In *Numerical Prediction of Flow, Heat Transfer, Turbulence and Combustion*, pages 54–73. Elsevier, 1983.

[105] Wolfgang Rodi. Prediction of laminar-turbulent transition with dns, les and rans methods, 2011.

[106] Robert J McGhee, Betty S Walker, and Betty F Millard. Experimental results for the eppler 387 airfoil at low reynolds numbers in the langley low-turbulence pressure tunnel. 1988.

[107] Genevieve Comte-Bellot and Stanley Corrsin. Simple eulerian time correlation of full-and narrow-band velocity signals in grid-generated,isotropicturbulence. *Journal of Fluid Mechanics*, 48(2):273 337, 1971.

[108] Initial conditions for large-eddy simulation of decaying homogeneous isotropic turbulence. www.stanford.edu/ hjbae/CBC.

[109] Carl U Buice and John K Eaton. Experimental investigation of flow through an asymmetrical plane diffuser. 1996.

[110] Simon E Gant. Reliability issues of les-related approaches in an industrial context. *Flow, turbulence and combustion*, 84(2):325, 2010.

[111] Syed R Ahmed, G Ramm, and G Faltin. Some salient features of the time-averaged ground vehicle wake. Technical report, SAE Technical Paper, 1984.

[112] J.-P. , R. Bonnet. Proc. 10th ercoftac/iahr/qnet-cfd workshop on refined turbulence modelling. *Laboratoire detudes Aerodynamiques, UMR CNRS 6609, Universite de Poitiers, France.*, 2003.

[113] Jester-Z urker R. Tropea C. Jakirlic, S. The 9th ercoftac/iahr/cost workshop on refined turbulence modelling. *Darmstadt, Germany*, 2001.

[114] Frohlich J. Rodi W. Mellen, C. P. Procedure for estimation and reporting of uncertainty due to discretization in cfd applications. *Proc. IMACS World Congress (ed. M. Deville R. Owens), Lausanne.*, 2000.

[115] Ulka Gaitonde, Y Gong, and FX Tanner. Quality criteria for large eddy simulation. *First year transfer report. School of MACE, University of Manchester*, 2008.

[116] Mårten T Landahl, Eric Mollo-Christensen, and Murray S Korman. Turbulence and random processes in fluid mechanics, 1989.

[117] Frohlich J. Rodi W. Mellen, C. P. Large eddy simulation of the flow over periodic hills. *Proc. IMACS World Congress (ed. M. Deville R. Owens), Lausanne.*, 2000.

[118] Jochen Fröhlich, Christopher P Mellen, Wolfgang Rodi, Lionel Temmerman, and Michael A LESchziner. Highly resolved large-eddy simulation of separated flow in a channel with streamwise periodic constrictions. *Journal of Fluid Mechanics*, 526:19–66, 2005.

[119] the University of Manchester. Computational fluid dynamics and turbulence mechanics. http://cfd.mace.manchester.ac.uk/twiki/bin/view/CfdTm.

[120] Breuer Rapp Manhart Froehlich Mellen Rodi, Temmerman Leschziner. Advanced turbulence simulation for aerodynamic application challenges: 2d periodic hill. http://cfd.mace.manchester.ac.uk/twiki/bin/view/ATAAC/TestCase001PeriodicHill.

[121] Ilhan Bayraktar, Drew Landman, and Oktay Baysal. Experimental and computational investigation of ahmed body for ground vehicle aerodynamics. Technical report, SAE Technical Paper, 2001.

[122] Hermann Lienhart, C Stoots, and Stefan Becker. Flow and turbulence structures in the wake of a simplified car model (ahmed modell). In *New Results in Numerical and Experimental Fluid Mechanics III*, pages 323–330. Springer, 2002.

[123] Hermann Lienhart and Stefan Becker. Flow and turbulence structure in the wake of a simplified car model. *SAE transactions*, pages 785–796, 2003.

[124] Walter Meile, Günter Brenn, Aaron Reppenhagen, Bernhard Lechner, and Anton Fuchs. Experiments and numerical simulations on the aerodynamics of the ahmed body. *CFD letters*, 3(1):32–39, 2011.

[125] Boris Conan, Jérôme Anthoine, and Philippe Planquart. Experimental aerodynamic study of a car-type bluff body. *Experiments in fluids*, 50(5):1273–1284, 2011.

[126] Adrien Thacker, S Aubrun, A Leroy, and Philippe Devinant. Effects of suppressing the 3d separation on the rear slant on the flow structures around an ahmed body. *Journal of Wind Engineering and Industrial Aerodynamics*, 107:237–243, 2012.

[127] FJ Bello-Millán, T Mäkelä, L Parras, C Del Pino, and C Ferrera. Experimental study on ahmed's body drag coefficient for different yaw angles. *Journal of Wind Engineering and Industrial Aerodynamics*, 157:140–144, 2016.

[128] Taeyoung Han. Computational analysis of three-dimensional turbulent flow around a bluff body in ground proximity. *AIAA journal*, 27(9):1213–1219, 1989.

[129] Patrick Gilliéron and Francis Chometon. Modelling of stationary three-dimensional separated air flows around an ahmed reference model. In *ESAIM: Proceedings*, volume 7, pages 173–182. EDP Sciences, 1999.

[130] Emmanuel Guilmineau. Computational study of flow around a simplified car body. *Journal of wind engineering and industrial aerodynamics*, 96(6-7):1207–1217, 2008.

[131] Christof Hinterberger, M Garcia-Villalba, and W Rodi. Large eddy simulation of flow around the ahmed body. In *The aerodynamics of heavy vehicles: trucks, buses, and trains*, pages 77–87. Springer, 2004.

[132] Sinia Krajnovi and Lars Davidson. Flow Around a Simplified Car, Part 1: Large Eddy Simulation. *Journal of Fluids Engineering*, 127(5):907–918, 05 2005.

[133] DE Aljure, O Lehmkuhl, I Rodríguez, and A Oliva. Flow and turbulent structures around simplified car models. *Computers & Fluids*, 96:122–135, 2014.

[134] Kuntz M. Menter FR. Development and application of a zonal des turbulence model for cfx-5. Technical report, CFX-Validation Report, 2003.

[135] Sagar Kapadia, Subrata Roy, Matthew Vallero, Kenneth Wurtzler, and James Forsythe. Detached-eddy simulation over a reference ahmed car model. In *Direct and large-eddy simulation V*, pages 481–488. Springer, 2004.

[136] Emmanuel Guilmineau, GanBo Deng, and Jeroen Wackers. Numerical simulation with a des approach for automotive flows. *Journal of Fluids and Structures*, 27(5-6):807–816, 2011.

[137] N Ashton, A Revell, and R Poletto. Grey-area mitigation for the ahmed car body using embedded ddes. In *Progress in Hybrid RANS-LES Modelling*, pages 119–129. Springer, 2015.

[138] E Guilmineau, GB Deng, A Leroyer, P Queutey, M Visonneau, and J Wackers. Assessment of hybrid rans-les formulations for flow simulation around the ahmed body. *Computers & Fluids*, 176:302–319, 2018.

[139] Christoph Strangfeld, Dirk Wieser, Hanns-Joachim Schmidt, Rene Woszidlo, Christian Nayeri, and Christian Paschereit. Experimental study of baseline flow characteristics for the realistic car model drivaer. Technical report, SAE Technical Paper, 2013.

[140] Dirk Wieser, Hanns-Joachim Schmidt, Stefan Müller, Christoph Strangfeld, Christian Nayeri, and Christian Paschereit. Experimental comparison of the aerodynamic behavior of fastback and notchback drivaer models. *SAE International Journal of Passenger Cars-Mechanical Systems*, 7(2014-01-0613):682–691, 2014.

[141] T Avadiar, MC Thompson, J Sheridan, and D Burton. Characterisation of the wake of the drivaer estate vehicle. *Journal of Wind Engineering and Industrial Aerodynamics*, 177:242–259, 2018.

[142] Brett C Peters, Mesbah Uddin, Jeremy Bain, Alex Curley, and Maxwell Henry. Simulating drivaer with structured finite difference overset grids. Technical report, SAE Technical Paper, 2015.

[143] Raman Yazdani. Steady and unsteady numerical analysis of the drivaer model. Master's thesis, Chalmers University of Technology, 2015.

[144] Neil Ashton, A West, S Lardeau, and A Revell. Assessment of rans and des methods for realistic automotive models. *Computers & Fluids*, 128:1–15, 2016.

[145] Suad Jakirlic, Lukas Kutej, Daniel Hanssmann, Branislav Basara, and Cameron Tropea. Eddy-resolving simulations of the notchback drivaermodel: Influence of underbody geometry and wheels rotation on aerodynamic behaviour. Technical report, SAE Technical Paper, 2016.

[146] DE Aljure, J Calafell, A Baez, and A Oliva. Flow over a realistic car model: Wall modeled large eddy simulations assessment and unsteady effects. *Journal of Wind Engineering and Industrial Aerodynamics*, 174:225–240, 2018.

[147] Mario Ruettgers, Junshin Park, and Donghyun You. Large-eddy simulation of turbulent flow over the drivaer fastback vehicle model. *Journal of Wind Engineering and Industrial Aerodynamics*, 186:123–138, 2019.

[148] Søren Nymand Lophaven, Hans Bruun Nielsen, and Jacob Søndergaard. Dace-a matlab kriging toolbox, version 2.0. 2002.

[149] Adam Lipowski and Dorota Lipowska. Roulette-wheel selection via stochastic acceptance. *Physica A: Statistical Mechanics and its Applications*, 391(6):2193–2196, 2012.

[150] Ka-Yen Yau. Application of computational fluid dynamics (cfd) hybrid turbulence model, struct-ε, on turbulent heated flow cases. Master's thesis, Massachusetts Institute of Technology, 2019.